Title

Exploring the thermal and chemical coupling between the silicate cores and hydrogen atmospheres of super-Earth and sub-Neptune exoplanets

Author

Misener, William

Publication Date

2024

UNIVERSITY OF CALIFORNIA
Los Angeles

Exploring the thermal and chemical coupling between the silicate cores and hydrogen atmospheres of super-Earth and sub-Neptune exoplanets

A dissertation submitted in partial satisfaction
of the requirements for the degree
Doctor of Philosophy in Planetary Science

by

William Kennedy Misener

2024

ABSTRACT OF THE DISSERTATION

Exploring the thermal and chemical coupling between the silicate cores and hydrogen atmospheres of super-Earth and sub-Neptune exoplanets

by

William Kennedy Misener
Doctor of Philosophy in Planetary Science
University of California, Los Angeles, 2024
Professor Hilke E. Schlichting, Chair

Planets with radii between 1 and 4 Earth radii and orbital periods shorter than Mercury's are the most common class of planet discovered to date. Detailed measurements of the masses and radii of these planets indicate that a 'radius valley' separates the smaller super-Earths, with densities consistent with an Earth-like composition, from the sub-Neptunes, larger planets with lower densities. A leading theory consistent with astronomical observations posits that these planets all formed with hydrogen atmospheres that greatly increase their observed radii. Over time, the super-Earths lost these atmospheres via a hydrodynamic wind, heated by the star's bolometric luminosity and sustained by the heat released from the silicate-rich interior, while sub-Neptunes retained them. My dissertation work reveals that the nature of the connection between the interior silicates and atmospheric hydrogen has broad implications for the atmospheric composition and evolution of these planets. I find that the thermal coupling of the interior and atmosphere, which sustains atmospheric escape, can also lead to its end, as the interiors cool more efficiently as the atmosphere is stripped. I demonstrate that chemical equilibrium in the deep envelopes of sub-Neptunes, which implies high silicate vapor concentrations that decline with altitude, leads to structural changes in the atmosphere. Convection is inhibited by the strong molecular weight gradients, creating a highly super-adiabatic region that increases the atmospheric mass inferred around observed planets. I show that reactions between the silicates and hydrogen produce novel reduced silicon species and abundant endogenic water vapor in sub-Neptunes. Finally, I apply a hydrodynamic radiative transfer model to core-powered mass loss for the first time, demonstrating that the inclusion of multi-band opacities fundamentally alters predicted mass loss rates. Together, this work opens a new window into the atmospheres and interiors of the most abundant planets known in the Galaxy.

The dissertation of William Kennedy Misener is approved.

Jonathan L. Mitchell

Erik A. Petigura

Edward D. Young

Hilke E. Schlichting, Committee Chair

University of California, Los Angeles

2024

TABLE OF CONTENTS

LIST OF FIGURES

ACKNOWLEDGMENTS

Firstly, I am incredibly grateful to my advisor, Hilke Schlichting, for giving me the opportunity to complete this work. Her care, support, insight, guidance, and curiosity have been essential to my development as a scientist and growth as a person over the course of completing this degree. I have greatly enjoyed exploring new and unfamiliar worlds with her, and I will miss her popping in to the office for a research update and chocolate. My scientific collaborators during my graduate student career have also been indispensable in making these scientific inroads: I thank Edward Young for the spirited conversations about chemical equilibrium, James Owen for the ever-insightful comments about planetary evolution (and for graciously forgiving me for missing a seconds-to-years conversion and claiming photo-evaporation was ineffective as the reviewer of my first PhD paper), and Matthäus Schulik for patiently helping me wrangle AIOLOS. I would also like to thank Jonathan Mitchell and Erik Petigura, who as members of my dissertation committee have been generous with their time and advice.

My time at UCLA would not have been complete without my friends and peers. I am especially indebted to my office mates Akash Gupta and James Rogers, whose generosity with their conversation, wisdom, and experience saved me from many scientific errors and emotional spirals. The other grad students made EPSS a department I was happy to be a part of, and I will forever be glad I crossed paths with Mark Hubbert, Leslie Insixiengmay, Taylor Dorn, Francisco Spaulding-Astudillo, David Yousavich, Tyler Powell, Ariel Graykowski, Kyle Webster, Emily Whittaker, Jaahnavee Venkatraman, Heather Kirkpatrick, Yufan Xu, Emily Hawkins, Ashley Schoenfeld, Colin Wilkins, Krista Sawchuk, Andrew Parisi, Kaitlyn McCain, Xiyuan Bao, Kevin Shao, Justin Higa, Jason Utas, Travis Gilmore, David James, Max Parks, Sarah Marcum, Valeria Jaramillo, Megan Li, Brandon Park Coy, Elisha Jhoti, Matthew Bogumil, Joshua Lee, Joseph Lewis-Merrill, Nathan Pulver, Lauren Tafla, Isabella Trierweiler, Jordan Bretzfelder, Rob Ulrich, Lizet Casillas, Hanzhang Chen, Saeed Mohanna, Julia Miller, Abe Amiri, and many others. I would like to thank the leadership of the UAW 2865 union, who fought for graduate students to an extent I did not previously realize was possible and indirectly led to my first appearance in the *Los Angeles Times*, kazoo and strike picket sign in hand. I am also grateful for staff at UCLA without whom conducting this research would not have been possible, especially Lauri Holbrook, Tasha Taylor, Carlene Brown, Kelli Yang, Elyse Chou, Eric Wessenauer, and the staff of the Music Cafe, whose caffeine powered much of this research. I also thank the operators of the Big Blue Bus. Lastly, I would like to acknowledge the UCLA Graduate Division for providing financial support for my final year, and the writing of much of this dissertation, via the Dissertation Year Fellowship.

I have been lucky enough to have the opportunity to meet so many wonderful scientists who have inspired my pursuits to new levels. One very valuable source of insight has been the AEThER collaboration, and I would particularly like to thank Anat Shahar, Peter Gao, Johanna Teske, Ray Pierrehumbert, Namrah Habib, Anjali Piette, Eliza Kempton, Matthew Nixon, and Jegug Ih for the opportunity to discuss planets and future directions with them. There are so many others I have met around the world that have given me not only exciting scientific directions to pursue but also kindness and a feeling of community that I am so grateful for, including David Rice, Sarah Milholland, Jonathan Fortney, Mark Swain, Raissa Estrela, Steve Markham, Ethan Schreyer, Tamara Rogers, Malena Rice, Shreyas Vissapragada, Leslie Rogers, and too many others to list here.

Many people gave their time and energy into making me the scientist I am today, so I would like to thank all of my teachers and mentors through my time at Stuart Hall for Boys, International High School, and the University of Chicago. Perhaps the most important and formative opportunity I have ever received was to work with Fred Ciesla and Sebastiaan Krijt on my first real scientific research as an undergraduate. I will be forever thankful for the opportunity and for the incredible mentorship they provided while launching my career in planetary science. I would also like to thank William Duncan; despite being the only person in 11th grade interested in HL Physics, I hope I made up for it by being *really* interested.

My longtime friends have long been a source of sanity and happiness in my life. Especially to Russell Bailey, Adie Tuohey, Jasmin Lee, Hadiya Hewitt, Sophia Chun, Hannah Saftler, Guard

Robinson, Erin Minus, and Elyssa Tong, thanks for putting up with a nerd. I would be remiss not to thank my Covid roommates Shah Khan, Sarah Harris, Adam Lessing, and Matthew Marquez, who sort of agreed to let me show up at their house in Daly City for a week or two in March 2020 and then graciously allowed me to stay for nine months. Thanks also to PB and the other friends. Lastly, thanks to the San Francisco Giants and *Animal Crossing* for giving me something else to worry about besides science.

My family has been so incredibly supportive of my scientific pursuits, and I am so grateful to them for their love, care, and encouragement. The deepest thanks to my mother, Kathleen Kennedy, and my father, James Misener, for making my academic journey possible in so many ways with their love and support. I have to imagine celebrating Moon Day and attending UCLA football games growing up led in no small part to this doctorate. I am also thankful for Colleen Serafin, Wiley Kennedy Jr., Ursula E. Kennedy, Wiley Kennedy III, Ursula Ann Roberts, Samantha Roberts, Kelly Roberts, Miranda Dershimer, and Paul Heer. The memories of Seiko Misener, Al Misener, and Scott Roberts will always be in my heart.

Last but not least, to Maya Subbakrishna, without whom this would not have been possible in so many ways. Her support has been the foundation underlying so much of the work contained here, and I will be eternally grateful for all she has done for me. I am so lucky to have her in my life, and I am so excited to see what our future holds.

VITA

2021	M.S., Geophysics and Space Physics, UCLA
2018	B.A., Physics with specialization in Astrophysics, University of Chicago

PUBLICATIONS

William Misener, Hilke E. Schlichting, and Edward D. Young. Atmospheres as windows into sub-Neptune interiors: coupled chemistry and structure of hydrogen-silane-water envelopes. *Monthly Notices of the Royal Astronomical Society*, 524:981. 2023.

William Misener and Hilke E. Schlichting. The importance of silicate vapour in determining the structure, radii, and envelope mass fractions of sub-Neptunes. *Monthly Notices of the Royal Astronomical Society*, 514:6025. 2022.

William Misener and Hilke E. Schlichting. To cool is to keep: residual H/He atmospheres of super-Earths and sub-Neptunes. *Monthly Notices of the Royal Astronomical Society*, 503:5658. 2021.

William Misener, Sebastiaan Krijt, and Fred J. Ciesla. Tracking Dust Grains During Transport and Growth in Protoplanetary Disks. *The Astrophysical Journal*, 885:118. 2019.

CHAPTER 1

Introduction

Exoplanets, planets outside of our Solar System, had long been presumed to exist, but their nature was uncertain. From a theoretical perspective, it was unclear whether the formation models that had been carefully constructed to explain the attributes of the familiar planets around the Sun were universal truths about the Universe, or one low-probability outcome of a stochastic process. This question is especially vital in the context of the potential for life elsewhere in the Galaxy: is the formation of Earth-like planets a common or rare outcome of planet formation, and what other types of planetary body could be suitable for life as we do or do not know it?

The discovery of the first exoplanet around a Sun-like star, 51 Pegasi b (Mayor & Queloz, 1995), which was coincidentally published the same month I was born, forced the field of planet formation to reckon with new possibilities in what formation and evolution processes a planet could undergo. It was a ‘Hot Jupiter’, a planet with a mass comparable to the Solar System gas giants, but with an orbital period of only 4 days. This is inconceivably close to its star by Solar System standards: the Parker Solar Probe has not, as of early 2024, reached a perihelion smaller than 51 Pegasi b’s semi-major axis.

While each discovery of a new exoplanet is an exciting window into an alien planetary system, the true power of exoplanetary science for understanding planet formation may come in its counting statistics. In the 28 years since the discovery of 51 Pegasi b, over 5,000 exoplanets have been found. The volume of discoveries, especially through carefully designed survey missions like the *Kepler Space Telescope*, has allowed tests of planet formation and evolution theories on a sample of thousands of planetary systems, rather than the one we had previously been constrained to.

One finding of these surveys is that Hot Jupiters like 51 Pegasi b are intrinsically rare outcomes of planet formation: only 1% of Sun-like stars have one in orbit, in spite of observational biases making their discovery relatively easy (e.g. Fressin et al., 2013). However, *Kepler*'s major discovery was the ubiquity of another class of planet: the super-Earths and sub-Neptunes. These planets are so-named because they have sizes in between those of Earth (1 Earth radius, $R_\oplus$) and Neptune ($\sim 4\ R_\oplus$). Due to the length of the survey, *Kepler* was only able to place occurrence constraints on planets with orbital periods less than 100 days, roughly the orbital period of Mercury. *Kepler* revealed that about 50% of Sun-like stars are orbited by at least one such close-in super-Earth or sub-Neptune (e.g. Fressin et al., 2013). These planets occupy both a size range and an orbital period range that the Solar System completely lacks. Their existence was unexpected by existing planet formation models, and their prevalence prevents them from being ascribed to an anomalous formation outcome. Simply put, nature favors producing such planets. It is now up to scientists to understand them, and in doing so turn these astronomical objects into the subject of (exo-)planetary science. The 2021 launch of the *James Webb Space Telescope*, which is capable of observing the upper stratospheres of small exoplanets (e.g. Kempton et al., 2023; Madhusudhan et al., 2023; Benneke et al., 2024), has brought even more urgency to the task of understanding these planets as physical and chemical systems.

My Ph.D. thesis work has applied the principles of physics and chemistry to increase our understanding of super-Earth and sub-Neptune exoplanets. In the chapters contained herein, I present a series of papers exploring the evolution of these planets. In particular, my thesis focuses on how the interior composition and thermal energy alters the atmospheric properties and evolution we should expect of small planets. My work demonstrates the importance of an approach that incorporates the whole planet system for interpreting observations of these exciting new worlds, and points the way toward exciting new directions in exoplanet science. To begin, in the following sections of this Introduction, I will present an overview of the relevant observational and theoretical work that has motivated my thesis chapters.

1.1 Observations

The planets and other bodies of the Solar System have been studied for thousands of years. Their proximity has made them the targets of space missions for decades and allows a host of techniques revealing details about their atmospheres, surfaces, and interiors. New missions and observations continue to shape our detailed knowledge of the Solar System planets and provide stringent constraints for their past evolution. In contrast, the measured physical constraints obtainable for most observed small exoplanets are constrained to their bulk properties: radii, masses, and orbital periods. In addition, the upper atmospheric composition of some small planets can be probed. These observables reflect the techniques used to characterize most of these planets. Exoplanets are usually not bright enough to be observed on their own, especially next to their very bright stellar hosts, although so-called ‘direct imaging’ of exoplanets has detected a handful of exceptional systems (e.g. Marois et al., 2010; Müller et al., 2018) with hopes to extend the technique to Earth-like planets, e.g. with the future *Habitable Worlds Observatory* recommended by the 2021 National Academies of Sciences Astronomy Decadal Survey (National Academies of Sciences & Medicine, 2021). In the meantime, the main methods used to detect exoplanets are indirect and rely on the effects a planet has on our observations of its host star. In the subsections below, I will briefly summarize the Solar System and exoplanet observations relevant to this thesis.

1.1.1 Solar System Observations

The Solar System has long been the basis for inferences about planet formation processes. The Solar System contains eight planets in addition to numerous other bodies. These planets have nearly co-planar orbits around the Sun and are fundamentally divided into the four inner, small, terrestrial planets and the four outer, large, hydrogen gas-rich planets. The four inner planets are all consistent with a rocky mantle and a metallic core of various sizes, with Mercury’s observed bulk density requiring a larger dense core than Earth and Mars a smaller one. Isotopic measurements indicate that Mars formed to roughly its current size within a few million years of the Solar System’s inception (Dauphas & Pourmand, 2011). Earth, on the other hand, seems to have experienced at least one giant impact tens of millions of years later that brought it to its current size and likely formed the Moon (e.g. Wiechert et al., 2001; Thiemens et al., 2019).

The atmospheres of the four inner planets are drastically different despite their relatively similar interior composition. Earth's atmosphere is currently one millionth ($10^{-6}\times$) the mass of the planet, and comprises primarily nitrogen and oxygen, with water an important condensable species. There is evidence that this has not been fixed in time: oxygen became a primary constituent due to biological activity about 2 billion years ago, and reducing conditions likely prevailed early in Earth's history (e.g. Kasting, 1993). These reducing conditions are hypothesized to have been important for abiogenesis (e.g. Wogan et al., 2023). A major unknown is how much water Earth has, and how much it may have accreted. Much of Earth's water budget may be stored in mantle minerals, though estimates vary (e.g. Karato et al., 2020). Earth also has an unknown constituent of its core that is lighter than iron-nickel, lowering the core's density by about 10% (Birch, 1964).

Despite being nearly the same size as Earth, Venus has drastically different surface conditions: its atmosphere is $\sim 100\times$ the mass of Earth's and composed mainly of carbon dioxide. *In situ* measurements of Venus's D/H ratio indicate that it likely experienced preferential escape of its initial hydrogen inventory (Donahue et al., 1982). Mars has a thin atmosphere $\sim 10^{-3}\times$ the mass of Earth's and also composed of carbon dioxide, which can condense at its poles, while Mercury maintains only a tenuous exosphere of evaporated surface rocks.

The outer Solar System planets have strongly reducing, hydrogen-rich atmospheres that are presumed to have been accreted from the protoplanetary disk. Jupiter and Saturn are hydrogen-dominated by mass. It has long been assumed that they have discrete cores made of denser materials like rock and metal. Recent measurements of the higher order gravitational moments of Jupiter by *Juno* (Wahl et al., 2017) and of gravitational harmonics in Saturn via their effects on the structure of its rings (Mankovich & Fuller, 2021) are most consistent with a smooth gradient from hydrogen to denser material, i.e. 'dilute cores'. Uranus and Neptune have hydrogen dominated atmospheres with significant enrichments in metals compared to solar composition. It is not entirely clear from the limited *in situ* observations obtained by Voyager whether their interiors have significant ices, or whether any gradients in composition with depth are smooth transitions or sharp discontinuities (e.g. Helled & Fortney, 2020). One constraint is the anomalously low heat output of Uranus, measured by *Voyager* to be a factor of ten lower than that of Neptune (Pearl et al., 1990; Pearl & Conrath, 1991). A future mission could probe the gravitational moments and reveal more about the interior structure of the outer planets (Movshovitz & Fortney, 2022).

1.1.2 Exoplanet Observations

1.1.2.1 Radii

Planet radii can be obtained via the transit method, in which the host star periodically dims by a consistent amount. The observed fractional reduction in flux is the ratio of the cross-sectional area of the planet to that of the star, leading to an inferred planet radius, given a stellar radius inferred from other observations. This technique relies on the planet's orbit crossing the star along our line of sight, a chance alignment that makes most planets undetectable. However, the transit technique is very amenable to large campaigns that monitor millions of stars to find thousands of planets, and the simple geometry of the alignment problem allows extrapolation of the observed detection rates to a general occurrence rate. This approach has been put into practice to find thousands of small exoplanets. The first large-scale space-based survey was conducted by the *Kepler Space Telescope*, which stared at a fixed small patch of sky. After the failure of one of its reaction wheels disabled consistent pointing, the *K2* mission found further planets across the sky. Currently, the *TESS* mission continues to find transiting exoplanets, with a focus on bright, nearby stars amenable to followup with other techniques. The *Plato* mission will also search for transiting planets.

Early results from the *Kepler* survey demonstrated that small planets, specifically, the aforementioned super-Earth and sub-Neptune population with radii between 1-4 $R_\oplus$ and orbital periods less than 100 days, are common, with about 50% of Sun-like stars appearing to have one in orbit (Fressin et al., 2013). Further developments have come not only from increasing planet discoveries, but also from refinement of the stellar parameters key to inferring actual planet radii from measured flux decreases. In particular, high-resolution spectral followup and the availability of *Gaia* data for *Kepler* host stars improved radius precision to less than 10% for many planets.

The most important development to arise from this increase in precision was the discovery that the small planet population is distributed bimodally in radius, with the so-called 'radius valley' or 'gap' at around 1.8 $R_\oplus$ (Fulton et al., 2017). Further research found that this gap was sloped in orbital period, or, equivalently, in incident flux received by the planet, with the gap occurring at smaller radii for planets further from their star, as shown in Figure 1.1 (e.g. Fulton & Petigura, 2018; Petigura et al., 2022). This observation provides powerful constraints on the formation and evolution of small planets, as I will discuss in Section 1.2. These measurements have also found that the radius valley location increases as a function of stellar mass. The radius valley has been detected in other datasets beyond *Kepler*, such as *K2* (Hardegree-Ullman et al., 2020), confirming its validity across the Galactic population.

1.1.2.2 Masses

Exoplanet masses can also be constrained by independent methods, both driven by the gravitational force exerted by the planet. In the radial velocity method, the orbit of the star around the planet-star center of mass is detected via Doppler shifts in its spectral lines. The maximum velocity is then proportional to the mass of the planet. The first exoplanets around main sequence stars, including 51 Pegasi b, were detected in this manner (Mayor & Queloz, 1995). For large, close-in hot Jupiters, the velocity signal is on the order of km/s, easily detectable even in the 1990s. But an Earth-like planet induces a velocity of only 10 cm/s on a Sun-like host star, making detection more difficult. Recent spectrometer advances have pushed the observational floor below 1 m/s (e.g. Thompson et al., 2016; Gibson et al., 2020; Petersburg et al., 2020; Pepe et al., 2021; Seifahrt et al., 2022). However, at these small signal amplitudes, other physics such as stellar activity become important, making the planetary signature difficult to extract from observational noise (Blunt et al., 2023). In addition, radial velocity measurements are only reliable with a long baseline and numerous

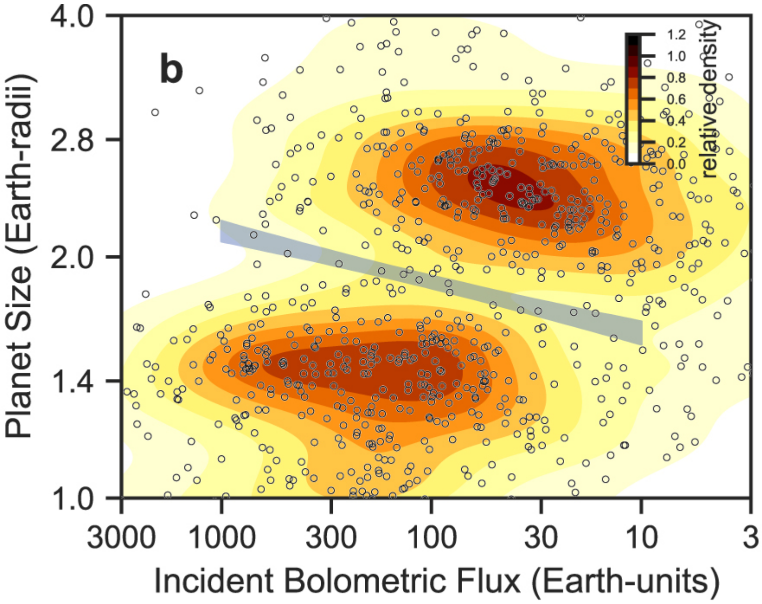

Figure 1.1: Radius distribution of small planets (in Earth radii) as a function of incident flux received (in Earth incident flux). Dots represent observed planets, while colored contours represent the inferred occurrence of planets accounting for observational biases (in arbitrary units). A minimum in planet occurrence termed the ‘radius valley’ (highlighted in blue) separates the larger ‘sub-Neptunes’ from the smaller ‘super-Earths’. The radius separating the populations decreases as the flux received by the planet decreases. Reproduced with permission from Petigura et al. (2022), their Figure 7, panel b.

measurements, making planetary mass measurements observationally expensive.

Another method for extracting planet masses is transit timing variations (e.g. Steffen et al., 2013; Agol & Fabrycky, 2018). In this method, which applies only to multi-planet systems, planet-planet gravitational interactions are detected via the timing of observed transits. In a single planet system, transits should be precisely periodic, but variations will be induced by multiple planets in the system. Detectable variations are mostly limited to systems close to orbital resonances, limiting the method's utility to the broader planet population. Transit timing-based mass measurements are also susceptible to hard-to-quantify systematic errors if there are additional unknown planets in the system (e.g. Libby-Roberts et al., 2024).

If a planet has both its mass and radius measured, a bulk density can be calculated, allowing constraints on the planet's composition. These measurements have shown that small planets have a wide variety of bulk densities, ranging from as low as the gas giants in the Solar System to larger than iron-rich Mercury. However, the population appears to be broadly separated into two categories: small planets, with radii in the 'super-Earth' range, tend to have larger bulk densities that are consistent with an Earth-like composition. Larger planets, with radii in the 'sub-Neptune' range, have lower bulk densities requiring some lighter, volatile component to explain them (Weiss & Marcy, 2014). However, density observations alone cannot determine the nature of the volatile component due to fundamental compositional degeneracies (see Section 1.2 below).

1.1.2.3 Atmospheric compositions

The composition of the atmospheres of exoplanets can be probed using spectroscopy. Two methods have been used to examine small planet atmospheres: transmission and emission spectroscopy. Transmission spectroscopy takes advantage of the fact that during a transit, the host star's light passes through the planet's upper atmosphere. Some of this light can be absorbed by any present molecular species, which manifests as absorption lines at particular wavelengths when an in-transit spectrum is subtracted from an out-of-transit stellar spectrum. Emission spectroscopy uses the different phases of a planet that appear to an observer as the planet orbits its host star. These are observed as a sinusoid change in flux over the course of a planetary orbit, with a sharp drop when the planet goes behind the star. Since it changes periodically, the emission of the planet can be disentangled from the stellar spectrum.

Transmission spectroscopy tends to be sensitive to abundances at pressures in the 10^{-4} to 10^{-6} bar range, while emission spectroscopy probes deeper into the upper atmosphere, down to 10^{-1} bar. The size of a feature, i.e. how much excess absorption or emission is detected, depends on the abundance of the species in question as well as the scale height of the atmosphere, with atmospheres composed of heavier species producing smaller feature sizes (Benneke & Seager, 2012; Fortney et al., 2013). Scattering by aerosols, such as clouds or hazes, can also obscure absorption features, producing a characteristic Rayleigh scattering slope instead. This means that clear, hydrogen-dominated atmospheres provide the strongest signals and are therefore the easiest to detect.

First pioneered on gas giants and brown dwarfs, spectroscopy has been extended to small planets in the last 5-10 years. Pioneering work was undertaken with the *Hubble Space Telescope*, which can probe the visible and near-IR (wavelengths of $\lambda \lesssim 2$ μm). Early results for small planets tended to find featureless spectra (e.g. Kreidberg et al., 2014). Such a non-detection could indicate a high mean molecular weight atmosphere but could not rule out high-altitude aerosols due to the large flux measurement uncertainties. Eventually some sub-Neptunes were found to have water features (e.g. Benneke et al., 2019b). But in a cautionary tale, it was later shown that in the *Hubble* wavelength range, the detected water feature was degenerate with methane (Bézard et al., 2022), highlighting the limitations of staying close to the visible wavelength range. Even so, it has been possible to use *Hubble* detections to make population inferences, such as a possible minimum in atmospheric detectability at intermediate ($\sim$ 700 K) equilibrium temperatures (Brande et al., 2024).

The *James Webb Space Telescope* (*JWST*) has ameliorated the previous concerns of insufficient precision and limited wavelengths, and in doing so is ushering in a revolution in small exoplanet atmospheres. By expanding into the mid-infrared ($\lambda \sim$ 1-25 μm), *JWST* can detect multiple features of water and methane, breaking the *Hubble* degeneracy and allowing estimates of both the abundances of individual species as well as the mean molecular weight in the upper atmosphere. *JWST* can also detect signatures of CO_2, CO, and other simple molecules thought to be important in exoplanet atmospheres. Already, several atmospheric detections have been made for sub-Neptune planets, indicating a wide diversity of atmospheric compositions (e.g. Kempton et al., 2023; Madhusudhan et al., 2023; Barat et al., 2023; Benneke et al., 2024). As this thesis is written, we enter a new age where the field can transition from individual detections to harnessing the counting statistical power of exoplanets to learn about planet formation and atmospheric processes (Batalha et al., 2023).

However, complications remain in the pursuit of small exoplanet atmospheric spectra. The strength of the signal depends on the transit depth, meaning that planets around smaller stars are favored (e.g. Kempton et al., 2018). However, these stars, i.e. late-type M dwarfs, can have molecular features in their photosphere, mimicking atmospheric species (Moran et al., 2023). This bias also introduces a dichotomy with demographic observations: the *Kepler* mission focused on Sun-like stellar hosts, and it is still debated how the trends identified in that population translate to planets around smaller stars (Cloutier & Menou, 2020; Petigura et al., 2022). In addition, accurate molecular weight and abundance inferences require knowing the mass of the planet, which is subject to the difficulties presented above in Section 1.1.2.2.

In addition to atmospheric composition, atmospheric escape can also be probed via transmission spectroscopy. Specifically, absorption in the hydrogen Lyman α wavelength in the UV has been used as a diagnostic of hydrogen escape (e.g. Kulow et al., 2014; Ehrenreich et al., 2015). This measurement is made difficult by the fact that the interstellar medium contains hydrogen, absorbing the core of the feature and leaving only its wings. In addition, this wavelength is absorbed by Earth's atmosphere, requiring space-based measurements. Some of these concerns are overcome by a similar measurement of a metastable helium absorption line at 1083 nm (e.g. Mansfield et al., 2018), which can be detected from ground-based telescopes. Some detections of outflows in the 10^9 g/s range have been made for small exoplanets (e.g. Ehrenreich et al., 2015; Mansfield et al., 2018). However, in both cases, generating a detectable signal depends not only on the escape speed, but on complex physics that determines whether the emitting atomic state is populated. In the former case, Lyman α is emitted by neutral hydrogen, but in a wind, hydrogen is progressively ionized by the solar wind, diminishing the signal (Owen et al., 2023). Similarly, the population of the metastable He state is not yet well-understood. These complexities may explain a number of unexpected non-detections (see Dos Santos (2023) for a recent review). They also make a precise inference of the escape rate more difficult. Another difficulty is that escape is expected to be most vigorous from the youngest planets, i.e. those that orbit the youngest stars. Young stars are both rare and difficult to observe, since they tend to be the most active.

In summary, the various main detection methods of exoplanets provide new windows into the formation and evolution of planets. However, persistent fundamental degeneracies, paired with the difficulty of measuring strong signals on small planets, leave many questions as yet unanswered by observations. Development of new testable hypotheses will be key to interpreting these observations.

1.2 Theory

1.2.1 Formation

Broadly, planet formation begins as micron-sized dust grains coagulate into cm-size pebbles. As a pebble's size increases beyond this, it becomes increasingly poorly coupled to the gaseous disk and experiences drag forces that lead to rapid in-spiraling (Weidenschilling, 1977; Misener et al., 2019). Therefore, rapid coalescence into larger, km-size planetesimals which have sufficient inertia to resist drag is typically invoked, perhaps through hydrodynamic mechanisms such as streaming instabilities (e.g. Yang et al., 2017). These planetesimals then collide with each other and continue accreting migrating pebbles to form larger bodies. Migration through the disk can occur once planets are sufficiently massive to open gaps (e.g. Tanaka et al., 2002), though the specifics of this migration are uncertain.

Planets can start accreting bound atmospheres when their radius of gravitational dominance exceeds the size of the planet. This happens when planets are relatively small, roughly Mars-sized (Ginzburg et al., 2016; Young et al., 2023). Gas accretes to fill the radius then must cool and contract to allow more material in (Lee & Chiang, 2015). If a planet accretes more than roughly its own mass in gas, atmosphere's own self-gravity becomes important, leading to runaway accretion and formation of a gas giant (Pollack et al., 1996). Many exoplanets, as well as Uranus and Neptune, have not undergone this runaway accretion. This implies that gas accretion must have been too slow to reach runaway before the host disks dispersed, which takes a few million years on average (e.g. Mamajek, 2009). This slow accretion can be difficult to reproduce: models tend to find that gas accretion onto sub-Neptune mass planets is faster than the disk lifetime (Lee et al., 2014).

1.2.2 Bulk composition

Typically, four main planet building materials are taken to comprise planets: metal (mostly iron and nickel), rock (mostly magnesium silicates), ices/volatiles (mostly water and methane), and hydrogen/helium gas. These materials reflect the elemental abundances presumed in protoplanetary disks per chondritic and solar abundances (e.g. Lodders, 2021); abundances in exoplanetary systems as measured by material accreted onto white dwarfs appear to be broadly similar (Doyle et al., 2019; Trierweiler et al., 2023). Going outward, rock and metal condense into solids first, at the highest temperatures in the inner disk. Rock and metal do not condense separately, but separate upon being sufficiently heated, initiating core-formation. Ices become stable in solid form beyond the 'ice line', implying that a body with substantial ice composition must have initially accreted in the outer regions of the natal disk. Hydrogen gas is always present.

Importantly, each material has a different typical density: metal is the densest, followed by rock. Ices have intermediate density, and gas is the least dense. This fact of nature means that measurements of density constrain bulk composition. But this inference is usually ambiguous: since there are four materials and only two measurements, the composition is fundamentally degenerate (e.g. Rogers & Seager, 2010; Huang et al., 2022). In a typical case, many sub-Neptunes can be equally well-explained by a water-rich composition of 50% by mass water, 50% Earth-like rock and metal or a 95% Earth-like, 5% low density hydrogen gas composition (e.g. Luque & Pallé, 2022; Rogers et al., 2023).

Each of these end-member degenerate compositions is supported by a hypothesis of sub-Neptune bulk composition. In one, sub-Neptunes accreted 50% or more ice by mass during formation in the outer disk that subsequently migrated inward to their observed locations (Zeng et al., 2019; Venturini et al., 2020; Emsenhuber et al., 2021). While earlier models used condensed water layers, more recent models have used improved water equations of state that allow for super-critical steam layers (e.g. Mousis et al., 2020; Burn et al., 2024). The so-called 'water worlds' hypothesis is supported by the rapid formation of planets near the water ice line, a typical outcome of disk models (e.g. Bitsch et al., 2019). However, such models have difficulty explaining the slope in radius valley with orbital period. In addition, models predicting high abundances of water worlds tend to predict a large population of sub-Neptunes very close to their host stars (Burn et al., 2024), precisely in the identified 'hot Neptune desert' where virtually no planets are observed despite high observational sensitivity (Mazeh et al., 2016). They also predict moderate water contents even for close-in super-Earths (Bitsch et al., 2019), but the densities of the shortest-period super-Earths are consistent with an Earth-like, dry composition (Dai et al., 2019). Migration also entails resonant chain formation, but most planets are not observed to be in resonance (Fabrycky et al., 2014). These resonant chains could later be broken by giant impacts (Izidoro et al., 2022), which are also extremely efficient at stripping primordial atmospheres (Biersteker & Schlichting, 2019). However, giant impacts tend to fill in the radius valley, which is observed to be nearly devoid of planets (Van Eylen et al., 2018), and erase any slope with orbital period. Under one modification to the water world hypothesis, invoked to explain observed observed low molecular weight upper atmospheres observed around some sub-Neptunes (Benneke et al., 2019b), a thin hydrogen envelope is placed over a water ocean (Madhusudhan et al., 2020). While such a composition is consistent with density measurements, it is hard to explain how the hydrogen is maintained against loss and why a condensed ocean is not warmed to super-criticality (Innes et al., 2023).

In the other hypothesis for sub-Neptune composition, planets form close to where they are observed today, implying a rocky interior. These planets then accreted significant hydrogen atmospheres in the disk phase. Some were later lost due to hydrodynamic escape, leaving behind super-Earths. Tenuous atmospheres are lost most easily, while even an atmosphere 1/100th the mass of the planet nearly doubles the planet's size (Lopez & Fortney, 2014), creating the radius valley. Much of my thesis consists of considering the implications of such a composition for sub-Neptune planets, and so I will elaborate on their structure and evolution in the following sections.

1.2.3 Planetary structure

Planetary structure models are necessary to convert between observable features of a planet and its chemical makeup and interior conditions. These models require knowledge of the material properties of the compositions being considered at the appropriate temperatures and pressures (i.e., equations of state), which can be very high in planetary interiors. These conditions are probed by laser-heating diamond anvil cell experiments when possible, but frequently *ab initio* simulations must be used. In the Solar System, interior structure models have been thoroughly refined due to the wealth of data available (e.g. French et al., 2012), but there still exist dramatic uncertainties in the properties of relevant planetary constituent materials, such as hydrogen, helium, and water (e.g. Wilson & Militzer, 2010; Stixrude et al., 2021). These uncertainties are compounded when considering exoplanets. Even the super-Earths and sub-Neptunes considered here have interiors likely to be at temperatures and pressures well beyond those in their Solar System analogs. Due to their formation and evolution, unfamiliar compositions and mixtures of materials are also possible.

The silicate interiors of super-Earths and sub-Neptunes are the subject of much uncertainty. Early studies indicate that the compressibility of silicate magma leads to mass increasing as radius to the $\sim 1/4$ power, more slowly than a constant density model (Valencia et al., 2006; Seager et al., 2007). While the basic mineralogy is presumed to be broadly similar to that of Earth, major differences have been proposed as mass increases, including the inhibition of core formation (Lichtenberg, 2021). One major unknown in light of the likely accretion of significant hydrogen gas from the nebula is how much hydrogen can be ingassed into the interior. Limited experimental data exists (Hirschmann et al., 2012), but large extrapolations are required to reach super-Earth interiors (Kite et al., 2019; Schlichting & Young, 2022). These ingassing rates have significant implications for the evolution (Chachan & Stevenson, 2018) and final atmospheric states (Rogers et al., 2024b) of exoplanets. In atmospheric evolution modeling, the core is often modeled as isothermal and thermally coupled to the base of the atmosphere (Lopez & Fortney, 2014; Ginzburg et al., 2016; Gupta & Schlichting, 2019), with a heat capacity appropriate for molten silicate (Scipioni et al., 2017; Biersteker & Schlichting, 2019).

Hydrogen envelopes are typically modeled as convective at depth, and therefore following an adiabat, then transitioning to an outer radiative region at a radiative-convective boundary (e.g. Rafikov, 2006; Piso & Youdin, 2014; Lee & Chiang, 2015). The outer radiative region is often modeled as isothermal (e.g. Piso & Youdin, 2014). However, the real temperature profile in the outer region depends on the relative opacities to incident stellar and outgoing thermal radiation, which, if not equal, can lead to upper atmosphere temperatures significantly higher or lower than the planet's equilibrium temperature (Hubeny et al., 2003; Guillot, 2010; Parmentier et al., 2015), as long observed in some giant exoplanets (Burrows et al., 2007; Fortney et al., 2008).

Typically, exoplanet compositions have been modeled as discrete layers of metal, rock, ice, and/or hydrogen (e.g. Lopez & Fortney, 2014; Dorn et al., 2017). But the interface between the hydrogen atmosphere and the interior is at very high temperatures, implying a molten surface amenable to significant interactions with the atmosphere. For example, at these temperatures and pressures, water and rock may be significantly miscible (Dorn & Lichtenberg, 2021; Vazan et al., 2022). Rock vapor may also enter the atmosphere (Fegley et al., 2016; Schlichting & Young, 2022; Piette et al., 2023). These chemical contacts between an oxidized magma ocean and reducing hydrogen should also lead to chemical redox reactions, producing abundant endogenic water (Schlichting & Young, 2022). Reactions to produce reduced silicon species, such as silane, SiH_4, are also expected at chemical equilibrium at these temperatures and pressures (Visscher et al., 2010a), though the exact species produced may depend on the atmospheric water content

(Bauschlicher et al., 2023). Diamond anvil cell experiments also observe the production of reduced magnesium and silicon species (Shinozaki et al., 2014, 2016; Kim et al., 2023). These chemical species can potentially produce signatures of the interior composition in the upper atmosphere. The chemical signatures of magma-atmosphere interactions have been studied in low mass hydrogen atmospheres (Zilinskas et al., 2023; Charnoz et al., 2023; Falco et al., 2024). But in this thesis, specifically Chapters 3 and 4, I focus on the magma-atmosphere interactions within the abundant sub-Neptune population, which are known to host hydrogen-rich atmospheres.

Of particular importance is that these rock vapor species act as condensables, decreasing in abundance as the temperature drops with altitude. This can affect planetary structure in a number of ways. For example, when a condensable species is present, then its latent heat changes the thermal profile, adjusting the atmospheric profile to the so-called the moist adiabat (e.g. Graham et al., 2021). Perhaps more drastically, the presence of heavy condensables in a light atmosphere inhibits convection if the induced gradient in molecular weight is strong enough. This gradient overcomes thermal buoyancy, leading to stable stratification of the atmosphere. This mechanism was first pointed out in relation to Solar System gas and ice giants, in which the expected condensable species would be water vapor (Guillot, 1995; Leconte et al., 2017; Markham & Stevenson, 2021) and has also been extended to theoretical water-rich exoplanets with hydrogen atmospheres (Innes et al., 2023). The inhibition of convection has also been shown to be stable to double-diffusive convection (Leconte et al., 2017) and persists in 3D simulations (Leconte et al., 2024). But the physics applies to any condensable species, including rock vapor in a hydrogen atmosphere, which is the subject of my thesis work (see also Markham et al. (2022), which probed similar effects contemporaneously and independently and which was published shortly after my work). Such a chemical gradient of silicates could arise during the initial accretion of small bodies (Brouwers & Ormel, 2020; Ormel et al., 2021; Steinmeyer & Johansen, 2024), but it is a natural byproduct of chemical equilibrium regardless of the details of formation. The temperature gradient in this region depends on the cooling rate of the planet as well as the opacity and conductivity of the region (Vazan & Helled, 2020). Most studies have found the internal flux to be high enough to support a super-adiabatic gradient (Leconte et al., 2017; Markham & Stevenson, 2021; Markham et al., 2022; Innes et al., 2023), but some formation models producing cold interiors can lead to large, highly sub-adiabatic regions (Ormel et al., 2021; Vazan & Ormel, 2023). In Chapter 3 of this thesis, I reveal the effects of these non-adiabatic regions, natural byproducts of the hydrogen-silicate interface, on sub-Neptune structure and evolution.

1.2.4 Evolution and Escape

Atmospheric escape has been studied in the Solar System for decades, but it has found new prominence in planetary science due to its hypothesized vital role in shaping exoplanet demographics. Specifically, ubiquitous atmospheric escape from small exoplanets is consistent with the observed radius valley (e.g. Owen & Wu, 2013, 2017; Gupta & Schlichting, 2019), including its trends in orbital period and stellar mass (Gupta & Schlichting, 2020; Rogers et al., 2021). In fact, Owen & Wu (2013) predicted the existence of the radius valley from models of atmospheric stripping before it was definitively observed. Under this paradigm, the observed super-Earth and sub-Neptune planets formed as a single population with hydrogen-rich atmospheres. Then, atmospheric escape stripped some planets of their primordial envelopes, leaving their exposed silicate cores as the observed super-Earth population. Meanwhile, the observed sub-Neptunes resisted stripping and maintained their low density hydrogen envelopes. These envelopes greatly increase the apparent size of the planet, forming the radius valley.

The theory of atmospheric escape has heritage in studies of the solar wind. In the solar wind problem as well as that of externally heated planets, the boundary conditions consist of one side, at low radius $r \sim 0$, with a high gas density and low gas velocity, and the opposite side, at $r \to \infty$, with a low gas density. The hydrodynamic solution that connects these two regions is a trans-sonic wind flowing away from the central body. In the isothermal limit, this outflow takes the form of a Parker wind, first derived in Parker (1958), which has a simple analytic value for the escape rate. This escape rate increases with the density and temperature at the sonic point, the radius where the outflow reaches the sound speed.

For the large escape rates expected of planets early in their evolution, the collision of hydrogen atoms with any other species present imparts sufficient energy to 'drag' them along. As the escape rate decreases, hydrogen becomes less able to drag these other species (Hunten et al., 1987). Eventually, the flow can become collisionless. At this point, each species effectively follows its own thermal profile, and the hydrogen is much more susceptible to escape than heavier species. This preferential escape of lighter species, i.e. Jeans escape, is hypothesized to have happened to early Venus, explaining its hydrogen-poor but D/H enriched modern atmosphere (Donahue et al., 1982). Under very specific circumstances, such enrichment in heavy species has also been proposed at late times for sub-Neptune planets (e.g. Malsky et al., 2023).

As the disk disperses, the removal of pressure support leads to adiabatic expansion of the accreted gas, unbinding a portion of it. This 'spontaneous mass loss' or 'boil-off' can strip a large fraction ($\gtrsim$ 90%) of the total accreted gas (Owen & Wu, 2016; Ginzburg et al., 2016). More recently, self-consistent simulations including the disk's evaporation, which occurs on timescales $\sim 10^5$ yr (e.g. Koepferl et al., 2013), showed that the mass loss proceeds via a sub-sonic breeze and that the planet's primary cooling mechanism is the advection of gas out of the system (Rogers et al., 2024a).

After spontaneous mass loss, there are two main mechanisms proposed to drive further escape and form the radius valley: photo-evaporation and core-powered mass loss. The difference in the two mechanisms is in the primary heating mechanism in the upper atmosphere. Photo-evaporation relies on the high-energy, XUV radiation from a planet's host star heating the planetary atmosphere, and therefore the outflowing gas, to $\sim 10^4$ K. This drives rapid atmospheric escape, stripping more tenuous atmospheres (Murray-Clay et al., 2009; Owen & Jackson, 2012; Lopez & Fortney, 2013; Owen & Wu, 2013). However, stellar XUV emission declines with time, after a period of 'saturation' lasting ~ 100 Myr (Jackson et al., 2012; Tu et al., 2015), limiting vigorous photo-evaporation to the earliest times in a planet's existence. Stellar XUV emission lasts for longer and is brighter compared to the star's overall luminosity for small M-type stars than around larger F-, G-, and K-type stars (e.g. McDonald et al., 2019), indicating it may be more effective for planets around the smaller stellar hosts that are most often targeted for atmospheric spectroscopy. Whether photo-evaporation is able to strip a planet's hydrogen envelope depends on whether sufficient energy is received over the planet's lifetime to unbind the atmosphere (Owen & Wu, 2017).

Under core-powered mass loss, on the other hand, the outflow is heated only by the bolometric luminosity of the host star (Ginzburg et al., 2016, 2018). This flux heats the atmosphere to roughly the 'equilibrium temperature', which is 500-1500 K for typical observed exoplanets. While high compared to the typical temperatures in the Solar System due to exoplanets' relative proximity to their host stars, these temperatures are much lower than those achieved in a photo-evaporative, XUV-heated wind. Therefore, the predicted mass loss rates are much lower in core-powered mass loss than those found in photo-evaporation. If the planet were gas-dominated by mass, the atmosphere would quickly contract as the planet cools (Lopez & Fortney, 2014), rapidly decreasing the density at the fixed sonic point and halting efficient atmospheric loss. Exactly how quickly depends on the opacity of the atmosphere, which is highly uncertain for exoplanets but tabulated for fiducial atmospheric compositions (e.g. Freedman et al., 2014).

To achieve complete atmospheric stripping, core-powered mass loss relies on the heat stored in the interior. During formation, gravitational binding energy is converted into heat. The surrounding optically thick hydrogen gas poses a bottleneck for cooling, keeping the interior hot for long timescales. For small planets with atmospheric masses a few percent of the planet's total mass, the heat capacity of the interior can be higher than that of the atmosphere (Ikoma & Hori, 2012; Ginzburg et al., 2016). Therefore, as the atmosphere cools into space, the silicate core, thermally coupled to the base of the atmosphere, can resupply sufficient energy to keep the atmosphere hot and inflated. This prevention of contraction sustains atmospheric escape at sufficient rates to completely unbind some primordial envelopes.

Both of these models can reproduce the observed characteristics of the radius valley (Gupta & Schlichting, 2020; Rogers et al., 2021). In particular, both processes predict a valley with a negative slope in radius-orbital period space. This is because with increasing orbital period, the stellar flux, bolometric or high-energy, received by the planet decreases, lowering the mass loss rates. The predicted slopes in radius-orbital period space are slightly different, but a much larger survey than is currently planned would be needed to discern them (Rogers et al., 2021). Both also predict similar core composition distributions, as the location of the radius valley is sensitive to core density; both core-powered mass loss and photo-evaporation find predominantly Earth-like cores to be most consistent with observations (Gupta & Schlichting, 2019; Rogers & Owen, 2021).

However, there are other predictions of each model that can be tested observationally. Since bolometric and high-energy radiation depend differently on stellar mass, observations of the radius valley around M dwarfs may be able to distinguish between the two mechanisms, though the trends around smaller stars currently remain debated in the literature (Cloutier & Menou, 2020; Petigura et al., 2022). In addition, photo-evaporation has been expected to act more quickly to change planet radii than core-powered mass loss. Recent work analyzing the evolution of the radius valley with stellar age tentatively support a longer evolution timescale for sub-Neptunes (Berger et al., 2020; David et al., 2021; Christiansen et al., 2023), but these studies are limited by small sample sizes and imprecision in stellar age estimates. Finally, direct measurements of escape from small exoplanets may also distinguish between the two models, since photo-evaporation tends to predict much larger loss rates for young planets than core-powered models (e.g. Gupta & Schlichting, 2021).

These tests will be aided by refining the predictions and implications of the two processes. Photo-evaporation is usually parameterized in evolution models by assuming a set fraction of the incident XUV energy is converted into liberating material from the planetary gravitational potential, the so-called ‘energy-limited’ escape model (Watson et al., 1981; Erkaev et al., 2007). Similarly, core-powered mass loss is also parameterized by an isothermal Parker wind at the equilibrium temperature of the planet (Ginzburg et al., 2016; Gupta & Schlichting, 2019). But while the energy-limited approximation has been rigorously bench-marked against complex hydrodynamic radiative transfer models (e.g. Murray-Clay et al., 2009; Owen & Jackson, 2012; Salz et al., 2016; Kubyshkina et al., 2018; Krenn et al., 2021; Schulik & Booth, 2023), core-powered mass loss’s approximations had not been before Chapter 5 of my thesis work. Another aspect is understanding how each process concludes and what its effects are for the super-Earths they leave behind. In photo-evaporation, as an atmosphere is eroded, the XUV photons can penetrate more deeply, driving more mass loss. The photo-evaporative model thus predicts complete stripping of tenuous atmospheres (Owen & Wu, 2017). But the end of core-powered mass loss for super-Earth is explored for the first time in Chapter 2 my thesis work.

Finally, an exciting avenue of future work is combining the two processes. Core-powered mass loss and photo-evaporation are not mutually exclusive processes, and they likely act together to enhance one another. This was first observed in Owen & Schlichting (2024). There, the authors found that which process dominates depends on whether the XUV radiation is absorbed beyond the isothermal sonic point. Information in a super-sonic region cannot be transmitted against the direction of flow. Thus, if the XUV radiation is absorbed when the flow is already super-sonic, it cannot affect the conditions at the sonic point and therefore cannot alter the mass loss rate. If the XUV radiation is absorbed slightly below the expected sonic point, it will boost loss rates, but its effect will be blunted by the cooler regions interior to it, which necessitate a sharp drop in density. Therefore, there may be an intermediate region of core-assisted photo-evaporation. But the exact delineation of these regimes, and the quantitative impact on loss rates and planet demographics, requires a more sophisticated model.

In summary, observational and theoretical advances in the last few years have revolutionized our understanding of planet formation and evolution. At the forefront has been the characterization of super-Earths and sub-Neptunes, the most abundant class of planet known to date. These planets have properties that appear to indicate formation and evolution processes quite distinct from those inferred for the Solar System. In particular, planets close to their stars with thick hydrogen envelopes surrounding rocky cores present a number of challenges to understanding them, as thermal and chemical interactions between the atmosphere and interior could play a major role in their evolution. My thesis work employs various theoretical methods, including analytic derivations, hydrodynamic simulations, atmospheric structure models, and chemical equilibrium calculations, to investigate the thermal and chemical coupling between silicates and hydrogen at sub-Neptune conditions.

CHAPTER 2

To cool is to keep: Residual H/He atmospheres of super-Earths and sub-Neptunes

[1]Super-Earths and sub-Neptunes are commonly thought to have accreted hydrogen/helium envelopes, consisting of a few to ten percent of their total mass, from the primordial gas disk. Subsequently, hydrodynamic escape driven by core-powered mass-loss and/or photo-evaporation likely stripped much of these primordial envelopes from the lower-mass and closer-in planets to form the super-Earth population. In this work we show that after undergoing core-powered mass-loss, some super-Earths can retain small residual H/He envelopes. This retention is possible because, for significantly depleted atmospheres, the density at the radiative-convective boundary drops sufficiently such that the cooling time-scale becomes shorter than the mass-loss time-scale. The residual envelope is therefore able to contract, terminating further mass loss. Using analytic calculations and numerical simulations, we show that the mass of primordial H/He envelope retained as a fraction of the planet's total mass, $f_{\rm ret}$, increases with increasing planet mass, $M_{\rm c}$, and decreases with increasing equilibrium temperature, $T_{\rm eq}$, scaling as $f_{\rm ret} \propto M_{\rm c}^{3/2} T_{\rm eq}^{-1/2} \exp\left\{ [M_{\rm c}^{3/4} T_{\rm eq}^{-1}] \right\}$. $f_{\rm ret}$ varies from $< 10^{-8}$ to about 10^{-3} for typical super-Earth parameters. To first order, the exact amount of left-over H/He depends on the initial envelope mass, the planet mass, its equilibrium temperature, and the envelope's opacity. These residual hydrogen envelopes reduce the atmosphere's mean molecular weight compared to a purely secondary atmosphere, a signature observable by current and future facilities. These remnant atmospheres may, however, in many cases be vulnerable to

---

[1] This chapter was previously published in similar form as Misener, W. and Schlichting, H. E. 2021, MNRAS 503, 5658.

long-term erosion by photo-evaporation. Any residual hydrogen envelope likely plays an important role in the long-term physical evolution of super-Earths, including their geology and geochemistry.

2.1 Introduction

Close-in exoplanets with sizes between that of Earth and Neptune are the most common exoplanets in our galaxy known to date (e.g. Petigura et al., 2013; Fressin et al., 2013). Significant work has been dedicated to understanding their formation and subsequent evolution (e.g. Hansen & Murray, 2012; Schlichting, 2014; Inamdar & Schlichting, 2015; Lee & Chiang, 2015; Ginzburg et al., 2016; Izidoro et al., 2017). The radii of a significant fraction of these planets are sufficiently large that they show evidence for substantial H/He envelopes containing a few percent of the planets' total mass (e.g. Wolfgang & Lopez, 2015). This implies that these worlds formed in the presence of the primordial gas disk. Since atmospheric mass loss is common after the dispersal of the gas disk, atmospheric masses that are observed today are generally not the same as those accreted in the presence of the primordial gas disk (e.g. Ikoma & Hori, 2012; Owen & Jackson, 2012; Lopez et al., 2012; Owen & Wu, 2016; Ginzburg et al., 2016). As a result, even super-Earths that appear as barren rocky cores today are consistent with having formed with primordial H/He envelopes (e.g. Schlichting, 2018). The two prevailing mechanisms which aim to explain the loss of these envelopes are photo-evaporation due to high energy flux from the host star (e.g. Owen & Jackson, 2012; Lopez et al., 2012) and core-powered mass loss, during which the cooling luminosity from the hot underlying planetary core fuels the atmospheric loss (e.g. Ginzburg et al., 2016). Both of these mechanisms yield a double peaked radius distribution of exoplanet sizes (e.g. Owen & Wu, 2017; Gupta & Schlichting, 2019, 2020) consistent with observations (e.g. Owen & Wu, 2013; Fulton et al., 2017; Van Eylen et al., 2018). While recent observations determining the ages of planet-hosting stars report a significant increase in super-Earths relative to sub-Neptunes on a gigayear time-scale, confirming one of the predictions from core-powered mass loss models (Berger et al., 2020; David et al., 2021), there is not yet consensus as to which mechanism dominates, if any, in sculpting the observed bimodality (e.g. Loyd et al., 2020).

Figure 2.1 schematically summarizes the key steps in the atmospheric mass-loss histories of super-Earths and sub-Neptunes. First, once the disk disperses, recently accreted envelopes are partially lost due to the loss of pressure support from the surrounding disk, provided the disk dispersal time-scale is shorter than the envelopes' cooling time-scales. As a result, planets shed their outer layers, a process termed spontaneous mass loss (e.g. Ikoma & Hori, 2012; Owen & Wu, 2016; Ginzburg et al., 2016). In the spontaneous mass loss phase, planets will lose several tens of percent of their envelope masses and shrink to envelope thicknesses that are of order their core radii on roughly megayear time-scales.

In the photo-evaporation model, atmospheric loss following this phase is powered by high energy radiation from the host star. If the time-scale to evaporate the atmosphere remains shorter than the duration of increased high energy flux from the star, the planet continues to lose mass until a bare super-Earth core remains. Otherwise, if insufficient energy is received to unbind the atmosphere, the planet retains most of its primordial gaseous envelope, roughly doubling its observed radius and corresponding to the observed sub-Neptune population. This loss process has been demonstrated to be consistent with the observed bimodal exoplanet radius distribution (e.g. Owen & Jackson, 2012; Lopez et al., 2012; Owen & Wu, 2017).

In contrast, in the core-powered mass loss model, the future of the planet's envelope is determined by its own thermal energy available for cooling and the bolometric luminosity of the host star, as this sets the gasses' escape speed at the sonic radius. If the core's heat capacity is negligible compared to that of the atmosphere after spontaneous mass loss, there is insufficient energy for loss and the atmosphere will remain bound. The planet will continue to cool and contract, which will quickly halt any further mass loss. This process leads to a planet which retains a substantial H/He envelope of order a few percent of the planet's total mass, corresponding to the observed sub-Neptune population. This general evolution is shown in Scenario (a) of Figure 2.1. Conversely, if the core has a larger heat capacity than the remaining atmosphere, the atmosphere's thermal evolution is coupled to that of the core. The core is in thermal equilibrium with the base

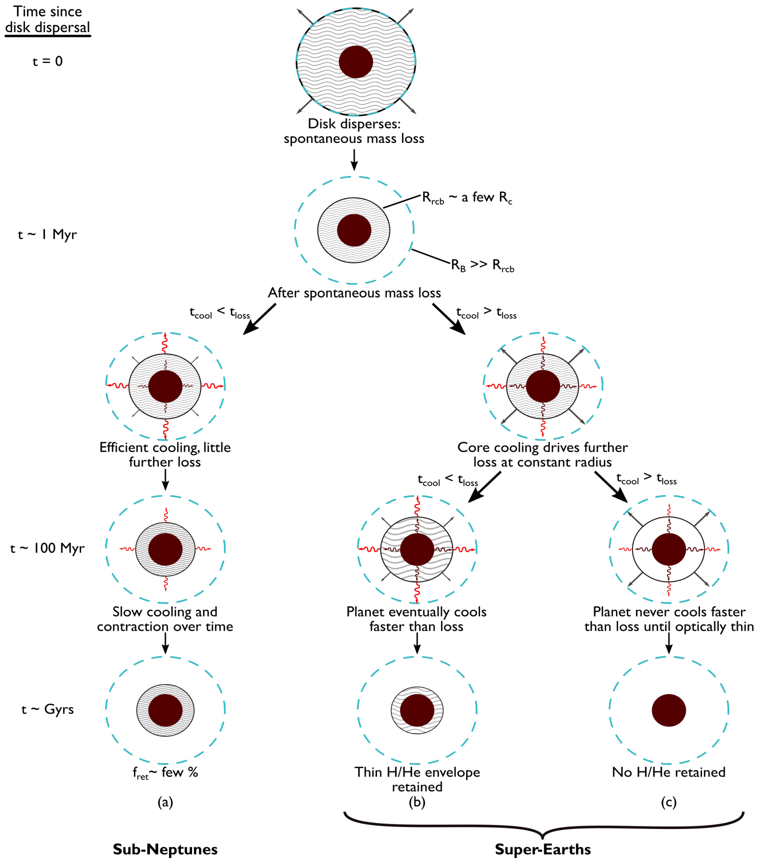

Figure 2.1: A schematic of sub-Neptune and super-Earth formation and evolution. Thermal cooling is shown by wavy arrows, while mass loss is depicted by straight gray arrows, where only the relative sizes of the arrows are important. A planet begins as a core (in maroon) embedded in the gaseous protoplanetary disk. It accretes an H/He envelope (in gray) which is bound interior to its Bondi radius, R_B (blue dashed circle). When the disk disperses, the planet quickly sheds its outer layers and contracts. Its radiative-convective boundary, R_{rcb}, (black circle) shrinks to a few core radii, R_c. In Scenario (a), the planet's available energy for cooling is dominated by the atmosphere at the end of spontaneous mass loss phase, so it can efficiently cool and contract, cutting off any further loss. The planet thus retains much of its primordial envelope and becomes a sub-Neptune with f_{ret} of order a few percent. If the thermal energy stored in the core instead dominates the available energy budget for cooling, the thermal energy released by the core into the atmosphere keeps the atmosphere inflated at a nearly constant R_{rcb}, which ensures continued atmospheric loss. Mass loss continues until either the atmosphere has lost so much mass that its density at R_{rcb} decreases sufficiently that it can start to cool more quickly than mass is lost, preserving some primordial H/He as in Scenario (b), or until the atmosphere becomes optically thin to outgoing radiation after nearly all H/He is lost, allowing the core to cool directly to space, illustrated by Scenario (c).

of the atmosphere, so as the upper atmosphere cools radiatively to space, the core also cools and resupplies heat to the atmosphere. This transfer of energy from the core to the atmosphere prevents further atmospheric contraction, keeping the atmosphere inflated and thus driving further mass loss. In this way the planet can lose much of its remaining envelope and become a super-Earth, as shown in previous work (Ginzburg et al., 2016; Gupta & Schlichting, 2019, 2020).

However, unlike in photo-evaporation, this atmospheric loss from super-Earths does not necessarily proceed to completion. The atmosphere's luminosity is determined by radiative diffusion across the radiative-convective boundary, R_{rcb}. As the atmosphere loses mass at constant radius, its density and therefore its optical depth at R_{rcb} decreases. Radiative diffusion thus becomes more efficient, and the planet becomes more luminous, decreasing the cooling time-scale. Therefore, just as for the sub-Neptunes, a super-Earth's cooling time-scale can become shorter than its mass loss time-scale. At this point, the atmosphere can once again contract, thereby exponentially increasing the mass loss time-scale and quenching loss. In this fashion, some primordial H/He can be saved by cooling even for super-Earths, as shown by Scenario (b) of Figure 2.1. However, in cases where mass loss is sufficiently fast, the atmospheric cooling time-scale may always be longer than the mass loss time-scale, and loss proceeds until the atmosphere becomes fully optically thin at very low residual atmospheric mass. For this end-member, virtually all the primordial H/He is lost, and any atmosphere at late times is essentially entirely outgassed (Figure 2.1, Scenario (c)).

The focus of this work is to investigate what ultimately determines the final primordial H/He atmospheres of close-in exoplanets and how much of their natal envelopes super-Earths and sub-Neptunes can retain after core-powered atmospheric loss. The properties of the residual primordial atmospheres of super-Earths are especially interesting for several reasons. For one, the residual atmospheres set the conditions for outgassing of any secondary atmospheres (e.g. Gaillard & Scaillet, 2014; Kite et al., 2020). In addition, any residual nebular hydrogen will significantly alter the redox state of rocky exoplanets and hence their geology and geochemistry (e.g. Wordsworth et al., 2018; Doyle et al., 2019). Preliminary investigations of the habitability of hydrogen-dominated super-Earth atmospheres (e.g. Seager et al., 2020) will gain more importance if such conditions are expected to be common. Finally, if rocky super-Earths can retain some residual hydrogen, their final envelopes will have lower mean molecular weights than pure secondary atmospheres, and correspondingly larger scale heights. These H-rich atmospheres could be distinguished from pure secondary atmospheres composed of heavier species by observations of their transmission spectra, features of which are sensitive to mean molecular weight (e.g. Benneke & Seager, 2012; Fortney et al., 2013). Such observational tests are already possible for sub-Neptunes (e.g. Benneke et al., 2019b), and upcoming facilities such as the *James Webb Space Telescope* and *Ariel* should also be able to distinguish H-rich super-Earth atmospheres from those with higher mean molecular weights (e.g. Greene et al., 2016; Edwards et al., 2019).

In the following sections, we calculate the amount of primordial H/He that a super-Earth is expected to retain assuming its evolution is dominated by core-powered mass-loss. We quantify the different stages of evolution through which these planets progress, and we show that our predictions will be testable by future observations. The paper is structured as follows. We define the key concepts of our mass-loss and thermal evolution models in Section 2.2. In Section 2.3 we determine the mass-loss and cooling time-scales in two regimes: the 'spontaneous mass loss' regime in which loss is driven by the atmosphere's own energy, and the 'core-powered' regime in which loss is instead driven by the cooling luminosity of the core. We describe how core-powered mass loss can naturally cease at low atmospheric masses and analytically determine the residual H/He envelope masses as functions of the planet mass and equilibrium temperature. To complement our analytic approximations, we present a numerical model of these phases of atmospheric evolution in Section 2.4 and compare the results to our analytic expressions. In Section 2.5 we present observational predictions. Discussions and conclusions follow in Sections 2.6 and 2.7, respectively.

2.2 Model and Approach

In this section, we summarize our model. We describe the key physical parameters that govern the mass loss and cooling of super-Earths, including our model of the core, the atmosphere, and their evolution over time.

2.2.1 Core model

We assume planets form in the protoplanetary disk as rocky cores of mass $M_{\rm c} \sim$ a few $M_\oplus$. We take the cores as similar to Earth in bulk density, accounting for compression. Their radii, $R_{\rm c}$, are thus determined by the mass-radius relation appropriate for rocky cores: $R_{\rm c}/R_\oplus = (M_{\rm c}/M_\oplus)^{1/\beta}$ where $R_\oplus$ and $M_\oplus$ are the radius and mass of Earth, respectively, and $\beta \simeq 4$ (e.g. Valencia et al., 2006; Seager et al., 2007). These assumptions are consistent with the underlying planet properties derived from both photo-evaporation (Rogers & Owen, 2021) and core-powered mass-loss models (Gupta & Schlichting, 2019). The planet's atmosphere is typically on the order of a few percent or less for the evolution we consider here, and so we ignore the atmosphere's effect on the planet's overall gravity.

We model the core as incompressible and isothermal, with a temperature, $T_{\rm c}$, that is coupled to the atmospheric temperature at its surface. For the purposes of this analysis, incorporating the true thermal gradient inside the core would not significantly alter the results. Therefore the thermal energy in the core is approximately

$$E_{\rm c} = C_{\rm c} T_{\rm c} \simeq \frac{1}{\gamma_{\rm c} - 1} N k_{\rm B} T_{\rm c}, \tag{2.1}$$

where $C_{\rm c}$ is the heat capacity of the core. In the second equality, we model the heat capacity using the form for an ideal gas, where $\gamma_{\rm c}$ is the adiabatic index of the core. Throughout this work, we use $\gamma_{\rm c} = 4/3$, following the Dulong-Petit law. This is an upper limit on the core's effective adiabatic index, as liquid silicates can have heat capacities higher than those of solids (e.g. Scipioni et al., 2017). The number of molecules in the core is given by $N = M_{\rm c}/\mu_{\rm c}$, where $\mu_{\rm c}$ is the mean molecular weight of the core. Motivated by our own Earth, we assume $\mu_{\rm c} = 60$ amu.

2.2.2 Atmospheric structure

While embedded in the primordial disk, a planet will capture any gas within its sphere of influence, which we approximate by the Bondi radius, R_{B}. The Bondi radius is the point where the escape velocity from the planet is equal to the thermal velocity of the gas molecules. The isothermal speed of sound is given by $c_{\mathrm{s}} = (k_{\mathrm{B}}T/\mu)^{1/2}$, where k_{B} is the Boltzmann constant, T is the temperature at R_{B}, and μ the mean molecular weight of the atmosphere. We assume throughout that $\mu = 2.2$ amu, as expected for a primordial H/He atmosphere. We can write the Bondi radius as $R_{\mathrm{B}} \simeq 2GM_{\mathrm{c}}\mu/(k_{\mathrm{B}}T_{\mathrm{eq}})$, where G is the gravitational constant and T_{eq} is the equilibrium temperature, determined by the incident flux of stellar radiation. The equilibrium temperature scales with the planet's semi-major axis, a, as

$$T_{\mathrm{eq}} = \left(\frac{L_*}{16\pi\sigma a^2}\right)^{1/4} = 279\ \mathrm{K}\left(\frac{a}{1\ \mathrm{au}}\right)^{-1/2}, \tag{2.2}$$

where L_* is the luminosity of the planet's host star, σ is the Stefan-Boltzmann constant, and the right-most expression is evaluated using $L_* = L_\odot$, matching the classic Hayashi (1981) profile. We paramaterize our results throughout this work in terms of T_{eq}, as this temperature determines the physical outflow behavior.

We model the structure of the planetary atmosphere as an inner convective region with an adiabatic profile and an outer radiative region that is isothermal at the equilibrium temperature T_{eq} (e.g. Lee & Chiang, 2015; Ginzburg et al., 2016). The transition between the two regions is labeled the radiative-convective boundary, R_{rcb}. Thus the density structure of the inner region $R_{\mathrm{c}} \le r \le R_{\mathrm{rcb}}$ is

$$\rho(r) = \rho_{\mathrm{rcb}}\left(1 + \frac{R'_{\mathrm{B}}}{r} - \frac{R'_{\mathrm{B}}}{R_{\mathrm{rcb}}}\right)^{1/(\gamma-1)}, \tag{2.3}$$

where r and R_{rcb} are measured from the center of the planet, γ is the adiabatic index of the atmosphere, $R'_{\mathrm{B}} \equiv (\gamma-1)/(2\gamma) \times R_{\mathrm{B}}$ is defined for convenience, and $\rho_{\mathrm{rcb}} = \rho(R_{\mathrm{rcb}})$. The density structure in the outer region, $R_{\mathrm{rcb}} \le r \le R_{\mathrm{B}}$, is well-described by

$$\rho(r) \simeq \rho_{\mathrm{rcb}} \exp\left\{\left[\frac{R_{\mathrm{B}}}{2r} - \frac{R_{\mathrm{B}}}{2R_{\mathrm{rcb}}}\right]\right\}. \tag{2.4}$$

Since the density decays exponentially past $R_{\rm rcb}$, almost all the atmospheric mass is contained in the inner convective region, so we approximate the atmospheric mass as the integral of the adiabatic density profile

$$M_{\rm atm} \equiv f M_{\rm c} \simeq 4\pi\rho_{\rm rcb} \int_{R_{\rm c}}^{R_{\rm rcb}} r^2 \left(1 + \frac{R'_{\rm B}}{r} - \frac{R'_{\rm B}}{R_{\rm rcb}}\right)^{1/(\gamma-1)} dr, \tag{2.5}$$

where we express the atmospheric mass throughout this work as a fraction of the core's mass, $f \equiv M_{\rm atm}/M_{\rm c}$, for convenience. We verify *a posteriori* that for the duration of mass loss, less than 10 percent of the total mass of the atmosphere is in the isothermal region for the vast majority of planets considered here. The assumption that we can neglect, to first order, the atmospheric mass in the isothermal region when calculating the residual envelope mass at the point when mass-loss ceases is therefore justified. The only planets for which we found isothermal regions comprising greater than 10 percent of the atmosphere's mass cease losing mass because the atmosphere becomes optically thin (see Section 2.3.5), which are not the topic of this paper. The phase space that is relevant to this optically-thin regime is marked as the shaded gray region in Figure 2.5.

The atmospheric specific energy is the sum of the (negative) gravitational and (positive) thermal energy and is given by

$$e(r) = -\frac{GM_{\rm c}}{r} + \frac{1}{\gamma - 1}\frac{k_{\rm B}T(r)}{\mu}, \tag{2.6}$$

where $T(r)/T_{\rm eq} = (\rho/\rho_{\rm rcb})^{\gamma-1}$ in the convective region and $T(r \geq R_{\rm rcb}) = T_{\rm eq}$ in the isothermal region. The total energy, too, is concentrated in the convective region and hence well approximated as

$$E_{\rm atm} = \int_{M_{\rm atm}} e dm \simeq \int_{R_{\rm c}}^{R_{\rm rcb}} 4\pi r^2 e(r)\rho(r) dr. \tag{2.7}$$

2.2.3 Atmospheric evolution

We fundamentally quantify the evolution of these atmospheres using the mass loss and cooling time-scales, given by $t_{\rm loss} = |M_{\rm atm}/\dot{M}_{\rm atm}|$ and $t_{\rm cool} = |E/\dot{E}|$, respectively. If $t_{\rm loss} > t_{\rm cool}$, the planet can efficiently cool and contract, suppressing any further mass loss. Conversely, if $t_{\rm loss} < t_{\rm cool}$, hydrodynamic mass loss is more efficient than cooling.

We treat the mass of the planet's H/He envelope at point of disk dispersal, $M_{\rm atm,init}$, as an input variable to our model, but assume it is on the order of a few to ten percent of the core's mass (e.g. Ginzburg et al., 2016). Motivated by observations (e.g. Koepferl et al., 2013), we assume that the disk dispersal time-scale is short compared to the cooling time-scale of the envelope. Therefore, after outside pressure support is lost due to disk dispersal, the atmospheres of these planets will quickly lose mass hydrodynamically. The mass loss rate is limited by the rate at which the gas molecules can escape at the outer radius (i.e. the smaller of the Hill and Bondi radius)

$$\dot{M}_{\rm B} = -4\pi R_{\rm out}^2 u_{\rm out} \rho_{\rm out} \simeq -4\pi R_{\rm s}^2 c_{\rm s} \rho_{\rm rcb} \exp\left\{\left[-\frac{2R_{\rm s}}{R_{\rm rcb}}\right]\right\}, \tag{2.8}$$

where $\rho_{\rm out}$ and $u_{\rm out}$ are the density and flow speed at the outer radius $R_{\rm out}$. In the second equality we have assumed that is outer radius is given by the radius of the sonic point $R_{\rm s}$, which we assume for simplicity throughout this paper, rather than the Hill radius.

After disk dispersal, energy is radiated from the planet with a luminosity given by (Ginzburg et al., 2016, Eq 15)

$$L = -\dot{E} \simeq \frac{64\pi\sigma T_{\rm eq}^4 R_{\rm B}'}{3\kappa\rho_{\rm rcb}}, \tag{2.9}$$

where σ is the Stefan-Boltzmann constant and κ the opacity at the $R_{\rm rcb}$. We assume a Rosseland mean opacity of the gas with $\kappa = 0.1$ cm^{2}g^{-1}, a constant suitable for H/He dominated atmospheres (e.g. Freedman et al., 2008). Using a more realistic scaling of opacity with atmospheric density only marginally affects our results, though we discuss other potential scalings in Section 2.6. Some portion of this luminosity goes into liberating mass out of the planet's potential. If all of the internal luminosity of the atmosphere goes into mass liberation, we find the maximum rate at which mass can be lost energetically, which we term the luminosity-limited mass loss rate:

$$\dot{M}_{\rm L} \simeq \frac{L M_{\rm atm}}{E_{\rm atm}}. \tag{2.10}$$

If $\dot{M}_{\rm L} < \dot{M}_{\rm B}$, there is insufficient energy available to lift mass to the radiative-convective boundary and maintain the Parker wind-type loss, and mass loss is limited by the underlying luminosity rather than by the rate at which gas molecules can escape from the Bondi radius. In this regime, the planet loses mass and cools on similar time-scales and $t_{\rm cool} \simeq t_{\rm loss,L}$.

Therefore, the mass loss rate at any time is the minimum of these two rates: $\dot{M}_{\rm atm} = \min[\dot{M}_{\rm L}, \dot{M}_{\rm B}]$. Typically, planets begin their evolution in the luminosity-limited regime due to their large $R_{\rm rcb}$, and transition into the Bondi-limited regime as the atmosphere contracts and the cooling of the core can become important. In the following section, we derive the cooling and mass loss time-scales analytically and show that cooling and contraction can preserve both the massive H/He-rich envelopes of sub-Neptunes as well as the light remnant primordial envelopes of super-Earths.

2.3 Analytic Results

2.3.1 Overview of results

To give context to our analytic results and provide physical intuition for the processes that preserve residual atmospheres of super-Earths, we start by presenting the basic outcomes of two numerical simulations. These simulations are described in detail in Section 2.4. Figure 2.2 shows the evolution in time of the atmospheric mass, $f = M_{\rm atm}/M_{\rm c}$, the radiative-convective boundary, $R_{\rm rcb}$, and ratio of the cooling and mass loss time-scales, $t_{\rm cool}/t_{\rm loss}$, of two planets: one that will turn into a super-Earth and one that will remain a sub-Neptune. These two planets have the same physical parameters, except that the planet in the bottom row, i.e. the sub-Neptune, starts with a more massive primordial envelope. Immediately post-disk dispersal, which occurs instantaneously at $t = 0$ in these simulations, the atmospheres quickly shed their loosely-bound outer layers, and both the atmospheric mass and radiative-convective boundary decrease. This is illustrated in the early times in both rows of Figure 2.2, where both planets lose $> 50\%$ of their initial envelopes in the first 10^6 to 10^7 years. Spontaneous mass loss continues until the mass loss becomes Bondi-limited rather than luminosity-limited, i.e., when the atmospheric cooling time-scale becomes less than the Bondi loss time-scale.

After this spontaneous mass loss phase the underlying rocky core, which is thermally coupled to the base of the atmosphere, may play a role in a planet's further evolution. As the core cools,

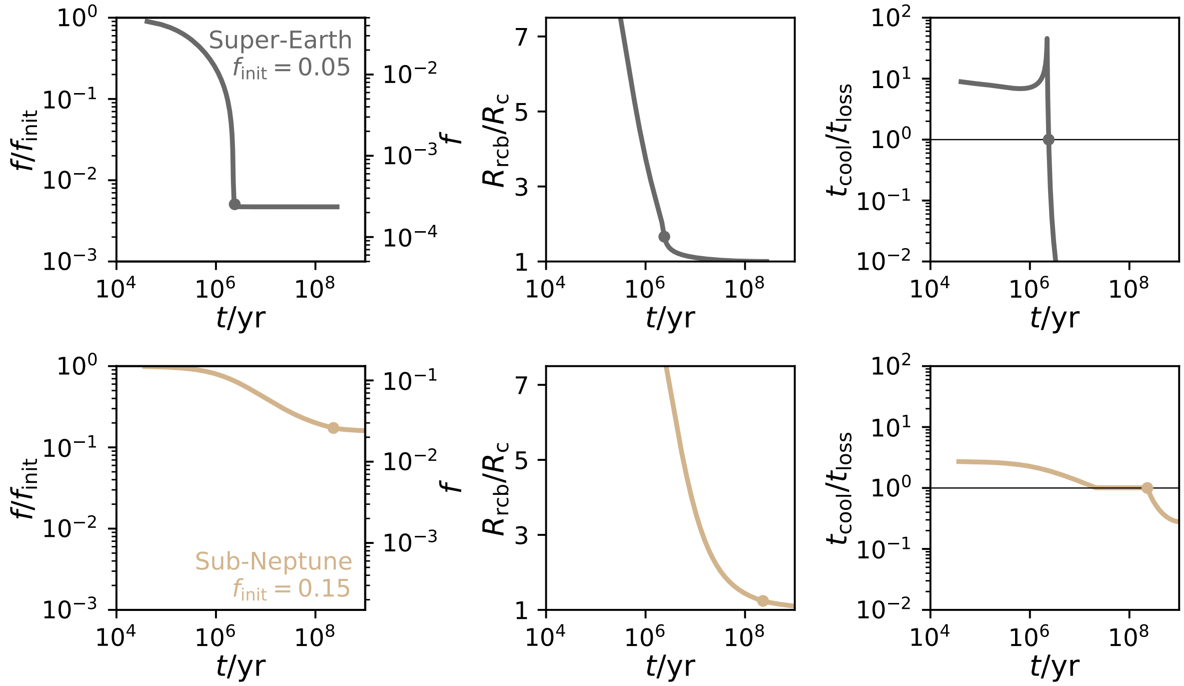

Figure 2.2: Example of numerical simulations comparing the time evolution of atmospheric mass, f, radiative-convective boundary radius, $R_{\rm rcb}$, and ratio of the cooling time-scale to the mass loss time-scale, $t_{\rm cool}/t_{\rm loss}$, of two planets: one that evolves into a super-Earth (top panel) and one that remains a sub-Neptune (bottom panel). Both planets have the same mass, $M_{\rm c} = 4M_{\oplus}$, and equilibrium temperature, $T_{\rm eq} = 1000$ K. The time at which $t_{\rm cool} = t_{\rm loss}$ in each simulation is marked by a dot. In the upper row, gray lines show the evolution of a planet with envelope mass at the time of disk dispersal $f_{\rm init} = 0.05$. In the bottom row, tan lines show evolution of a planet with $f_{\rm init} = 0.15$. Both planets begin by undergoing spontaneous mass loss and shrinking until their radiative-convective boundaries are of order the core radius. At this transition point, the planet on the top row has sufficient thermal energy remaining in the core w.r.t. the envelope to power further mass loss. This mass loss proceeds until f decreases enough to lower $t_{\rm cool}$ below $t_{\rm loss}$. This planet loses nearly all of its initial envelope and becomes a super-Earth, but it retains a thin primordial layer of hydrogen, $f_{\rm ret} \sim 10^{-4}$. Meanwhile, the planet on the bottom row ceases to lose mass by the end of the spontaneous mass loss phase, because the energy available for cooling is dominated by the envelope and not the core. The mass-loss is therefore terminated at the end of the spontaneous mass-loss phase and the cooling of the underlying core does not significantly effect the planet's evolution and the planet cools and contracts over gigayear time-scales. This specific planet retains 20% of its initial envelope and corresponds to a sub-Neptune.

it deposits thermal energy into the atmosphere. So long as the energy of the atmosphere itself dominates the available energy for cooling in the system, the core's cooling does not significantly affect the atmosphere's evolution. But if after spontaneous mass loss the core dominates the available cooling energy, then the cooling of the core can supply energy to the envelope as energy is lost by radiative diffusion across the radiative-convective boundary. This keeps the atmosphere inflated, which drives further mass loss. This effect was examined in detail in Ginzburg et al. (2016), which found that the core's released thermal energy can be sufficient to unbind entire atmospheres. This is the core-powered mass loss mechanism, which can transform sub-Neptunes into super-Earths. The influence of the core is illustrated in Figure 2.2: after spontaneous mass loss, the atmosphere's available cooling energy is much larger than the core's thermal energy in the $f_{\rm init} = 0.15$ case (bottom). Therefore, the planet's cooling time-scale is nearly unaffected by the core and is already less than the mass loss time-scale from the contraction due to spontaneous mass loss alone. This planet will slowly cool and contract on gigayear time-scales without losing further atmospheric mass. These planets correspond to observed sub-Neptunes, and they typically retain $\sim 20\%$ of their initial envelopes. Conversely, in the $f_{\rm init} = 0.05$ case (top), the core's thermal energy keeps the atmosphere inflated at $R_{\rm rcb} \sim 2R_{\rm c}$, thereby lengthening the planet's cooling time-scale and enabling further mass loss. This planet loses most of its atmosphere and becomes a super-Earth (Ginzburg et al., 2018; Gupta & Schlichting, 2019).

While super-Earths are produced under the core-powered mass loss mechanism, Figure 2.2 shows that their primordial envelopes are not necessarily totally stripped. If the hot core can eventually cool on a shorter time-scale than mass loss occurs, the atmosphere will contract and cut off any further loss in the same fashion as the sub-Neptunes. Here, we briefly describe the physics of this process, which we derive more thoroughly in the remainder of the section.

The two basic physical quantities that evolve with time in the system are the atmospheric mass, $M_{\rm atm} \equiv f M_{\rm c}$, and the radius of the radiative-convective boundary, $R_{\rm rcb}$. After the atmosphere transitions into the Bondi loss regime, the mass loss rate is set by the density of the outflow: $\dot{M}_{\rm atm} \propto \rho_{\rm rcb}$ (see Equation 2.8). This density depends linearly on the mass of the atmosphere:

$\rho_{\rm rcb} \propto M_{\rm atm}$ (see Equation 2.5). Therefore, the mass loss time-scale, $t_{\rm loss} = M_{\rm atm}/\dot{M}_{\rm atm}$, is independent of the atmospheric mass. However, the planet's cooling time-scale, $t_{\rm cool} = E/\dot{E}$, is not independent of the atmospheric mass. The core's thermal energy is independent of the atmospheric mass. But as mass is lost at nearly constant radius, the density of the atmosphere, and therefore $\rho_{\rm rcb}$, decreases. Radiative diffusion across the radiative-convective boundary thus becomes more efficient, and the luminosity of the planet increases: $L = \dot{E} \propto 1/\rho_{\rm rcb} \propto 1/M_{\rm atm}$ (see Equation 2.9). In this way, as the atmospheric mass decreases, the cooling time-scale, $t_{\rm cool} \propto M_{\rm atm}$, also decreases. In summary, as $M_{\rm atm}$ decreases at nearly constant $R_{\rm rcb}$, $t_{\rm loss}$ is constant, while $t_{\rm cool}$ decreases. Thus there exists an atmospheric mass, which we term $f_{\rm ret}$, at which the cooling time-scale will become shorter than the mass loss time-scale. Once f decreases to this value, the envelope will quickly contract and cut off further mass loss, preserving the remaining primordial gas. This cross-over occurs for the $f_{\rm init} = 0.05$ case that we show on the top row of Figure 2.2 at the time marked with dots on each panel. In this case, the core cooling time-scale $t_{\rm cool}$ becomes shorter than $t_{\rm loss}$ when $f/f_{\rm init} \sim 5 \times 10^{-3}$, after which no further mass is lost. This super-Earth then cools and contracts at constant atmospheric mass, just as the sub-Neptune does.

Our aim in this section is to quantify the residual H/He gas we expect these planets to retain after core-powered mass loss, $f_{\rm ret}$. To find this mass fraction, we analytically solve for the atmospheric mass at which the planet's cooling rate becomes faster than its mass loss rate. In the remainder of this section, we divide the atmospheric evolution into two tractable analytic regimes. First we quantify the spontaneous mass loss mechanism in Section 2.3.2. In this mass loss phase, we focus on the envelope's own energy as the main source of available cooling energy. This regime sets the radiative-convective boundary radius and atmospheric mass for the next phase of evolution. After spontaneous mass loss phase, the remaining gravitational and thermal energy of the atmosphere can exceed the thermal energy of the core. In this case, the atmosphere contracts and cools without further significant mass loss, and the planet remains a sub-Neptune. On the other hand, if the underlying core's thermal energy is larger than the atmospheric energy, the core's cooling will play a dominant role in the evolution of the atmosphere and the resulting atmospheric loss can turn a sub-Neptune into a super-Earth. In this case, presented in Section 2.3.3, we focus on the core's thermal energy as main cooling energy source.

2.3.2 Spontaneous mass loss

When the disk disperses, the planet will cool by radiative diffusion across the $R_{\rm rcb}$ with a cooling time-scale, $t_{\rm cool} \equiv |E/L|$. Here L is the luminosity of the envelope expressed in Equation 2.9. While the atmosphere extends significantly, $R_{\rm rcb} \gg R_{\rm c}$, the adiabatic gradient of the atmosphere keeps the core nearly constant in temperature as the atmosphere contracts. Thus, we neglect any energy contribution from the core's cooling in this stage. The energy available for cooling the envelope is therefore its integrated thermal and gravitational potential energy as expressed in Equation 2.7. Assuming that the energy is concentrated in the interior of the convective region (true for $\gamma < 3/2$), this integral can be approximated as (see Ginzburg et al., 2016, Eq 10)

$$E_{\rm atm} \simeq -\frac{(\gamma-1)^2}{\gamma(3-2\gamma)} G M_{\rm c} 4\pi R_{\rm c}^2 \rho_{\rm rcb} \left(\frac{R'_{\rm B}}{R_{\rm c}}\right)^{\frac{1}{\gamma-1}}. \tag{2.11}$$

The density at the $R_{\rm rcb}$, $\rho_{\rm rcb}$, can be expressed in terms of the atmospheric mass, $M_{\rm atm}$, by integrating the density profile given in Equation 2.3. We approximate this integral in this 'thick' regime as (see Ginzburg et al., 2016, Eq 11)

$$M_{\rm atm} \simeq A 4\pi R_{\rm rcb}^3 \rho_{\rm rcb} \left(\frac{R'_{\rm B}}{R_{\rm rcb}}\right)^{\frac{1}{\gamma-1}}, \tag{2.12}$$

where A is an integration constant equal to $5\pi/16$ in the limit $R_{\rm rcb} \gg R_{\rm c}$. This expression is derived under the assumption that $R_{\rm c} \ll R_{\rm rcb} \lesssim R'_{\rm B}$, $\gamma > 4/3$, and the mass in the isothermal region is negligible. The first approximation will begin to fail as $R_{\rm rcb}$ approaches $R_{\rm c}$, which will be treated in the thin regime section below. Thus the density at $R_{\rm rcb}$ is

$$\rho_{\rm rcb} \simeq \frac{M_{\rm atm}}{A 4\pi R_{\rm B}^{\prime\frac{1}{\gamma-1}} R_{\rm rcb}^{3-\frac{1}{\gamma-1}}}. \tag{2.13}$$

This approximation allows us to simplify Equation 2.11 as

$$E_{\rm atm} \simeq -\frac{(\gamma-1)^2 G M_{\rm c} M_{\rm atm}}{A\gamma(3-2\gamma) R_{\rm c}} \left(\frac{R_{\rm c}}{R_{\rm rcb}}\right)^{3-\frac{1}{\gamma-1}}. \tag{2.14}$$

Combining this expression with Equation 2.9, we derive the cooling time-scale in the regime for which the atmospheric potential energy dominates the energy available in the system:

$$\begin{aligned} t_{\mathrm{cool}} &\simeq K_{\mathrm{cool}}(\gamma) f^2 M_{\mathrm{c}}^{2-\frac{1}{\gamma-1}} R_{\mathrm{c}}^{2-\frac{1}{\gamma-1}} T_{\mathrm{eq}}^{-3+\frac{1}{\gamma-1}} R_{\mathrm{rcb}}^{-2(3-\frac{1}{\gamma-1})} \\ &\simeq 6.80 \times 10^{14} \left(\frac{f}{0.05}\right)^2 \left(\frac{M_{\mathrm{c}}}{3M_{\oplus}}\right)^{-7/8} \left(\frac{T_{\mathrm{eq}}}{1000\ \mathrm{K}}\right)^{-1/2} \left(\frac{R_{\mathrm{rcb}}}{R_{\mathrm{c}}}\right)^{-1} \mathrm{s}, \end{aligned} \tag{2.15}$$

where $K_{\mathrm{cool}}(\gamma) = 3\kappa(\gamma-1)^2 G/(256\pi^2 A^2 \gamma(3-2\gamma)\sigma)[(\gamma-1)G\mu/(\gamma k_{\mathrm{B}})]^{-1-\frac{1}{\gamma-1}}$, and we have evaluated the second line using $\gamma = 7/5$, an adiabatic index appropriate for an atmosphere of diatomic hydrogen.

To assess whether the mass loss rate is limited initially by the internal luminosity or the hydrodynamic outflow, we compare the luminosity-limited mass loss time-scale to the Bondi mass loss time-scale. The luminosity-limited mass loss time-scale, $t_{\mathrm{loss,L}} \equiv |M_{\mathrm{atm}}/\dot{M}_{\mathrm{L}}| \simeq E_{\mathrm{atm}}/L$, is, to first order, equivalent to the cooling time-scale. The Bondi mass loss time-scale, $t_{\mathrm{loss,B}} \equiv |M_{\mathrm{atm}}/\dot{M}_{\mathrm{B}}|$, is, combining Equations 2.8 and 2.12

$$\begin{aligned} t_{\mathrm{loss,B}} &\simeq K_{\mathrm{loss}}(\gamma) M_{\mathrm{c}}^{-2+\frac{1}{\gamma-1}} T_{\mathrm{eq}}^{\frac{3}{2}-\frac{1}{\gamma-1}} R_{\mathrm{rcb}}^{3-\frac{1}{\gamma-1}} \exp\{[R_{\mathrm{B}}/R_{\mathrm{rcb}}]\} \\ &\simeq 421 \left(\frac{M_{\mathrm{c}}}{3M_{\oplus}}\right)^{5/8} \left(\frac{T_{\mathrm{eq}}}{1000\ \mathrm{K}}\right)^{-1} \left(\frac{R_{\mathrm{rcb}}}{R_{\mathrm{c}}}\right)^{1/2} \exp\{[R_{\mathrm{B}}/R_{\mathrm{rcb}}]\}\ \mathrm{s}, \end{aligned} \tag{2.16}$$

where $K_{\mathrm{loss}}(\gamma) = A/\mathrm{e}(k_{\mathrm{B}}/\mu)^{\frac{3}{2}-\frac{1}{\gamma-1}} G^{-2+\frac{1}{\gamma-1}}$ and the second line is again evaluated for $\gamma = 7/5$. The loss time-scale is much shorter than the cooling time-scale initially, when $R_{\mathrm{rcb}} \gg R_{\mathrm{c}}$. Therefore, atmospheres lose mass at the luminosity-limited mass loss rate: $\dot{M}_{\mathrm{atm}} = \dot{M}_{\mathrm{L}}$ and $t_{\mathrm{loss}} = t_{\mathrm{cool}}$. However, as the planet cools and loses mass, the atmosphere contracts. The Bondi mass loss time-scale is independent of f, and as R_{rcb} decreases, this time-scale increases exponentially and can become longer than the luminosity-limited time-scale, $t_{\mathrm{cool}} \propto R_{\mathrm{rcb}}^{-1} f^2$. Once this occurs, the atmospheric mass loss rate transitions from $\dot{M}_{\mathrm{L}}$ to $\dot{M}_{\mathrm{B}}$. This change in mass loss rate has important consequences for the future of the planet: rather than the loss rate increasing as mass is lost, which would cause runaway atmospheric loss, the mass loss rate is independent of the atmospheric mass and exponentially decreases as the planet contracts, which can save the remaining atmosphere.

We quantify the crossover point when the Bondi loss rate decreases below the luminosity-limited rate by setting the two time-scales equal. Since the loss time-scale is independent of f and the cooling time-scale depends only weakly on it compared to the exponential dependence on $R_{\rm rcb}$ in the loss time-scale, we take the mass as roughly constant for this analytic derivation and set $t_{\rm loss,B} = t_{\rm cool}$ to solve for $R_{\rm rcb}$. This value is the radiative-convective boundary to which the atmosphere must shrink for the Bondi mass loss rate to become equal to the rate limiting atmospheric loss.

Equating Equations 2.15 and 2.16 yields

$$R_{\rm rcb}^n \simeq Z \exp\{[-R_{\rm B}/R_{\rm rcb}]\}, \tag{2.17}$$

where $n \equiv 3(3 - 1/(\gamma - 1))$ and $Z = K_{\rm cool}/K_{\rm loss} f^2 M_{\rm c}^{4-\frac{2}{\gamma-1}} R_{\rm c}^{2-\frac{1}{\gamma-1}} T_{\rm eq}^{-\frac{9}{2}+\frac{2}{\gamma-1}}$. This equation has no exact solution for $R_{\rm rcb}$ in terms of elementary functions. However, in the limit where $R_{\rm B}/R_{\rm rcb}$ is large, the exponential term on the right-hand side of Equation 2.17 changes much faster than the power-law term on the left-hand side with changing $R_{\rm rcb}$. We therefore approximate the power-law term as a constant: $R_{\rm rcb}^n \approx (\epsilon R_{\rm B})^n$. This approach requires an estimate of the expected final result, so we take $\epsilon \approx 0.03$. Varying the value of ϵ by a factor of a few does not have a large effect on the solution, however.

Solving for the remaining $R_{\rm rcb}$ term in the exponential term of Equation 2.17 yields the critical radius $R_{\rm rcb}$ at which $t_{\rm cool} = t_{\rm loss,B}$

$$\begin{aligned} R_{\rm rcb} &\simeq \frac{-R_{\rm B}}{\ln\left[\epsilon^n R_{\rm B}^n/Z\right]} \\ \frac{R_{\rm rcb}}{R_{\rm c}} &\approx \frac{38.0 \times \left(\frac{M_{\rm c}}{3M_\oplus}\right)^{3/4} \left(\frac{T_{\rm eq}}{1000\ {\rm K}}\right)^{-1}}{27.9 - 1.5\ln\left[\frac{\epsilon}{0.03}\right] + 2\ln\left[\frac{f}{0.05}\right] + 2\ln\left[\frac{T_{\rm eq}}{1000\ {\rm K}}\right] - 2.625\ln\left[\frac{M_{\rm c}}{3M_\oplus}\right]}, \end{aligned} \tag{2.18}$$

where we have again taken $\gamma = 7/5$ in the last line.

Using this new $R_{\rm rcb}$, we estimate the mass lost in this initial spontaneous mass loss phase. The mass that was initially contained between this new radius and the initial $R_{\rm rcb}$ is taken to be lost in this phase. An analytic prediction can thus be made for $M_{\rm lost}$ by approximating the density profile in Equation 2.3 as $\rho_{\rm init}(r) \approx \rho_{\rm rcb}(R'_{\rm B}/r)^{1/(\gamma-1)}$. This simplification of the r dependence allows the mass lost to be integrated analytically:

$$\frac{f_{\rm lost}}{f_{\rm init}} \simeq \frac{R_{\rm rcb,init}^{3-1/(\gamma-1)} - R_{\rm rcb,crit}^{3-1/(\gamma-1)}}{R_{\rm rcb,init}^{3-1/(\gamma-1)} - R_{\rm c}^{3-1/(\gamma-1)}}, \tag{2.19}$$

where $R_{\rm rcb,init} = R'_{\rm B}$. The mass lost found is typically near 75% of the planet's initial captured atmosphere, which is consistent results given in Ginzburg et al. (2016) for $\gamma = 7/5$.

2.3.3 Core cooling regime

At the end of the spontaneous mass loss phase, mass loss stops being limited by the planet's cooling luminosity and becomes instead limited by the rate at which gas molecules can escape at the Bondi radius. Additionally, since the radius of the envelope is of order the core's radius, the thermal energy available for cooling in the hot underlying core, $E_{\rm c}$, can be released and can contribute to the further evolution of the atmosphere. If $E_{\rm c} \lesssim |E_{\rm atm}|$, then the thermal energy of the core is insufficient to significantly affect the atmosphere's evolution. Now, any slight atmospheric contraction causes the mass loss time-scale to increase exponentially. Meanwhile, the cooling time-scale, previously coupled to the mass loss time-scale, does not substantially change even with the core's additional contribution. Thus the mass loss time-scale quickly becomes longer than the planet's cooling time-scale. Such planets will slowly cool and contract on gigayear time-scales and will lose no more atmospheric mass. These planets correspond to observed sub-Neptunes.

Conversely, if $E_{\rm c} \gtrsim |E_{\rm atm}|$, then there is more energy available for cooling than we considered above. Therefore, $t_{\rm cool} \propto E$ is still longer than $t_{\rm loss}$, so mass loss continues until the core has cooled sufficiently for the envelope to contract. In what follows in this section, we assume that the core's thermal energy dominates the total energy available for cooling. We use this to determine a planet's further evolution by again setting the cooling and mass loss time-scales equal, as above.

The core's thermal energy available for cooling is determined by the temperature of the base of the atmosphere, because the core and atmosphere are thermally coupled (see Equation 2.1). The temperature at the base of the atmosphere is in turn is related to the temperature at the radiative-convective boundary via the adiabatic profile of the envelope. If $R_{\rm rcb} \gtrsim 2R_{\rm c}$, the temperature at the base of the atmosphere, and thus the core temperature, $T_{\rm c} = T(R_{\rm c})$, varies little as $R_{\rm rcb}$ changes. Therefore we approximate the core temperature, in this regime, as independent to first order of $R_{\rm rcb}$: $T_{\rm c} \simeq T_{\rm eq} R'_{\rm B}/R_{\rm c}$. Once $R_{\rm rcb} \lesssim 2R_{\rm c}$, however, the temperature at the core-atmosphere boundary does decrease substantially, thereby releasing thermal energy into the envelope, as the radiative-convective boundary approaches the core (see Ginzburg et al., 2016, Eq 19):

$$T_{\rm c}(R_{\rm rcb} < 2R_{\rm c}) \simeq T_{\rm eq} \frac{R'_{\rm B} \Delta R_{\rm a}}{R_{\rm c}^2}, \tag{2.20}$$

where we define the width of the atmosphere $\Delta R_{\rm a} \equiv R_{\rm rcb} - R_{\rm c}$. We note here that the core temperature does not depend on the mass of the atmosphere in either regime.

Inserting these temperatures into Equation 2.1, we derive the core energy available for cooling relevant for the end of a planet's evolution when the cooling time-scales and mass-loss time-scales can become comparable:

$$E_{\rm c} \simeq \begin{cases} \dfrac{\gamma - 1}{\gamma(\gamma_{\rm c} - 1)} \dfrac{\mu}{\mu_{\rm c}} \dfrac{G M_{\rm c}^2}{R_{\rm c}} & \text{if } R_{\rm rcb} > 2R_{\rm c} \\ \dfrac{\gamma - 1}{\gamma(\gamma_{\rm c} - 1)} \dfrac{\mu}{\mu_{\rm c}} \dfrac{G M_{\rm c}^2}{R_{\rm c}} \dfrac{\Delta R_{\rm a}}{R_{\rm c}} & \text{if } R_{\rm rcb} \lesssim 2R_{\rm c} \end{cases}. \tag{2.21}$$

As the core cools in tandem with the base of the atmosphere, it releases its thermal energy into the envelope. This energy input impedes further atmospheric contraction, thereby sustaining mass loss until the planet's core has cooled significantly.

If $R_{\rm rcb} \gtrsim 2R_{\rm c}$, we still approximate the atmospheric mass by Equation 2.12. However, the integration factor, A, is no longer necessarily approximately equal to $5\pi/16$, so we now use its integral form

$$A \simeq \int_{R_{\rm c}/R_{\rm rcb}}^{1} x^2 \left(\frac{1}{x} - 1 \right)^{\frac{1}{\gamma - 1}} {\rm d}x, \tag{2.22}$$

where $x \equiv r/R_{\rm rcb}$. This integration factor is smaller than $5\pi/16$ and decreases as the atmosphere contracts.

If the atmosphere is sufficiently thin, $R_c \lesssim 2R_{rcb}$, the atmospheric mass is instead better approximated as

$$M_{atm} \simeq \frac{\gamma - 1}{\gamma} 4\pi R_c^2 \Delta R_a \rho_{rcb} \left(\frac{R'_B \Delta R_a}{R_c^2} \right)^{\frac{1}{\gamma-1}}. \tag{2.23}$$

Since the core is thermally coupled to the atmosphere, its cooling rate is limited by the rate of radiative diffusion across the radiative-convective boundary of the envelope (see Equation 2.9). In the core cooling regime, the cooling time-scale can therefore be approximated as the ratio of the core's thermal energy and the luminosity, $t_{cool} = |E_c/L|$. For $R_{rcb} \gtrsim 2R_c$, the cooling time-scale is

$$\begin{aligned} t_{cool} &\simeq \frac{C_{cool}(\gamma)}{A} f M_c^{2-\frac{1}{\gamma-1}} R_c^{-1} T_{eq}^{-3+\frac{1}{\gamma-1}} R_{rcb}^{-3+\frac{1}{\gamma-1}} \\ &\simeq 7.2 \times 10^{14} \left(\frac{f}{0.01} \right) \left(\frac{M_c}{3M_\oplus} \right)^{-7/8} \left(\frac{T_{eq}}{1000\ \mathrm{K}} \right)^{-1/2} \left(\frac{R_{rcb}}{R_c} \right)^{-1/2} \mathrm{s}, \end{aligned} \tag{2.24}$$

while for $R_{rcb} \lesssim 2R_c$, the dependence on the radiative-convective boundary changes to

$$\begin{aligned} t_{cool} &\simeq C_{cool}(\gamma) \frac{\gamma}{\gamma - 1} f M_c^{2-\frac{1}{\gamma-1}} R_c^{-4+\frac{2}{\gamma-1}} T_{eq}^{-3+\frac{1}{\gamma-1}} \Delta R_a^{-\frac{1}{\gamma-1}} \\ &\simeq 5.05 \times 10^{14} \left(\frac{f}{0.01} \right) \left(\frac{M_c}{3M_\oplus} \right)^{-7/8} \left(\frac{T_{eq}}{1000\ \mathrm{K}} \right)^{-1/2} \left(\frac{\Delta R_a}{R_c} \right)^{-5/2} \mathrm{s}, \end{aligned} \tag{2.25}$$

where $C_{cool}(\gamma) = 3\kappa k_B/(256\pi^2 \mu_c \sigma(\gamma_c - 1))[(\gamma - 1)G\mu/(\gamma k_B)]^{-1/(\gamma-1)}$. In both cases we evaluate the second line for $\gamma = 7/5$.

The mass loss time-scale, now in the Bondi-limited regime after spontaneous mass loss, remains as given in Equation 2.16 for $R_{rcb} \gtrsim 2R_c$. For $R_{rcb} \lesssim 2R_c$, we can solve for the mass loss time-scale using Equations 2.8 and 2.23:

$$\begin{aligned} t_{loss} &\simeq C_{loss}(\gamma) M_c^{-2+\frac{1}{\gamma-1}} R_c^{2-\frac{2}{\gamma-1}} T_{eq}^{\frac{3}{2}-\frac{1}{\gamma-1}} \Delta R_a^{1+\frac{1}{\gamma-1}} \exp\{[R_B/(R_c + \Delta R_a)]\} \\ &\simeq 122 \left(\frac{T_{eq}}{1000\ \mathrm{K}} \right)^{-1} \left(\frac{M_c}{3M_\oplus} \right)^{5/8} \left(\frac{\Delta R_a}{R_c} \right)^{7/2} \exp\{[R_B/(R_c + \Delta R_a)]\}\ \mathrm{s}, \end{aligned} \tag{2.26}$$

where $C_{loss}(\gamma) = [(\gamma - 1)/\gamma]^{1+1/(\gamma-1)} (k_B/\mu)^{3/2-1/(\gamma-1)} G^{-2+1/(\gamma-1)}$. For typical parameters, loss time-scales can be short during this late stages of evolution ($\approx$ 700 years for $M_c = 3M_\oplus, T_{eq} = 1000$ K, and $R_{rcb} = 2R_c$), but the time-scales depend exponentially on the core mass and the inverse of the equilibrium temperature. This analytically-derived mass loss time-scale is independent of the atmospheric mass f, as $\dot{M}_{\rm atm}$ depends linearly on the atmospheric mass and hence cancels out.

The results for the mass loss and cooling time-scales are compared in Figure 2.3, varying $M_{\rm c}$, $T_{\rm eq}$, and f in (a), (b), and (c) respectively, with fixed $R_{\rm rcb} = 2R_{\rm c}$. This figure shows that $t_{\rm cool}$ decreases as f decreases and is only weakly dependent on other planetary parameters. Conversely, $t_{\rm loss}$ is independent of f but depends exponentially on $M_{\rm c}$ and $T_{\rm eq}$ as shown in Equation 2.26, so this time-scale varies widely over typical super-Earth parameters. As shown in Figure 2.3, as a planet of given $M_{\rm c}$ and $T_{\rm eq}$ evolves and loses mass, it will naturally reach a critical atmospheric mass $f_{\rm ret}$ for which $t_{\rm cool} = t_{\rm loss}$, shown by the solid and dashed lines intersecting. That these two time-scales intersect is guaranteed because a planet starts out with $t_{\rm loss} < t_{\rm cool}$, but as it loses atmospheric mass $t_{\rm cool}$ deceases while the mass-loss rate remains almost unchanged (see panel (c) in Figure 2.3). This allows $t_{\rm cool}$ to catch up with $t_{\rm loss}$ at a critical atmospheric mass, $f_{\rm ret}$. Once a planet reaches this critical atmospheric mass cooling becomes faster than loss. The core will cool, allowing the atmosphere to contract further. This contraction exponentially lowers the mass loss rate, shutting off mass loss. In this way, we expect this mass $f_{\rm ret}$ to be the final primordial envelope mass these planets retain, absent other factors affecting mass loss. The value of $f_{\rm ret}$ which balances the time-scales varies by orders of magnitude from 10^{-2} to 10^{-10} over typical super-Earth parameters.

We can analytically solve for this intersection point by setting the the mass loss and cooling time-scales equal. This is the atmospheric mass we expect these planets to retain after core-powered mass loss. Solving for $R_{\rm rcb} \gtrsim 2R_{\rm c}$:

$$\begin{aligned} f_{\rm ret} &\simeq \frac{K_{\rm loss} A}{C_{\rm cool}} M_{\rm c}^{-4+\frac{2}{\gamma-1}} R_{\rm c} T_{\rm eq}^{\frac{9}{2}-\frac{2}{\gamma-1}} R_{\rm rcb}^{2(3-\frac{1}{\gamma-1})} \exp\{[R_{\rm B}/R_{\rm rcb}]\} \\ \frac{f_{\rm ret}}{0.01} &\simeq 1.2 \times 10^{-13} \left(\frac{M_{\rm c}}{3M_{\oplus}}\right)^{3/2} \left(\frac{T_{\rm eq}}{1000\ {\rm K}}\right)^{-1/2} \left(\frac{R_{\rm rcb}}{R_{\rm c}}\right) \exp\{[R_{\rm B}/R_{\rm rcb}]\} \end{aligned} \tag{2.27}$$

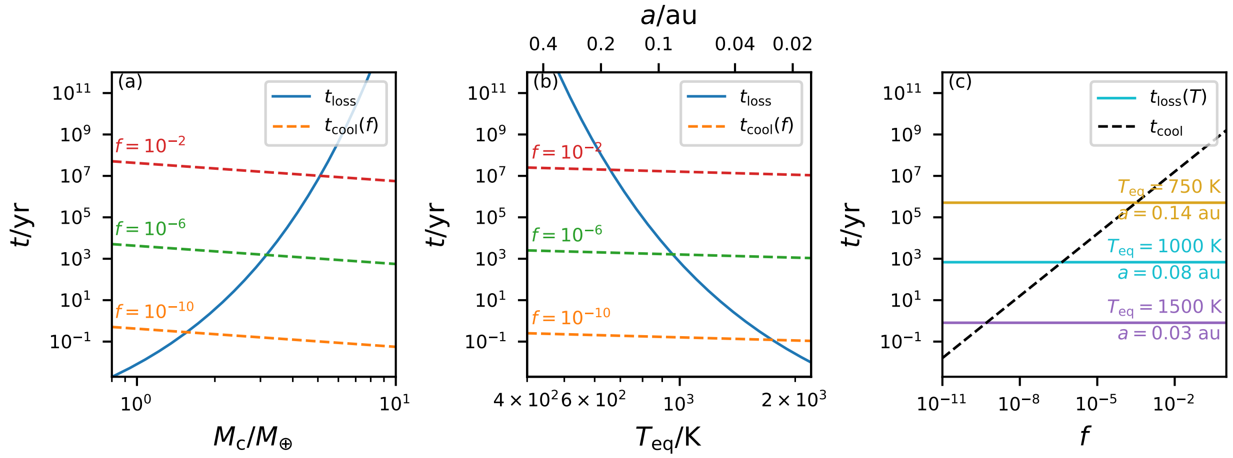

Figure 2.3: Comparison of the analytically derived thin regime mass loss and cooling time-scales, $t_{\rm loss}$ and $t_{\rm cool}$ respectively, for planets towards the end of their evolution with $R_{\rm rcb} = 2R_{\rm c}$. Panel (a) shows the time-scales as functions of core mass, $M_{\rm c}$, at fixed equilibrium temperature, $T_{\rm eq} = 1000$ K. Panel (b) displays how these time-scales depend on $T_{\rm eq}$ at fixed $M_{\rm c} = 3M_{\oplus}$. We also show a conversion of equilibrium temperature to distance from a star of solar luminosity, a, via Equation 2.2. Finally, in panel (c) we plot $t_{\rm cool}$ and $t_{\rm loss}$ as a function of atmospheric mass fraction, f, at fixed $M_{\rm c} = 3M_{\oplus}$. All time-scales are evaluated using $\gamma = 7/5$. Only one line is plotted for $t_{\rm loss}$ in (a) and (b), as $t_{\rm loss}$ is independent of f (see Equation 2.26). Similarly, $t_{\rm cool}$ is nearly independent of $T_{\rm eq}$ (see Equation 2.25, $t_{\rm cool} \propto T_{\rm eq}^{-1/2}$), such that the lines are indistinguishable on the scale shown in (c). The intersections between the lines yield the set of parameters for which $t_{\rm cool} = t_{\rm loss}$. As shown in (a), for a planet at given $T_{\rm eq}$, $t_{\rm loss}$ increases exponentially with increasing $M_{\rm c}$, while $t_{\rm cool}$ is nearly independent of $M_{\rm c}$ but is proportional to f. Thus as $M_{\rm c}$ is increased, the f value for which the two lines intersect increases exponentially. Similarly, (b) shows that this critical f decreases exponentially with increasing $T_{\rm eq}$. In (c), we demonstrate the final atmospheric mass fraction, $f_{\rm ret}$, at which $t_{\rm cool} = t_{\rm loss}$ increases for decreasing $T_{\rm eq}$, which corresponds to increasing $t_{\rm loss}$ values since the loss time-scale for a given $T_{\rm eq}$ is independent of f. Taken together, these results show that as a planet of given core mass and equilibrium temperature loses atmosphere, its loss time-scale is nearly constant, and its cooling time-scale decreases. Thus the planet will encounter a critical f at which $t_{\rm cool} = t_{\rm loss}$. This $f_{\rm ret}$ is exponentially dependent on $M_{\rm c}$ and $T_{\rm eq}$ and so varies widely over typical super-Earth values, and once a planet reaches this envelope fraction, mass loss will quickly halt as the planet cools and contracts.

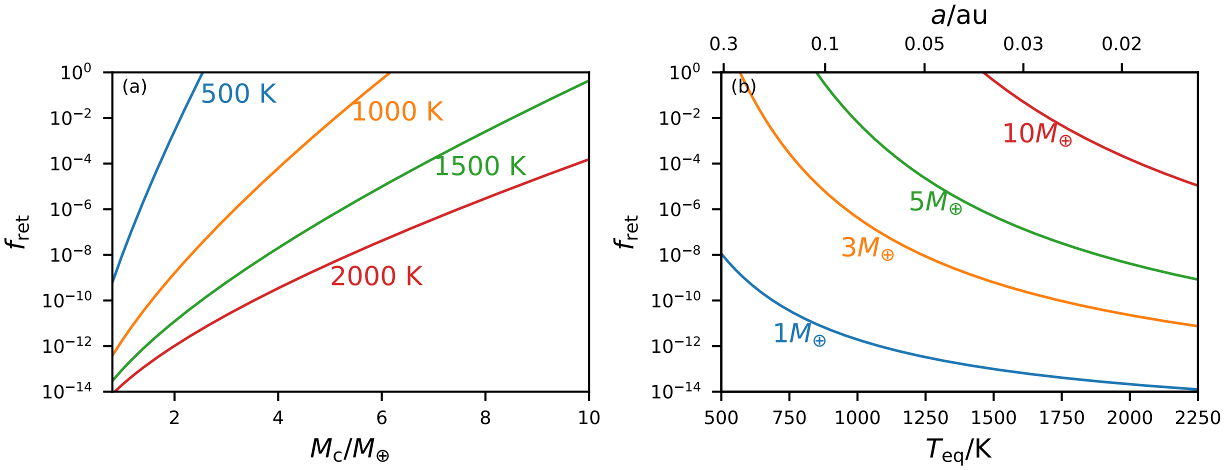

Figure 2.4: Analytical estimates of the atmospheric mass $f_{\rm ret}$ retained after core-powered mass loss in the thin regime as a function of (a) core mass, $M_{\rm c}$, and (b) equilibrium temperature, $T_{\rm eq}$. In panel (a) we plot lines corresponding to four equilibrium temperatures spanning typical super-Earth environments, whereas in (b) we show four typical core masses. These values are calculated using Equation 2.28, with $\gamma = 7/5$ and $R_{\rm rcb} = 2R_{\rm c}$. $f_{\rm ret}$ varies exponentially over the super-Earth regime, with negligibly small envelopes retained for the least massive and hottest planets and thicker envelopes retained for cooler and more massive planets.

and for $R_{\rm rcb} \lesssim 2R_{\rm c}$:

$$
\begin{aligned}
f_{\rm ret} &\simeq \frac{C_{\rm loss}}{C_{\rm cool}} \frac{\gamma - 1}{\gamma} M_{\rm c}^{-4+\frac{2}{\gamma-1}} R_{\rm c}^{6-\frac{4}{\gamma-1}} T_{\rm eq}^{\frac{9}{2}-\frac{2}{\gamma-1}} \Delta R_{\rm a}^{1+\frac{2}{\gamma-1}} \exp\{[R_{\rm B}/(R_{\rm c}+\Delta R_{\rm a})]\} \\
\frac{f_{\rm ret}}{0.01} &\simeq 2.43 \times 10^{-13} \left(\frac{M_{\rm c}}{3M_\oplus}\right)^{3/2} \left(\frac{T_{\rm eq}}{1000\ {\rm K}}\right)^{-1/2} \left(\frac{\Delta R_{\rm a}}{R_{\rm c}}\right)^{6} \\
&\qquad \exp\left\{\left[19.0\left(\frac{M_{\rm c}}{3M_\oplus}\right)^{3/4}\left(\frac{T_{\rm eq}}{1000\ {\rm K}}\right)^{-1}\right\}\left(\frac{R_{\rm c}+\Delta R_{\rm a}}{2R_{\rm c}}\right)^{-1}\right].
\end{aligned}
\tag{2.28}
$$

The solutions to Equation 2.28 are shown in Figure 2.4, taking $R_{\rm rcb} = 2R_{\rm c}$. As indicated by Figure 2.3, $f_{\rm ret}$ is smaller for less massive, hotter planets, and larger for more massive, cooler planets. The mass fraction of this leftover H/He envelope ranges from negligible ($f \sim 10^{-10}$), to comparable to Earth's modern secondary atmosphere ($f \sim 10^{-6}$), all the way to many times more massive than the modern secondary atmosphere of Venus ($f > 10^{-4}$).

2.3.4 Final pressures

Given these final atmospheric masses, we can calculate the corresponding surface pressures. These pressures have implications for the chemistry possible near the surface, including the outgassing and final atmospheric compositions. The final surface pressure, once the atmosphere has contracted such that $R_{\rm rcb} \sim R_{\rm c}$, is

$$P_{\rm surf} \simeq \frac{GfM_{\rm c}^2}{4\pi R_{\rm c}^4} \simeq 1\ {\rm bar}\frac{f}{10^{-6}}\frac{M_{\rm c}}{M_\oplus}. \tag{2.29}$$

This approximation holds as the atmosphere contracts from $R_{\rm rcb} \sim$ a few $R_{\rm c}$ to a fully isothermal profile up to an order unity constant, which accounts for the appropriate atmospheric mass distribution.

2.3.5 Optically thin limit

Our assumptions for the luminosity of the atmosphere only hold if the atmosphere is optically thick, i.e., if the integrated optical depth $\tau \gg 1$. If the atmosphere becomes optically thin, i.e., if $\tau \lesssim 1$, the core can cool on time-scales much shorter than when the core's heat is absorbed and re-radiated by the atmosphere. Therefore, we expect the atmospheric mass that a planet has at the time when the atmosphere becomes optically thin to be retained. The optical depth of the whole atmosphere is given by integrating the density profile

$$\tau = \int_{R_{\rm c}}^{R_{\rm rcb}} \rho(r)\kappa dr \tag{2.30}$$

which can be evaluated numerically. In the thin limit ($R_{\rm rcb} \lesssim 2R_{\rm c}$) and taking κ as a constant, the optical depth can be approximated as:

$$\begin{aligned} \tau &\simeq \kappa\rho_{\rm rcb}\frac{\gamma-1}{\gamma}R_{\rm c}\left(\frac{R'_{\rm B}}{R_{\rm c}}\right)^{1/\gamma-1} \\ &\simeq \left(\frac{f}{4.8\times10^{-9}}\right)\left(\frac{\kappa}{0.1\ {\rm cm^2g^{-1}}}\right)\left(\frac{M_{\rm c}}{3M_\oplus}\right)^{1/2}, \end{aligned} \tag{2.31}$$

where we use Equation 2.23 to express $\rho_{\rm rcb}$ as a function of f and evaluate for $\gamma = 7/5$ in the second equality. This approximation differs from the exact integral by less than a factor of two for all relevant atmosphere widths. Equation 2.31 indicates that the atmosphere transitions to being optically thin at $f \sim 10^{-8}$, equivalent to a surface pressure of a few hundredths of a bar for typical planetary masses. Therefore, we expect core-powered mass loss to cease at residual atmospheric mass fractions of about 10^{-8}.

2.3.6 Combining the different regimes

Now that we have derived the retained atmospheric mass fraction $f_{\rm ret}$ in all these regimes of planet evolution, we can combine them into one analytic model. The core can only cool enough to impact the evolution of planets if $E_{\rm c} > E_{\rm atm}$ at the end of the spontaneous mass loss phase. By equating Equations 2.14 and 2.21 for $R_{\rm rcb} \sim 2R_{\rm c}$, we find that a planet's available energy for cooling is mostly stored in the core if the atmospheric mass remaining after spontaneous mass loss $f_{\rm sml} \lesssim \mu/\mu_{\rm c} \simeq 0.03$. This value corresponds to planets with $f_{\rm init} \lesssim 0.15$, since planets typically lose $\sim 80\%$ of their initial mass in the spontaneous mass loss phase. We determine whether a planet is in the thick or thin core cooling analytic regime by whether its radiative convective boundary as derived in Section 2.3.2 is greater than or less than $2R_{\rm c}$, respectively. The thick and thin regimes are combined in Figure 2.5, showing the final atmospheric masses and surface pressures predicted by this analytic treatment. In this figure we also include the optically thin limit, i.e., the parameter space in which planets reach this limit before $t_{\rm cool} < t_{\rm loss}$, which is shaded in gray. The thick and thin regimes do not connect smoothly due to their different atmospheric mass and core temperature approximations, but the trends with planet mass and equilibrium temperature continue across the boundary. We expect the smallest and hottest planets to become optically thin before they can cool enough to keep their envelopes. Slightly larger and/or colder planets reach the thin regime and span orders of magnitude in their final envelope masses. Finally, the largest and coldest planets evolve in the thick regime and typically have final envelope mass fractions $f \sim 10^{-3} - 10^{-2}$.

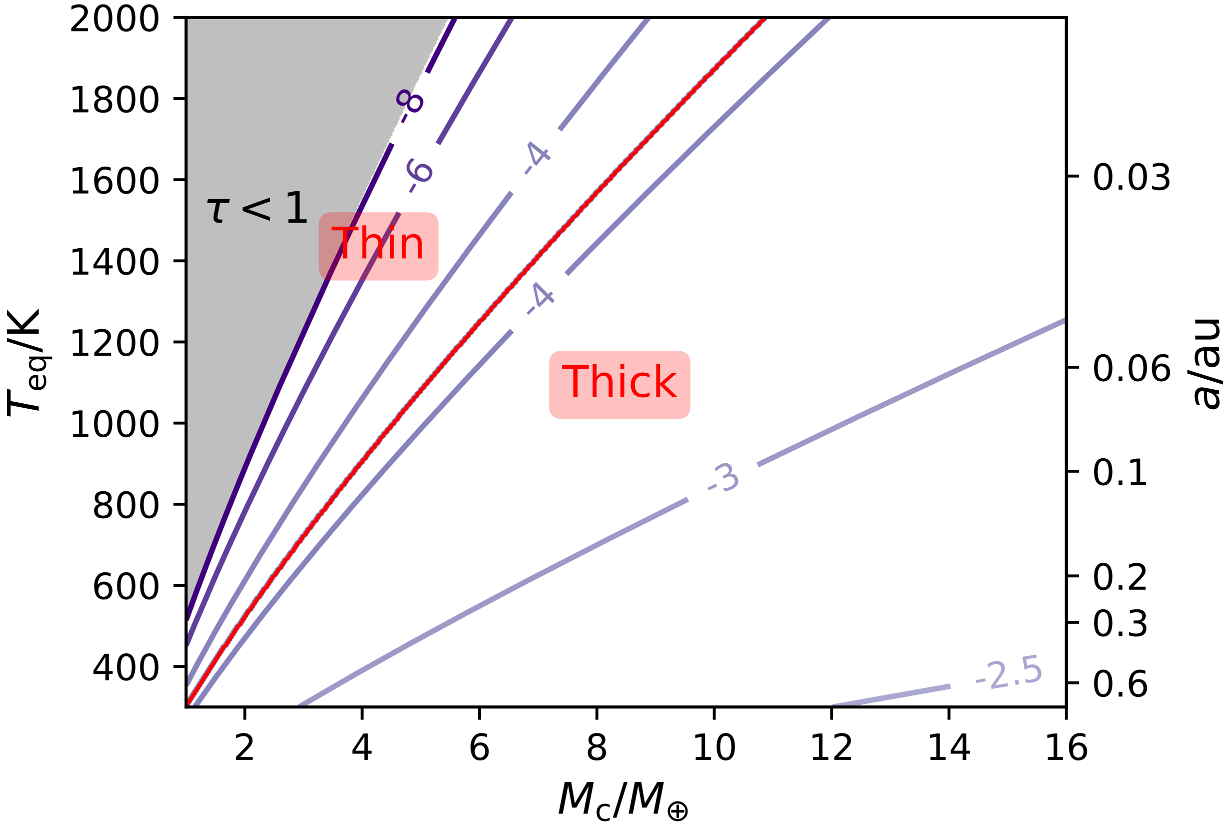

Figure 2.5: Analytical estimates of the final atmospheric mass fraction $f_{\rm ret}$ at which $t_{\rm cool} = t_{\rm loss}$ in the thick and thin regimes taken together. The lines represent contours of $\log_{10}(f_{\rm ret})$, ranging from $f_{\rm ret} = 10^{-8}$ to $10^{-2.5}$. These $f_{\rm ret}$ values are calculated analytically as a function of $M_{\rm c}$ and $T_{\rm eq}$, using Equation 2.27 in the thick regime and Equation 2.28 in the thin regime. The analytic thin regime calculations are independent of $f_{\rm init}$, so long as planets enter the core cooling regime. The thick regime, as well as the location of the transition between the two, depend on $f_{\rm init}$ due to the dependence of $R_{\rm rcb,crit}$ on $f_{\rm init}$, and the results shown are for $f_{\rm init} = 0.03$. The transition between the thick and thin regimes is shown as a red line, and the region of parameter space for which the atmosphere becomes optically thin ($\tau < 1$) are shaded in gray.

2.4 Numerical Method and Scaling Comparison

To complement the analytical results presented in Section 2.3, we implement the energy and mass loss evolution described in Section 2.2 numerically. In our simulation, we begin with an initial mass fraction, $f_{\rm init}$, and radiative-convective boundary location, $R_{\rm rcb,init} = R'_{\rm B}$. These values, along with the planet's mass and equilibrium temperature, are sufficient initial conditions to calculate the atmospheric profile.

We use an Euler method to evolve the atmosphere, calculating the mass and energy lost over a short time-step, $\Delta t = 0.1 \min \left(|E_{\rm atm}/L|, t_{\rm loss}\right)$, using the mass loss rates and luminosity derived above. We then use the new total mass and energy to derive the new location of the radiative-convective boundary, which results in a new atmospheric profile. This new profile begets new mass- and energy-loss rates, and we carry on evolving the atmosphere. To illustrate the general results of these simulations, we consider in greater detail the super-Earth and sub-Neptune from Figure 2.2. Figure 2.6 shows the evolution with time of an expanded set of physical parameters for these two planets. In the top row we show (a) the total energy of the atmosphere and thermal energy of the core, (b) the energy loss rates, and (c) the cooling time-scale. The middle row displays (d) the atmospheric mass, (e) the mass loss rate, and (f) the loss time-scale. Finally on the bottom row we plot (g) the radius of the radiative convective boundary ($R_{\rm rcb}$), (h) the density at the $R_{\rm rcb}$, and (i) the ratio of the cooling and loss time-scales. As in Figure 2.2, the planet that becomes a super-Earth, with $f_{\rm init} = 0.05$, is shown in gray, and the planet that becomes a sub-Neptune, starting with $f_{\rm init} = 0.15$, is in tan.

Initially, mass loss and cooling are rapid in both simulations, and the atmospheres loses mass and contract. In this initial spontaneous mass loss phase, mass loss is limited by the rate at which energy can escape from the planet by diffusion across the radiative-convective boundary. In this regime, the mass-loss rate is directly coupled to the envelope's cooling rate, as shown by comparison of panels (b) and (e) of Figure 2.6. In the $f_{\rm init} = 0.15$ case shown in tan, the atmosphere's total energy becomes more negative with mass-loss and contraction and starts to exceed in magnitude

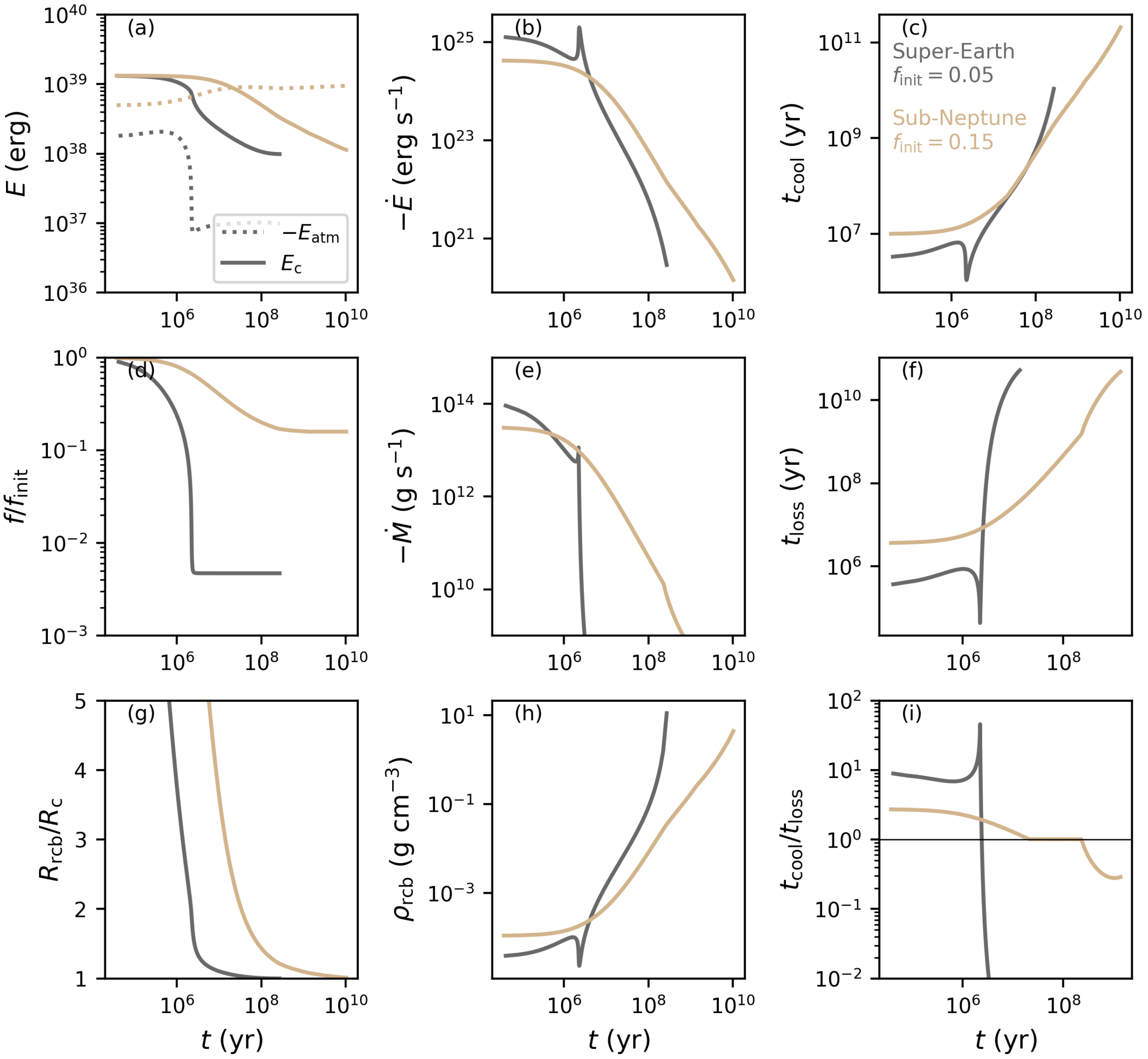

Figure 2.6: Evolution of a super-Earth and a sub-Neptune over time. In the top row we show (a) the total energy of the atmosphere and thermal energy of the core, (b) the energy loss rate, and (c) the cooling time-scale. The middle row displays (d) the atmospheric mass, (e) the mass loss rate, and (f) the mass loss time-scale. Finally on the bottom row we plot (g) the radius of the radiative convective boundary, (h) the density at $R_{\rm rcb}$, and (i) the ratio of the cooling and loss time-scales. Both planets have mass $M_{\rm c} = 4M_\oplus$ and equilibrium temperature $T_{\rm eq} = 1000$ K. The planet shown in gray starts with $f_{\rm init} = 0.05$, undergoes significant core-powered mass loss, and becomes a super-Earth, but it cools quickly enough to retain a modest H/He envelope: $f_{\rm ret} \sim 10^{-4}$. In contrast, the planet shown in tan starts with $f_{\rm init} = 0.15$, never undergoes core-powered mass loss, and becomes a sub-Neptune, with $f_{\rm ret} \sim 3\%$.

the core's thermal energy available for cooling, as shown in panel (a). Therefore, the cooling of the core cannot release enough energy to impact the atmospheric evolution significantly. The atmosphere retains $\sim 20\%$ of its initial mass at the end of the spontaneous mass loss phase (panel (d)), and it goes on to cool and contract on gigayear time-scales. The evolution of this planet is representative of exoplanets seen in the observed sub-Neptune population.

In contrast, in the $f_{\rm init} = 0.05$ case, plotted in gray in Figure 2.6, panel (a) shows that the atmospheric energy is much less than the available thermal energy in the core. As the envelope contracts, the temperature of the core decreases. This core cooling releases thermal energy into the atmosphere. In this way, the super-Earth's atmospheric energy increases with time while the core's energy slowly declines. This increase in energy slows the envelope's contraction relative to the sub-Neptune case, as shown by panel (g). While the envelope never stops contracting completely as we approximate in our analytic treatment, this slowing of the contraction sustains mass loss at a faster rate than if the atmosphere were allowed to contract without core heating once the mass-loss rate transitions to being Bondi-limited. The planet thus loses most of its primordial envelope and becomes a super-Earth. This core-powered mass loss phase continues until $\rho_{\rm rcb}$ begins to decrease, as shown in panel (h). This decrease makes radiative diffusion through the atmosphere easier, and the envelope's luminosity increases, as demonstrated in panel (b). Therefore, the cooling time-scale, $t_{\rm cool}$, decreases (panel (c)). Meanwhile, the mass loss time-scale, $t_{\rm loss}$ (panel (f)), increases rapidly once the planet transitions to the Bondi-limited mass-loss regime. In this way, the cooling time-scale becomes less than the mass loss time-scale, shown by the horizontal line in panel (i). Once this occurs, the planet can cool more quickly than mass is lost. As the planet continues to contract, the mass loss rate decreases rapidly due to its exponential dependence on the radiative-convective boundary radius, $R_{\rm rcb}$, as shown in panel (e). The mass loss time-scale grows longer than the planet's age (panel (f)), effectively halting loss. This remnant atmosphere then cools and contracts without loss on gigayear time-scales, and the planet becomes a super-Earth with a $f \sim 10^{-4}$ H/He envelope.

We perform a set of numerical simulations spanning a wide range in parameter space to facilitate

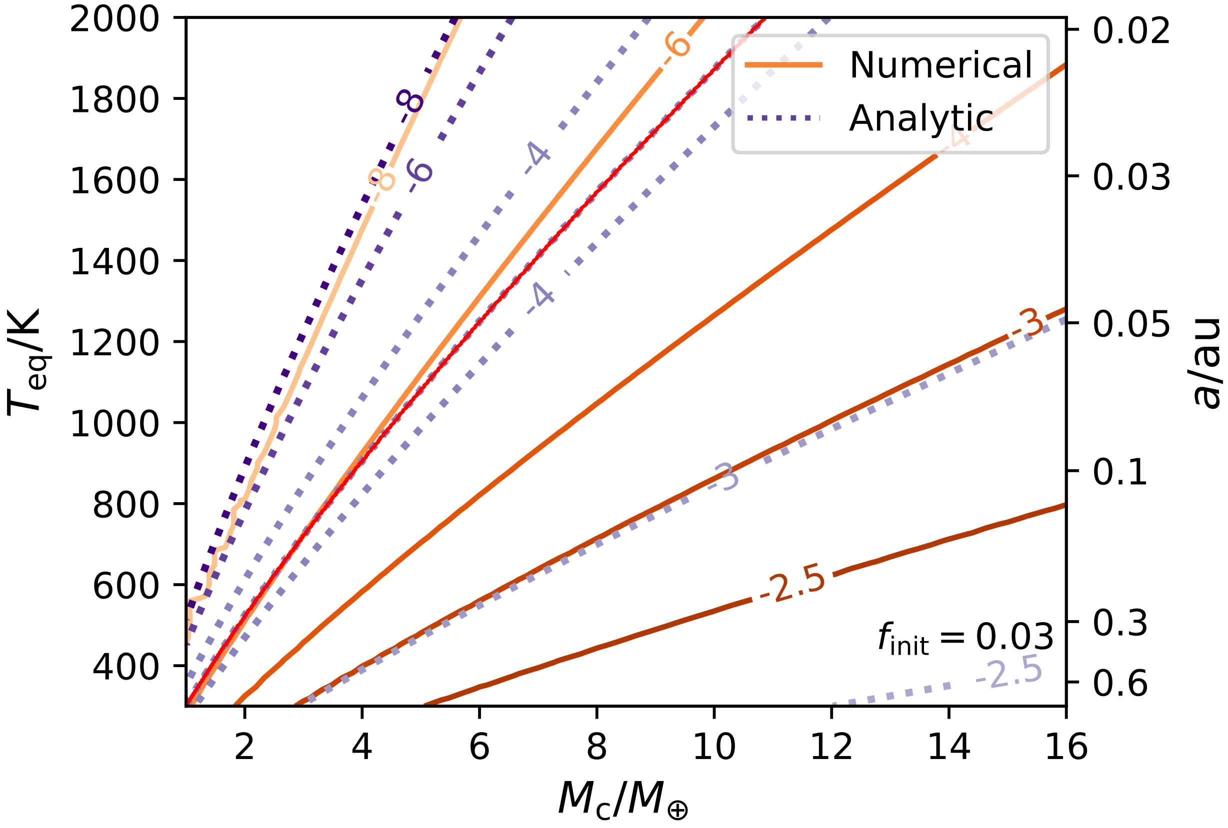

Figure 2.7: Contours of the logarithm of the retained atmospheric mass fractions, $\log_{10} f_{\rm ret}$, of an ensemble of ~ 2500 planets evolved using our numerical scheme, plotted as functions of core mass, $M_{\rm c}$, and equilibrium temperature, $T_{\rm eq}$, depicted by orange solid lines. All planets began with $f_{\rm init} = 0.03$. Overlaid in purple dotted lines are the analytic results previously shown in Figure 2.5, including the transition between the thick and thin regimes shown as red line. These results show that our analytic approximations capture the scaling of final atmospheric mass fractions found in our numerical simulations. Differences between the numerical and analytical results include (i) a smooth transition between the thick and thin regimes and (ii) a difference in absolute values of $f_{\rm ret}$ due to its dependence on $f_{\rm init}$, both of which are not captured in our analytic approximations (see text for details).

comparison between our analytic and numerical results. To compare across the entire super-Earth parameter space, Figure 2.7 shows in orange contours of the final atmospheric mass fractions of simulated planets, all starting with the same initial mass fraction, $f_{\rm init} = 0.03$, for ease of comparison to our previous analytic results. It is apparent from Figure 2.7 that the hotter and less massive planets are able to retain less primordial atmosphere after core-powered mass loss, while cooler and more massive planets can conversely maintain more. These scaling agree quantitatively with our analytic predictions of retained atmospheric mass with core mass and equilibrium temperature (see Figure 2.5). These numerical results smooth the discontinuity in our analytic approximations between the thick and thin regimes. We find both numerically and analytically that there exists a portion of parameter space where super-Earths should be expected to retain modest envelopes of hydrogen and helium. However, the predicted atmospheric mass a planet can retain depends on its initial cooling properties, and hence its initial atmospheric mass fraction, something that is not fully captured in our analytic results.

We show this dependence on initial atmospheric mass in Figure 2.8. This figure shows the evolution of seven planets with identical core mass and equilibrium temperature, but which vary in their initial mass fractions at the time of disk dispersal. Figure 2.8 displays a strong dependence of $f_{\rm ret}$ on the initial envelope mass fraction. For example, a planet with $f_{\rm init} = 0.04$ retains only 10^{-4} times its initial envelope, while a planet with $f_{\rm init} \simeq 0.1$ retains $\sim 10\%$ of its initial envelope. This dependence on the initial envelope mass fraction can be understood as follows. While the analytic results presented in Section 2.3.3 are independent of $f_{\rm init}$ for a given $R_{\rm rcb}$, the $R_{\rm rcb}$ at which most mass is lost is determined in part by $f_{\rm init}$. We predict this dependence of $R_{\rm rcb}$ on $f_{\rm init}$ in Equation 2.18. This result arises, because planets with larger initial atmospheric fractions have longer initial atmospheric cooling time-scales, $t_{\rm cool} \propto f^2$, per Equation 2.15. Therefore, the Bondi-limited mass loss rate has to decrease further to become less than the luminosity-limited mass loss rate, equivalent to the atmosphere contracting more. In the highest atmospheric masses we show in Figure 2.8 ($f_{\rm init} \gtrsim 0.10$), the initial atmospheric energies are sufficiently high that the core's cooling has negligible input on atmospheric evolution: these planets never undergo core-powered

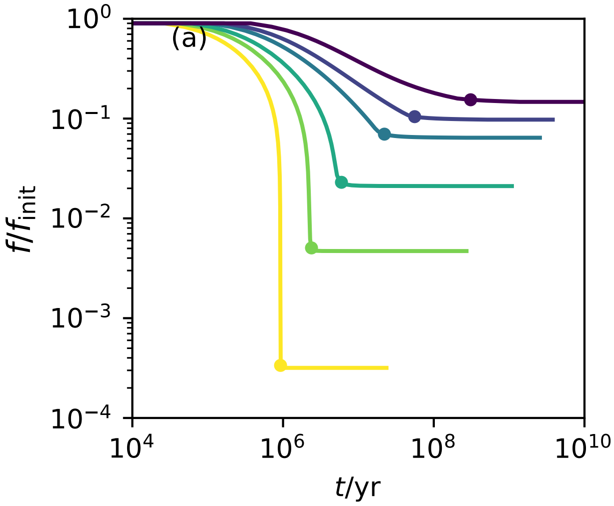

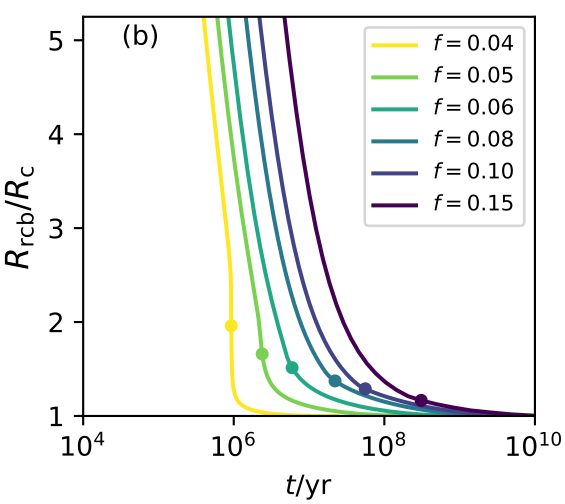

Figure 2.8: Evolution of atmospheric mass, f, and radiative-convective boundary radius, R_rcb, over time for seven planets. Each planet has the same core mass, $M_\mathrm{c} = 4M_\oplus$, and equilibrium temperature, $T_\mathrm{eq} = 1000$ K, but different initial atmospheric mass fractions ranging from 4 to 15 percent. The time at which each planet's cooling time-scale becomes shorter than its mass loss time-scale is denoted by a dot. These planets conclude mass loss with final atmospheric masses varying by many orders of magnitude as a fraction of each planet's initial atmospheric mass. This strong dependence on initial atmospheric mass is due to the different R_rcb planets are able to contract to as their atmospheres cool and lose mass during the spontaneous mass loss phase.

mass loss at all and become sub-Neptunes.

In summary, although the analytic and numerical scalings for $f_{\rm ret}$ shown in 2.7 are general and independent of $f_{\rm init}$, the absolute values of $f_{\rm ret}$ do depend on $f_{\rm init}$. The values shown on the contours in Figure 2.7 correspond to initial envelope fractions of 3%. Since we do not know the initial mass fractions of observed super-Earths *a priori*, these results therefore do not predict the atmospheric masses we expect observed super-Earths to have. Figure 2.7 only compares our numerical simulations to analytic results with the same initial conditions. We discuss possible observational signatures in the following section.

2.5 Observational Tests

A fundamental result of this work is that some super-Earths can retain significant H/He envelopes after core-powered mass loss. This finding implies that super-Earths, which form by core-powered mass loss, can have much lower mean molecular weight atmospheres than planets with entirely outgassed secondary atmospheres. This low mean molecular weight could enhance the detectability of super-Earth atmospheres. The scale height of an atmosphere which has cooled and contracted such that $R_{\rm rcb} \simeq R_{\rm c}$ is $H = k_{\rm B} T_{\rm eq}/(\mu g)$, where $g = GM_{\rm c}/R_{\rm c}^2$ is the gravitational acceleration at the planet's surface. The scale height of a hydrogen-dominated atmosphere, with $\mu = 2.2$ amu, is an order of magnitude larger than one composed of even the lightest proposed secondary species, such as water ($\mu = 18$ amu). Other possible constituents, such as N_2, CO and CO_2 have even larger mean molecular weights, and thus atmospheres including them would possess even smaller scale heights. Input of heavier secondary components from surface outgassing would increase the mean molecular weight of any residual primordial atmosphere and therefore decrease its scale height. However, the presence of H/He would increase the atmospheric scale height above what it would be for a purely out-gassed atmosphere.

This large difference in mean molecular weight between residual primordial and pure secondary atmospheres means that super-Earths which retain some primordial hydrogen gas will be distinguishable from those with entirely secondary atmospheres, even if their bulk densities are consistent with a rocky core. Spectroscopic measurements can distinguish between high- and low-μ atmospheres by the prominence of molecular features, which increases with scale height (e.g. Benneke & Seager, 2012; Fortney et al., 2013). Such measurements have already been performed for sub-Neptunes with the *Hubble Space Telescope* (e.g. Benneke et al., 2019a,b), and measurements of the hydrogen content of super-Earth atmospheres will be within the capabilities of the upcoming *James Webb Space Telescope* (e.g. Greene et al., 2016; Wunderlich et al., 2021) and *Ariel* missions (e.g. Edwards et al., 2019). While clouds can obscure these molecular features (e.g. Kreidberg et al., 2014), high-resolution spectroscopy may enable differentiation even of cloudy high-μ and low-μ atmospheres (e.g. Gandhi et al., 2020). These observations will test our hypothesis that some super-Earths can retain primordial H/He, provided that they are not subsequently eroded by photo-evaporation (see discussion in Section 2.6.4 for details). Any residual H/He will also enhance the detectability of other features of interest, such as potential biosignatures (e.g. Wunderlich et al., 2021).

To test this mechanism of retaining H/He atmospheres, we can predict what atmospheres we would expect planets to retain as a function of their initial atmospheric mass fractions. The initial mass fraction at the time of disk dispersal, f_{init}, is a major uncertainty which depends on both the planet's cooling time-scale and the disk lifetime. While predictions of the initial atmospheric mass's scaling with parameters such as planet mass, equilibrium temperature, and disk lifetime exist (e.g. Ginzburg et al., 2016), their dependence on unknowns such as the disk lifetime make these relations uncertain for observed planetary systems. We therefore cannot predict a unique relationship between a planet's mass and temperature and its final atmospheric mass fraction. However, we can invert the problem and use a super-Earth's residual hydrogen envelope (when observed) to infer its initial atmospheric mass at the time of disk dispersal. To this end, we show in Figure 2.9 contours of constant final atmospheric mass fraction, f_{ret}, as a function of initial atmospheric mass, f_{init}, and core mass in panel (a). Panel (b) is the same as (a) but the dependence on equilibrium temperature is shown instead of core-mass.

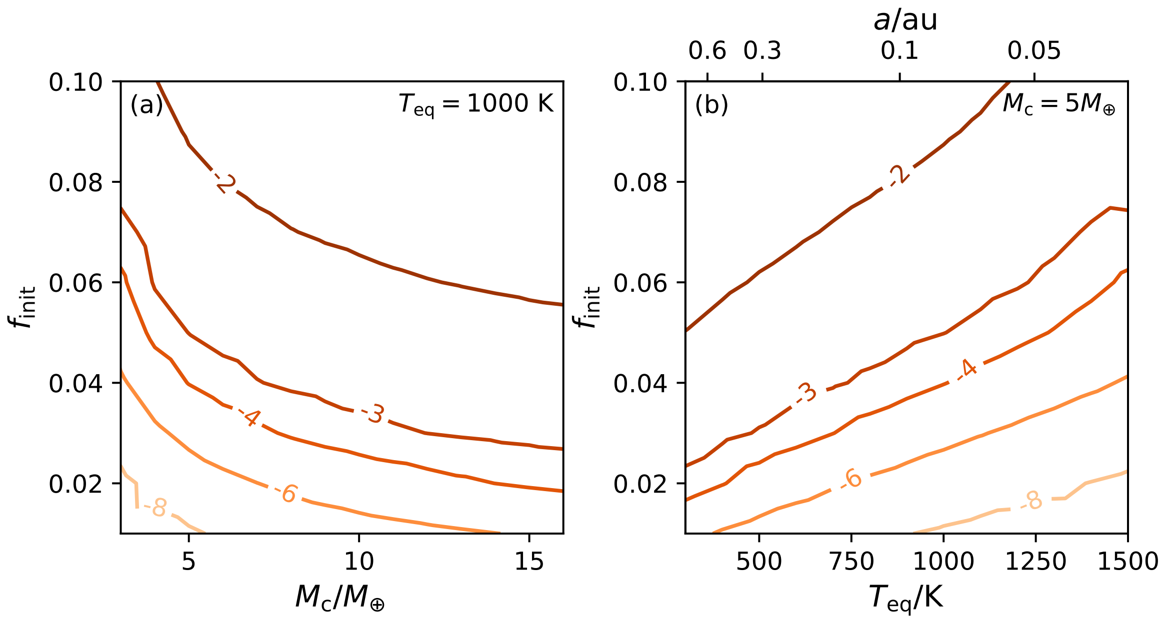

Figure 2.9: Contours of the logarithm of the retained atmospheric mass fraction, $\log_{10} f_{\mathrm{ret}}$, of an ensemble of numerically-evolved planets, demonstrating the dependence of final atmospheric mass on initial atmospheric mass. In panel (a), each planet has the same equilibrium temperature, $T_{\mathrm{eq}} = 1000$ K, but a different core mass. In panel (b), each planet instead has the same core mass, $M_c = 5M_{\oplus}$, but varies in equilibrium temperature.

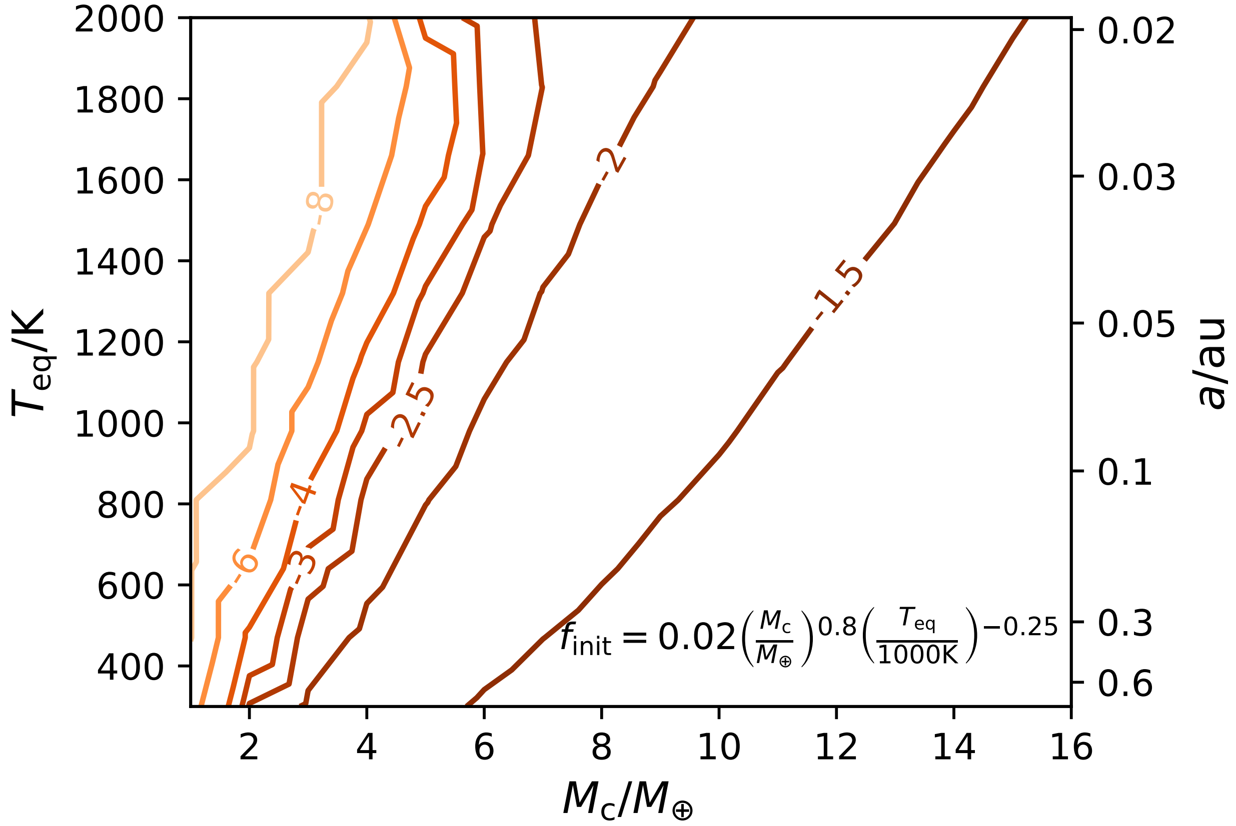

Figure 2.10: Logarithmic contours of the retained atmospheric mass fractions, $\log_{10} f_{\mathrm{ret}}$, of an ensemble of numerically evolved planets, plotted as a function of core mass, M_{c}, and equilibrium temperature, T_{eq}. These planets differ from Figure 2.7 in their initial envelope mass fraction. Instead of assuming $f_{\mathrm{init}} = 0.03$ for all planets, these planets start with atmospheric masses that scale with core mass and equilibrium temperature as given by $f_{\mathrm{init}} = 0.02(M_{\mathrm{c}}/M_\oplus)^{0.8}(T_{\mathrm{eq}}/1000\ \mathrm{K})^{-0.25}$. This scaling is a prediction taken from Ginzburg et al. (2016) for a constant disk lifetime of 1 Myr. The transition between sub-Neptune and super-Earth planets is more sudden in this figure than in Figure 2.7, and smaller mass planets are able to retain H/He envelopes at cooler equilibrium temperatures. Both of these feature are consistent with the observed radius valley (Fulton et al., 2017) and past works that demonstrated that the radius valley can be formed by the core-powered mass loss mechanism (e.g. Ginzburg et al., 2018; Gupta & Schlichting, 2019).

Furthermore, by using predictions from gas-accretion models for the atmospheric mass fractions as a function of core mass and equilibrium temperature at the time of disk dispersal, we can calculate the expected final envelope masses fractions. For example, in Figure 2.10 we show the resulting final retained atmospheric mass fractions as a function of core mass and equilibrium temperature using the prediction from Ginzburg et al. (2016) given in their Eq. 18, which yield $f_{\rm init} = 0.02(M_{\rm c}/M_{\oplus})^{0.8}(T_{\rm eq}/1000\ {\rm K})^{-0.25}$ for a disk lifetime of 1 Myr.

The transition from massive retained envelopes to nearly-stripped cores with tenuous retained envelopes is more sudden in Figure 2.10 than in Figure 2.7, and smaller mass planets are able to retain H/He envelopes if they are at cooler equilibrium temperatures. Both of these feature are consistent with the observed radius valley (Fulton et al., 2017) and past works that demonstrated that the radius valley can be formed by the core-powered mass loss mechanism (e.g. Gupta & Schlichting, 2019, 2020).

2.6 Discussion

The work presented here demonstrates that some super-Earths can retain small residual H/He envelopes at the end of the core-powered mass loss phase. Such residual H/He envelopes can potentially alter the long-term surface chemistry of these planets and can also increase the scale height of the atmospheres, making atmospheric observations of such planets feasible in the near future. In this section, we discuss the implications of planets having different atmospheric properties than we assume throughout this manuscript. We also quantify the effects of different atmospheric loss processes and discuss how these mechanisms relate to our results.

2.6.1 Adiabatic index

The adiabatic index depends on the number of degrees of freedom of the main constituent of the atmosphere. We assume throughout this work that the atmosphere is primarily diatomic hydrogen. This molecular composition results in an adiabatic index $\gamma = 7/5$. However, other values of γ are possible due to, for example, the dissociation of hydrogen at high temperatures in the deep interior or heating of the outer parts of the envelope due to absorption of high energy EUV radiation. We thus present our results in terms of γ in all analytic expressions throughout the manuscript. Increasing the adiabatic index leads to the mass and energy of the atmosphere being more concentrated in the outer portion of the convective region, leading to more mass loss and less contraction in the spontaneous mass loss phase. However, we do not expect this to significantly alter the overall results of this paper.

2.6.2 Opacity

The opacity at the radiative-convective boundary controls the atmosphere's cooling rate, $L \propto 1/\kappa$, and as such is key to understanding the evolution of super-Earth atmospheres. As discussed in Section 2.2, we use a constant value of the atmosphere's opacity, $\kappa = 0.1$ cm^{2}g^{-1}, throughout this work. This choice is based on the typical order of magnitude value expected for H/He-dominated atmospheres (e.g. Freedman et al., 2008). In reality, the atmospheric opacity depends on many factors which are likely to vary over the course of super-Earth atmospheric evolution. More complex opacity models can include a power law increase in opacity with density (e.g. Gupta & Schlichting, 2019), and power law increases with temperature and atmospheric metallicity in addition to density (e.g. Lee & Chiang, 2015). We found that implementing an opacity dependence on density did not have a major effect on our final atmospheric masses. The strongest effect, on the critical radiative convective boundary to which a planet cools during spontaneous mass loss, is only logarithmic (Equation 2.18). However, if the overall composition of the atmosphere changes significantly as the super-Earths lose atmospheric mass, an increase in opacity with metallicity over time could affect our results. To test whether we expect the hydrodynamic outflow to significantly fractionate the atmosphere, thereby increasing the metallicity of the remnant atmosphere, we compute the cross-over mass, $\mu_\mathrm{c} = \mu + k_\mathrm{B} T_\mathrm{eq} \dot{M}/(4\pi b \mu G M_\mathrm{c})$, where b is the binary diffusion coefficient between the two species. This is the molecular weight above which a species cannot be liberated from the planet by the hydrodynamic wind, as the drag forces cannot overcome gravity (Hunten et al., 1987).

Using $b \sim 5 \times 10^{17} T^{0.75}$ cm^{-1}s^{-1}, a value typical of the binary diffusion coefficients of common secondary species in hydrogen gas (Zahnle & Kasting, 1986), we find – given our mass-loss rates – the smallest value for the cross-over mass for the planets considered in this paper is about $\mu_c \sim 10^3$ amu. This is much larger than any potential heavy species in these atmospheres. We therefore conclude that secondary species are efficiently carried away by the outflow and that the atmosphere does not become significantly enhanced in heavy elements due to the wind itself for the planets considered in this paper.

Other processes could also influence the atmosphere's opacity as mass loss proceeds. For example, as the overlying pressure decreases, the rate of outgassing may increase (e.g. Kite et al., 2020), increasing both the metallicity and availability of potential condensates. In this way, the opacity of the atmosphere could increase as primordial H/He is lost. This increase in opacity would decrease the luminosity of the planet and thus increase the cooling time-scale, allowing more mass to be lost before the planet is able to cool on a shorter time-scale than mass is lost. However, this effect may be offset by the increasing difficulty of unbinding the now-heavier atmosphere, as $f_{\rm ret} \propto \mu^{7/2} \exp\{[\mu]\}$, aiding in the retention of whatever mixture of primordial and secondary gas remains. The overall effect of these processes is therefore difficult to quantify without a detailed outgassing and opacity model, which is beyond the scope of this work.

2.6.3 Collisionless limit

The hydrodynamic mass loss rate (Equation 2.8) applies only in the hydrodynamic limit, where a Parker-type outflow is sustained across the sonic point R_s. If the flow becomes collisionless before reaching the sonic point, then the sonic point is no longer causally connected to the radiative-convective boundary and a hydrodynamic out-flow is no longer possible. Instead, in this regime, the loss occurs ballistically via Jeans escape, and is much slower than in the hydrodynamic case (e.g. Owen & Mohanty, 2016).

We can solve for the $R_{\rm rcb}$ at which the flow becomes collisionless at the sonic point with the same parameterization as used in Equation 2.18, again with $\gamma = 7/5$:

$$R_{\rm rcb,coll} = \frac{-R_{\rm B}}{\ln\left[\epsilon^n R_{\rm B}^n / Y\right]}$$
$$\frac{R_{\rm rcb,coll}}{R_{\rm c}} \simeq \frac{38.0 \times \left(\frac{M_{\rm c}}{3M_\oplus}\right)^{3/4}\left(\frac{T_{\rm eq}}{1000\ {\rm K}}\right)^{-1}}{41.0 - 0.5\ln\left[\frac{\epsilon}{0.03}\right] + \ln\left[\frac{f}{0.05}\right] + 2\ln\left[\frac{T_{\rm eq}}{1000\ {\rm K}}\right] - \ln\left[\frac{M_{\rm c}}{3M_\oplus}\right]}, \tag{2.32}$$

where $Y \equiv \sigma_{\rm coll} R_{\rm s} {\rm e}^2 f_{\rm init} M_{\rm c} / (8\pi A \mu R_{\rm B}'^{1/(\gamma-1)})$ and in the second line we have taken $\gamma = 7/5$. From comparison of the denominators of Equations 2.18 and 2.32, the critical radius for collisionless flow is less than the critical cooling radius for all $M_{\rm c} > 0.06 M_\oplus$. This implies that cooling will halt mass loss before the outflow becomes collisionless for all the planets we consider here.

2.6.4 Stability to photo-evaporation

In order for these remnant primordial atmospheres to be observed today, they must be stable on gigayear time-scales to a range of processes which could destroy them. One such process is photo-evaporation: mass loss driven by the absorption of high energy radiation from the planet's host star. We can quantify an atmosphere's stability to photo-evaporation after core-powered mass loss by comparing the remaining atmospheric binding energy to the energy the planet receives. The atmospheric energy remaining is $E_{\rm atm} \simeq \gamma/(2\gamma-1) G f M_{\rm c}^2 \Delta R_{\rm a} / R_{\rm c}^2$, where f is the final atmospheric mass fraction (Ginzburg et al., 2016). The energy received is the time-integrated high energy flux of the star absorbed by the planet: $E_{\rm rec} = E_{\rm out} R_{\rm rcb}^2 / (4a^2)$, where a is the semi-major axis and we assume the planet's cross-sectional radius is approximately $R_{\rm rcb}$. However, photo-evaporation is not perfectly efficient in converting incident energy to mass loss. We quantify the energy available for driving loss as the energy received multiplied by an efficiency factor, η: $E_{\rm av} = \eta E_{\rm rec}$. We adopt the nominal value $\eta_{\rm nom} = 0.1$, which is based on detailed hydrodynamic simulations (e.g. Owen & Wu, 2017). The energy output by the host star, $E_{\rm out}$, is given by its time-integrated XUV luminosity. For Sun-like hosts, one commonly-used XUV luminosity evolution track (e.g. Owen

& Wu, 2017) is that found by Jackson et al. (2012): $L_{\rm XUV} = 1.2 \times 10^{33} (t/{\rm Myr})^{-1.5}$ erg s^{-1} for $t > 100$ Myr. For this nominal evolution track, the integrated energy output from 100 Myr to 1 Gyr is $E_{\rm out,nom} = 5.2 \times 10^{45}$ erg.

Comparing these two energies gives us a criterion for determining the atmosphere's stability to photo-evaporation, $\Phi \equiv E_{\rm atm}/E_{\rm av}$. Expressing this criterion in terms of planet parameters, we find:

$$\begin{aligned}\Phi &\simeq \frac{\gamma}{2\gamma - 1} \frac{G f M_c^2 a^2}{R_{\rm rcb}^2 R_{\rm c} \eta E_{\rm out}} \\ &\simeq \frac{f}{3.3 \times 10^{-3}} \left(\frac{E_{\rm out}}{5.2 \times 10^{45} {\rm erg}}\right)^{-1} \left(\frac{\eta}{0.1}\right)^{-1} \\ &\qquad \left(\frac{M_{\rm c}}{3 M_\oplus}\right)^{5/4} \left(\frac{T_{\rm eq}}{1000{\rm K}}\right)^{-4} \left(\frac{R_{\rm rcb}}{R_{\rm c}}\right)^{-2}.\end{aligned} \tag{2.33}$$

If $\Phi \lesssim 1$, then sufficient energy is received to photo-evaporate the atmosphere. It is clear from Equation 2.33 that many of the tenuous atmospheres we predict are vulnerable to photo-evaporation on gigayear timescales. However, the order of magnitude observed difference in the XUV luminosity evolution of fast- and slow-rotating stars of the same type (Tu et al., 2015) can have major impacts on the gigayear-time-scale evolution of super-Earths and sub-Neptunes (e.g. Poppenhaeger et al., 2021). Specifically, a planet's remnant atmosphere is more resistant to erosion by photo-evaporation if the planet's host star emits less XUV energy than implied by the XUV evolution track of **?**, and/or if the photo-evaporative efficiency is lower: $\Phi \propto (E_{\rm out}\eta)^{-1}$.

We examine this vulnerability in more detail in Figure 2.11. In this figure, we plot the stability criterion, $\Phi = 1$, in gray dash-dotted lines for the residual atmospheres of the suite of simulated planets with $f_{\rm init} = 0.03$ previously presented in Figure 2.7. The different shades represent different values of the product of the XUV energy output by the host star and the efficiency factor, scaled to the nominal values: $E_{\rm out}\eta/(E_{\rm out,nom}\eta_{\rm nom}) = 10^{-5}$, 10^{-3}, 10^{-1}, and 1 from lightest to darkest. We take $E_{\rm atm}$ as the atmosphere's energy after it cools and contracts to $R_{\rm rcb} \sim R_{\rm c}$. Meanwhile, $E_{\rm av}$ is the energy the planet would receive between 100 Myr and 1 Gyr of its host star's evolution. These calculations are overlain on the $f_{\rm ret}$ values previously depicted in Figure 2.7. The residual

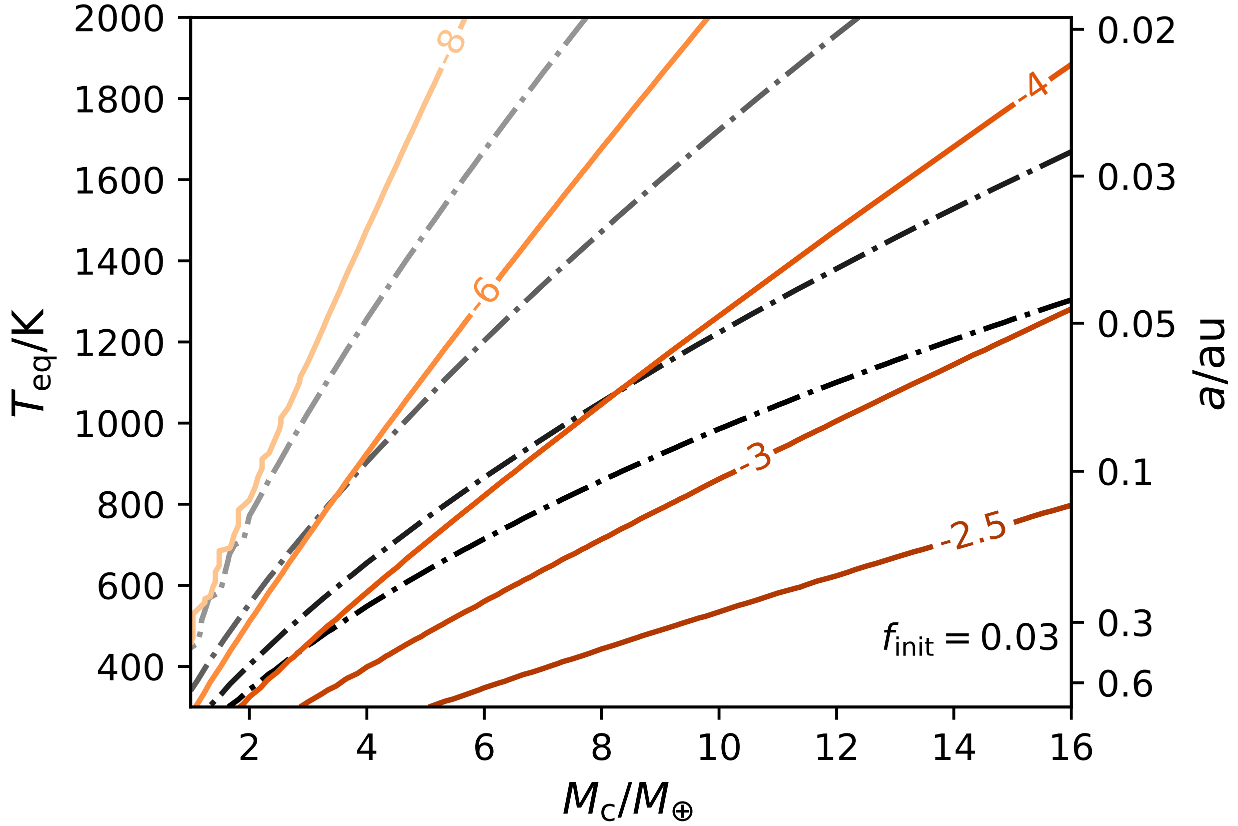

Figure 2.11: Contours of the atmospheric stability criterion, $\Phi = 1$ (see Equation 34), for the ensemble of ~ 2500 simulated planets with $f_{\rm init} = 0.03$ previously presented in Figure 2.7. The $\Phi = 1$ contours are plotted in gray dash-dotted lines. The shades represent variations in the product of the XUV energy output by the host star and the photo-evaporative efficiency, scaled to our adopted nominal values: $E_{\rm out}\eta/(E_{\rm out,nom}\eta_{\rm nom}) = 10^{-5}$, 10^{-3}, 10^{-1}, and 1 from lightest to darkest. The residual atmospheric mass fractions, $\log_{10} f_{\rm ret}$, at the end of core-powered mass-loss are shown as solid orange contours and are identical to those of Figure 2.7. The residual atmosphere of a planet lying along a particular contour (shown in solid orange) is stable to photo-evaporation if it falls below a given photo-evaporation contour.

atmosphere of a planet lying along a particular contour (shown in solid orange) is stable to photo-evaporation if it falls below a given photo-evaporation contour. Figure 2.11 demonstrates that only the residual atmospheres of cooler and more massive planets can survive photo-evaporation, unless a planet orbits a slow rotator with low XUV output. Smaller residual atmospheres could also be preserved if photo-evaporation is much less efficient than typically assumed. In this way, observations of super-Earth atmospheres provide a test of the efficacy of photo-evaporation. If these primordial atmospheres can survive to be observed, then photo-evaporation may not be as effective on long time-scales as predicted.

The argument presented above only accounts for the effects of photo-evaporation after the first 100 Myr once the XUV luminosity has decayed from its peak intensity. However, it is possible, in some regions of parameter space, for super-Earths to form by core-powered mass loss on time-scales shorter than this. In this case, the energy received from XUV radiation would be significantly increased. To determine the final envelope mass fraction in this case requires a coupled core-powered mass loss and photo-evaporation model. Such a combined model is beyond the scope of this paper but is planned for future work.

2.7 Summary & Conclusions

In this work, we have demonstrated that despite appearing to be bare cores from their radii and bulk densities, some super-Earth planets may possess thin primordial H/He envelopes at the end of the core-powered mass loss phase. This occurs because after rapid hydrodynamic loss strips a super-Earth of the bulk of its atmosphere, the accompanying decrease in density at the radiative-convective boundary allows the envelope to cool more efficiently. Once the cooling time-scale becomes shorter than the mass loss time-scale, the envelope can contract, which preserves the remaining primordial gas. This occurs even if sufficient heat energy remains in the core to unbind the entire atmosphere, as its cooling is mediated by radiative transfer through the envelope. Super-Earths with larger core masses and lower equilibrium temperatures retain larger mass fractions of gas. These fractions range from negligible ($f \sim 10^{-8}$) to much thicker than the present-day atmosphere of Venus ($f > 10^{-4}$). These retained envelopes following core-powered mass loss differ from the predicted outcomes of primordial super-Earth atmospheres in photo-evaporation models. Under photo-evaporative mass loss, as the atmosphere loses mass, the high-energy photons penetrate further into the atmosphere, and heating and loss become more effective. Thus if sufficient energy is received, the expectation is that photo-evaporation completely unbinds the original envelopes, unlike core-powered mass loss. However, many of the tenuous primordial atmospheres, which we predict core cooling to save, are susceptible to long-term erosion by photo-evaporation, at least for nominal photo-evaporation models. Higher mass planets further from their stars are less vulnerable to photo-evaporative stripping, as are those orbiting slower rotators with lower XUV outputs.

Any residual H/He atmosphere could significantly affect redox states and the resultant chemistry on the surfaces of these early planets, as well as the initial conditions for outgassing. Any H/He dominated super-Earth atmospheres would have mean molecular weights close to those of the primordial disk, $\mu \sim 2.2$ amu. Such a composition would lead to scale heights an order of magnitude larger than would be expected from purely secondary atmospheres, which are usually expected to be made of heavier constituents. A lower mean molecular weight would make these super-Earths more favorable for spectroscopic observations, and H-rich super-Earths should be distinguishable from those with pure secondary atmospheres by their scale heights in the near future.

Acknowledgements

We thank James Owen and Sivan Ginzburg for insightful comments which improved the manuscript. H.E.S. gratefully acknowledges support from the National Aeronautics and Space Administration under grant No. 17 NAI18_ 2 – 0029 issued through the NExSS Program. In this work we use the NUMPY (Harris et al., 2020), MATPLOTLIB (Hunter, 2007), and SCIPY (Virtanen et al., 2020) packages.

CHAPTER 3

The importance of silicate vapor in determining the structure, radii, and envelope mass fractions of sub-Neptunes

[1] Substantial silicate vapor is expected to be in chemical equilibrium at temperature conditions typical of the silicate-atmosphere interface of sub-Neptune planets, which can exceed 5000 K. Previous models of the atmospheric structure and evolution of these exoplanets, which have been used to constrain their atmospheric mass fractions, have neglected this compositional coupling. In this work, we show that silicate vapor in a hydrogen-dominated atmosphere acts as a condensable species, decreasing in abundance with altitude. The resultant mean molecular weight gradient inhibits convection at temperatures above $\sim$ 4000 K, inducing a near-surface radiative layer. This radiative layer decreases the planet's total radius compared to a planet with the same base temperature and a convective, pure H/He atmosphere. Therefore, we expect silicate vapor to have major effects on the inferred envelope mass fraction and thermal evolution of sub-Neptune planets. We demonstrate that differences in radii, and hence in inferred atmospheric masses, are largest for planets which have larger masses, equilibrium temperatures, and atmospheric mass fractions. The effects are largest for younger planets, but differences can persist on gigayear time-scales for some sub-Neptunes. For a $10M_\oplus$ planet with T_{eq} = 1000 K and an age of $\sim$ 300 Myr, an observed radius consistent with an atmospheric mass fraction of 10% when accounting for silicate vapor would be misinterpreted as indicating an atmospheric mass fraction of 2% if a H/He-only atmosphere were assumed. The presence of silicate vapor in the atmosphere is also expected to have important

---

[1] This chapter was previously published in similar form as Misener, W. and Schlichting, H. E. 2022, MNRAS 514, 6025.

implications for the accretion and loss of primordial hydrogen atmospheres.

3.1 Introduction

Exoplanet survey missions have revealed that the most common planets orbiting in less than 100 days around their host stars have radii in between those of Earth and Neptune (e.g. Fressin et al., 2013). Further refinements in these planets' properties have revealed that this population has a bimodal radius and density distribution, dividing the planets into hydrogen gas-rich sub-Neptunes and gas-poor super-Earths (Weiss & Marcy, 2014; Fulton et al., 2017).

The ubiquity of sub-Neptunes in the Galaxy has prompted numerous works investigating the physical and chemical mechanisms that determine their radii as we observe them today. A clear outcome is that the radius of a planet with a thick hydrogen envelope is not constant with age, but shrinks with time as the planet radiates energy and cools (e.g. Lopez & Fortney, 2014). Furthermore, the atmospheric mass of a planet may not be constant in time. A common hypothesis to explain the radius dichotomy is that super-Earths and sub-Neptunes began as a single population of silicate-dominated cores which accreted a few percent of their mass in nebular hydrogen and helium. Subsequent processes, such as photo-evaporation (e.g. Owen & Jackson, 2012) and core-powered mass loss (Ginzburg et al., 2016), then drove atmospheric mass loss, completely stripping the eventual super-Earths of their primordial gas. Sub-Neptunes were able to mostly resist this stripping and remain today as silicate-dominated cores overlain by a thick hydrogen atmosphere. Both photo-evaporation and core-powered mass loss can explain trends in the observed radius distribution (e.g. Owen & Wu, 2017; Gupta & Schlichting, 2019), with no clear consensus on which is the dominant mechanism (Loyd et al., 2020; Rogers et al., 2021).

However, attempts at modeling these planets' evolution reveal that the problem of inferring internal composition from the bulk densities of even the most well-characterized small planets is highly degenerate. Many sub-Neptunes can be modeled as containing solely silicates, metals, and hydrogen, but their observed properties can also accommodate significant fractions of volatiles, such as water (e.g. Rogers & Seager, 2010; Dorn et al., 2017), which have densities intermediate to hydrogen gas and silicate. Whether one expects such volatile fractions depends in part on the formation location of these planets' cores in the protoplanetary disk, which is not currently clear. One constraint on the volatile fractions comes from mass loss models, as lower density cores would more easily lose their hydrogen envelopes. Atmospheric mass loss models are most consistent with observations if cores are Earth-like in composition, with less than 20 percent of their mass in icy material (Gupta & Schlichting, 2019; Rogers & Owen, 2021). The densities of ultra-short period planets are also consistent with predominantly rocky composition (Dai et al., 2019). Nevertheless, the bulk composition of sub-Neptunes remains uncertain, as formation and interior models can also reproduce the sizes of sub-Neptune planets by modeling them as hydrogen-poor and water-rich (e.g. Zeng et al., 2019; Mousis et al., 2020).

Extensive work has been done on inferring the internal compositions of well-characterized exoplanets, that is, those with precisely measured masses and radii, such as those orbiting TRAPPIST-1 (e.g. Unterborn et al., 2018) and K2-18 (Madhusudhan et al., 2020). Such models tend to assume a layered structure for the interiors of these planets, with a pure metal core at the center, a rocky silicate mantle, a potential high-pressure ice layer, and finally a gaseous hydrogen layer (e.g. Lopez & Fortney, 2014; Dorn et al., 2017). In reality, however, these layers may not be so discrete. For example, recent *Juno* measurements have provided evidence that Jupiter's assumed high-density core may be dilute rather than segregated from its surroundings (Wahl et al., 2017). While the conditions at the center of Jupiter are in a different pressure regime than sub-Neptunes, recent work has shown that under the interior pressures typical of sub-Neptunes, water and rock may be significantly miscible (Vazan et al., 2022), calling in to question the discrete layers typically assumed.

Similarly to the deep interior, the outer hydrogen envelope is not isolated from its underlying layers either. Instead, there may be significant interaction at the surface of the silicate mantle. Experiments on hydrogen solubility in silicate melt indicate that significant hydrogen may in-gas into the mantle (Hirschmann et al., 2012). This in-gassing could have important effects on the planets' long-term evolution, potentially buffering atmospheric loss via gradual outgassing (e.g. Chachan & Stevenson, 2018) and leading to the migration of light elements to the metal core (Schlichting & Young, 2022). Similarly, the chemical coupling of the silicate mantle and atmosphere could lead to out-gassing of interior volatiles. These volatiles could have significant effects on the atmospheric structure in a number of ways. First, their absorption characteristics can affect the atmosphere's overall radiative properties, which can change how the atmosphere cools with time as well as modify the observable spectral features. Such observable features are also affected by the volatile species' large mean molecular weights compared to hydrogen, which decrease the atmosphere's scale height. Additionally, if the outgassed species can condense somewhere in the atmosphere, this could modify the atmosphere's structure due to the release of latent heat (e.g. Lichtenberg et al., 2021).

Since gas can hold more of the condensable species at higher temperature, abundant condensable species can set up a mean molecular weight gradient within the atmosphere. If the gradient becomes too steep, convection can be inhibited, failing to satisfy the Ledoux criterion (Ledoux, 1947). This can lead to development of a radiative region deep in the atmosphere. This inhibition of convection has been studied in the context of the Solar System gas and ice giants (Guillot, 1995; Leconte et al., 2017; Vazan et al., 2018; Markham & Stevenson, 2021). The typical condensables considered in these previous studies are water and methane. Such a radiative region may also be caused by entropy gradients that arise during accretion (Cumming et al., 2018).

Recent work has found that at the time of their formation, the surfaces of the silicate cores of sub-Neptunes are expected to be very hot, over 10^4 K (e.g. Ginzburg et al., 2016). At chemical equilibrium at such large temperatures, substantial silicate vapor is stable in the gas phase (Fegley & Schaefer, 2012; Visscher & Fegley, 2013; Biersteker & Schlichting, 2021; Schlichting & Young, 2022). This silicate vapor then condenses as the temperature of the atmosphere drops with increasing altitude, with condensation being mostly complete once temperatures are below 2000 K. Therefore, for young sub-Neptunes, silicate vapor acts as a condensable, with a large reservoir available at the base of the atmosphere. Biersteker & Schlichting (2021) suggested that the presence of such silicates could significantly change the overall mean molecular weight of the atmosphere, but that this effect may be counteracted if the vapor is kept concentrated near the surface. Some works, focused on accretion processes, have also considered the effect of this silicate vapor, finding that molecular weight gradients form as pebbles evaporate during infall (Brouwers & Ormel, 2020). Subsequent structural modeling concluded that convection could be inhibited by these molecular weight gradients (Ormel et al., 2021), but these works consider only the disk-phase of accretion, not the long-term effects on a planet's thermal evolution and the resulting changes in the corresponding mass-radius relation.

In this work, we model the atmospheric structure and evolution of sub-Neptune planets, accounting for the presence of silicate vapor in equilibrium with an underlying magma ocean. We demonstrate that the condensation of silicate vapor has a major effect on the overall radii of sub-Neptunes, especially at young ages. The silicate vapor is sufficiently abundant at the base of the atmosphere to form a mean molecular weight gradient, independent of the formation mechanism of the planet. Such a gradient inhibits convection and forms a radiative layer at the base of the atmosphere. The size of the radiative layer depends sensitively on the opacity, but we show that using common values for high density hydrogen leads to a very steep temperature gradient. This has the effect of significantly shrinking the envelope width compared to a fully adiabatic atmosphere with the same surface temperature. We outline our methods in Section 3.2, present our results regarding the atmospheric structure and evolution of these planets and discuss their implications for inferred atmospheric masses in Section 3.3, analyze key assumptions and the prospects for future work in Section 3.4, and summarize our conclusions in Section 3.5.

3.2 Model and Approach

In this section, we describe our model. We detail the key parameters that govern sub-Neptune atmospheres, including our model of the core, the atmosphere, and their evolution in time. Many of the basic model parameters follow those used in Misener & Schlichting (2021), with modifications to include silicate vapor and to ignore any mass-loss.

3.2.1 Interior model

Motivated by comparisons of atmospheric loss models to observed demographics (Gupta & Schlichting, 2019; Rogers & Owen, 2021) and the measured densities of ultra-short period planets (Dai et al., 2019), in this work we model sub-Neptunes as consisting of a silicate magma ocean core in contact with a hydrogen-rich atmosphere. We assume these cores to have densities consistent with the silicate-metal composition of Earth, accounting for compression. However, we note that observations do not preclude potentially large variations in bulk water content between individual planets and systems (e.g. Rogers & Seager, 2010; Dorn et al., 2017; Zeng et al., 2019; Mousis et al., 2020). We discuss the potential effects of volatile species such as water in Section 3.4.4. The core radius, R_c, is determined by the core mass, M_c, via the mass-radius relation $R_c/R_\oplus = (M_c/M_\oplus)^{1/\beta}$, where $R_\oplus$ and $M_\oplus$ are the radius and mass of Earth, respectively. A power law scaling of $\beta \simeq 4$ has been shown to be in good agreement with internal structure models of super-Earths with Earth-like compositions (e.g. Valencia et al., 2006; Seager et al., 2007). Since we focus on sub-Neptunes, which are thought to have atmospheric masses on the order of a few percent of the planets' total masses, we ignore the atmosphere's contribution to the gravity field.

We take the energy available for cooling in the silicate core as its thermal energy,

$$E_c = C_c T_c \simeq \frac{1}{\gamma_c - 1} N k_B T_c. \tag{3.1}$$

Here, C_c is the heat capacity of the core and T_c is the temperature, which we take as coupled to the temperature at the base of the atmosphere. This energy formulation assumes the silicate interior is isothermal, though incorporating the true thermal gradient within the core would not significantly change its overall heat capacity. In the second equality, we model the heat capacity in the form of an ideal gas, where k_B is the Boltzmann constant. We assume throughout this work that the effective adiabatic index of the core $\gamma_c = 4/3$, following the Dulong-Petit law. As liquid silicate can have a higher heat capacity than the solid form (e.g. Scipioni et al., 2017), this value for the adiabatic index represents an upper limit. The number of molecules in the core $N = M_c/\mu_c$, where μ_c is the mean molecular weight of the core. We assume $\mu_c = 60$ amu, similar to that of Earth.

3.2.2 Atmospheric Structure

We model the atmospheric structure as containing an outer isothermal radiative region, which transitions to a convective region at the radiative-convective boundary, $R_{\rm rcb}$ (e.g. Lee & Chiang, 2015; Ginzburg et al., 2016; Misener & Schlichting, 2021). This outer region, and therefore the radiative-convective boundary, is in thermal equilibrium with the incident stellar radiative flux and therefore has a temperature, $T_{\rm eq}$, that scales with the planet's semi-major axis, a:

$$T_{\rm eq} = \left(\frac{L_*}{16\pi\sigma a^2}\right)^{1/4} = 279\ {\rm K}\left(\frac{a}{1\ {\rm au}}\right)^{-1/2}, \tag{3.2}$$

where L_* is the luminosity of the planet's host star, σ is the Stefan-Boltzmann constant, and the right-most expression is evaluated assuming a Sun-like stellar host, using $L_* = L_\odot$. This result matches the classic Hayashi (1981) profile. The upper isothermal region has negligible mass compared to the regions below (Misener & Schlichting, 2021), and so we assume the entire mass of the atmosphere is contained inside the radiative-convective boundary.

To construct the atmospheric profile, we increase the pressure from the radiative-convective boundary in small pressure steps, ΔP. After each of these steps, we calculate the new pressure, $P_{\rm new} = P + \Delta P$, the new radius, $R_{\rm new} = R + \Delta P/(\partial P/\partial R)$, and the new temperature, $T_{\rm new} = T + \Delta P(\partial T/\partial P)$. The change in radius over the small pressure step is found assuming hydrostatic equilibrium:

$$\frac{\partial P}{\partial R} = -\frac{GM_c}{R^2}\frac{\mu P}{k_B T}, \tag{3.3}$$

where G is the gravitational constant and μ is the local mean molecular weight. The temperature gradient, as well as the radial gradient through its dependence on the mean molecular weight, both depend on the abundance of silicate vapor in the atmosphere, which we detail in the next section.

In order to fully determine an atmosphere, we must specify the planet's core mass and equilibrium temperature, the mass of the atmosphere, $M_{\rm atm}$, and the planet's total available energy for cooling, E. We then solve for the atmospheric profile, including the radiative-convective boundary radius, that satisfies these boundary conditions. The atmospheric mass is integrated from its density profile:

$$M_{\rm atm} = \int_{R_{\rm c}}^{R_{\rm rcb}} 4\pi R^2 \rho(R) dR, \tag{3.4}$$

where the density $\rho = \mu P/(k_{\rm B}T)$. Similarly, the total energy available for cooling is the sum of the available energy of the core and atmosphere: $E = E_{\rm c} + E_{\rm atm}$. Since we model the core as incompressible, we neglect its gravitational potential energy, and $E_{\rm c}$ is given by the thermal energy presented in equation (3.1). Meanwhile, the atmosphere's total energy is

$$E_{\rm atm} = \int_{M_{\rm atm}} e dm \simeq \int_{R_{\rm c}}^{R_{\rm rcb}} 4\pi R^2 e(R) \rho(R) dR, \tag{3.5}$$

where e is the atmospheric specific energy, the sum of the (negative) gravitational and (positive) thermal energy:

$$e(R) = -\frac{GM_{\rm c}}{R} + \frac{1}{\gamma - 1}\frac{k_{\rm B}T}{\mu}. \tag{3.6}$$

3.2.2.1 Effects of silicate vapor

Condensable minor species can affect atmospheric structure in two main ways. First, the release of the latent heat of condensation as the atmosphere convects changes the energy balance and therefore the profile of the atmosphere. Second, as hotter gas can hold more condensate, a mean molecular weight gradient as a function of temperature can develop. In hydrogen-dominated atmospheres, since condensates will have larger molecular weights than the hydrogen gas, this molecular gradient will increase with depth, which acts against convective instability. Leconte et al. (2017) examined the effects of the condensables water and methane on the structure of Uranus and Neptune. They found that at the typical temperatures of these planets, water could fully inhibit convection in their atmospheres, forming a radiative region with a steep temperature gradient.

The conditions in young, close-in sub-Neptunes typical of the known exoplanet population are different than the Solar System ice giants. Their equilibrium temperatures are usually hotter than the boiling temperature of water; in fact, they can approach ~ 2000 K, a typical sublimation temperature for rock, and their interiors can easily exceed this, especially when young. Here we apply the equations derived in Leconte et al. (2017), using silicates as the condensate rather than a more volatile species.

We assume that the atmosphere is in thermal and chemical equilibrium with the underlying silicate interior. Thermal equilibrium implies that the temperature at the base of the atmosphere is the same as that of the silicate core, $T_\mathrm{c} = T(R_\mathrm{c})$, and that for the atmosphere to cool, the core must also cool. This coupling is the basis of core-powered mass-loss (e.g. Ginzburg et al., 2016; Misener & Schlichting, 2021), though we do not consider mass-loss in this work. Meanwhile, chemical equilibrium implies that the atmosphere is saturated in silicate vapor. For simplicity, we assume all silicate vapor is in the form of SiO. More detailed chemical equilibrium calculations, such as those using the MAGMA code (Fegley & Cameron, 1987; Schaefer & Fegley, 2004), find that SiO predominates at equilibrium over much of the temperature range we consider here. However, in equilibrium with pure silicate, there can also be substantial amounts of O_2, O, and SiO_2. In addition, we do not consider any other elements besides silicon and oxygen. At temperatures below 2500 K, gas in equilibrium with bulk silicate Earth composition includes Na and Zn gas in addition to silicate vapor (e.g. Visscher & Fegley, 2013). However, full chemical equilibrium calculations are beyond the scope of this study, so we do not include the effects of the less refractory species.

For the vapor pressure of silicate gas, P_svp, we take the expression of Fegley & Schaefer (2012) and Visscher & Fegley (2013), based on the MAGMA code:

$$\log_{10}\left(\frac{P_\mathrm{svp}}{\mathrm{bar}}\right) = 8.203 - \frac{25898.9}{T/\mathrm{K}}. \tag{3.7}$$

Due to our neglect of less refractory species, this approximation underestimates the true vapor pressure of bulk silicate Earth species at temperatures below 2500 K, with errors becoming more substantial at lower temperatures. However, since the overall vapor pressure is low at low temperatures, this approximation does not have a substantial effect on our overall findings. This method also overestimates the true bulk silicate Earth vapor pressure by a factor of a few at temperatures above 2500 K (Visscher & Fegley, 2013). No matter the exact approximation, the key feature of the vapor pressure equation is that it is a strongly increasing function of temperature.

In the convective region, silicate vapor modifies the profile due to the release of latent heat. Its condensation causes the overall atmospheric profile to follow the so-called wet adiabat, well-studied in the context of Earth's atmosphere. The general temperature gradient can be expressed as:

$$\frac{\partial \ln T}{\partial \ln P} = \frac{k_\mathrm{B}}{\mu} \frac{1 + \dfrac{P_\mathrm{svp}}{P_\mathrm{H}} \dfrac{\partial \ln P_\mathrm{svp}}{\partial T}}{c_\mathrm{p} + \dfrac{P_\mathrm{svp}}{P_\mathrm{H}} \dfrac{k_\mathrm{B}}{\mu} T^2 \left(\dfrac{\partial \ln P_\mathrm{svp}}{\partial T} \right)^2}, \tag{3.8}$$

where $P_\mathrm{H} = P - P_\mathrm{svp}$ is the partial pressure of hydrogen/helium (e.g. Leconte et al., 2017). Following from this definition, the local mean molecular weight, μ, is:

$$\mu = \frac{\mu_\mathrm{H} P_\mathrm{H} + \mu_\mathrm{sv} P_\mathrm{svp}}{P}, \tag{3.9}$$

where we take $\mu_\mathrm{H} = 2.4$ amu, typical for a nebular hydrogen/helium mixture. The mean molecular weight of pure SiO vapor is 44 amu. However, detailed chemical equilibrium simulations, e.g., those performed by the MAGMA code, find that the mean molecular weight of vapor at equilibrium with a $\sim$ 6000 K magma ocean is slightly lower, $\mu_\mathrm{sv} \sim 36$ amu, due to the presence of atomic Si and O. In order to capture the effects of these lower weight components, we use this latter value as the condensable mean molecular weight (e.g. Biersteker & Schlichting, 2021). However, since SiO still dominates the composition, throughout this work we use its thermodynamic properties for all other calculations. We find the heat capacity of the mixture, c_p, to be

$$c_\mathrm{p} = \frac{k_\mathrm{B}}{\mu} \frac{\gamma}{\gamma - 1}, \tag{3.10}$$

where γ is the adiabatic index. We assume ideal gas behavior, which for the diatomic molecules SiO and H_2 yields $\gamma = 7/5$. It is easy to see that equation (3.8) reduces to the dry adiabatic case, $\partial \ln T / \partial \ln P \simeq (\gamma - 1)/\gamma$, when $P_\mathrm{svp} \ll P_\mathrm{H}$.

If the condensable vapor pressure increases enough, it will begin to have an effect on the overall mean molecular weight of the atmosphere. In an atmosphere primarily composed of a light species, such as hydrogen, this acts to increase the mean molecular weight as the temperature increases. This increases the stability of the gas against convection, as a lifted gas parcel will have a larger mean molecular weight than its surroundings. The balance between the temperature gradient and the molecular weight gradient depends on the mass mixing ratio, $q = \mu_{\mathrm{sv}} P_{\mathrm{svp}}/(\mu_{\mathrm{H}} P_{\mathrm{H}})$. Once the temperature increases such that the gas reaches a critical mass mixing ratio, $q \geq q_{\mathrm{crit}}$, convection is no longer possible. Convection is inhibited no matter how super-adiabatic the temperature gradient becomes: an increase in the temperature gradient merely increases the molecular weight gradient. Therefore, an inner radiative region forms (Guillot, 1995). Such a region is also stable to double-diffusive convection (Leconte et al., 2017).

This critical mixing ratio, q_{crit}, depends on the weights of the constituent species and on the vapor pressure gradient (Guillot, 1995; Leconte et al., 2017)

$$q_{\mathrm{crit}} = \frac{1}{\left(1 - \frac{\mu_{\mathrm{H}}}{\mu_{\mathrm{sv}}}\right) \frac{\partial \ln P_{\mathrm{svp}}}{\partial \ln T}}. \tag{3.11}$$

The critical mixing ratio increases slowly with temperature, and is typically on the order of 10 weight percent in sub-Neptune atmospheres. This value is of the same order of magnitude as the value for other volatiles in Solar System gas giants (Leconte et al., 2017).

Below the location at which this mixing ratio is achieved, the atmosphere cannot convect, and therefore must transfer energy via radiation. The energy flux that must be transported across this radiative region must in steady state be equal to the radiative flux into space. This luminosity is determined by the outer boundary conditions of the atmosphere

$$L = \frac{\gamma - 1}{\gamma} \frac{64 \pi G M_{\mathrm{c}} \sigma T_{\mathrm{eq}}^4}{3 \kappa_{\mathrm{rcb}} P_{\mathrm{rcb}}}, \tag{3.12}$$

where κ_{rcb} is the atmospheric Rosseland mean opacity at the radiative-convective boundary, and similarly $P_{\mathrm{rcb}} = P(R_{\mathrm{rcb}})$ (Ginzburg et al., 2016). The opacity is a function of temperature, pressure, and the atmospheric composition. At the outer boundary, typically we find $P_{\mathrm{svp}} \ll P$, so opacities for pure hydrogen/helium are appropriate. We use the analytic opacity approximation presented in Freedman et al. (2014), which is based on more detailed line opacity data.

The temperature gradient necessary to transport a given energy flux, L, in the radiative region is:

$$\frac{\partial \ln T}{\partial \ln P} = \frac{3\kappa P L}{64\pi G M_{\mathrm{c}} \sigma T^4}. \tag{3.13}$$

In the interior, the opacity may be quite different than at the outer radiative-convective boundary, due not only to the typically large temperatures and pressures but also due to the highly enhanced silicate content compared to solar. Hydrogen opacity is typically taken to increase linearly with metal content, as the presence of metals enhances the production of H^-, the primary opacity source at high temperatures (e.g. Lee et al., 2014). However, this trend was not extrapolated to the high metal contents we encounter here. Therefore, the magnitude of the impact of this silicate content on the overall opacity is difficult to determine without a detailed radiative model, which is beyond the scope of this work. For simplicity, we use the same Freedman et al. (2014) relation as at the radiative-convective boundary, but acknowledge that these values are very uncertain. We discuss the effects of different opacity scalings in Sec. 3.4.1.

We summarize the general planet structure we find in Fig. 3.1. Radiative layers are shown in red, while the convective layer is blue. The outer radiative layer is isothermal at T_{eq}. It transitions at the radiative-convective boundary radius R_{rcb} to a convective region. Within the convective region, the temperature gradient follows the wet adiabat, given by Equation (3.8). The mass mixing ratio q increases with depth through the convective region. If q exceeds q_{crit}, then convection is inhibited below this radius. In this case, the atmosphere transitions to a radiative layer until it reaches the surface of the silicate core, shown in grey, at $R = R_{\mathrm{c}}$. Within this radiative layer, the temperature gradient follows Equation (3.13).

Fig. 3.1 is not to scale, and the relative sizes of the regions depends on the assumed planet conditions. Typically, we find the energy flux and opacity to be sufficiently high that the radiative gradient is very steep: temperature increases quickly in the radiative region with pressure and radius. This steep gradient is similar to the findings of Leconte et al. (2017). However, the inner boundary

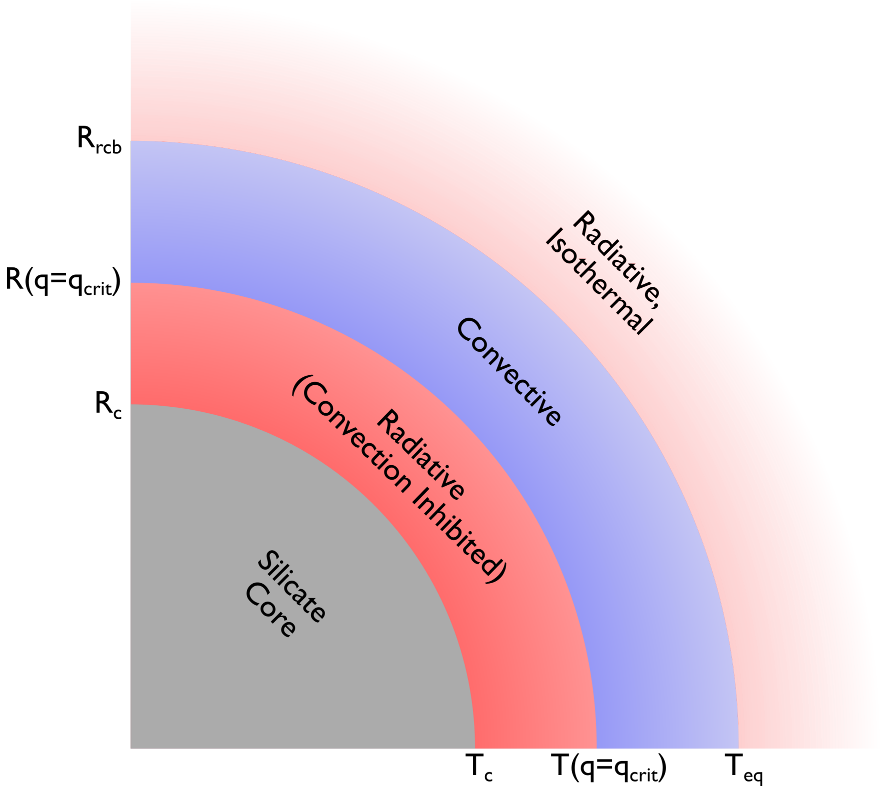

Figure 3.1: Illustration of the general structure of hot sub-Neptune planets. Key radii are shown on the y-axis, while key temperatures are on the x-axis. The silicate core (grey) is overlain by a hydrogen-dominated atmosphere, which is divided into radiative (red) and convective (blue) regions. An outer radiative region, isothermal at $T_{\rm eq}$, transitions to a convective region at the radiative-convective boundary radius, $R_{\rm rcb}$. If q exceeds $q_{\rm crit}$ while $R > R_{\rm c}$, then convection becomes inhibited. A radiative region thus forms, extending to the base of the atmosphere.

condition in the ice giants considered there is when the mixing ratio of the condensable reaches a prescribed inner value. In contrast, in sub-Neptune case we consider, the inner boundary condition is instead the surface of the silicate magma ocean, at $R = R_\mathrm{c}$, which is in our approximation entirely silicate. For some planets, this can be reached in the radiative region. However, for planets with the lowest core and atmospheric masses and highest core temperatures we consider, the hydrogen pressure in the inner regions may not be as high as the silicate vapor pressure as indicated by equation (3.7). In this case, we assume the atmosphere becomes composed of entirely silicate vapor, with no hydrogen gas. Such a layer is fully dry convective.

3.2.3 Evolution

We define our initial atmospheric state by its base temperature, T_c. This value, along with the planet's core mass, equilibrium temperature, and atmospheric mass, is sufficient to define an atmospheric profile and a luminosity. A convenient method of quantifying the atmospheric evolution is through the planet's cooling timescale, t_cool. The cooling timescale is the characteristic evolution timescale of the available energy for cooling at the current planetary luminosity, $t_\mathrm{cool} = E/L$.

To evolve these planets in time, we subtract the energy lost by the system by radiative luminosity over one timestep, Δt, defined as one-hundredth of the cooling timescale: $E_\mathrm{new} = E - L\Delta t$. We then calculate a new profile that has the new available energy, and proceed as such.

3.3 Results

In this section we describe our main results. We begin with a general picture of the atmospheric structure we derive. We then explore the implications for the radial evolution of sub-Neptune planets. We present how our results vary as a function of planet parameters such as planet mass, atmospheric mass, equilibrium temperature, and age.

3.3.1 Atmospheric structure

In Fig. 3.2, we show the structure we find for a planet with a hydrogen-rich atmosphere in equilibrium with the silicate magma ocean below it, such that silicate vapor extends into the atmosphere at the saturation pressure. The magma ocean-atmosphere interface is at 5500 K, and the outer temperature is 1000 K. Coloured lines indicate the radial profiles we calculate for this silicate-containing atmosphere, in (a) pressure P, (b) mass mixing ratio of silicate vapor q_{s}, (c) temperature T, (d) lapse rate $\mathrm{d}\log T/\mathrm{d}\log P$, (e) mean molecular weight μ, and (f) density ρ. For comparison, the profiles of an atmosphere composed of H/He with the same mass and planet characteristics but without any silicate vapor are shown as black lines. Solid lines show regions where the atmosphere is convective, while dotted lines show radiative regions. In panel (a), the dashed line shows the partial pressure of silicate vapor, while in (b) the dashed line represents the critical mixing ratio, q_{crit}, as defined in equation (3.11), and in (e) the dashed line is the mean molecular weight of the whole atmosphere, $\bar{\mu}$.

Near the outer radiative-convective boundary (shown by the large dot), the silicate content of the atmosphere is negligible ($q_{\mathrm{s}} < 10^{-10}$). Therefore, the atmospheric profile is very similar to the convective profile of a pure H/He atmosphere. Some deviation in the lapse rate (panel (d)) occurs with increasing depth due to the latent heat released from condensing silicate vapor (see equation (3.8)). However, this deviation is on the order of a ~ 10 percent change in lapse rate, so this moist adiabatic profile remains similar to the dry case.

A more substantial change occurs when the mixing ratio reaches the critical mixing ratio, $q_{\mathrm{s}} = q_{\mathrm{crit}}$ (panel (b)). At silicate vapor mixing ratios larger than this, convection is inhibited, and the atmosphere becomes radiative. The temperature structure of the inner radiative region is qualitatively different than that of the convective region, but depends sensitively on the opacity in the radiative region, as shown by equation (3.13). In Fig. 3.2, we use a constant opacity, $\kappa = 0.1\ \mathrm{cm^2 g^{-1}}$, and the radiative lapse rate is lower than that of the convective region (panel (d)).

As the temperature increases inward, more and more silicate vapor is stable at equilibrium

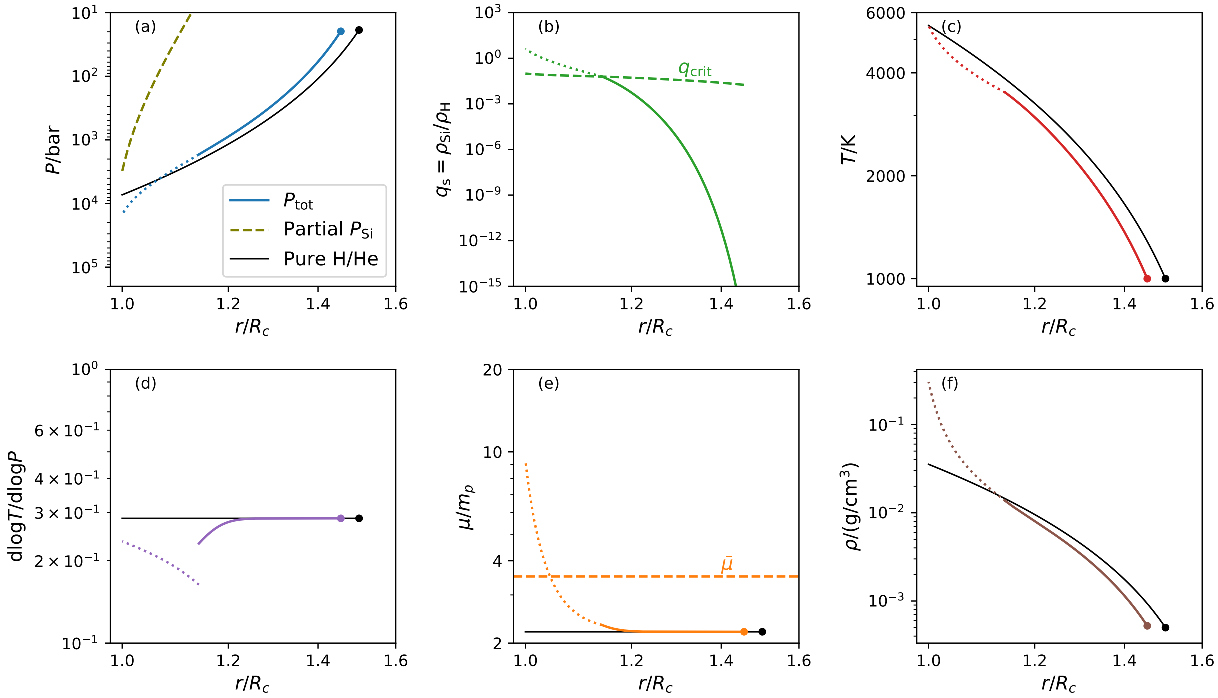

Figure 3.2: Atmospheric structure of a planet with a hydrogen/helium atmosphere in thermal and chemical equilibrium with a silicate core of temperature 5500 K. Coloured lines show the variation with radius r, of (a) total and silicate partial pressure (dashed), $P_{\rm tot}$ and $P_{\rm Si}$ respectively, (b) mass mixing ratio of silicate vapor $q_{\rm s}$, with the critical mixing ratio $q_{\rm crit}$ shown as a dashed line, (c) temperature T, (d) lapse rate $\mathrm{d}\log T/\mathrm{d}\log P$, (e) mean molecular weight μ, with the entire atmosphere's mean molecular weight shown as a dashed line, and (f) density ρ. The profiles of a pure hydrogen/helium atmosphere of the same base temperature, mass, and outer temperature are shown as black lines for comparison. The outer, convective atmosphere (solid lines) has similar characteristics to the pure hydrogen case, until the critical mixing ratio is reached. Then the atmosphere becomes radiative (dotted lines), changing the temperature profile and ultimately the planet's observable radius ($R_{\rm rcb}$, shown by the large dot) to $1.46R_{\rm c}$, compared to $R_{\rm rcb} = 1.50R_{\rm c}$ in the pure H/He case. In the case shown here, we assume the opacity is constant in the radiative region, $\kappa = 0.1$ cm^{2}g^{-1}.

according to equation (3.7), resulting in consequent increases in the silicate partial pressure (panel (a)), the mass mixing ratio (panel (b)), and the mean molecular weight (panel (e)). These increases with depth steepen the radial pressure gradient, which scales with mean molecular weight (equation (3.3)). In this case, the steeper radial pressure gradient more than offsets the lower pressure lapse rate, and the overall radial temperature gradient in the radiative region is slightly steeper than in the fully convective case (panel (c)). Therefore, the combination of these temperature and pressure structure effects works to slightly contract the overall radius of the planet compared to a pure H/He case, from about 1.50 to 1.46 core radii. While the atmosphere's mean molecular weight is increased by the silicate vapor to 3.5 amu, the mean molecular weight at the top of the atmosphere remains consistent with pure H/He: none of the silicate vapor appears to be able to reach heights observable via transmission spectroscopy.

As mentioned, while the inhibition of convection is a robust finding, the structure of the radiative region can vary greatly depending on the scaling assumed for the Rosseland mean opacity in the region. In Fig. 3.3, we use the opacity scaling presented for pure H/He in Freedman et al. (2014) rather than a constant value. This opacity tends to be much higher than the $0.1\ \mathrm{cm^2 g^{-1}}$ value assumed in Fig. 3.2 for the high temperature, high pressure conditions at the base of the atmosphere. Since $\partial \ln T / \partial \ln P \propto \kappa$ in the radiative region (equation (3.13)), the radiative gradient becomes very steep, with $\mathrm{d}T/\mathrm{d}P$ more than 100 times larger than that of the moist adiabat (panel (d)). Additionally, the radial pressure gradient increases by a factor of a few due to the increasing mean molecular weight (panel (e)). The combination of these effects, though in this case dominated by the lapse rate effect, leads to a steep radial temperature profile, and the radiative region thus forms nearly a step in temperature at the base of the atmosphere (panel (c)). This narrow radiative region significantly decreases the radius of a planet with the same mass and base temperature: its atmosphere extends essentially the same amount as a fully convective atmosphere with a base temperature equal to the temperature at which the atmosphere transitions from convective to radiative. This acts to decrease the observable radius from the pure H/He atmosphere value of 1.50 core radii to 1.28 core radii, nearly a factor of two in atmospheric width. While the opacity of a gas containing significant

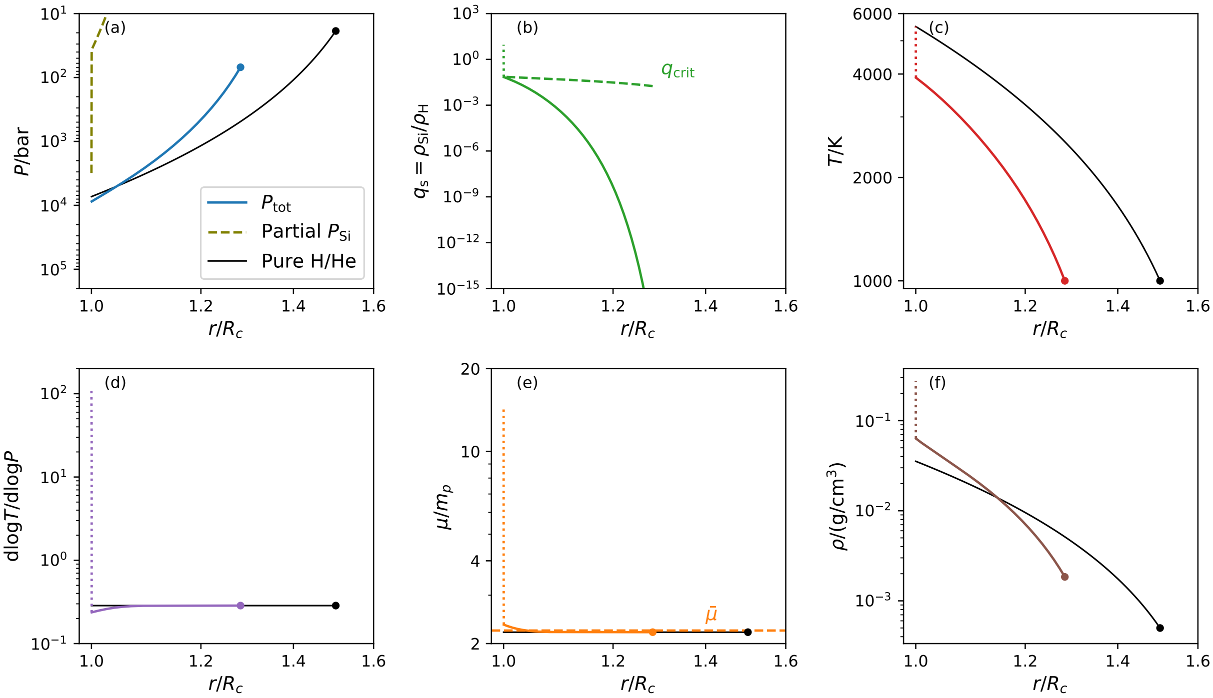

Figure 3.3: Same as Fig. 3.2, but for a radiative region with an opacity that scales with pressure and temperature following the hydrogen opacities of Freedman et al. (2014), who predict much higher opacities than the constant value of 0.1 $\mathrm{cm^2 g^{-1}}$ used in Fig. 3.2. Due to this high opacity, the lapse rate becomes very steep in the radiative region, following equation (3.13), and the region becomes very narrow in width. This significantly decreases the planet's total radius, to $R_{\rm rcb} = 1.28 R_{\rm c}$, compared to the pure H/He case, which remains at $1.50 R_{\rm c}$ as in Fig. 3.2.

silicate vapor may deviate from that of a pure H/He composition, the exact effects are uncertain, so we use the pure H/He scaling from Freedman et al. (2014) in the remainder of the work. We discuss the effects of different opacity scalings in Section 3.4.1.

To provide further intuitive understanding of the radii we expect for these contracted planets, we analytically approximate the size of an planet with a silicate-induced radiative region in the limit that the radiative region is thin. We can use the fact that at the base of the convective region, $q = q_{\rm crit}$. Inserting the definitions of q and $q_{\rm crit}$ from section 3.2.2.1, we obtain

$$\frac{\mu_{\rm v} P_{\rm v}}{\mu_{\rm H} P_{\rm H}} = \frac{1}{\left(1 - \frac{\mu_{\rm H}}{\mu_{\rm sv}}\right) \frac{\partial \ln P_{\rm svp}}{\partial \ln T}}. \tag{3.14}$$

We convert equation (3.7) to an exponential functional form of the saturation vapor pressure: $P_{\rm v} \equiv \exp\{[A - B/T]\}$, from which it follows that $\partial \ln P_{\rm svp}/\partial \ln T = B/T$. For convenience, we define $\beta \equiv (1 - \mu_{\rm H}/\mu_{\rm sv})B$. The hydrogen pressure, $P_{\rm H}$, depends on the weight of overlying atmosphere. Assuming mass is concentrated in the interior of the atmosphere (valid for our choice of γ), the hydrogen pressure at the base of the atmosphere can be approximated as $P_{\rm H} \approx GM_{\rm c}M_{\rm atm}/(4\pi R_{\rm c}^4)$ (e.g. Misener & Schlichting, 2021). Substituting the temperature dependencies into equation (3.14) yields

$$\frac{\mu_{\rm sv}}{\mu_{\rm H} P_{\rm H}} \exp\left\{\left[A - \frac{B}{T}\right]\right\} = \frac{T}{\beta}. \tag{3.15}$$

This equation has no solution for T in terms of elementary functions. However, at the conditions relevant to the sub-Neptunes we study here, the exponential term changes much faster than the linear term. This allows us to approximate the right-hand side as a constant, given some estimate of the temperature we expect. We use an estimate of $T_{\rm est} \sim 4500$ K, though the result does not depend strongly on the exact value chosen. Now, we can solve equation (3.15) for the temperature at which $q = q_{\rm crit}$:

$$T_{\rm q} = \frac{B}{A - \ln\left[\frac{\mu_{\rm H} P_{\rm H} T_{\rm est}}{\mu_{\rm sv}\beta}\right]}. \tag{3.16}$$

We can convert this temperature to a radius using the fact that if the radiative region is concentrated near the surface, the planet is equivalent in size to a fully convective planet with a base temperature given by equation (3.16). To do so, we assume the convective region is dry adiabatic, such that

$$R_{\rm rcb} = \frac{R'_{\rm B}}{1 + R'_{\rm B}/R_{\rm c} - T_{\rm q}/T_{\rm eq}}, \tag{3.17}$$

where $R'_{\rm B} \equiv (\gamma - 1)/\gamma \times GM_{\rm c}\mu_{\rm H}/(k_{\rm B}T_{\rm eq})$, following Misener & Schlichting (2021). This approximation neglects the effects of moist convection on the atmospheric structure. However, since the high temperature portion of the atmosphere is very close to the surface, little silicate vapor extends far from the surface. The mean molecular weight of the entire atmosphere is accordingly nearly the same as for pure H/He (Fig. 3.3, panel (e)). Equation (3.16) yields a temperature at the base of the convective region $T_{\rm q} = 4013$ K for the parameters of Fig. 3.3. Via Equation (3.17), this temperature corresponds to a planet radius of $R_{\rm rcb} = 1.29 R_{\rm c}$. Both of these values are in good agreement with the numerical results. This analytic approximation illustrates that the size of these planets is equivalent to that of a planet with a fully convective atmosphere and a base temperature determined by $T_{\rm q}$, the temperature at which $q = q_{\rm crit}$. This radius can be approximated as solely a function of $M_{\rm c}$, $M_{\rm atm}$, and $T_{\rm eq}$, which may be useful for comparing these findings to observations.

3.3.2 Radial evolution

The presence of a radiative region when the planet is hot leads to differences in the evolution of radius and temperature compared to a fully convective atmosphere. We depict these differences in Fig. 3.4, showing the evolution in core temperature and radiative-convective boundary of two planets. The dotted line represents the evolution of a pure H/He atmosphere with an initial base temperature of 6500 K, while the solid line shows an atmosphere with the same mass and initial conditions containing silicate vapor, with an opacity following Freedman et al. (2014). As described above, when base temperatures are high, the silicate/hydrogen atmosphere is contracted relative to the pure H/He case, with a much lower radiative-convective boundary at the same temperature. This contracted state increases the pressure and density at the radiative-convective boundary, which

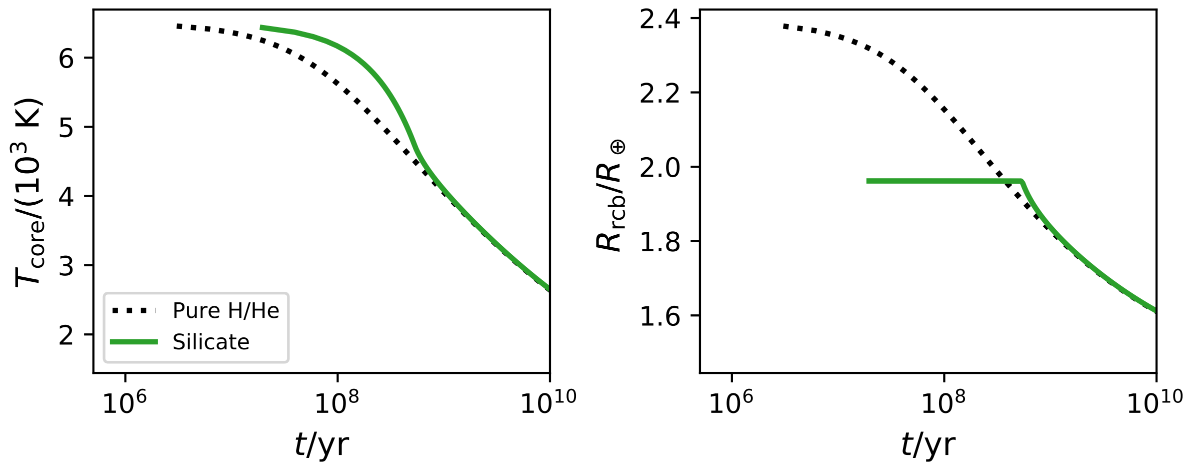

Figure 3.4: Evolution in temperature at the silicate core-atmosphere interface T_c (left) and outer radiative-convective boundary $R_{\rm rcb}$ (right) of a $4M_\oplus$ planet with equilibrium temperature $T_{\rm eq}$ = 1000 K. The black dotted line is the time evolution of a pure H/He atmosphere. The green solid line depicts the evolution of an atmosphere containing silicate vapor. For both planets, $t = 0$ when the core temperature T_c = 6500 K. The silicate vapor atmosphere begins at a much lower radius when the core is hot and a significant radiative layer exists, and its evolution differs on a gigayear timescale.

inhibits cooling, as $L \propto 1/P_{\rm rcb}$ by equation (3.12). Therefore, the silicate-containing atmosphere has a lower initial luminosity than the pure H/He case. Its core temperature consequently goes down more slowly in the early stages of evolution, keeping the atmospheric radius relatively constant as the pure H/He case rapidly contracts.

This slow cooling persists for $\gtrsim 10^8$ years, by which point the radiative-convective boundary of the pure H/He case has decreased to and below that of the silicate/hydrogen case. Now the silicate/hydrogen atmosphere is relatively inflated, with a correspondingly higher luminosity. Therefore, the silicate/hydrogen atmosphere cools relatively rapidly.

A shift in behavior occurs once $T_c \lesssim 4000$ K. At this point, the mixing ratio at the base of the atmosphere decreases below $q_{\rm crit}$. Therefore, the radiative region disappears and the atmosphere becomes fully convective. At this point, the silicate/hydrogen atmosphere can contract as it cools, and rapid contraction decreases its radius until it is of similar size to the pure H/He case. From this point on, the radial and thermal evolution of the two atmospheres are very similar.

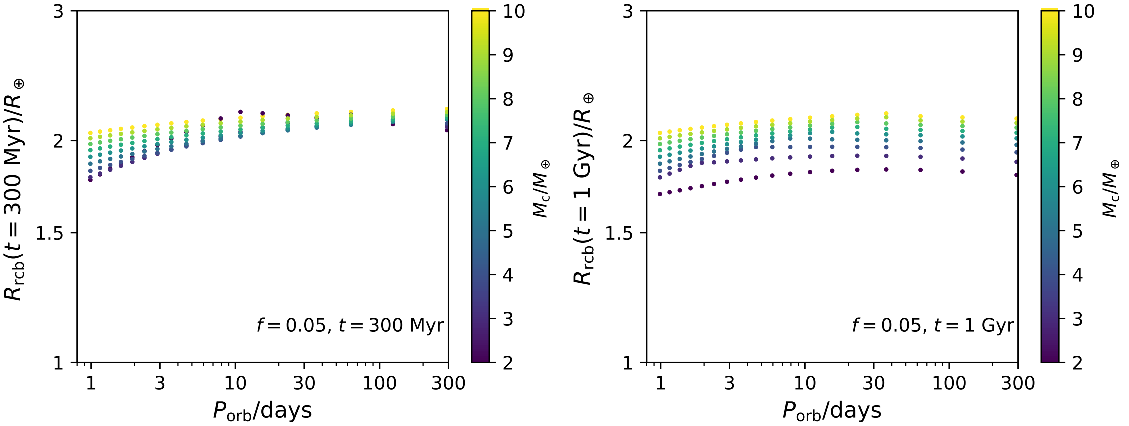

Figure 3.5: Planet radius evolution when silicate vapor is included in the atmosphere. Plotted are the outer radiative-convective boundary radius as a function of orbital period around a Sun-like star, for different planet masses denoted by colors. The left panel shows the radii at 300 Myr after the planets had base temperatures of 6500 K, while the right panel shows the radii after 1 Gyr. Cooler planets at longer orbital periods have larger radii for the same initial base temperature but cool more quickly, making intermediate temperature planets the largest for a given mass.

3.3.3 Population statistics

These differences in atmospheric structure and evolution between planets with pure H/He and silicate/hydrogen atmospheres manifest on a population level, affecting the radii planets have and how they depend on attributes like core mass, atmospheric mass, and equilibrium temperature. In Fig. 3.5, we show the radii of a suite of planets with varying orbital periods. The color gradient of the dots represents different core masses. On the left panel, we show the radii at $t = 300$ Myr since the planets had core temperatures of 6500 K, whereas on the right panel we show the same planets after 1 Gyr of thermal evolution. All these planets have the same atmospheric mass fraction, $f = 0.05$.

The presence of a silicate/hydrogen atmosphere does not affect these planets equally. Fig. 3.5 demonstrates that while more massive planets still tend to have larger radii than less massive planets, the difference is less, and in some cases the less massive planets have larger radii than those more massive. This is due to their weaker gravity leading to more inflated atmospheres for planets with the same base temperature and atmospheric mass fraction. However, these more extensive

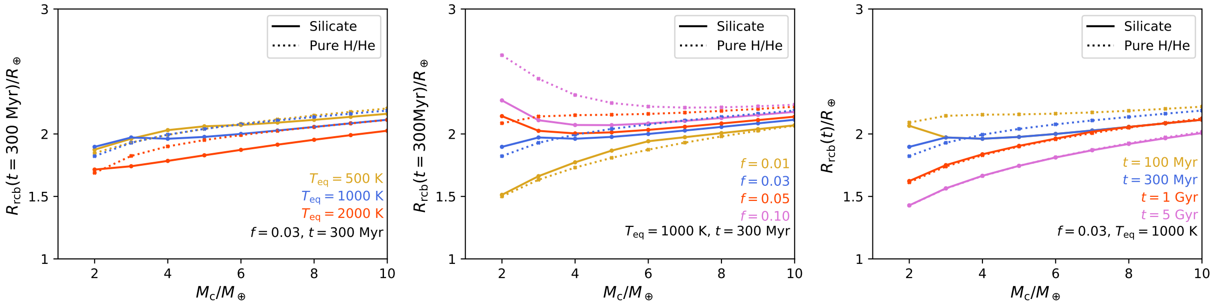

Figure 3.6: Comparison of the evolution of planet radius if silicate vapor condensation in the atmosphere is considered (solid lines) to a model with a convecting pure H/He atmosphere (dotted lines) as a function of planet mass. Colors represent (left) different equilibrium temperatures, (center) different atmospheric mass fractions, and (right) different times since the initial base temperature.

envelopes lead to larger luminosities and more rapid cooling. Therefore, planets at longer orbital periods become fully convective and contract more rapidly than shorter-period planets. This leads to a non-monotonic scaling of radiative-convective boundary at a given time with orbital period: intermediate period planets have larger radii than those with shorter or longer periods. The planet with the largest radius is the coolest planet that has not yet begun to contract. At 300 Myr, this occurs at periods of about 10 days for $M_{\rm c} = 2M_\oplus$, whereas the more massive planets all remain in the radiative region for $P > 300$ days. At 1 Gyr, the $2M_\oplus$ planets have all contracted, while the peak radius is at hotter temperatures for less massive planets.

3.3.3.1 Comparison with H/He only models

One major implication of these results is that the radial evolution of sub-Neptune planets may be substantially different if the silicate-induced radiative layer is accounted for than in a model assuming a pure H/He atmosphere, which is fully convective between $R_{\rm c}$ and $R_{\rm rcb}$. In Fig. 3.6 we plot the radiative-convective boundary radius for a pure H/He model, shown by dotted lines, and our hydrogen/silicate model, shown by solid lines, as a function of core mass. In all cases, evolution begins, i.e. $t = 0$, when the temperature at the base is 6500 K, and the times provided are times since this the planet had this initial base temperature. The colors represent different equilibrium temperatures (left), atmospheric mass fractions (center), and times since $T_c = 6500$ K.

In the left panel, we compare the radii of three sets of planets at a constant time, $t = 300$ Myr, and atmospheric mass fraction, $f = 0.03$. The different colors denote equilibrium temperatures of 500, 1000, and 2000 K. Hotter, more massive planets in models which include silicate vapor tend to have smaller radiative-convective boundaries relative to the pure H/He case, as these atmospheres are still hot enough at their bases to maintain a radiative region. Lower mass and cooler planets with hydrogen/silicate atmospheres, on the other hand, can be comparable in size or even inflated relative to the pure H/He case, as their atmospheres have cooled sufficiently such that the radiative region is no longer present. Therefore, these planets have begun to contract.

In the center panel, we similarly compare four sets of planets, this time varying the atmospheric mass fraction between 1 and 10 percent of a planet's mass. The silicate/hydrogen case is the most contracted relative to the H/He case when the atmospheric mass fraction is highest, since more massive atmospheres cool more slowly. Meanwhile, rapid evolution leads to less massive Si/H atmospheres being comparable in size to H atmospheres, or even slightly inflated.

Finally, on the right panel we compare planets in time. For $f = 0.03$ and $T_{\rm eq} = 1000$ K, the more massive planets maintain silicate-induced radiative layers, preventing significant radius change, for > 1 Gyr. However, the corresponding H/He-only atmosphere cools and contracts in this time, approaching the silicate/hydrogen atmosphere's radius. Therefore, the silicate/hydrogen atmosphere evolves from relatively contracted at early times to similar in extent to the hydrogen-only case at 1 Gyr. Less massive planets evolve on shorter timescales: the $4M_\oplus$ planet with a Si/H atmosphere is only relatively contracted for < 300 Myr, while a $2M_\oplus$ planet with a Si/H atmosphere is already contracting at 100 Myr.

Evolution models conceptually similar to those presented above are typically used to infer the atmospheric mass for exoplanets with constrained planet radii, masses, ages, and equilibrium temperatures. However, such models typically assume a fully convective hydrogen/helium atmosphere, neglecting the silicate vapor we have demonstrated to be important to the structure and evolution of these planets (e.g. Lopez & Fortney, 2014). In Fig. 3.7, we compare the atmospheric mass inferred

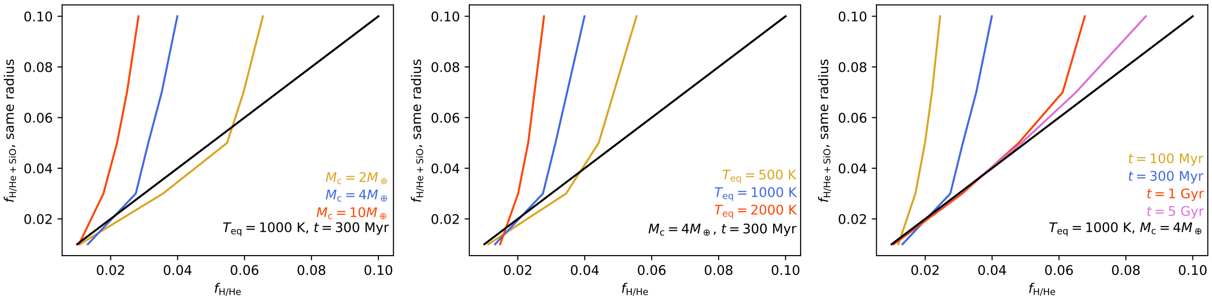

Figure 3.7: Comparison of atmospheric mass fraction inferred assuming the atmosphere is composed of pure H/He which is fully convecting to a model which includes a silicate-induced radiative layer with the same outer radiative-convective boundary radius. On the left is the trend in inferred mass fraction for three different planet masses at the same time and equilibrium temperature. The center panel compares planets of fixed mass at three equilibrium temperatures at a given time. The right-most panel shows the same planet mass and equilibrium temperature at four different times. Young planets close to their stars with large core and atmospheric masses tend to cool relatively slowly and thus retain a radiative layer at the base of the atmosphere for longer. This radiative layer decreases their radius compared to the pure H/He case, meaning the same radius corresponds to a larger atmospheric mass. Conversely, low mass, low f, and older planets with low equilibrium temperatures cool quickly and lose their inner radiative layers. These planets therefore have similar radii in both models, and so come close to lying along the one-to-one line in black. Atmospheric models which do not include silicate condensation could underestimate the masses of sub-Neptune planets by a factor of 5 for the most extreme cases shown here.

using a purely convective structure to that which we obtain from our models which include SiO in the atmosphere for the same planet radius.

On the left we show a comparison for three different planet masses with fixed t and T_{eq}. Generally, most planets for which silicate vapor is included have higher inferred atmospheric masses than those inferred for the same radii assuming a pure H/He, convective structure. The black line shows a one-to-one relationship for reference. This is most apparent at high atmospheric masses and high planet masses: a $2M_\oplus$ planet with $f = 0.10$ modeled to include silicate vapor has a radius equivalent to that of a pure H/He planet with $f \approx 0.06$, and a $10M_\oplus$ planet with $f = 0.10$ has a radius for which one would infer $f \approx 0.02$ if a pure H/He composition was assumed. For lower atmospheric mass fractions, the inferred atmospheric masses are comparable between the two models. This is because lower mass atmospheres have lower densities, and therefore cool more quickly per equation (3.12). This relatively fast cooling leads to the silicate/hydrogen atmospheres becoming fully convective sooner, and their radii therefore approach the radii of planets with equal mass pure H/He atmospheres. Some silicate-containing atmospheres, such as the $2M_\oplus$ planets with intermediate atmospheric masses, $f = 0.03$ or 0.05, are actually slightly larger than pure hydrogen atmospheres at the same time since $T_{\mathrm{c}} = 6500$ K and therefore have lower inferred atmospheric masses. At this time, the planets with silicate-induced radiative regions remain at their initial fixed radius, but the hydrogen-only atmospheres have contracted to radii smaller than this. Such an effect is visible in Fig. 3.4 at a few hundred Myr. This relatively inflated state does not last long, as these planets now cool quickly relative to the more contracted pure H/He atmospheres. This cooling allows the formerly-inflated planets to become fully convective and shrink, catching up to their H/He-only counterparts. The overall effect of this inflated state is minor compared to the difference in radii at earlier times.

Similarly to the left panel, the center panel compares three equilibrium temperatures at fixed t and M_{c}, while on the right we show planets with the same core mass and equilibrium temperature at four different ages. Increasing equilibrium temperature inhibits cooling. Hence, a hotter planet will exhibit a larger discrepancy in inferred envelope mass between the silicate/hydrogen and pure H/He models than a cooler planet. This is illustrated in Fig. 3.7: for fixed core mass, $M_c = 4M_\oplus$, and time, $t = 300$ Myr, a close-in planet with $T_{eq} = 2000$ K and a silicate/hydrogen atmosphere of mass $f = 0.10$ is the same size as a planet with a H/He-only atmosphere with one fifth the atmospheric mass ($f \approx 0.02$). But an equal-mass atmosphere around a planet with $T_{eq} = 500$ K matches the size of a pure-H/He atmosphere only a factor of 2 smaller in mass ($f \approx 0.05$). Meanwhile, as planets age, they cool sufficiently such that the atmosphere becomes fully convective. This allows the silicate/hydrogen atmospheres to contract as they cool, narrowing the difference between the extents of silicate/hydrogen and pure hydrogen atmospheres. For example, for $T_{eq} = 1000$ K and $M_c = 4M_\oplus$, at 100 Myr after $T_c = 6500$ K, there are significant differences between these two models for $f > 0.01$. At this time, consideration of silicate condensation produces at least a factor of 2 difference in inferred mass for $f = 0.03$, up to a factor of 5 for larger atmospheric mass fractions. By $t = 1$ Gyr, the lower atmospheric mass planets with silicate/hydrogen atmospheres have become indistinguishable from the pure H/He atmospheres, but differences persist for $f > 0.05$. These differences become smaller with time, as shown by the contours approaching the one-to-one black line, but discrepancies of 20 percent between the modeled masses persist even at 5 Gyr for the most massive atmospheres we consider.

To summarize, we find that the silicate-induced radiative region causes H/He-only models to under-estimate the true atmospheric mass of sub-Neptunes. The mass inferred is most disparate for planets with higher core mass, higher atmospheric mass, higher equilibrium temperatures, and younger ages. This follows from the relatively contracted radii of planets with hot interiors when silicate vapor is considered. As these planets cool, their radiative regions disappear, and they begin contracting. However, in certain cases this contraction does not occur until the planet is larger than a pure H/He planet at the same age. In this case, the silicate/hydrogen atmosphere will appear inflated relative to the H/He case, and the mass inferred will consequently be smaller, causing excursions below the one-to-one line in Fig. 3.7. Over time, planets approach the radius one would expect for a pure H/He atmosphere. Differences can persist for planets with the largest initial differences for > 5 Gyr. These differences in radii, which translate to a factor of ~ 5 difference in inferred atmospheric mass for the youngest, most massive, or hottest planets we consider here, indicate there could be substantial error in inferred hydrogen mass fractions for observed exoplanets when the effects of silicate vapor are not considered.

3.4 Discussion and Future Work

In the section above, we have shown that silicate-induced radiative regions deep in the interiors of sub-Neptune atmospheres can have a large effect on the size, and therefore the inferred atmospheric mass fraction, of this common class of exoplanets. Below we discuss the effects of some uncertainties in our model. These uncertainties include the opacity behavior in the deep atmosphere, the initial base temperature with which planets begin their evolution, and the effect of condensables besides silicate vapor. We also outline prospects for future work, including the integration of these novel atmospheric structures with models of atmospheric mass loss.

3.4.1 Opacities

In Sec. 3.3, we demonstrated that the opacity structure has a large effect on the extent of the radiative region. A low, constant opacity such as 0.1 $\mathrm{cm}^2\mathrm{g}^{-1}$ leads to a slow increase in temperature with increasing pressure. Consequently, the radiative layer becomes thick, extending out to one third of the atmosphere's width in Fig. 3.2. Conversely, an opacity that scales with density as in Freedman et al. (2014) leads to larger opacity values in the interior, typically exceeding 1000 $\mathrm{cm}^2\mathrm{g}^{-1}$. These large opacities produce a very steep temperature gradient in the interior, narrowing the radiative region to a small fraction of the planet's total radius, as depicted in Fig. 3.3. While there are many theorized opacity scalings, which likely depend on the exact silicate content of the atmosphere (e.g Freedman et al., 2014; Lee et al., 2014), the steepness of the temperature gradient in the high opacity case makes our results insensitive to the exact opacity scaling used. So long as the opacity is sufficiently high such that the width of the radiative region becomes much less than the total width of the atmosphere, the exact structure has little effect on observables such as the planet's radius and inferred atmospheric mass. This is because the planet's radius is dominated by the structure of the convective region, and therefore the temperature at which $q = q_{\rm crit}$, which is independent of the opacity of the radiative layer.

We can quantify the effect of the opacity on the thickness of the atmosphere by combining hydrostatic equilibrium (equation (3.3)) and the radiative lapse rate (equation (3.13)) to solve for the width of the radiative region, ΔR, given the change in temperature across it, ΔT. We find that

$$\begin{aligned}\frac{\Delta R}{R_0} &= \frac{64\pi}{3} R_0 \frac{k_{\rm B}\Delta T}{\mu}\frac{\sigma T_0^4}{\kappa L P_0} \\ &\approx 0.01\left(\frac{R_0}{10^9\ {\rm cm}}\right)\left(\frac{\Delta T}{2000\ {\rm K}}\right)\left(\frac{T_0}{4000\ {\rm K}}\right)^4\left(\frac{\kappa}{10\ {\rm cm^2 g^{-1}}}\right)^{-1} \\ &\left(\frac{L}{10^{22}\ {\rm ergs^{-1}}}\right)^{-1}\left(\frac{P_0}{10^5\ {\rm bar}}\right)^{-1}\end{aligned} \tag{3.18}$$

where R_0, T_0, and P_0 represent the radius, temperature, and pressure at the radiative-convective transition. Specifically, in the thin radiative region limit, $R_0 \approx R_{\rm c}$. In the second equality, we scale this equation using typical values for the super-Earths we consider. Using these typical values, equation (3.18) shows that if the opacity $\kappa > 10\ {\rm cm^2 g^{-1}}$, the width of the radiative region $\Delta R < 0.01 R_0$, negligibly thin compared to the width of the whole atmosphere. This opacity condition is easily met by extrapolations of the opacity laws described in, e.g., Freedman et al. (2014) and Lee et al. (2014). In summary, while the exact opacity prescription best-suited to a hydrogen atmosphere containing substantial silicate vapor may be uncertain, the effects of alternative opacity scalings on atmospheric observables will be negligible so long as the opacity remains sufficiently high.

3.4.2 Conduction

At the typical temperatures and pressures in the deep non-convective regions of sub-Neptunes we consider in this work, conduction may be competitive with radiation in transporting heat (e.g. Vazan & Helled, 2020). As with the opacities discussed in the preceding paragraph, the thermal conductivities in these regions, λ, are uncertain and depend on the material properties of the atmosphere. Under sufficiently high pressure and temperature, hydrogen gas becomes metallic, which frees electrons that can easily transport thermal energy and thus leads to high conductivities. However, *ab initio* calculations and experimental evidence indicate this transition mostly takes place at higher temperatures and pressures than we consider (e.g. French et al., 2012; McWilliams et al., 2016). In the sub-Neptune regime, thermal conductivities are typically on the order of 10^5 to 10^6 erg s^{-1} cm^{-1} K^{-1}, i.e., 1 to 10 W m^{-1} K^{-1} (e.g. McWilliams et al., 2016). These values for hydrogen are similar to the thermal conductivity typically used for Earth-like silicate in planetary interiors, $\lambda \sim 4$ W m^{-1} K^{-1} (e.g. Stevenson et al., 1983; Vazan & Helled, 2020), and that derived from *ab initio* simulations of silicate liquids at planetary conditions (Scipioni et al., 2017). Using these conductivity values, we find that conductive heat transport can be similar in magnitude to radiation for the conditions considered here but does not significantly exceed it.

To verify these results, we modeled the atmospheric structure including both conduction and radiation. For the thermal conductivities, we use the electrical conductivity scaling of McWilliams et al. (2016), based on experimental results for pure hydrogen, and convert to thermal conductivities using the Wiedemann-Franz law. At lower temperatures and pressures, where the electrical conductivity is low, we use a minimum value of $\lambda = 2 \times 10^5$ erg s^{-1} cm^{-1} K^{-1}, appropriate for the nucleic contribution over a broad range of relevant temperatures and pressures (French et al., 2012). We found that the overall atmospheric radii were not measurably different when both conduction and radiation were included than the previous, radiation-only results presented in Section 3.3. In both cases, the widths of the non-convective regions were negligibly thin compared to the overall planet radius, even for the most massive planets and atmospheres we consider in this work. These results support the conclusion that while conduction could be competitive with radiation deep in some of these atmospheres, it does not affect the overall qualitative and quantitative findings of this work for the temperatures and pressures we consider.

3.4.3 Initial base temperature

The initial base temperatures chosen throughout this work are in the range suggested by accretion models (e.g. Ginzburg et al., 2016), but it is possible the initial temperature at the base of sub-Neptunes could be higher, up to 10000 K. An increased starting base temperature results in more core thermal energy available for cooling. However, the initial radius is virtually unchanged, due to the steepness of the radiative region. Therefore, the cooling timescale becomes longer, prolonging evolution and contraction to longer timescales than presented in Sec. 3.3. The qualitative effect of silicate vapor decreasing the radius, and therefore increasing the inferred atmospheric mass, of sub-Neptune planets holds so long as the initial base temperature is $\gtrsim$ 4000 K, i.e., high enough for a radiative region to form.

Additionally, this initial base temperature may vary from planet to planet a function of a planet's physical parameters, as more massive planets may begin with hotter base temperatures. This effect would magnify the increase in cooling timescales already present with increasing planet mass. Determining these initial conditions in detail requires modeling the formation of these planets and their H/He accretion from the protoplanetary disk, which is beyond the scope of this work. These higher temperatures also go beyond the temperature range for which the silicate vapor pressure relation we employ (Visscher & Fegley, 2013) was originally intended.

3.4.4 Other condensables

While equilibrium chemistry models find silicate vapor to be by far the most abundant vapor species in equilibrium at the magma ocean-atmosphere interface of sub-Neptunes (Schlichting & Young, 2022), other species are expected to be present in lower concentrations. One such species is water vapor, which may be present at the $\sim$ 10 percent level above an Earth-composition magma ocean. Water vapor abundance constrains both habitability and planet migration in early stellar systems, so accurately quantifying the endogenic water concentrations we expect from sub-Neptunes is important. Enhanced atmospheric abundances of water are possible if sub-Neptunes have a more ice-rich composition than Earth, which are also consistent with measured bulk densities (e.g. Rogers & Seager, 2010; Dorn et al., 2017; Zeng et al., 2019; Mousis et al., 2020). If sub-Neptunes are water-rich, high-pressure ice layers could form between the silicate core and H/He atmosphere (e.g. Nixon & Madhusudhan, 2021), which could impede the interaction between the silicate and H/He investigated in this work. Additionally, the endogenic production of water vapor could affect the quantity of SiO vapor expected above a magma ocean (Schlichting & Young, 2022), behavior which we aim to more fully capture in future work.

Since water vapor is expected to be at lower concentrations than silicate vapor in equilibrium with a magma ocean (Schlichting & Young, 2022), we expect its importance in influencing atmospheric structure to be of lower order. However, since water condenses at a much lower temperature than silicate vapor, whatever water is at equilibrium at the base of the atmosphere may extend into regions observable by transmission spectroscopy. Additionally, this lower condensation temperature could mean that this endogenic water's effects could impact a different region of the atmosphere than the silicate vapor, even if the magnitude is smaller. However, this region of maximum effect may be at a temperature lower than T_{eq} for some of the sub-Neptunes we consider here, so water's effect on the atmospheric structure may be small for these hotter planets.

3.4.5 Mass loss processes

Besides the observable consequences of different planet radii, the inhibition of convection by silicate vapor atmospheres could also affect the mass loss processes thought to shape the radius valley, such as photo-evaporation (e.g. Owen & Wu, 2017) and core-powered mass loss (e.g. Gupta & Schlichting, 2019). The implications of silicate-induced radiative regions on the accretion of hydrogen gas from the protoplanetary disk and subsequent hydrodynamic mass loss should be carefully considered. We intend to integrate these novel silicate-induced structures into models of mass loss processes in future work.

3.5 Summary and Conclusions

In this work, we have demonstrated that silicate vapor has significant effects on the structure of sub-Neptune atmospheres. At high temperatures, condensation of silicate vapor in a hydrogen-rich atmosphere can induce a mean molecular weight gradient that inhibits convection, leading to a radiative atmospheric profile near the magma ocean-atmosphere interface of these planets. The exact temperature gradient depends on the opacity dependence of the atmosphere, but for opacities typical of high-density hydrogen, the gradient is very steep. Therefore, the temperature drops sharply above the magma ocean until the silicate abundance is low enough to allow for convection. This radiative layer decreases the overall radius of a planet compared to a fully convective, pure H/He atmosphere with the same base temperature. We simulate the thermal evolution in time of these planets and find that young planets with silicate/hydrogen atmospheres and base temperatures $\gtrsim$ 4000 K are much smaller than pure H/He atmospheres with the same base temperatures. As these planets cool, all the change in temperature at the base is accommodated by the radiative region, preventing contraction: a planet with any inner radiative region has nearly constant radius no matter the base temperature. This shrunken state leads to slower cooling, allowing equivalent convective H/He atmospheres to cool and contract until they approach and are briefly smaller than the silicate/hydrogen atmospheres. Once the abundance of silicate vapor is low enough, the planet can contract, and eventually the two cases converge. This convergence happens more slowly for planets with larger masses and atmospheric mass fractions, and silicate/hydrogen atmospheres can have substantially different inferred atmospheric masses on gigayear timescales.

We survey the sub-Neptune parameter space to quantify how these differences in evolution depend on a planet's physical parameters. We find that high mass planets with high atmospheric mass fractions differ most substantially at any given time. While lower mass planets with smaller atmospheric mass fractions also have large radius differences, these planets also cool more quickly, thereby losing their radiative regions and erasing the initial dichotomy. Meanwhile, while planets at cooler equilibrium temperatures start the most inflated, they also cool the fastest, leading to intermediate temperature planets being the largest at any given time. Finally, we compare the atmospheric masses inferred from a pure H/He atmospheric model to those inferred from the same radius in a silicate/hydrogen atmospheric model. We find that for a $10 M_\oplus$ planet with an equilibrium temperature of 1000 K, a hydrogen-dominated atmosphere containing silicate vapor with $f = 0.10$ has the same radius as hydrogen-only model with $f \approx 0.02$, if both planets have cooled for 300 Myr from an initial temperature at the bases of their atmospheres of 6500 K. In essence, the silicate-induced radiative layer typically makes the atmosphere more contracted than it would be if the atmosphere were pure H/He. Such differences can persist for gigayears, especially for more massive planets with larger atmospheric mass fractions. Therefore, atmospheric masses inferred from measured exoplanet radii can be substantially under-estimated if compositional equilibrium with the underlying silicates is not considered.

CHAPTER 4

Atmospheres as windows into sub-Neptune interiors: coupled chemistry and structure of hydrogen-silane-water envelopes

[1] Sub-Neptune exoplanets are commonly hypothesized to consist of a silicate-rich magma ocean topped by a hydrogen-rich atmosphere. Previous work studying the outgassing of silicate material has demonstrated that such atmosphere-interior interactions can affect the atmosphere's overall structure and extent. But these models only considered SiO in an atmosphere of hydrogen gas, without considering chemical reactions between them. Here we couple calculations of the chemical equilibrium between H, Si, and O species with an atmospheric structure model. We find that substantial amounts of silane, SiH_4, and water, H_2O, are produced by the interaction between the silicate-rich interior and hydrogen-rich atmosphere. These species extend high into the atmosphere, though their abundance is greatest at the hottest, deepest regions. For example, for a 4 $M_\oplus$ planet with an equilibrium temperature of 1000 K, a base temperature of 5000 K, and a 0.1 $M_\oplus$ hydrogen envelope, silicon species and water can comprise 30 percent of the atmosphere by number at the bottom of the atmosphere. Due to this abundance enhancement, we find that convection is inhibited at temperatures $\gtrsim$ 2500 K. This temperature is lower, implying that the resultant non-convective region is thicker, than was found in previous models which did not account for atmospheric chemistry. Our findings show that significant endogenous water is produced by magma-hydrogen interactions alone, without the need to accrete ice-rich material. We discuss the observability of the signatures of atmosphere-interior interaction and directions for future work, including condensate

---

[1] This chapter was previously published in similar form as Misener, W., Schlichting, H. E., and Young E. D. 2023, MNRAS 524, 981.

lofting and more complex chemical networks.

4.1 Introduction

Exoplanet surveys have revealed that planets with radii between 1 and 4 Earth radii with orbital periods shorter than 100 days are the most intrinsically common type of planet yet observed (e.g. Fressin et al., 2013). Precise mass and radius measurements indicate that these planets are distributed bimodally in radius and bulk density (Weiss & Marcy, 2014; Fulton et al., 2017). These measurements separate the small planet population into super-Earths, smaller planets consistent with bulk-Earth composition, and larger sub-Neptunes, which must contain some low-density material to explain their measured radii and densities.

Typically, sub-Neptunes are assumed to contain some combination of terrestrial rock and metal, icy material, and/or hydrogen gas (e.g. Rogers & Seager, 2010; Dorn et al., 2017; Zeng et al., 2019). As hydrogen is the lowest density of these three materials, an envelope containing a small amount of it, of order one percent of a planet's total mass, can greatly increase a planet's size and thus decrease its bulk density. It is therefore possible to model most sub-Neptunes as Earth-like cores with hydrogen envelopes of a few percent the planet's mass (e.g. Lopez & Fortney, 2014). However, density measurements do not rule out compositions with large mass fractions in ices, such as water, with correspondingly smaller hydrogen atmospheres (e.g. Zeng et al., 2019; Luque & Pallé, 2022).

Due to their ubiquity, a large number of models of sub-Neptune atmospheric evolution and composition have been put forward. Crucially, neither the radii nor masses of these envelopes are expected to remain constant in time. Rather, sub-Neptune atmospheres shrink in extent as the planets cool into space (Lopez & Fortney, 2014), and they can be susceptible to atmospheric stripping. This stripping, which can be due to either photo-evaporative (Owen & Jackson, 2012; Owen & Wu, 2017) or core-powered mass-loss mechanisms (Ginzburg et al., 2016; Gupta & Schlichting, 2019), is thought to have stripped some sub-Neptunes entirely, turning them into super-Earths and forming the observed radius valley. The sub-Neptunes that remain were able to mostly resist this stripping. The attributes of the observed radius valley are best matched by mass-loss models if the cores of sub-Neptunes are mostly rocky, with little ice (Gupta & Schlichting, 2019; Rogers & Owen, 2021).

However, these and other models typically assume each compositional constituent of the planet is contained its own layer. Such a structure may be the simplest model to first order, but it may not accurately describe the interactions between these constituents at the high temperatures and pressures expected within sub-Neptunes. Awareness of mixing between layers previously modeled as separate is gaining traction across planetary science. In the Solar System, Jupiter and Saturn show evidence for non-discrete cores which have blended with their metallic H surroundings (Wahl et al., 2017; Mankovich & Fuller, 2021). Similar mixing between water and hydrogen has been proposed in the ice giants (Bailey & Stevenson, 2021), and water and rock may be miscible at the temperature-pressure conditions of sub-Neptune interiors (Vazan et al., 2022).

Another blurred line between layers arises from the interaction between a hydrogen atmosphere and the potential rocky, silicate-dominated core beneath it. Recent work has shown that at chemical equilibrium, significant silicate vapor is stable in the gas at the base of young sub-Neptune atmospheres (Schlichting & Young, 2022), where temperatures can exceed 5000 K (Ginzburg et al., 2016). As silicate vapor will decline in abundance with decreasing temperatures, this implies a compositional gradient deep within sub-Neptunes. This gradient in composition, and thus in mean molecular weight, has been demonstrated to inhibit convection (Misener & Schlichting, 2022; Markham et al., 2022). The inhibition occurs because a deeper parcel is heavier than one higher up, which overcomes its thermal buoyancy. Such an effect has long been known to apply at the conditions within the Solar system gas and ice giants, where the condensable considered is usually water vapor (Guillot, 1995; Leconte et al., 2017; Markham & Stevenson, 2021). But it has only recently been applied to sub-Neptune planets with magma oceans. In addition to arguments from chemical equilibrium, gradients in Si abundance in a hydrogen dominated atmosphere, and therefore a non-convective region, could also form as a consequence of the accretion of pebbles during formation (Brouwers & Ormel, 2020; Ormel et al., 2021), though the subsequent evolution of such structures remain unclear.

These studies mark initial forays into understanding the interiors of this ubiquitous class of planet, sub-Neptunes composed of hydrogen and silicate. Much work remains to be done to further quantify the effects of interaction between the interior and atmosphere. In particular, both Misener & Schlichting (2022) and Markham et al. (2022) assume the gas released into the atmosphere is pure SiO vapor. However, oxidized SiO is not inert in a hydrogen-dominated background gas. Rather, it will react with the hydrogen, producing water (H_2O) and silane (SiH_4). These species will alter the impact of magma condensation on the overall atmospheric structure. It will also change the observable signatures of interior-atmosphere interactions we expect. In this paper, we construct a coupled atmospheric-chemical model which captures the interactions we expect vaporizing silicate magma to have with a hydrogen atmosphere.

4.2 Model

In this section we detail our atmospheric and chemical model of a sub-Neptune consisting of a silicate-dominated interior and a hydrogen-dominated atmosphere.

4.2.1 Chemistry

In Misener & Schlichting (2022), to quantify the partial pressure of rock vapor in the atmosphere above a pure SiO_2 magma ocean, the authors use an exponential relationship between SiO and temperature appropriate for congruent evaporation of SiO_2 melt, taken from Visscher & Fegley (2013). The evaporation reaction can be written as:

$$\mathrm{SiO}_{2,l} \rightleftharpoons \mathrm{SiO} + 0.5\mathrm{O}_2, \tag{4.R1}$$

where on the left hand side, the l subscript denotes a liquid species; here and going forward, all chemical species without this subscript are gaseous. Reaction 4.R1 can be quantified using an equilibrium constant:

$$K_{\mathrm{eq,R1}} = \frac{P_{\mathrm{SiO}} P_{\mathrm{O_2}}^{0.5}}{a_{\mathrm{SiO_2}}}, \tag{4.1}$$

where P_i denotes the partial pressure of species i, and $a_{\mathrm{SiO_2}}$ is the activity of SiO_2 in the melt, which we take to be 1, i.e., we assume the silicate melt is fully SiO_2. This and following equilibrium constants are found by taking the difference between the Gibbs free energies of the products and reactants. All Gibbs free energy values are calculated from the NIST Chemistry WebBook parameterizations of enthalpy and entropy, based on data from the JANAF tables (Chase, 1998). For $SiO_{2,l}$, the NIST data extends to a maximum temperature of 4500 K; in this work we extrapolate the NIST fit to 5000 K, following Schlichting & Young (2022). We also extrapolate the NIST fit below 1996 K, where solid $SiO_{2,s}$ should be the predominant species. We verify that using the NIST values for the Gibbs free energy of the solid form does not alter our results. The equilibrium constant is a strong function of temperature, where higher temperatures produce relatively more evaporation and thus higher partial pressures of the gaseous species. We demonstrate the temperature dependence of $K_{\mathrm{eq,R1}}$, as well as the equilibrium constants defined in Eqs. 4.2 and 4.3 below, in Appendix 4.6.1. Application of this equilibrium constant produces good agreement with the Visscher & Fegley (2013) equation, though there are slight differences due to the different thermodynamic values used.

However, both species on the right-hand side of Reaction 4.R1 are oxidized, and therefore neither is expected to be inert in the presence of H_2 gas, a strong reducer. Rather, each product should interact with the background hydrogen. Oxygen combines with hydrogen to produce water

$$0.5\mathrm{O_2} + \mathrm{H_2} \rightleftharpoons \mathrm{H_2O} \tag{4.R2}$$

while SiO reacts with hydrogen to produce silane, SiH_4

$$\mathrm{SiO} + 3\mathrm{H_2} \rightleftharpoons \mathrm{SiH_4} + \mathrm{H_2O}. \tag{4.R3}$$

The production of silane has been suggested to occur deep within Jupiter, at low concentrations (e.g. Fegley & Lodders, 1994), due to silane being more thermochemically favorable than SiO at the relevant temperature-pressure conditions (Visscher et al., 2010a). More recently, the same reaction has been suggested to occur in sub-Neptune atmospheres which interface with magma oceans (Markham et al., 2022), where plentiful oxidized silicate is presumed to exist. Moreover, diamond-anvil cell experiments indicate that mixtures of SiO_2 and H_2 fluid produce silane and water in the fluid at 2×10^4 bar and 1700 K (Shinozaki et al., 2014), and similar silane production was observed in a $MgSiO_3$–H_2 mixture at 3.6×10^4 bar and 2000 K (Shinozaki et al., 2016). These pressures and temperatures are relevant both to the inner mantle of Earth and to the sub-Neptune conditions we consider here (see Fig. 4.2 below).

The relative abundances of these species in the atmosphere are determined by the equilibrium constants for the reactions, respectively:

$$K_{\mathrm{eq,R2}} = \frac{P_{\mathrm{H_2O}}}{P_{\mathrm{H_2}} P_{\mathrm{O_2}}^{0.5}} \tag{4.2}$$

and

$$K_{\mathrm{eq,R3}} = \frac{P_{\mathrm{SiH_4}} P_{\mathrm{H_2O}}}{P_{\mathrm{SiO}} P_{\mathrm{H_2}}^{3}}. \tag{4.3}$$

As with Eq. 4.1, these equilibrium constants are calculated from Gibbs free energies taken from NIST and are functions of temperature.

To calculate the atmospheric composition at each level of the atmosphere, we use the temperature, T, and total pressure, P, derived from the atmospheric structure equations detailed below in Sec. 4.2.2. We then apply the fact that in our model, the changes in atmospheric composition are driven by the evaporation and condensation of SiO_2. Therefore, we can use the stoichiometric relationship that for every Si atom at a given level in the atmosphere, there must be two O atoms. More quantitatively, we can calculate the "partial pressures" of each element, which both convert through common factors to the numbers at each pressure level,

$$\sum P_{\mathrm{Si}} \equiv P_{\mathrm{SiO}} + P_{\mathrm{SiH_4}} \tag{4.4}$$

and

$$\sum P_{\mathrm{O}} \equiv P_{\mathrm{SiO}} + 2P_{\mathrm{O_2}} + P_{\mathrm{H_2O}}. \tag{4.5}$$

We can then mandate that

$$\sum P_{\mathrm{O}} = 2 \sum P_{\mathrm{Si}} \tag{4.6}$$

at each level of the atmosphere.

Eqs. 4.1, 4.2, 4.3, and 4.6 are sufficient to solve for the partial pressures of each component. We detail our analytic method in Appendix 4.6.2.

4.2.2 Atmospheric Structure

This atmospheric structure model builds on Misener & Schlichting (2022), which added consideration of compositional gradients and moist convection to the model of Misener & Schlichting (2021). Here, as in both of those works, we model the outer atmosphere as being in thermal equilibrium with the incident flux from the star and thus isothermal at the planet's equilibrium temperature, T_{eq} (e.g. Lee & Chiang, 2015; Ginzburg et al., 2016).

The atmosphere transitions to convective at the outer radiative-convective boundary (R_{rcb}). The radial pressure gradient is found following hydrostatic equilibrium:

$$\frac{\partial P}{\partial R} = -\frac{G M_{\mathrm{c}}}{R^2} \frac{\mu P}{k_{\mathrm{B}} T}, \tag{4.7}$$

where G is the gravitational constant, M_{c} is the planet mass, k_{B} is the Boltzmann constant, and μ is the local mean molecular weight. The mean molecular weight is a function of temperature and pressure, and is calculated using chemical equilibrium, as detailed in the previous section.

The temperature profile in the convective region follows a moist adiabat:

$$\frac{\partial \ln T}{\partial \ln P} = \frac{k_{\mathrm{B}}}{\mu} \frac{1 + \dfrac{P_{\mathrm{Si}}}{P_{\mathrm{H}}} \dfrac{\partial \ln P_{\mathrm{Si}}}{\partial T}}{c_{\mathrm{p}} + \dfrac{P_{\mathrm{Si}}}{P_{\mathrm{H}}} \dfrac{k_{\mathrm{B}}}{\mu} T^2 \left(\dfrac{\partial \ln P_{\mathrm{Si}}}{\partial T} \right)^2}, \tag{4.8}$$

where P_{H} is the partial pressure of hydrogen, and P_{Si} is the combined partial pressures of Si-bearing species (e.g. Leconte et al., 2017). The determination of these partial pressures via chemical equilibrium was described in Section 4.2.1. The specific heat capacity c_p is a mass-weighted average of the specific heat capacities of each component:

$$c_\mathrm{p} = \sum_i q_i c_{\mathrm{p},i} \tag{4.9}$$

where q_i is the mass mixing ratio, defined as $q_i \equiv \mu_i P_i/(\mu P)$, with μ_i being the molecular weight of species i. $c_{\mathrm{p},i}$, the heat capacity of each species, is given by

$$c_{\mathrm{p},i} = \frac{k_\mathrm{B}}{\mu_i}\frac{\gamma_i}{\gamma_i - 1}. \tag{4.10}$$

where γ_i is the adiabatic index of a species. For the diatomic molecules O_2, H_2, and SiO, we assume $\gamma = 7/5$, while for H_2O we take $\gamma = 4/3$ and for SiH_4 we take $\gamma = 1.3$, following that of similarly-structured methane. We use fixed values of each species' heat capacity for simplicity; we verify that temperature-dependent values from NIST (Chase, 1998) deviate by less than a factor of two from these constant values over the adiabatic region, which only marginally alters the atmospheric structure we obtain. Generally, we find that the atmospheric composition in the adiabatic regime is hydrogen-dominated, so the heat capacity is very near that of hydrogen alone. We assume the hydrogen remains fully diatomic throughout the atmosphere. Hydrogen dissociation is expected at sufficiently high pressures and temperatures. Molecular dynamics simulations indicate that hydrogen likely remains diatomic throughout most of our atmospheric structure, though it may start to dissociate at the highest temperatures and pressures we consider (e.g. Tamblyn & Bonev, 2010; French et al., 2012; Soubiran et al., 2017). If hydrogen begins to dissociate, the effective adiabatic index of the atmosphere would be lower due to the energy required for breaking the H–H bonds (Lee & Chiang, 2015), similar to the effect of latent heat of vaporization, making the adiabatic temperature gradient shallower.

To construct the atmospheric structure, we begin from the outer radiative-convective boundary, where $R = R_\mathrm{rcb}$ and $P(R_\mathrm{rcb})$ are chosen, and $T(R_\mathrm{rcb}) = T_\mathrm{eq}$. We increment in small pressure steps: $P_\mathrm{new} = P + \Delta P$. The new radius is thus $R_\mathrm{new} = R + \Delta P/(\partial P/\partial R)$, and the new temperature, $T_\mathrm{new} = T + \Delta P(\partial T/\partial P)$, employing Eqs. 4.7 and 4.8 respectively.

As described in Misener & Schlichting (2022), the change in composition of the atmosphere with temperature due to condensation causes a mean molecular weight gradient. In a hydrogen-dominated atmosphere, these condensation effects cause the mean molecular weight to increase with temperature, stabilizing the gas against convection. This is in contrast to an Earth-like atmosphere, in which the major condensable, water, is lighter than the background air. In previous work, in which one condensable species was considered, the tipping point beyond which convection is inhibited could be quantified by a critical mass mixing ratio $q_{\rm crit}$ (Guillot, 1995; Leconte et al., 2017; Misener & Schlichting, 2022; Markham et al., 2022):

$$q_{\rm crit} = \frac{1}{\left(1 - \dfrac{\mu_{\rm H}}{\mu_{\rm cond}}\right)\dfrac{\partial \ln P_{\rm cond}}{\partial \ln T}}. \tag{4.11}$$

In an atmosphere with multiple species changing abundance, this relationship is in principle more complex. However, the inhibition of convection can be quantified by calculating a "convection criterion" for each non-hydrogen species χ_i:

$$\chi_i = q_i\left(1 - \frac{\mu_{\rm H}}{\mu_{\rm i}}\right)\frac{\partial \ln P_{\rm i}}{\partial \ln T}, \tag{4.12}$$

where q_i is the mass-mixing ratio of species i. Convection is inhibited if $\sum_i \chi_i \geq 1$. In the case of a single species, this method yields the same results as Eq. 4.11. We derive the fact that the overall stability criterion is the sum of the criteria for each species in Appendix 4.6.3.

4.2.2.1 Non-convective region

In regions where the criterion is fulfilled, convection is inhibited, no matter how super-adiabatic the temperature profile becomes. In these regions, heat must be transported by either radiation or conduction. At the typical temperatures and pressures in the deep non-convective regions of sub-Neptunes we consider in this work, conduction may be competitive with radiation in transporting heat (e.g. Vazan & Helled, 2020; Misener & Schlichting, 2022).

We quantify the competition between conduction and radiation by comparing the conductivity, $\lambda_{\rm cond} = L/(4\pi r^2)/(\partial T/\partial r)_{\rm cond}$, to the equivalent radiative heat transport term, $\lambda_{\rm rad} \equiv L/(4\pi r^2)/(\partial T/\partial r)_{\rm rad} = 16\sigma T^3/(3\kappa\rho)$, where where σ is the Stefan-Boltzmann constant and κ is the local Rosseland mean opacity. Conduction dominates radiation when $\Lambda \equiv \lambda_{\rm cond}/\lambda_{\rm rad} > 1$, or, written in scaling form:

$$\begin{aligned}\Lambda \approx & \left(\frac{\lambda_{\rm cond}}{7\times10^4\ {\rm erg\ s^{-1}cm^{-1}K^{-1}}}\right)\left(\frac{\kappa}{10^3\ {\rm cm^2g^{-1}}}\right) \\ & \left(\frac{\rho}{1\ {\rm g\ cm^{-3}}}\right)\left(\frac{T}{6000\ {\rm K}}\right)^{-3} \\ & > 1.\end{aligned} \tag{4.13}$$

From equation (4.13), it is apparent that larger conductivities, opacities, and gas densities favor conduction over radiation.

Due to the widely varying atmospheric compositions, the atmospheric Rosseland mean opacity κ is difficult to determine without a detailed radiative model, which is beyond the scope of this work. Therefore, following Misener & Schlichting (2022) and Markham et al. (2022), we use the Freedman et al. (2014) relation for solar metallicity gas throughout the atmosphere. We extend these opacities to pressures beyond their asserted validity, so we acknowledge that the opacity of the interior is a source of uncertainty in our model. We discuss the relevance of different opacity choices in Section 4.3.

As with the opacities, the conductivities in these regions are uncertain and depend on the material properties of the atmosphere, which are not entirely clear for the exotic mixtures we encounter. Therefore, we employ a simple approach based on the behavior of pure H/He, as described in Misener & Schlichting (2022). To calculate the thermal conductivity, we use the electrical conductivity scaling with temperature and pressure from McWilliams et al. (2016), which is based on experimental results for pure hydrogen. We then convert these to thermal conductivities using the Wiedemann-Franz law. At relatively low temperatures and pressures, where the electrical conductivity is low, we use a minimum value of $\lambda_{\rm cond} = 2\times10^5$ erg s^{-1} cm^{-1} K^{-1}, appropriate for the nucleic contribution over a broad range of relevant temperatures and pressures (French et al., 2012) and consistent with approximations used in previous work modeling Earth-like silicate in planetary interiors (e.g. Stevenson et al., 1983; Vazan & Helled, 2020).

We can incorporate both conduction and radiation by adding the thermal conductivity to the equivalent radiative term to make an "effective conductivity", $\lambda_{\text{eff}} \equiv \lambda_{\text{cond}} + \lambda_{\text{rad}}$. An alternative, but equivalent, framing is to employ an effective opacity, κ_{eff} (Vazan & Helled, 2020):

$$\kappa_{\text{eff}} = \frac{1}{\dfrac{1}{\kappa} + \dfrac{1}{\kappa_{\text{cond}}}} \tag{4.14}$$

where κ_{cond}, the "conductive opacity", is given by

$$\kappa_{\text{cond}} = \frac{16\sigma T^3}{3\rho\lambda_{\text{cond}}}. \tag{4.15}$$

The temperature gradient of the non-convective region is then determined by the energy flux, L, as well as the local pressure, temperature, and the effective opacity κ_{eff}:

$$\frac{\partial \ln T}{\partial \ln P} = \frac{3\kappa_{\text{eff}} P L}{64\pi G M_{\text{c}} \sigma T^4}. \tag{4.16}$$

In steady state, the energy flux that must be transported across the radiative boundary is equal to the radiative flux of the planet into space, i.e., the luminosity at the radiative-convective boundary:

$$L = \frac{\gamma - 1}{\gamma} \frac{64\pi G M_{\text{c}} \sigma T_{\text{eq}}^4}{3\kappa_{\text{rcb}} P_{\text{rcb}}}, \tag{4.17}$$

where 'rcb' subscripts represent values calculated at the conditions of the radiative-convective boundary. Here, the atmosphere is dominated by hydrogen, so we use the adiabatic index for pure H_2 gas and opacity relations of Freedman et al. (2014) for solar composition gas.

4.3 Results

In this section, we present the atmospheric profile and chemical abundances we obtain for our fiducial planet, a 4 $M_{\oplus}$ planet with an equilibrium temperature of 1000 K. The atmosphere has a total hydrogen mass of 2.5% the core's total mass. These values are all typical of sub-Neptunes (e.g. Lopez & Fortney, 2014). This planet has a base temperature of 5000 K, which is a reasonable value early in the planet's evolution (e.g. Ginzburg et al., 2016; Misener & Schlichting, 2022). We begin by examining the region interior to the outer radiative-convective boundary in Section 4.3.1, where the chemistry has the largest effect on the atmospheric structure. We then describe the chemical equilibrium of the outer radiative region in Section 4.3.2, which has implications for the observability of these interior-atmosphere interactions.

4.3.1 Inner atmosphere

In this section we focus on the region interior to the outer radiative-convective boundary, which is at $\sim 1.19 R_\mathrm{c}$ in our fiducial model. This radius and corresponding pressure $P(R_\mathrm{rcb})$ are found by iterating the atmospheric profile until the desired planet characteristics, i.e. the hydrogen mass and base temperature $T(R_\mathrm{c})$, are achieved, following the method of Misener & Schlichting (2022). In Fig. 4.1 we show the partial pressures of the species we consider, namely H_2 (gray), H_2O (blue dashed), SiH_4 (yellow), SiO (red solid), and O_2 (pink), as functions of radius. In Fig. 4.2, we show aspects of the overall atmospheric profile, namely the temperature, pressure, and mean molecular weight as functions of radius, and in Fig. 4.3 we present an alternative view of the same model as in Fig. 4.1, but in pressure-temperature space.

The atmosphere is hydrogen-dominated by number at all radii (i.e., $P_{\mathrm{H}_2} > P_i$ for all other species i). The dominance of hydrogen by number is demonstrated in Fig. 4.4, which shows the number fraction of the species we consider throughout the atmosphere. The abundances of all the secondary species we consider, namely H_2O, SiH_4, SiO, and O_2, increase in abundance with depth as the temperature increases. Water and silane have partial pressures a factor of $\sim 10^{-7}$ lower than that of H_2 at the outer radiative-convective boundary, while SiO is lower still, with a number fraction of $\sim 10^{-14}$, and O_2 many orders of magnitude less than this. However, at the magma-atmosphere interface, $r = R_\mathrm{c}$, secondary species abundances are much higher, with SiO, H_2O, and SiH_4 together making up nearly 40% of the atmosphere by number and overtaking H_2

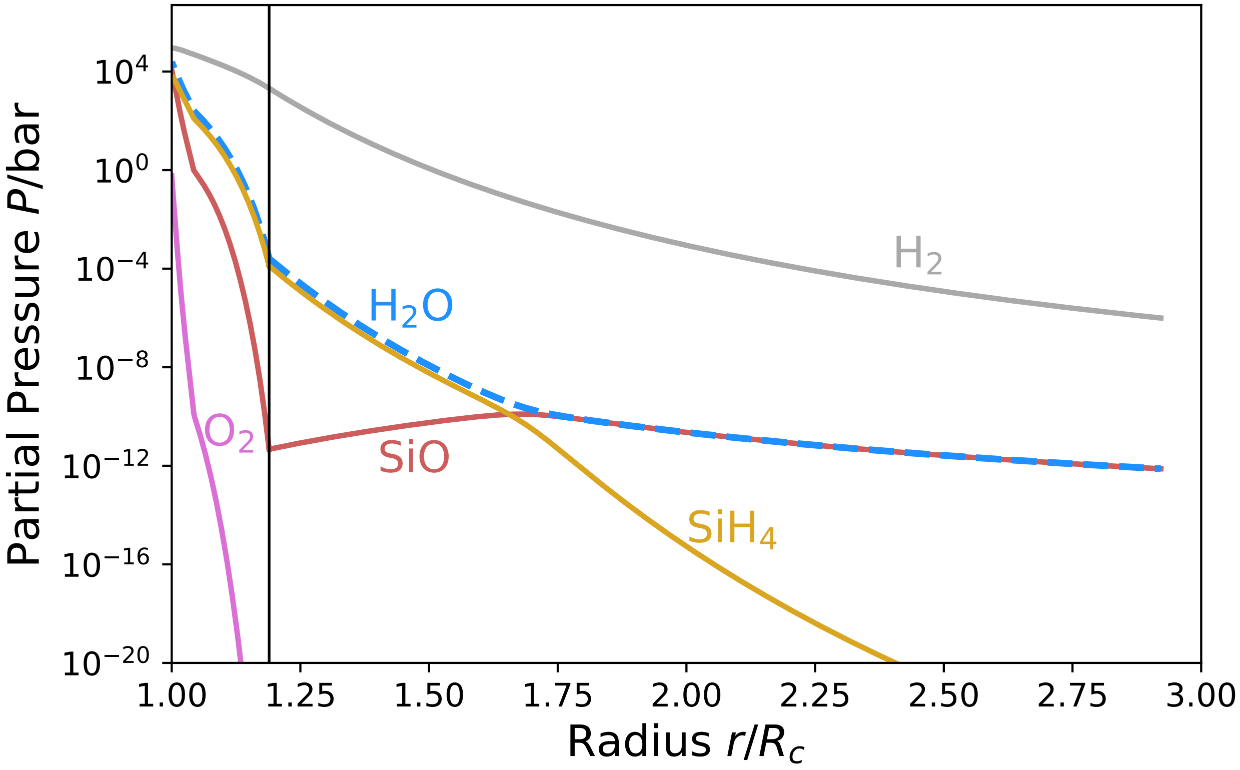

Figure 4.1: Partial pressures of the chemical species present in the atmosphere as a function of radius, in core radii R_c, for a 4 $M_\oplus$ planet with an equilibrium temperature of 1000 K, a base temperature of 5000 K, and an atmospheric hydrogen mass fraction of 2.5%. The species we consider are H_2 (gray), H_2O (blue dashed), SiH_4 (yellow), SiO (red solid), and O_2 (pink). For comparison, the SiO abundance derived from the congruent evaporation equation in Visscher & Fegley (2013) is shown as a red dotted line. The outer vertical black line at 1.19 R_c represents the outer radiative convective boundary, while the inner black line at 1.04 R_c represents the inner transition within which convection is inhibited.

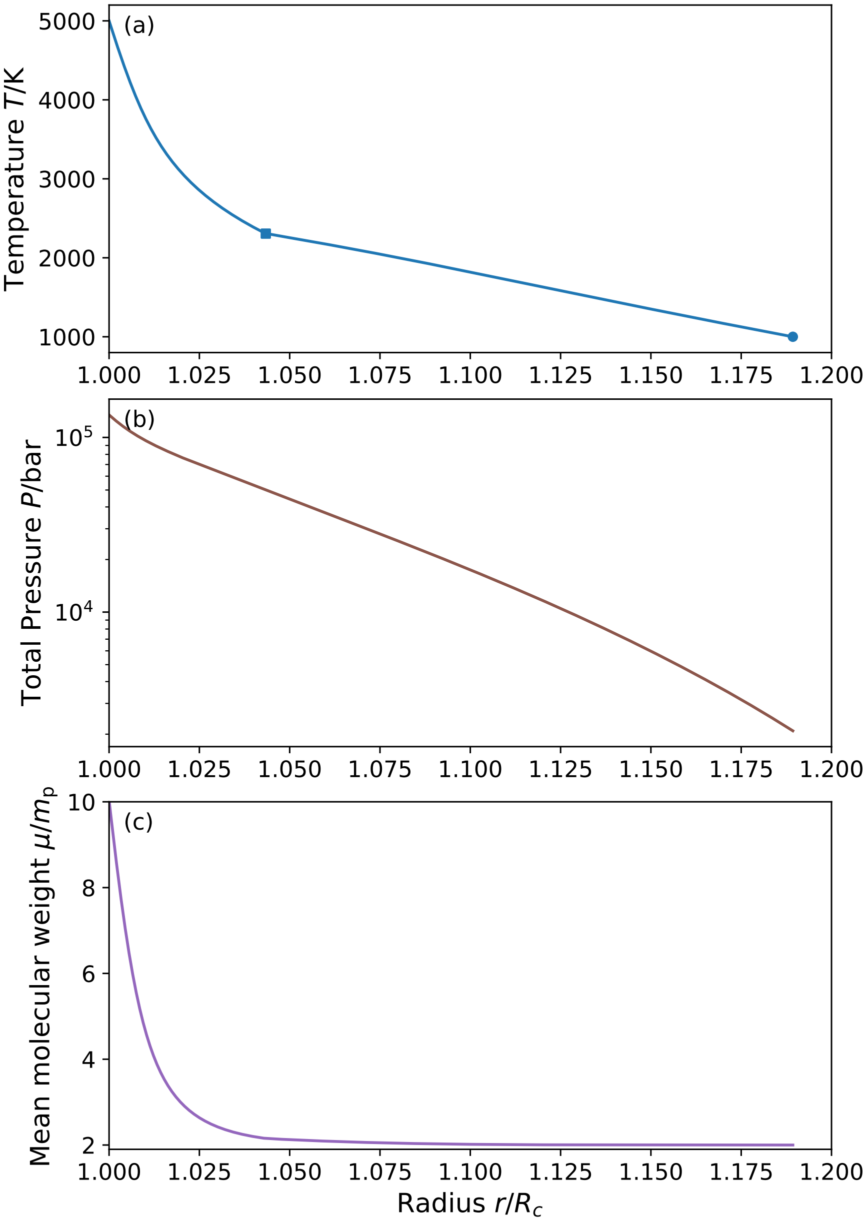

Figure 4.2: Example of sub-Neptune envelope structure. Panel (a) shows the temperature T in kelvin, (b) the total pressure P in bar, and (c) the mean molecular weight μ in proton masses m_p, as functions of radius, in core radii R_c. The model is the same one as shown in Fig. 4.1: a 4 $M_\oplus$ planet with an equilibrium temperature of 1000 K, a base temperature of 5000 K, and an atmospheric hydrogen mass fraction of 2.5%. In the top panel, the dot represents the outer radiative-convective boundary, while the square represents the inner transition, inside of which convection is inhibited.

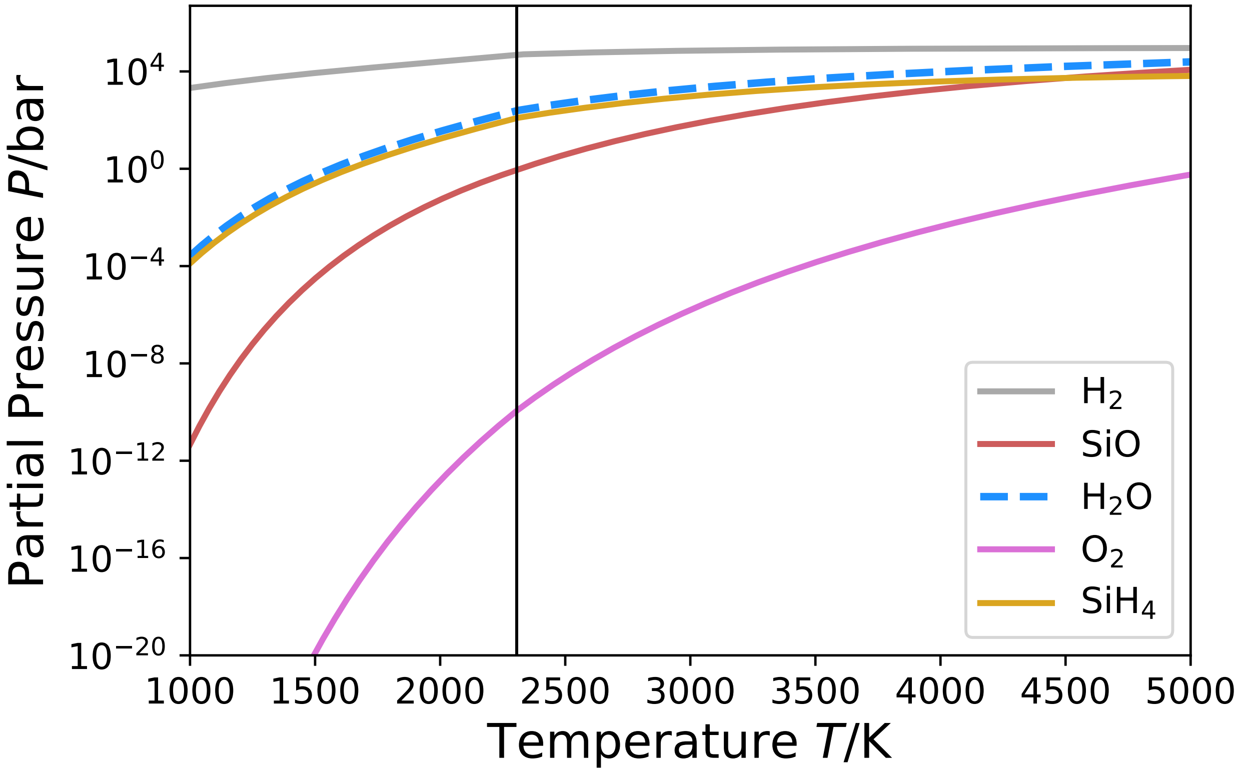

Figure 4.3: Partial pressures of the chemical species present in the atmosphere as a function of temperature. The line meanings remain the same as those in Fig. 4.1, as do the physical parameters: a 4 $M_\oplus$ planet with an equilibrium temperature of 1000 K, a base temperature of 5000 K, and an atmospheric hydrogen mass fraction of 2.5%. The black line at 2300 K represents the point at which convection becomes inhibited at hotter temperatures.

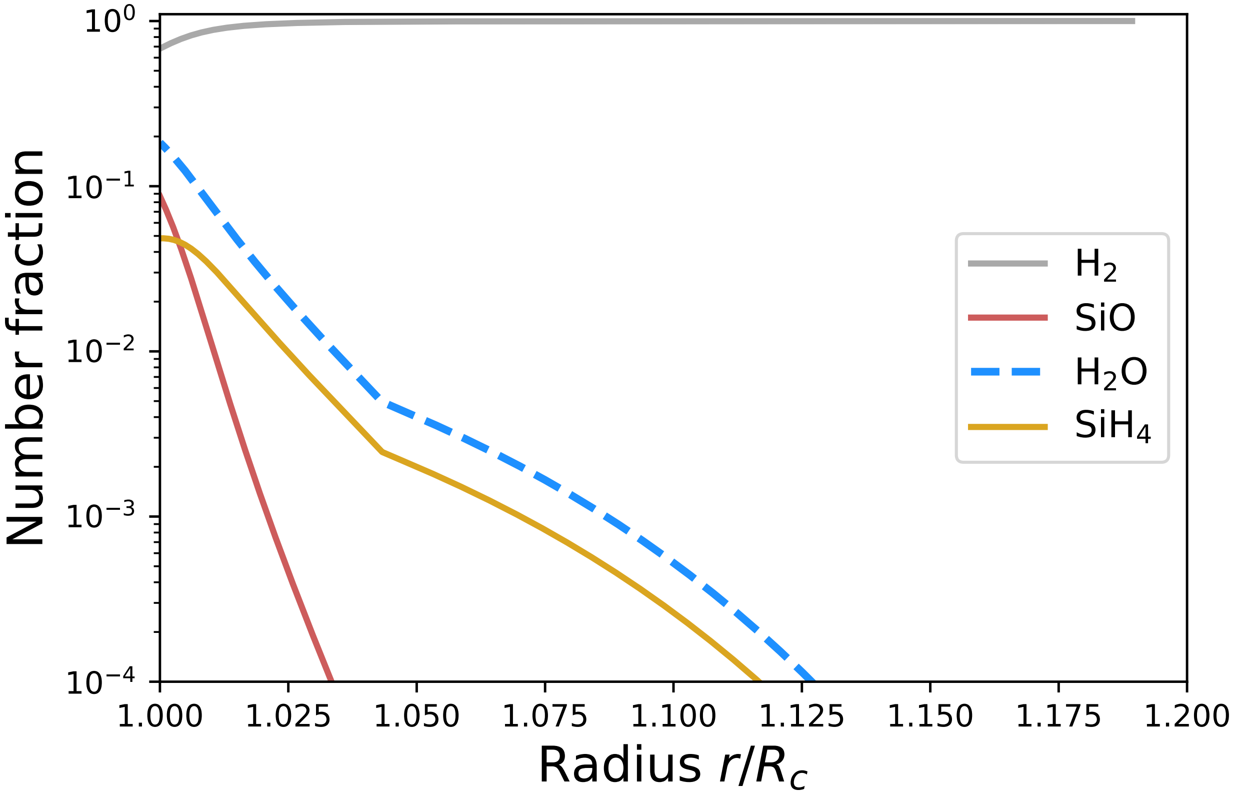

Figure 4.4: The number fraction of the species we consider as a function of radius, in core radii R_c. The line meanings remain the same as those in Fig. 4.1, as do the physical parameters: a 4 $M_\oplus$ planet with an equilibrium temperature of 1000 K, a base temperature of 5000 K, and an atmospheric hydrogen mass fraction of 2.5%. The number fraction of oxygen remains less than 10^{-4} and so is not shown. The atmosphere remains hydrogen dominated by number.

by mass, as shown in Fig. 4.5. Accordingly, the mean molecular weight, displayed in panel (c) of Fig. 4.2, remains near 2 m_p, that of H_2, throughout most of the atmosphere but rises sharply to larger than 8 m_p near the inner edge.

We show the number ratios of H_2O to SiO (in purple) and SiH_4 to SiO (in orange) in Fig. 4.6. Throughout most of the atmosphere, SiH_4 dominates over SiO, except at the very base for our chosen parameters, and H_2O dominates SiO in the entire atmosphere. This dominance of reduced species compared to oxidized ones is due to the presence of hydrogen gas as the background species. In contrast to inert background gases such as nitrogen, hydrogen is highly reactive and will act to reduce the outgassed magma ocean species, per Reactions 4.R2 and 4.R3. We find these

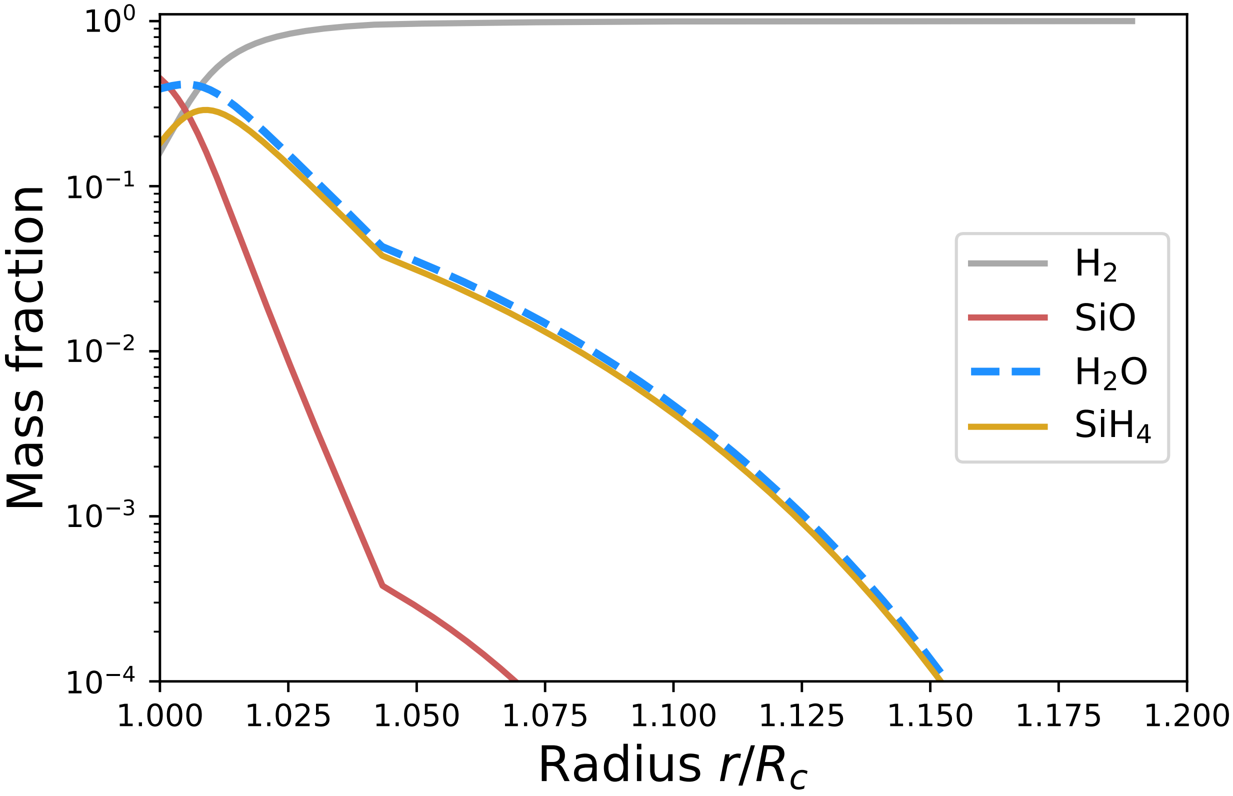

Figure 4.5: The mass fraction of the different species as a function of radius, in core radii R_c. The line meanings remain the same as those in Fig. 4.1, as do the physical parameters: a 4 $M_\oplus$ planet with an equilibrium temperature of 1000 K, a base temperature of 5000 K, and an atmospheric hydrogen mass fraction of 2.5%. The mass fraction of oxygen remains less than 10^{-4} and so is not shown. Near the base of the atmosphere, when $T \sim 5000$ K, the atmosphere becomes dominated in mass by water and SiO.

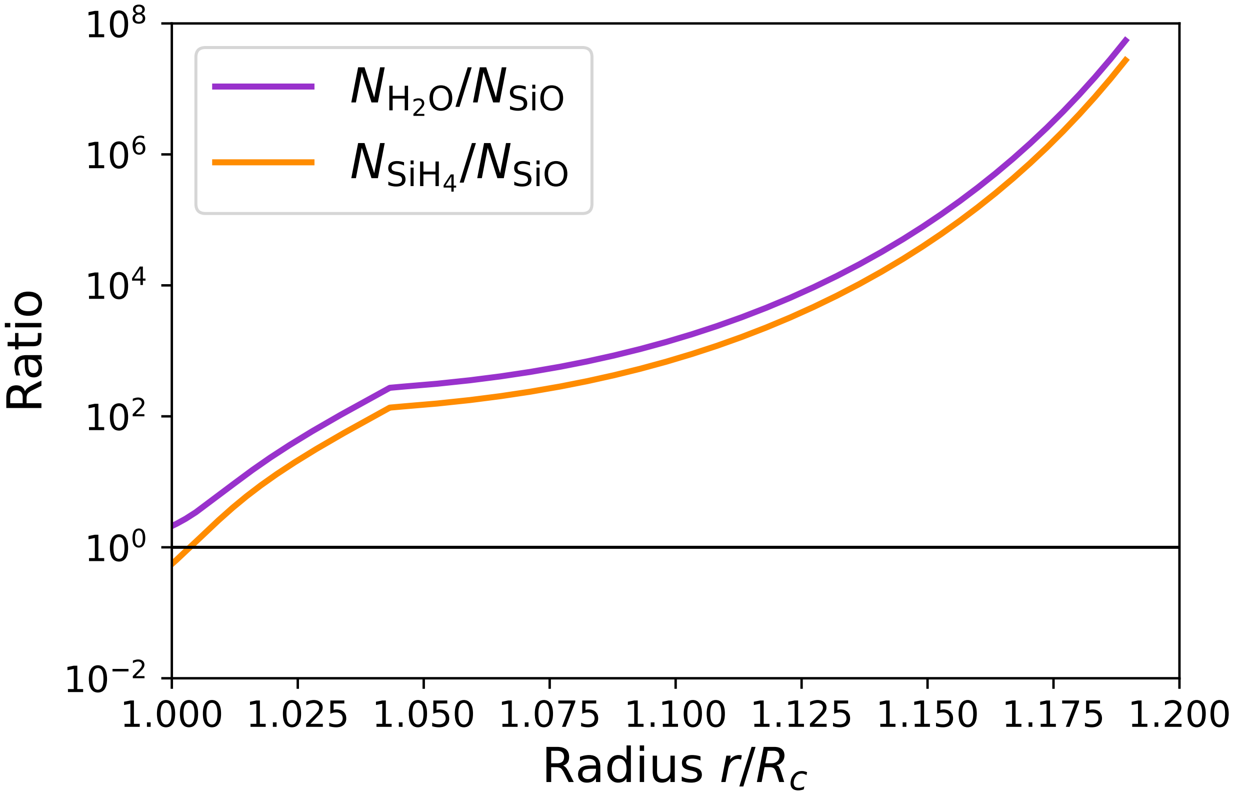

Figure 4.6: Number ratios of H_2O to SiO (in purple) and SiH_4 to SiO (in orange) as a function of radius, in core radii R_c. The model is the same one as shown in Fig. 4.1: a 4 $M_\oplus$ planet with an equilibrium temperature of 1000 K, a base temperature of 5000 K, and an atmospheric hydrogen mass fraction of 2.5%. The more reduced species, H_2O and SiH_4, dominate at nearly all points in the atmosphere, except near the hot base.

equations are typically driven toward the products at the temperatures and hydrogen gas fractions we consider, favoring the production of water and silane as the primary oxygen and silicon carriers in the atmosphere, respectively. This is in contrast to previous work on the atmosphere-interior interaction, such as Misener & Schlichting (2022) and Markham et al. (2022), which considered only SiO as the main carrier of the silicon and oxygen taken up from the underlying magma ocean.

Due to the numbers of silicon and oxygen atoms remaining in a fixed ratio, as described by Eq. 4.6, the partial pressures of water and silane are similar, and remain in lockstep as the temperatures increase. At sufficiently high temperatures deep in the atmosphere, SiH_4 production is no longer favored over SiO, and the abundance of SiO approaches and, for the conditions we consider, just surpasses that of SiH_4, as shown most clearly in Fig. 4.4. This behavior appears qualitatively similar to the CH_4–CO transition, extensively studied in the context of exoplanet observations (e.g. Burrows & Sharp, 1999; Visscher et al., 2010b; Fortney et al., 2020), though that transition occurs at much lower temperatures (see also Section 4.3.2 below).

Another notable result shown by Fig. 4.1 is that the overall abundance of silicon-bearing species is much higher than was previously found in Misener & Schlichting (2022). In that work, the authors used a vapor pressure formula appropriate for congruent evaporation of silicate magma into a vacuum taken from Visscher & Fegley (2013). This value for rock vapor is denoted in Fig. 4.1 with a red dotted line. However, Misener & Schlichting (2022) ignored the chemical effects of the non-inert background gas, H_2. When we account for the hydrogen chemistry, we find that the production of silane and water via Reaction 4.R3 draws out more SiO from the interior in order to continue to satisfy the relationship with $K_{\mathrm{eq,R3}}$, which is solely a function of temperature, in Equation 4.3. In order to maintain the equality of Equation 4.1, the oxygen partial pressure decreases to the values in Fig. 4.1. These values are much lower than the congruent ratio of 0.5 mole of O_2 for every mole of SiO.

Meanwhile, water is the most abundant product of magma-hydrogen interaction in our model, despite no water being present in the system initially. Water as a fundamental byproduct of silicate-hydrogen chemistry has previously been found in the context of sub-Neptunes (Schlichting & Young, 2022; Zilinskas et al., 2023) and early Earth (Young et al., 2023). This result shows that the presence of water in a sub-Neptune atmosphere does not necessarily indicate it formed with substantial ices, as has been suggested for some sub-Neptunes (e.g. Zeng et al., 2019; Venturini et al., 2020; Madhusudhan et al., 2020; Emsenhuber et al., 2021). We investigate factors that could alter the abundance of water in a sub-Neptune in Section 4.4.2.

The increased abundances of condensable species alters the overall atmospheric structure compared to the previous SiO-only model of Misener & Schlichting (2022). These increased abundances increase the value of the convective criterion, and therefore lower the temperature at which the atmosphere transitions from convective to radiative to $\sim$ 2300 K, as marked in Fig. 4.2 by the square, a temperature significantly lower than the typical transition temperature of $\sim$ 4000 K found in Misener & Schlichting (2022) for similar planet parameters.

A transition at lower temperatures means the atmosphere is non-convective for a larger range of temperatures in the deep interior of sub-Neptune planets, as can be seen in Fig. 4.2. The gas density at the transition point is also lower. Since the opacities and conductivities we expect are lower at lower densities, the temperature-pressure profiles are not as steep in the non-convective region as was found in Misener & Schlichting (2022). We compare the opacities we use in Fig. 4.7. We find that radiation and conduction are comparably efficient in transporting energy deep in sub-Neptune atmospheres, as found in Misener & Schlichting (2022), with conduction dominating as the temperatures and pressures increase. As discussed in Section 4.2.2.1, the opacity we use is extrapolated beyond the pressure regime fit in Freedman et al. (2014). However, it is apparent in Fig. 4.7 that the effective opacity is close to the conductive opacity in the interior, with the radiative opacity being larger. If the opacity were larger than the solar value we use ($\sim 10^3$ cm^2 g^{-1}), as might be expected in a hot, high-metallicity region, heat transport would be even more conduction-dominated than we find here, with little effect on the structure we obtain. We therefore conclude that our results are insensitive to the exact value of the opacity in the interior so long as it is higher than the conductive opacity. This is similar to the conclusion reached regarding opacities in Misener & Schlichting (2022). Fig. 4.7 also confirms that radiation dominates conduction at the outer radiative-convective boundary.

4.3.2 Outer atmosphere

We now examine the implications of this interior chemistry and structure on the outer atmosphere, the region accessible to spectroscopic observations. We model the outer atmosphere as isothermal at $T = T_{\rm eq}$, which for our model planet is set to 1000 K. In this region, the total pressure falls off exponentially. We assume chemical equilibrium is maintained throughout the atmosphere and that the vapor is saturated in SiO_2, with the SiO_2 activity always equal to one. In particular, by assuming chemical equilibrium we implicitly assume that the region we probe is below the homopause, above

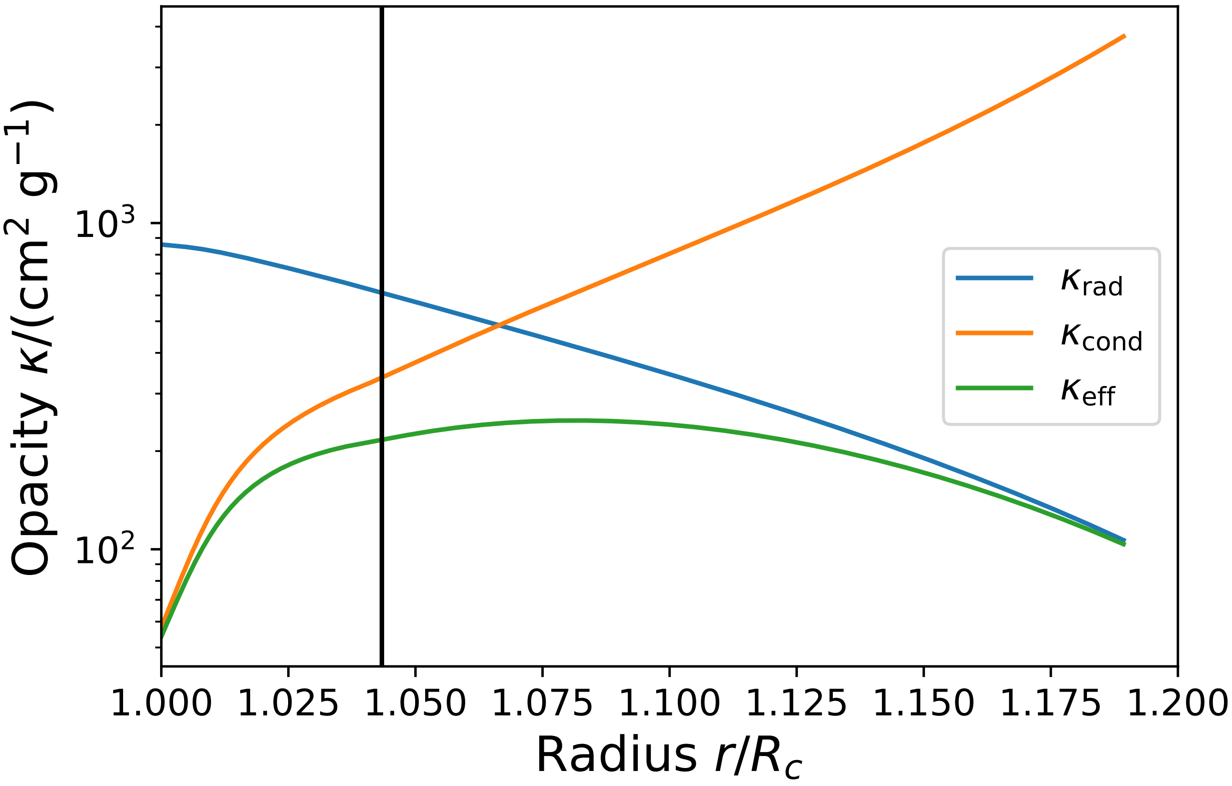

Figure 4.7: Comparison of the radiative opacity $\kappa_{\rm rad}$ (in blue), the conductive opacity $\kappa_{\rm cond}$ (in orange), and the effective opacity $\kappa_{\rm eff}$ (in green), as a function of radius, in core radii $R_{\rm c}$. The model is the same one as shown in Fig. 4.1: a 4 $M_\oplus$ planet with an equilibrium temperature of 1000 K, a base temperature of 5000 K, and an atmospheric hydrogen mass fraction of 2.5%. The black line represents the inner non-convective boundary. Radiation dominates at the outer radiative-convective boundary, as expected, while conduction becomes more important than radiation in the interior, though by a factor of 10 or less.

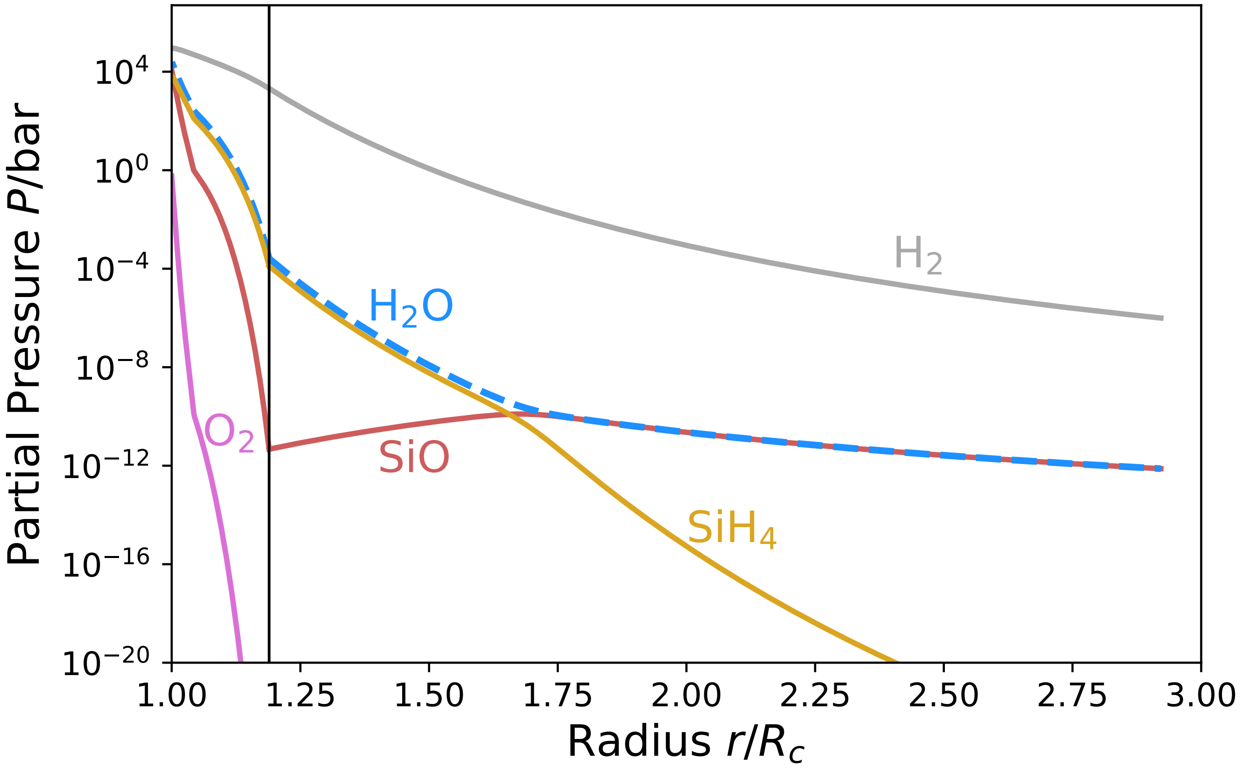

Figure 4.8: Partial pressures of the chemical species present in the atmosphere as a function of radius, in core radii R_c, through the entire atmosphere out to $P = 10^{-6}$ bar ($r \sim 3R_c$), including the outer radiative region. The profile is for a 4 $M_\oplus$ planet with an equilibrium temperature of 1000 K, a base temperature of 5000 K, and an atmospheric hydrogen mass fraction of 2.5‰. The species we consider are H_2 (gray), H_2O (blue dashed), SiH_4 (yellow), SiO (red solid), and O_2 (pink). The outer vertical black line at 1.19 R_c represents the outer radiative convective boundary.

which each species follows its own scale height, and that mixing is always faster than the chemical kinetic timescale, i.e., the reactions we consider are never quenched. In Fig. 4.8 we show the partial pressures of the chemical species we consider as a function of planet radius over the whole atmosphere. The interior region, $r < R_{\rm rcb} \approx 1.19 R_{\rm c}$, contains the same abundances presented in Fig. 4.1.

Fig. 4.8 shows sharp kinks in the abundances of the species we consider as the temperature ceases declining. Intriguingly, not only do the abundances change with altitude in the isothermal region, but the relative proportions of the different species do as well. The changes in relative abundances is shown more clearly in Fig. 4.9, which displays the number fraction of each species as a function of the total pressure in the isothermal region only. This total pressure is very nearly the pressure of H_2, as evidenced by its number fraction being nearly 1 in this region. The relative abundance of SiO increases throughout the isothermal region, while the relative abundance of SiH_4 decreases. The two become equal near 10^{-1} bar: at lower pressures (i.e. higher altitudes) than this, SiO is the dominant silicon-bearing species, rather than SiH_4.

The increasing dominance of SiO over SiH_4 can be understood by examining Eq. 4.3. At constant temperature, $K_{\rm eq,R3}$ is constant. As $P_{\rm H_2}$ decreases with altitude, the partial pressure of SiO must increase to maintain the equilibrium. In other words, the reaction no longer so strongly favors the production of SiH_4. Due to the fixed Si:O atomic number ratio, Eq. 4.6, the abundance of water first decreases with decreasing pressure, tied to the abundance of SiH_4, then increases in lockstep with SiO once the latter becomes dominant.

This transition from SiH_4 to SiO as the dominant silicon-bearing species occurs at an observationally relevant pressure for the planet parameters studied here. Therefore, the relative SiO/SiH_4 abundance could serve as a probe of the overall chemistry of the interior and atmosphere, similarly to the well-studied CO–CH_4 transition, which occurs due to a similar reaction (e.g. Burrows & Sharp, 1999; Visscher et al., 2010b; Fortney et al., 2020) . Future work will elucidate how this transition point varies across the sub-Neptune parameter space and in time, as well as with more complex interior compositions. It will also further constrain the absolute abundances we expect.

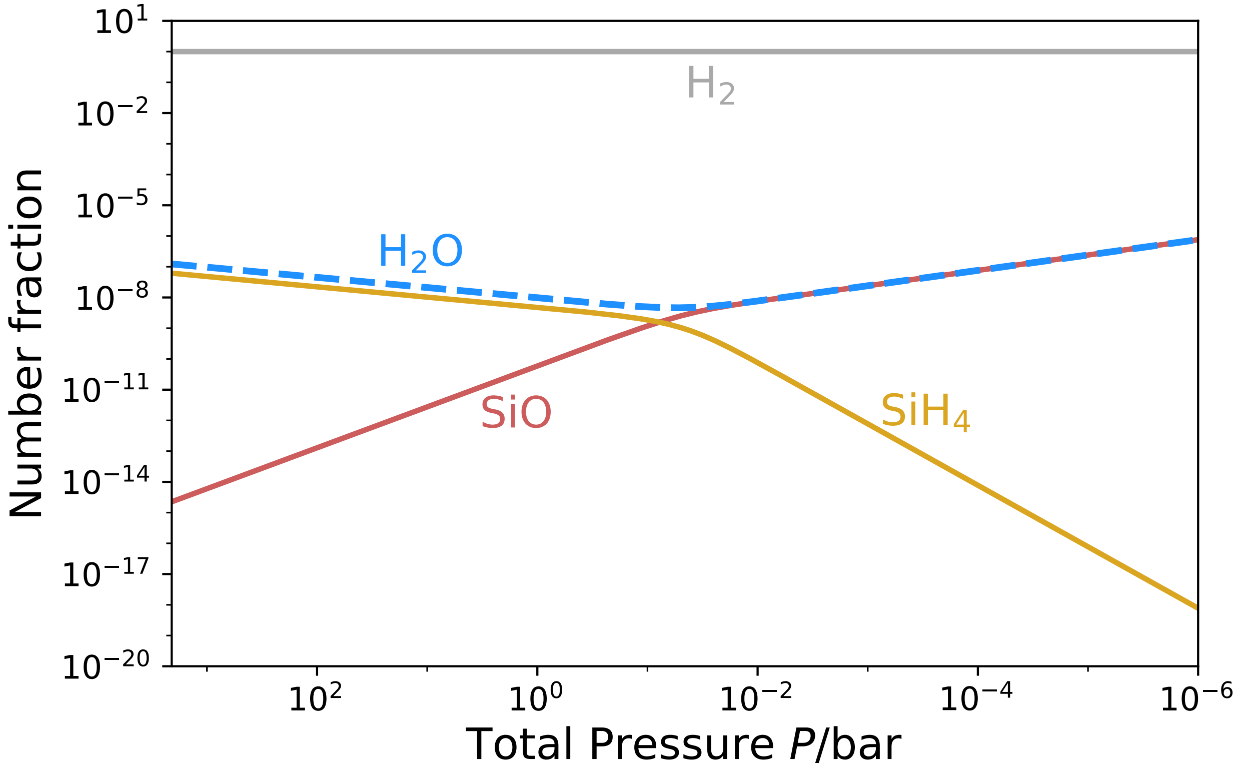

Figure 4.9: Number fraction of each chemical species as a function of total pressure in the outer isothermal region. The temperature is fixed at 1000 K. The number fraction of O_2 remains less than 10^{-20} and so is not shown. SiO becomes the dominant silicon-bearing species over SiH_4 at $\sim 10^{-1}$ bar.

We note that our simple model assumes the initial atmosphere comprises pure hydrogen, such that all heavier species in our results are due to outgassing from the magma interior. This results in elemental abundances in the upper atmosphere which are sub-solar, and which do not match solar ratios. Specifically, the solar abundance of silicon is $3.3 \times 10^{-5} N_{\mathrm{H}}$, and that of oxygen is $5.7 \times 10^{-4} N_{\mathrm{H}}$, where N_{H} is the hydrogen abundance (Lodders, 2021), implying an oxygen-to-silicon ratio of $N_{\mathrm{O}}/N_{\mathrm{Si}} = 17.3$. Our abundances and oxygen-to-silicon ratio are lower than these values throughout the isothermal region. We further discuss the effects of different compositions of core and atmosphere on our results in Section 4.4.2.

4.4 Discussion and Future Directions

In Sec. 4.3, we demonstrated that silane and water are expected to be byproducts of silicate-hydrogen interactions in sub-Neptunes with underlying magma oceans. In this section, we discuss the observability of these species with current and future facilities. We then discuss how other species beyond the simplified chemical network we consider here could alter the atmospheric profiles we obtain, how these new profiles could alter the evolution in time of these atmospheres, and how our assumptions about opacities could impact these results.

4.4.1 Observability

The two most abundant species in our model besides hydrogen are water and silane. Water vapor has numerous strong absorption bands in the infrared, which JWST is well-suited to exploit. Due to its potential as a tracer of planet formation and its importance for life, water vapor has been extensively searched for in the atmospheres of sub-Neptunes in previous campaigns with Hubble and JWST. Water features have been detected in Hubble observations of sub-Neptunes (Benneke et al., 2019a,b) and in the atmospheres of giant exoplanets using JWST (e.g. Alderson et al., 2023; Rustamkulov et al., 2023), with observations of smaller planets underway. Our results show that detections of water vapor in sub-Neptune atmospheres is not necessarily diagnostic of formation beyond the snow-line. Instead, it could be produced endogenously via magma-hydrogen interactions.

Silane also has features in the mid-infrared, with the largest cross-section at $\sim 4.5\ \mu$m (Owens et al., 2017) according to the ExoMol database (Tennyson et al., 2016). This feature is squarely within the wavelength capabilities of JWST's NIRSpec and PRISM instruments, as evidenced by the detections of features at similar wavelengths, such as CO_2 in the hot Jupiter WASP-39 b (JWST Transiting Exoplanet Community Early Release Science Team et al., 2023). Silane has previously been considered in small exoplanet atmospheres due to its potential as a biosignature photosynthetic product in reducing conditions, though it was deemed unlikely to occur (Seager et al., 2013). In the case studied in this work, silane would instead be a product of magma-atmosphere interactions.

We assume throughout this work that the condensate, in our case liquid SiO_2, is present in small enough quantities that it does not affect the atmospheric properties, such as, e.g., its opacity or heat capacity. However, some liquid must remain suspended in the gas. Lofting of condensates could alter the atmospheric profile, due to the liquid's larger specific heat (Graham et al., 2021). Such condensate retention would also by definition produce clouds, which we do not explicitly model but which may have dramatic effects on the observability of these features. Therefore, such lofting should be investigated further, despite its reliance on complex microphysical processes. Possibly helpful analogs include more massive bodies such as hot Jupiters and brown dwarfs, in which silicate clouds have been previously studied (e.g. Burningham et al., 2021; Gao & Powell, 2021).

4.4.2 Other species and compositions

We considered a chemical network including three reactions, in order to demonstrate the potential importance of these reactions on the atmospheric structure. Chemical networks involving more species and reactions have been employed in the study of sub-Neptune atmospheres in general, as well as magma-atmosphere interactions in various planetary contexts (e.g. Moses et al., 2013; Schlichting & Young, 2022; Zilinskas et al., 2023), though these works did not couple the products of silicate-hydrogen reactions with atmospheric structure in the sub-Neptune regime as we have here. In this section, we highlight possible extensions of the chemistry we consider that could influence the structure and evolution of sub-Neptune planets.

First, we considered an interior composed of pure SiO_2. However, including a more realistic, Earth-like composition would alter the products outgassed into the atmosphere. For example, if the rocky interior were approximated as pure $MgSiO_3$ instead, we would expect the evaporation products to be atomic Mg, SiO, and O_2, in equal molar proportions. This increase in the proportion of oxygen to silicon would likely lead to increased water production compared to our model. However, experimental results indicate that silicon may preferentially dissolve into H_2 compared to magnesium (Shinozaki et al., 2013, 2016), potentially affecting, e.g., the Mg/Si ratio we would predict. We also do not consider that more complex chemistry in the melts will lower the activities of the relevant melt species and thus affect the equilibrium vapor pressures of SiO and O_2, which may in turn alter the physics of convection inhibition. This example illustrates that interior composition can alter the atmospheric composition of sub-Neptunes, but that such interactions may be complex.

We do not expect an ice layer to form at the base of the atmosphere. Extrapolations indicate water and hydrogen are likely miscible at these temperatures and pressures, though experiments are needed to confirm this (Bailey & Stevenson, 2021). Additionally, solid phases of water are not stable at the temperatures and pressures at the base of the atmosphere (e.g. Madhusudhan et al., 2020). In fact, the temperatures and pressures are above the critical temperature and pressure of pure water, though the bulk behavior depends on the properties of the hydrogen-water-silane mixture, which is poorly constrained, not those of water alone (Markham et al., 2022). The critical temperature of the silicate interior is likely higher than the 5000 K base temperature we assume (e.g Xiao & Stixrude, 2018), indicating the overall mixture may not be super-critical, but more modeling of such mixtures is needed. If the mixture is super-critical, condensation of silicate vapor can no longer occur, and so convection would no longer be inhibited in the super-critical region of the envelope (Markham et al., 2022; Pierrehumbert, 2023).

While not yet super-critical, the incompressibility of the melt and gasses at high pressures can lead to changes to the Gibbs free energies of formation not captured in our equilibrium model, which assumes ideal gasses and melt behavior. The equation of state of silicate melt is relatively well-constrained (e.g. De Koker & Stixrude, 2009), allowing calculation of its molar volume as a function of pressure and therefore its change in chemical potential (e.g. Schlichting & Young, 2022). We find the change in chemical potential of the melt at the base of our atmosphere to be approximately 230 kJ/mol, enough to significantly alter the equilibrium state. However, this change in chemical potential may be compensated by non-ideal behavior in the product gaseous species on the other side of Reaction 4.R1. Specifically, an increase in the fugacity coefficient of SiO of approximately 40 to 100 at the conditions of the base of the atmosphere ($P \sim 10^5$ bar, $T \sim 5000$ K) would balance the PV effects on the chemical potential of the melt. Unfortunately, the equations of state, and thus the fugacities, of the silicon vapor species we consider are not well-constrained.

The observed behavior of other species, such as water vapor, indicate that such fugacities are plausible at the pressure conditions we consider (e.g. Otsuka & Karato, 2011). However, their precise determination is beyond the scope of this work.

We also ignore ingassing reactions, such as the solubility of hydrogen and water into the interior. Such reactions may be important in driving the interior composition and long-term atmospheric evolution of sub-Neptunes and super-Earths, although the relevant solubilities are highly uncertain (e.g. Chachan & Stevenson, 2018; Olson & Sharp, 2019; Dorn & Lichtenberg, 2021; Schlichting & Young, 2022).

Finally, we assume that the entire atmosphere, i.e. a given mass of hydrogen gas, has chemically equilibrated with the underlying magma ocean, similar to previous work on magma-hydrogen interactions (e.g. Schlichting & Young, 2022; Markham et al., 2022; Zilinskas et al., 2023). This chemical processing leads to the sub-solar abundances we predict in the outer atmosphere: most of the oxygen and silicon is segregated to the deep atmosphere where it is more thermodynamically favorable. The result is an atmosphere that is overall strongly super-solar in e.g. oxygen abundance – O makes up 2 percent of the total atmosphere by number – but with strong variations with depth. The likelihood of reaching full chemical equilibrium depends on the mixing efficiency in the atmosphere during and after formation. If there is sufficient transport between atmospheric layers over the age of the planet, then we would expect chemical equilibrium to be achieved throughout the whole planet system, as modeled here. Conversely, higher elemental abundances of Si and O in the outer atmosphere than predicted here could indicate that chemical equilibrium between the outer and inner layers of the planet has not been reached, and therefore that the interior and atmosphere are poorly coupled chemically (e.g. Zilinskas et al., 2023). Enhancement in these species could come from a higher metallicity in the initial accreted gas, although some of these enhanced metals would have condensed into refractory materials. Another source could be the ablation of accreting solid material; however, ablation is thought to occur in deeper regions than those probed by spectroscopic observations (e.g. Brouwers & Ormel, 2020).

4.4.3 Time evolution

Atmospheric loss processes are expected to affect a significant portion of sub-Neptunes, so the interplay between such processes and any evolution of the atmospheric composition should be considered carefully. We find that compositional gradients at depth tend to shrink the overall planet radius, if everything else is kept constant. A smaller radius tends to inhibit atmospheric loss, as the atmosphere must be removed from deeper within the gravitational potential well. However, atmospheric accretion dictates that planets' initial radiative-convective boundaries are close to the Bondi radius (e.g. Ginzburg et al., 2016) and deep non-convective layers slow thermal contraction over time (Misener & Schlichting, 2022). Therefore, whether the overall effect of the compositional gradients examined here inhibits or furthers atmospheric loss remains to be determined, highlighting the need for fully self-consistent accretion and loss models.

Another possibility is that hydrogen could be preferentially lost, increasing the molecular weight of the atmosphere (e.g. Malsky et al., 2023). The two major loss processes thought to shape exoplanet demographics, core-powered mass loss and photoevaporation, are hydrodynamic. Their strong winds are sufficient to drag along heavier species such as those we find could be present in this study (e.g. Misener & Schlichting, 2021). However, due to the gradient in molecular weight, a wind escaping from the top of the atmosphere is relatively less enriched in outgassed species than the mean overall atmosphere, which could produce effective fractionation. Additionally, as hydrogen is depleted, the chemistry of the atmosphere could change, with the magma-hydrogen interaction producing more oxidized species (e.g. Zilinskas et al., 2023). A model which simultaneously evolves the thermal state, atmospheric composition, and atmospheric mass could investigate these potential interplays further.

4.5 Conclusions

We analyze the chemical equilibrium between hydrogen gas and species vaporized from the surface of a silicate magma ocean, a condition likely to be present in the depths of young sub-Neptune planets. We find that SiO and O_2 react with hydrogen gas to produce significant amounts of silane (SiH_4) and water vapor (H_2O). The resulting depletion of SiO_2 draws more magma ocean products into the atmosphere, greatly increasing the atmosphere's silicon content compared to a model which does not account for the reducing conditions of the atmosphere. The amounts and proportions of these products likely vary depending on the chemical state of the interior. This implies that the atmospheric compositions of planets with magma oceans are a window into their interior composition, a promising prospect since such atmospheric abundances are observable with current and future telescopes. The chemical products of magma-atmosphere interaction in turn alter the atmospheric structure, inhibiting convection in the interior to a larger extent than previously found. These results imply that the presence of a magma ocean must be considered in order to understand the chemical abundances and overall atmospheric mass fractions of sub-Neptune planets.

Acknowledgements

In this work we use the NUMPY (Harris et al., 2020), MATPLOTLIB (Hunter, 2007), and SCIPY (Virtanen et al., 2020) packages. This research has been supported in part by the Alfred P. Sloan Foundation under grant G202114194 as part of the AEThER collaboration and by NASA under grant number 80NSSC21K0392 issued through the Exoplanet Research Program.

4.6 Appendices

4.6.1 Equilibrium constant values

In Figures 4.10, 4.11, and 4.12, we plot the equilibrium constants we use in this work as functions of temperature. As described in Section 4.2.1, all values are calculated from the Gibbs free energies in NIST.

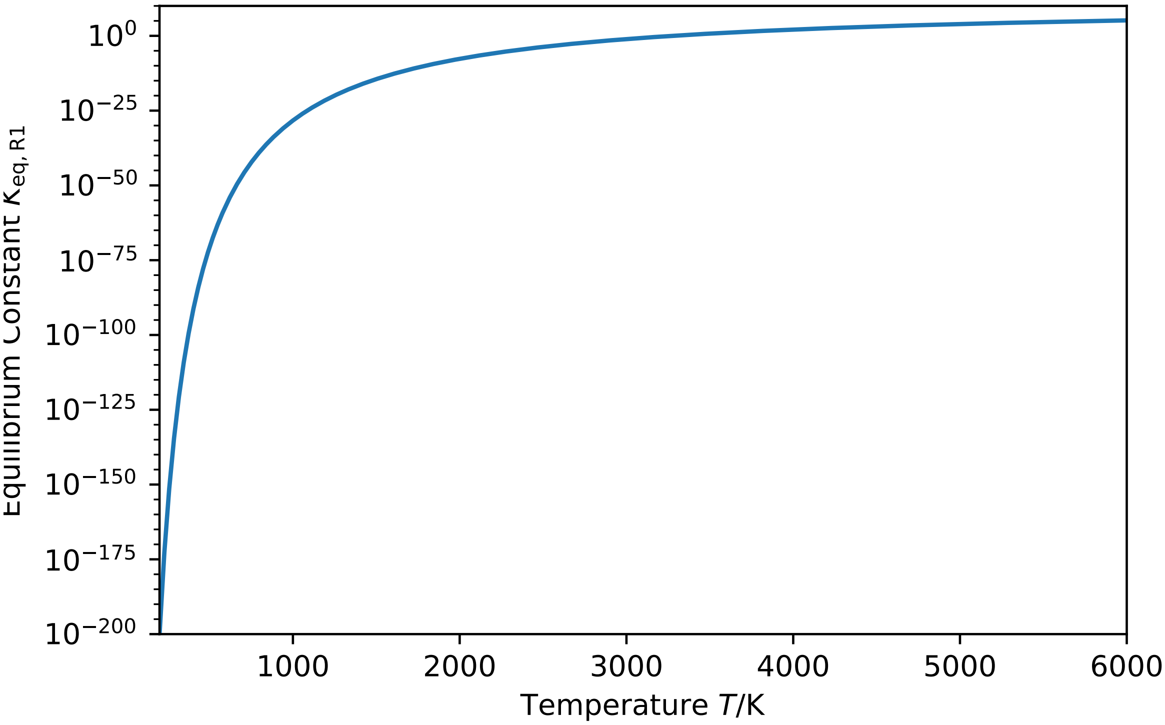

Figure 4.10: The equilibrium constant describing reaction 4.R1, as defined in Eq. 4.1, as a function of temperature.

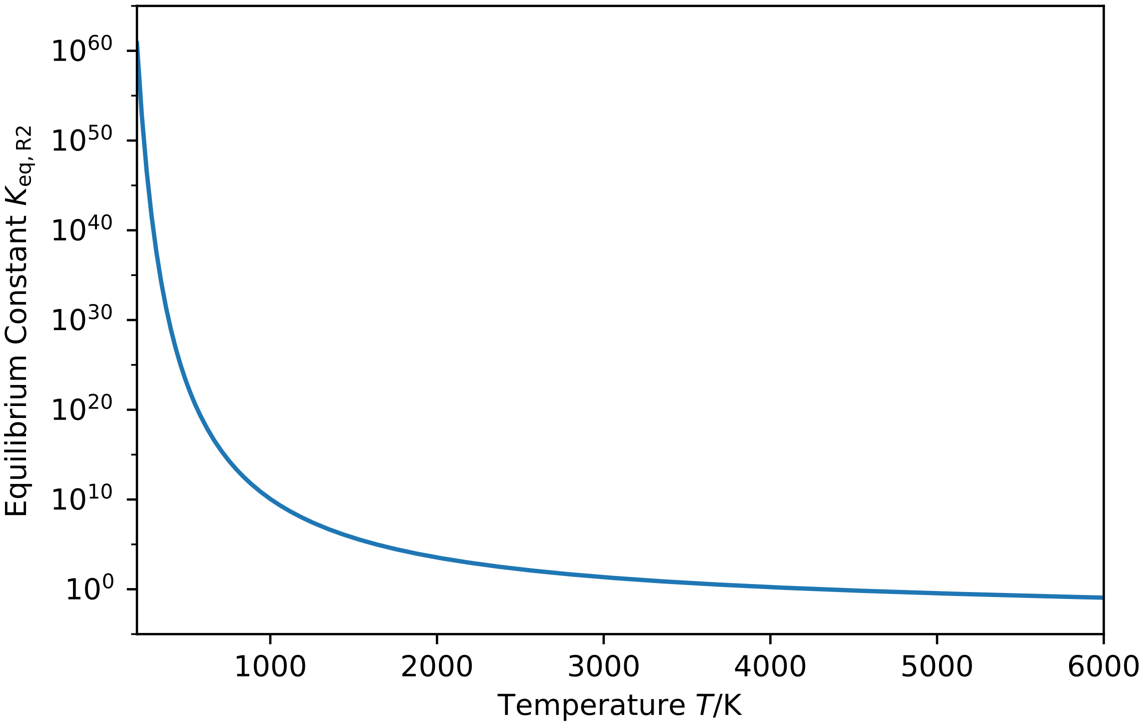

Figure 4.11: The equilibrium constant describing reaction 4.R2, as defined in Eq. 4.2, as a function of temperature.

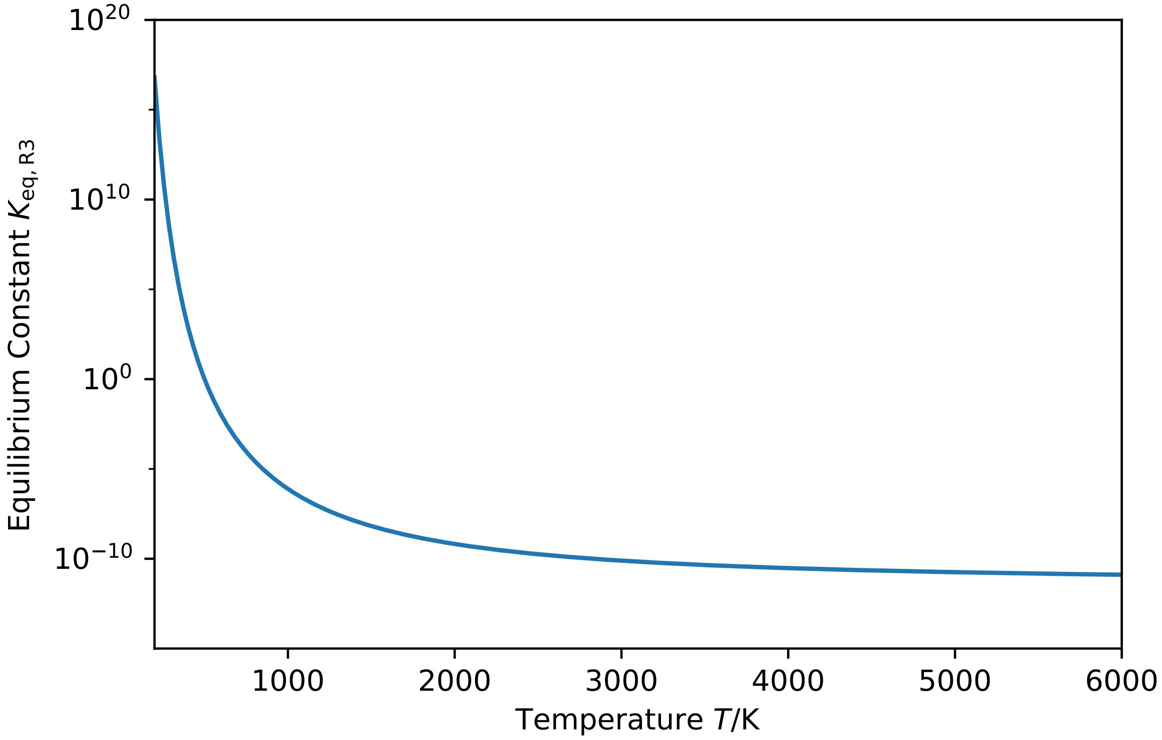

Figure 4.12: The equilibrium constant describing reaction 4.R3, as defined in Eq. 4.3, as a function of temperature.

4.6.2 Derivation of partial pressures

As stated in Section 4.2.1, Eqs. 4.1, 4.2, 4.3, and 4.6, along with the total pressure P and temperature T, are sufficient to solve for the partial pressures of all components of the atmosphere at a given level, specifically $P_{\mathrm{H_2}}$, $P_{\mathrm{H_2O}}$, P_{SiO}, $P_{\mathrm{SiH_4}}$, and $P_{\mathrm{O_2}}$. In practice, we use the following method, though many alternative derivations are possible in principle.

We begin by assuming an oxygen partial pressure, $P_{\mathrm{O_2}}$. We choose to guess this value because it varies by many orders of magnitude over a typical atmospheric profile, the most of any of the unknowns in our problem. Therefore, small changes in the other inferred partial pressures lead to large changes in the inferred $P_{\mathrm{O_2}}$, making it more amenable to solve for via numerical techniques than the other values, which vary slowly and therefore lead to failures to converge. Given the assumed $P_{\mathrm{O_2}}$ and the temperature, which yields values for all three equilibrium constants, it is easy to use Eq. 4.1 to solve for the partial pressure of SiO:

$$P_{\mathrm{SiO}} = K_{\mathrm{eq,R1}}/P_{\mathrm{O_2}}^{1/2}. \tag{4.18}$$

Similarly, we can invert Eq. 4.2 to solve for the partial pressure of water as a function of the partial pressure of H_2, which is as yet unknown:

$$P_{\mathrm{H_2O}} = K_{\mathrm{eq,R2}} P_{\mathrm{H_2}} P_{\mathrm{O_2}}^{1/2}. \tag{4.19}$$

Inserting Eq. 4.19 into Eq. 4.3, we can solve for $P_{\mathrm{SiH_4}}$:

$$P_{\mathrm{SiH_4}} = \frac{K_{\mathrm{eq,R3}} P_{\mathrm{SiO}} P_{\mathrm{H_2}}^2}{K_{\mathrm{eq,R2}} P_{\mathrm{O_2}}^{1/2}}, \tag{4.20}$$

which also depends on the unknown $P_{\mathrm{H_2}}$. We can leverage the definition of P as the sum of all partial pressures to express $P_{\mathrm{H_2}}$ in terms of the other species:

$$P_{\mathrm{H_2}} = P - P_{\mathrm{H_2O}} - P_{\mathrm{SiO}} - P_{\mathrm{O_2}} - P_{\mathrm{SiH_4}}. \tag{4.21}$$

Inserting Eq. 4.19 into this equation and collecting terms of $P_{\mathrm{H_2}}$ allows us to solve for $P_{\mathrm{H_2}}$ as a function of known values and $P_{\mathrm{SiH_4}}$:

$$P_{\mathrm{H_2}} = \frac{P - P_{\mathrm{SiO}} - P_{\mathrm{O_2}} - P_{\mathrm{SiH_4}}}{1 + K_{\mathrm{eq,R2}} P_{\mathrm{O_2}}^{1/2}}. \tag{4.22}$$

Such an expression allows us to substitute P_{H_2} in Eq. 4.20, eliminating all other unknown variables. This yields a simple quadratic equation:

$$P_{\mathrm{SiH}_4} = \alpha(\beta - P_{\mathrm{SiH}_4})^2 \tag{4.23}$$

where

$$\alpha \equiv \frac{K_{\mathrm{eq,R3}} P_{\mathrm{SiO}}}{K_{\mathrm{eq,R2}} P_{\mathrm{O}_2}^{1/2} \left(1 + K_{\mathrm{eq,R2}} P_{\mathrm{O}_2}^{1/2}\right)^2} \tag{4.24}$$

and

$$\beta \equiv P - P_{\mathrm{SiO}} - P_{\mathrm{O}_2} \tag{4.25}$$

are functions of known quantities defined for simplicity. Eq. 4.23 can be solved using the quadratic formula:

$$P_{\mathrm{SiH}_4} = \frac{2\alpha\beta + 1 \pm \sqrt{4\alpha\beta + 1}}{2\alpha}. \tag{4.26}$$

Mathematically, this yields two solutions; however, in all cases only the negative branch is physically reasonable (i.e., yields $P_i > 0$ for all species). Once P_{SiH_4} is known, P_{H_2} can be solved via Eq. 4.22, and $P_{\mathrm{H}_2\mathrm{O}}$ can be solved via Eq. 4.19. This yields a full set of partial pressures, which correctly sum to the total pressure, and conform to chemical equilibrium at a given temperature, for a guessed P_{O_2}. The only constraint not yet used is the number of atoms constraint, Eq. 4.6. We now calculate the "atomic partial pressures" using Eqs. 4.4 and 4.5, and calculate the difference $\sum P_{\mathrm{O}} - \sum P_{\mathrm{Si}}$. This difference will vary as a function of the input P_{O_2}, with one unique solution where the difference is zero. We solve for this P_{O_2} which balances the reactions correctly numerically for each layer, using the `fsolve` function of the SCIPY.OPTIMIZE package (Virtanen et al., 2020). In practice, since we solve the atmospheric structure layer-by-layer in small steps, the previous value of P_{O_2} provides a good starting guess for the value in the next layer deeper, which we use to increase computational speed compared to a fully naive guess.

4.6.3 Derivation of multi-species convection criterion

As discussed in Section 4.2.2, in this work we derive a multi-species convection criterion, which turns out to be the sum of the individual convection criteria of each species, $\sum_i c_i \geq 1$, where c_i

is given by Eq. 4.12. It is non-trivial that the overall convection criterion is the sum of those of each species, so we demonstrate that here. For demonstration purposes, we consider the case of two condensables, but the argument applies to n condensables equally well. Let us define a three component atmosphere, composed of a dry component with mass mixing ratio q_d and molecular weight μ_d, and two condensable species with mass mixing ratios q_1 and q_2 and molecular weights μ_1 and μ_2 respectively. By definition, $q_\mathrm{d} + q_1 + q_2 = 1$. Meanwhile, the overall mean molecular weight μ is given by

$$\mu = \frac{\mu_\mathrm{d}\mu_1\mu_2}{\mu_1\mu_2 + (\mu_\mathrm{d}\mu_2 - \mu_1\mu_2)q_1 + (\mu_\mathrm{d}\mu_1 - \mu_1\mu_2)q_2}. \tag{4.27}$$

For convection to be inhibited, the density gradient in the environment must be steeper than that of a parcel moved adiabatically (e.g. Leconte et al., 2017):

$$\left(\frac{\partial \ln T}{\partial \ln P} - \frac{\partial \ln \mu}{\partial \ln P}\right)_\mathrm{env} > \left(\frac{\partial \ln T}{\partial \ln P} - \frac{\partial \ln \mu}{\partial \ln P}\right)_\mathrm{ad}. \tag{4.28}$$

Therefore, to assess whether convection operates in a regime with multiple species changing in abundance, we must compute the change in molecular weight with pressure $\partial \ln \mu / \partial \ln P$. The molecular weight changes with pressure for two reasons: due to changes in the abundance of species 1, or due to changes in the abundance of species 2. Quantitatively, we can express this as a sum of partial derivatives with the mixing ratio of the other species held constant:

$$\frac{\partial \ln \mu}{\partial \ln P} = \left.\frac{\partial \ln \mu}{\partial \ln P}\right|_{q_2} (q_1) + \left.\frac{\partial \ln \mu}{\partial \ln P}\right|_{q_1} (q_2). \tag{4.29}$$

Here the first term is the change in molecular weight due to changing q_1, with q_2 held fixed, and the second term is the change in molecular weight due to changing q_2, with q_1 held fixed.

Examining the first term in Eq. 4.29, it can be expanded into the product of two partial derivatives

$$\left.\frac{\partial \ln \mu}{\partial \ln P}\right|_{q_2} = \left.\frac{\partial \ln \mu}{\partial \ln q_1}\right|_{q_2} \left.\frac{\partial \ln q_1}{\partial \ln P}\right|_{q_2}. \tag{4.30}$$

The first term in the product can be computed using the definition of μ in Eq. 4.27 and simplifies to

$$\left.\frac{\partial \ln \mu}{\partial \ln q_1}\right|_{q_2} = \mu q_1 \left(\frac{1}{\mu_\mathrm{d}} - \frac{1}{\mu_1}\right). \tag{4.31}$$

Meanwhile, the second term in Eq. 4.30 can be expressed as the sum of two terms: the change in condensable mass mixing ratio as the total pressure changes at fixed temperature, and the change in condensable mass mixing ratio as the temperature changes due to the T–P relation:

$$\left.\frac{\partial \ln q_1}{\partial \ln P}\right|_{q_2} = \left.\frac{\partial \ln q_1}{\partial \ln P}\right|_{T,q_2} + \left.\frac{\partial \ln q_1}{\partial \ln T}\right|_{P,q_2} \frac{\partial \ln T}{\partial \ln P} \tag{4.32}$$

The first term in this equation can be solved using the definition of the mass mixing ratio, $q_1 = \mu_1 P_1/(\mu P)$, and reduces to

$$\left.\frac{\partial \ln q_1}{\partial \ln P}\right|_{T,q_2} = -\frac{\mu_\mathrm{d}}{\mu}. \tag{4.33}$$

We note that this term is negative, because increasing the total pressure without changing the temperature leaves the partial pressure of the condensable unchanged, therefore decreasing the mass mixing ratio.

The derivative of q_1 with respect to T, which appears in the second term of Eq. 4.32, can also be solved by inserting the definition of the mass mixing ratio, but it simplifies considerably less and introduces cross-terms dependent on q_2:

$$\left.\frac{\partial \ln q_1}{\partial \ln T}\right|_{P,q_2} = \left[\frac{\mu_\mathrm{d}}{\mu} + q_2\left(1 - \frac{\mu_\mathrm{d}}{\mu_2}\right)\right]\frac{\partial \ln P_1}{\partial \ln T} - q_2\left(1 - \frac{\mu_\mathrm{d}}{\mu_2}\right)\frac{\partial \ln P_2}{\partial \ln T}. \tag{4.34}$$

Eqs. 4.33 and 4.34 can then be inserted into Eq. 4.32, which can be substituted along with Eq. 4.31 into Eq. 4.30. After some algebraic manipulation, this substitution leads to an expression for the overall gradient as a function of q_1 with q_2 fixed:

$$\begin{aligned}\left.\frac{\partial \ln \mu}{\partial \ln P}\right|_{q_2} &= q_1\left(1 - \frac{\mu_\mathrm{d}}{\mu_1}\right)\left[\frac{\partial \ln P_1}{\partial \ln T}\frac{\partial \ln T}{\partial \ln P} - 1\right] \\ &\quad + \frac{\mu}{\mu_\mathrm{d}} q_1 q_2 (1 - \frac{\mu_\mathrm{d}}{\mu_1})(1 - \frac{\mu_\mathrm{d}}{\mu_2})\frac{\partial \ln T}{\partial \ln P}.\end{aligned} \tag{4.35}$$

As q_1 and q_2 are completely symmetrical in these equations, the expression for $\partial \ln \mu/\partial \ln P\ |_{q_1}$ can be obtained by swapping the 1 and 2 subscripts in Eq. 4.35. Upon adding these equations together per Eq. 4.29, it is immediately clear that the second terms cancel, leaving

$$\begin{aligned}\frac{\partial \ln \mu}{\partial \ln P} &= q_1\left(1 - \frac{\mu_\mathrm{d}}{\mu_1}\right)\left[\frac{\partial \ln P_1}{\partial \ln T}\frac{\partial \ln T}{\partial \ln P} - 1\right] \\ &+ q_2\left(1 - \frac{\mu_\mathrm{d}}{\mu_2}\right)\left[\frac{\partial \ln P_2}{\partial \ln T}\frac{\partial \ln T}{\partial \ln P} - 1\right] \\ &= \alpha_1\gamma_1\frac{\partial \ln T}{\partial \ln P} - \alpha_1(1 - \varpi_1 q_1 - \varpi_2 q_2) \\ &+ \alpha_2\gamma_2\frac{\partial \ln T}{\partial \ln P} - \alpha_2(1 - \varpi_1 q_1 - \varpi_2 q_2)\end{aligned} \tag{4.36}$$

using the notation of Leconte et al. (2017), where

$$\alpha_i \equiv \mu q_i\left(\frac{1}{\mu_\mathrm{d}} - \frac{1}{\mu_i}\right), \tag{4.37}$$

$$\gamma_i \equiv \frac{\mu_\mathrm{d}}{\mu}\frac{\partial \ln P_i}{\partial \ln T}, \tag{4.38}$$

and

$$\varpi_i \equiv 1 - \frac{\mu_\mathrm{d}}{\mu_i}. \tag{4.39}$$

Finally, we can insert Eq. 4.36 into Eq. 4.28 to obtain the convection criterion. We note that the second and fourth terms of Eq. 4.36 will be the same on either side of the inequality in Eq. 4.28 and therefore cancel, eliminating all further cross terms. This leaves the inequality as

$$\left[\left(\frac{\partial \ln T}{\partial \ln P}\right)_\mathrm{env} - \left(\frac{\partial \ln T}{\partial \ln P}\right)_\mathrm{ad}\right](1 - \alpha_1\gamma_1 - \alpha_2\gamma_2) > 0. \tag{4.40}$$

Since the environmental temperature gradient will not be less than the adiabatic gradient, this inequality implies that

$$1 > \alpha_1\gamma_1 + \alpha_2\gamma_2 \tag{4.41}$$

where $\alpha_i\gamma_i = \chi_i$ as defined in Eq. 4.12: the inhibition criteria solely add.

CHAPTER 5

Gone with the non-isothermal wind: hydrodynamic modeling of core-powered mass loss with non-grey opacities

[1]The mass loss rates of planets undergoing core-powered escape are usually modeled using an isothermal Parker-type wind at the equilibrium temperature, $T_{\rm eq}$. However, the upper atmospheres of sub-Neptunes may not be isothermal if there are significant differences between the opacity to incident visible and outgoing infrared radiation. We model bolometrically-driven escape using AIOLOS, a hydrodynamic radiative-transfer code that incorporates multi-band opacities, to investigate the process's dependence on the visible-to-infrared opacity ratio, γ. For a value of $\gamma \approx 1$, we find that the resulting mass loss rates are well-approximated by a Parker-type wind with an isothermal temperature $T = T_{\rm eq}/2^{1/4}$. However, we show that over a range of physically plausible values of γ, the mass loss rates can vary by orders of magnitude, ranging from $10^{-5}\times$ the isothermal rate for low γ to $10^{5}\times$ the isothermal rate for high γ. The differences in mass loss rates are largest for small planet radii, while for large planet radii, mass loss rates become nearly independent of γ and approach the isothermal approximation. We incorporate these opacity-dependent mass loss rates into a planetary mass and energy evolution model and show that lower γ values lead to more hydrogen being retained after core-powered mass loss. In some cases, the choice of opacities determines whether a planet can retain a significant primordial hydrogen atmosphere. The dependence of escape rate on the opacity ratio may allow atmospheric escape observations to directly constrain a planet's opacities and therefore its atmospheric composition.

---

[1] This chapter is in preparation to be published

5.1 Introduction

Small planets, with radii $R < 4R_\oplus$, close to their stars, with orbital periods $P < 100\,\mathrm{d}$, are abundant. Transit surveys have revealed that around 50 per cent of Sun-like stars have at least one such planet in orbit (Fressin et al., 2013). Furthermore, these planets are distributed bimodally in radius, with the smaller 'super-Earths' separated by the 'radius valley' at $\sim 1.8R_\oplus$ from the larger 'sub-Neptunes' (Fulton et al., 2017). For the subset of these planets with measured masses, the radius valley is also reflected in bulk density. The smaller super-Earths have high densities consistent with a terrestrial composition, while 'sub-Neptunes' have lower bulk densities requiring a volatile component (e.g. Weiss & Marcy, 2014). The local minimum in the radius distribution also decreases as incident bolometric flux decreases (Van Eylen et al., 2018; Fulton & Petigura, 2018).

These observations can be well-explained by the effects of hydrodynamic escape (Owen & Wu, 2013; Ginzburg et al., 2018). In this paradigm, rocky cores form while the natal disk was still present and accrete a few to 10 per cent of their total mass in hydrogen gas. As the disk disperses, the removal of external pressure support and resulting adiabatic expansion of the gas removes some of the accreted envelope in a process termed 'spontaneous mass loss' (Ginzburg et al., 2016) or 'boil-off' (Owen & Wu, 2016). Following the spontaneous mass loss phase, trans-sonic, hydrodynamic winds unbind the remaining primordial hydrogen atmospheres to varying degrees. Some planets, the existing 'sub-Neptune' population, retained most of their primordial envelopes, producing their observed low bulk densities and large radii. Meanwhile, the less massive and closer-in planets were completely stripped, leading to the smaller 'super-Earths' with bulk densities consistent with an Earth-like composition. Alternative explanations for the radius bimodality, including ubiquitous water-rich interiors (e.g. Zeng et al., 2019; Madhusudhan et al., 2020; Burn et al., 2024), are the subject of ongoing work in the community, although none have been as successful in explaining the observed demographics, such as the change in the location of the radius valley as functions of stellar mass and orbital period, as hydrodynamic escape (Gupta & Schlichting, 2020; Rogers et al., 2021).

Hydrodynamic escape theories are separated into two categories distinguished by the heating mechanism of the upper atmosphere: photo-evaporation (e.g. Owen & Wu, 2013) and core-powered mass loss (Ginzburg et al., 2016). In the photo-evaporation framework, high-energy XUV radiation from the host star heats the upper atmosphere to many thousand kelvins, driving rapid escape. However, the XUV output of a typical star declines rapidly with time (Jackson et al., 2012), limiting the most vigorous stripping to the first few hundred million years of a planet's existence. Meanwhile, under core-powered mass loss, the bolometric radiation of the host star maintains a temperature close to the equilibrium temperature in the outer atmosphere. Atmospheric loss is sustained by the high heat capacity of the silicate core relative to the atmosphere. As the planet cools into space, the core, thermally coupled to the base of the atmosphere, resupplies heat into the envelope, preventing radius contraction and promoting atmospheric stripping for longer time spans. Both photo-evaporation and core-powered mass loss reproduce the aforementioned demographic observations (Owen & Wu, 2017; Gupta & Schlichting, 2019; Rogers et al., 2021). The two mechanisms are also not mutually exclusive but rather should occur together, potentially enhancing one another (Owen & Schlichting, 2024). Whether photo-evaporative or core-powered mass loss drives the escape is determined by whether XUV radiation is absorbed interior to the sonic radius of a bolometrically-driven Parker wind (Bean et al., 2021; Owen & Schlichting, 2024).

For the purposes of planet evolution models, both photo-evaporative and core-powered mass loss rates are often estimated analytically. For example, for photo-evaporation, the energy-limited approximation (Watson et al., 1981; Erkaev et al., 2007) is often applied (e.g. Lopez & Fortney, 2013; Owen & Wu, 2017). Meanwhile, core-powered mass loss is usually modeled as a trans-sonic Parker wind at the equilibrium temperature of the planet (Ginzburg et al., 2018; Gupta & Schlichting, 2019; Misener & Schlichting, 2021), which has a simple analytic mass loss rate (Parker, 1958). This approximation was used because core-powered mass loss relies on bolometric heating of the outer atmosphere, which is expected to produce a nearly isothermal outer atmosphere at the equilibrium temperature (Piso & Youdin, 2014), appropriate conditions for a Parker-type wind model. However, while photo-evaporation has been subject to detailed hydrodynamic simulations which benchmark the analytic approximations (e.g. Murray-Clay et al., 2009; Owen & Jackson, 2012; Salz et al., 2016; Kubyshkina et al., 2018; Krenn et al., 2021; Schulik & Booth, 2023), core-powered mass loss has not yet been thoroughly modeled with a coupled hydrodynamic radiative-transfer model, which is the focus of this manuscript.

Importantly, the outer atmospheres of sub-Neptunes need not be isothermal. For example, if the opacity to the infrared outgoing radiation, $\kappa_{\mathrm{P,therm}}$ is not the same as the opacity to the incident visible radiation, $\kappa_{\mathrm{P},\odot}$, then the upper atmosphere will have a more complex, non-isothermal temperature structure (Hubeny et al., 2003; Guillot, 2010). This difference in opacities between spectral bands is often quantified as a ratio

$$\gamma \equiv \kappa_{\mathrm{P},\odot}/\kappa_{\mathrm{P,therm}}. \tag{5.1}$$

Non-isothermal temperature structures in the optically thin regions of atmospheres have been extensively studied in exoplanetary contexts (e.g. Burrows et al., 2007; Fortney et al., 2008; Ito et al., 2015), due to their effects on observed transmission spectra and upper atmospheric chemical equilibrium. But by changing the density profile of the upper atmosphere, such non-isothermal profiles also affect mass loss rates (Schulik & Booth, 2023).

This paper is structured as follows. In Section 5.2, we present the atmospheric structure and evolution theory that form the basis of this work and describe our simulation methods. In Section 5.3, we present and analyze our atmospheric mass loss rate and evolution simulation results. In Section 5.4, we discuss our key assumptions and future possible directions, followed by a conclusion in Section 5.5.

5.2 Methods

We begin this section by detailing the basic equations governing the model of atmospheric structure and evolution we employ in this work, including the ranges of atmospheric opacities we explore. We then detail our approach linking radiative-transfer hydrodynamic models of the upper atmosphere with evolution self-consistently.

5.2.1 Atmospheric structure theory

The basic picture of sub-Neptune composition and structure that we adopt in this work closely follows that of Misener & Schlichting (2021), which is one of a silicate-rich core surrounded by a hydrogen-rich envelope, motivated by extensive previous work (e.g. Lopez & Fortney, 2014; Ginzburg et al., 2016; Owen & Wu, 2017). This composition is supported by comparison of mass loss models to the radius valley's location and its dependence on orbital period and stellar mass (Owen & Wu, 2017; Gupta & Schlichting, 2019). In our model, an incompressible silicate core of mass M_p extends to a core radius $R_\mathrm{c}/R_\oplus = (M_\mathrm{p}/M_\oplus)^{1/4}$ (Valencia et al., 2006; Seager et al., 2007). Above the core, the hydrogen-rich envelope can be modeled to first order as a convective region at the base topped by a radiative region. The transition between these two regions occurs at the radiative-convective boundary (RCB) radius, R_rcb. In this work, we ignore the effects of compositional mixing between silicates and hydrogen that can lead to non-convective regions deep within sub-Neptunes (Misener & Schlichting, 2022; Markham et al., 2022).

In the convective region, the atmosphere follows an adiabatic profile, such that the density goes as:

$$\rho(r) = \rho_\mathrm{rcb}\left(1 + \frac{R'_\mathrm{B}}{r} - \frac{R'_\mathrm{B}}{R_\mathrm{rcb}}\right)^{1/(\gamma_\mathrm{ad}-1)}, \tag{5.2}$$

where $\rho_\mathrm{rcb} = \rho(r = R_\mathrm{rcb})$ is the density at the radiative-convective boundary and γ_ad is the adiabatic index of the atmosphere (not to be confused with the ratio of the visible and infrared opacities, which will be referred to as γ throughout this work). The so-called 'modified Bondi radius' is defined for convenience as $R'_\mathrm{B} \equiv (\gamma_\mathrm{ad} - 1)/\gamma_\mathrm{ad} \times GM_\mathrm{p}\mu/(k_\mathrm{B}T_\mathrm{rcb})$, where G is the gravitational constant, $\mu = 2m_\mathrm{p}$ is the molecular weight of H_2, k_B is the Boltzmann constant, and $T_\mathrm{rcb} = T(r = R_\mathrm{rcb})$ is the temperature at the radiative-convective boundary. Since the mass in the radiative region is typically negligible, the mass contained in the atmosphere, M_atm, can be found by integrating Equation 5.2 over the convective region. Meanwhile, to calculate the planet's available energy for cooling, we follow Misener & Schlichting (2021). As described there, the total energy is the sum of the available energy in the core and atmosphere, $E = E_{\rm core} + E_{\rm atm}$. Since we take the core to be incompressible, the core's available energy is purely thermal: $E_{\rm core} = \frac{1}{\gamma_{\rm c}-1} M_{\rm p}/\mu_{\rm c} k_{\rm B} T_{\rm c}$, where $\gamma_{\rm c} \sim 4/3$ is the core's adiabatic index and $\mu_{\rm c} = 60$ amu is the core's mean molecular weight. We assume the core is isothermal and thermally coupled to the base of the atmosphere, such that $T_{\rm c} = T(r = R_{\rm c})$. The atmosphere's energy is the sum of its gravitational potential and thermal energies:

$$E_{\rm atm} = \int_{R_{\rm c}}^{R_{\rm rcb}} 4\pi r^2 \left(-\frac{GM_{\rm c}}{r} + \frac{1}{\gamma - 1} \frac{k_{\rm B} T(r)}{\mu} \right) \rho(r) {\rm d}r. \tag{5.3}$$

As with the mass, the atmospheric energy is typically concentrated in the convective region (e.g. Misener & Schlichting, 2021), so we do not consider the radiative region in its calculation.

For the atmospheres we consider, the radiative-convective boundary is highly optically thick. Therefore, the radiative diffusion approximation applies, and the temperature gradient is:

$$\frac{\partial \ln T}{\partial \ln P} = -\frac{3\kappa_{\rm R} P L}{64\pi G M_{\rm p} \sigma T^4}, \tag{5.4}$$

where R, P, and T are the local radius, pressure, and temperature, respectively, and L is the planet's luminosity into space. The Rosseland mean opacity, $\kappa_{\rm R}$, is calculated using Equation 5.8, as described below in Section 5.2.2. The radiative-convective boundary radius is then the location where the temperature gradient is equal to the value for a diatomic hydrogen adiabat, $\partial \ln T/\partial \ln P = (\gamma_{\rm ad} - 1)/\gamma_{\rm ad} = 2/7$, satisfying the Schwarzschild criterion. As radius increases and the Rosseland mean opacity and pressures decrease, Eq. 5.4 tends to 0 and the temperature becomes roughly constant. The radial pressure gradient in the radiative diffusion region is well-approximated by hydrostatic equilibrium, since the outflow velocities are negligible deep in the envelope:

$$\frac{\partial P}{\partial R} = -\frac{GM_{\rm p}}{R^2} \frac{\mu P}{k_{\rm B} T}. \tag{5.5}$$

This explicit calculation of the RCB radius is more elaborate that that used in previous work examining core-powered mass loss (e.g. Ginzburg et al., 2016, 2018; Gupta & Schlichting, 2019; Misener & Schlichting, 2021). In those works, the entire upper, radiative region of the atmosphere is approximated as isothermal at the planet's equilibrium temperature, $T_{\rm eq}$, such that $T_{\rm rcb} = T_{\rm eq}$, Where the equilibrium temperature depends solely on the stellar bolometric flux incident on the planet:

$$T_{\rm eq} = \left(\frac{L_*}{16\pi a^2 \sigma}\right)^{1/4}, \tag{5.6}$$

where L_* is the luminosity of the host star, a is the planet's semi-major axis, and σ is the Stefan-Boltzmann constant.

Equation 5.4 applies until radiative diffusion no longer dominates energy transport, i.e. the optical depth by the Rosseland mean opacity $\tau_{\rm R} < 1$. In the results presented in this work, we use a full radiative-transfer hydrodynamic model to self-consistently calculate the temperature and density profiles above this point, but it is useful to understand the key physical processes. Previous work has shown that to first order, the radiative atmosphere can be characterized by two temperature regimes (e.g. Guillot, 2010). In the bottom of this region, where the optical depth to outgoing blackbody radiation, $\tau_{\rm P,therm} > 1$, the expected temperature $T_{\rm in} \approx T_{\rm eq}/2^{1/4}$. This inner temperature is achieved in the limit that $\gamma \gg 1$ or $\gamma \ll 1$, while $T_{\rm in}$ is expected to be closer to $T_{\rm eq}$ when $\gamma \sim 1$ (Parmentier & Guillot, 2014). Meanwhile, we term the expected temperature in the outer atmosphere, where the optical depth to incident stellar radiation $\tau_{\rm P,\odot} < 1$, $T_{\rm out}$. This outer or skin temperature depends on the thermal and stellar opacities and their ratio and can be expressed as $T_{\rm out} = T_{\rm eq}(\gamma/4)^{1/4}$ (Guillot, 2010; Schulik & Booth, 2023). If the opacity to incoming stellar radiation is lower than the opacity to outgoing thermal radiation ($\gamma < 1$), then the radiative upper stratosphere will be colder than the deeper regions ($T_{\rm out} < T_{\rm in}$). Conversely, if the opacity to incoming stellar radiation is higher than the opacity to outgoing thermal radiation ($\gamma > 1$), then the upper atmosphere will be hotter than the optically thick regions, causing a temperature inversion ($T_{\rm out} > T_{\rm in}$).

Related to these $\tau = 1$ surfaces is the transit radius, $R_{\rm trans}$. The transit radius is the radius at which the chord optical depth to incident stellar radiation is equal to 1, i.e.:

$$1 = 2\int_{R_{\rm trans}}^{\infty} \rho(r)\kappa_{\rm P,\odot} {\rm d}s \tag{5.7}$$

where $s = (r^2 - R_{\rm trans}^2)^{1/2}$ is the chord length.

In Figure 5.1, we summarize the key atmospheric physics described in this and the following sections. In each panel of the schematic, which is not to scale, we show example temperature profiles as functions of radii for three prototypical cases: an atmosphere with $\gamma \gg 1$, $\gamma \sim 1$, and $\gamma \ll 1$ from top to bottom. We show three key radii with dashed black vertical lines: the radiative-convective boundary radius $R_{\rm rcb}$, the transit radius $R_{\rm trans}$, and the sonic radius of the outflow $R_{\rm s}$ (see Eq. 5.10 below). We also show with dash-dotted lines the radii at which the optical depth reaches unity for the three opacities that determine the structure of the atmosphere: the thermal Rosseland optical depth $\tau_{\rm R}$ in blue, the thermal Planck optical depth $\tau_{\rm P,therm}$ in red, and the two-temperature stellar Planck optical depth $\tau_{\rm P,\odot}$ in yellow. The domain of our hydrodynamic simulation is shown by the tan shading, extending outwards from its inner boundary $R_{\rm domain}$ (see Sec. 5.2.6 below for details). Finally, we show the key temperatures defined in this section with gray horizontal dotted lines: the equilibrium temperature $T_{\rm eq}$, temperature at the radiative-convective boundary $T_{\rm rcb}$, temperature in the inner radiative region $T_{\rm in}$, and temperature in the outer radiative region $T_{\rm out}$.

In all three cases shown in Fig. 5.1, at depth the temperatures are high and defined by an adiabat until the radiative-convective boundary is reached at some temperature $T_{\rm rcb}$, which, despite being shown as higher than is $T_{\rm eq}$, in reality may be higher or lower depending on the outgoing flux. In the radiative, optically thick regime, thermal diffusion determines the temperature gradient. This gradient begins equal to the adiabatic gradient but tends to zero as the radius increases and the pressure drops, per Eq. 5.4, leading to a constant temperature close to $T_{\rm in}$.

From this point, the cases diverge. In the $\gamma > 1$ case, the $\tau_{\rm P,therm} = 1$ surface is interior to the $\tau_{\rm P,\odot} = 1$ surface. Beyond the $\tau_{\rm P,therm} = 1$ surface, in the region optically thin to outgoing radiation but optically thick to incoming radiation, the temperature increases with radius until $\tau_{\rm P,\odot} < 1$ and the atmosphere reaches a constant temperature at $T_{\rm out}$, which is higher than $T_{\rm eq}$. Conversely, in the $\gamma < 1$ case, the $\tau_{\rm P,\odot} = 1$ surface is interior to the $\tau_{\rm P,therm} = 1$ surface. In this case, the atmospheric temperature is nearly isothermal near $T_{\rm in}$ until $\tau_{\rm P,therm} < 1$, at which point it begins declining to $T_{\rm out}$. Both of these temperatures, and thus the entire outer atmosphere, are lower than the equilibrium

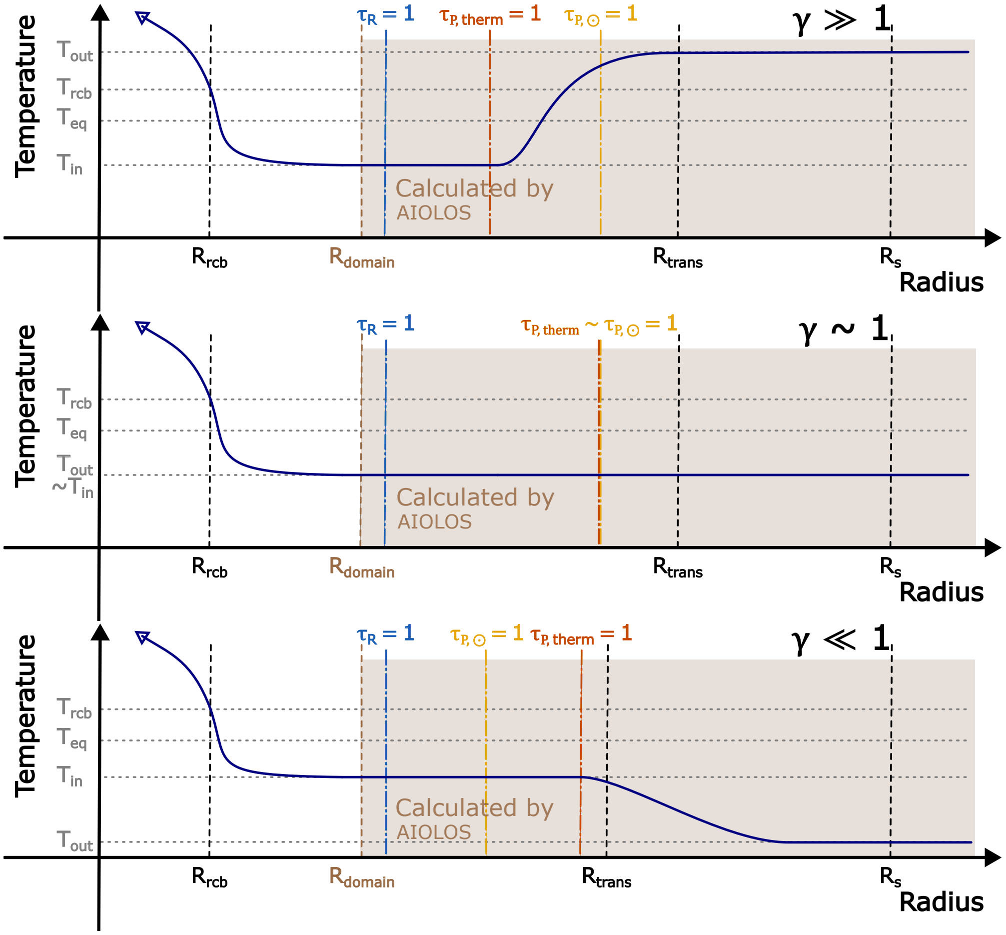

Figure 5.1: Schematic, not-to-scale representation of the typical temperature-radius profiles for different optical-to-infrared opacity ratios, γ. Three idealized cases $\gamma \gg 1$, $\gamma \sim 1$, and $\gamma \ll 1$ are illustrated on the top, middle, and bottom panels, respectively. Vertical black dashed lines show three key radii discussed in the text: the radiative-convective boundary radius $R_{\rm rcb}$, the transit radius $R_{\rm trans}$, and the sonic radius of the outflow $R_{\rm s}$. Additionally, three surfaces where the optical depth in different opacities is equal to 1 are shown by colored dash-dotted vertical lines: the thermal Rosseland optical depth, $\tau_{\rm R}$, in blue; the thermal Planck optical depth, $\tau_{\rm P,therm}$, in red; and the two-temperature stellar Planck optical depth, $\tau_{\rm P,\odot}$, in yellow. The tan shaded region denotes the domain of our AIOLOS hydrodynamic simulation domain, extending from its lower boundary $R_{\rm domain}$. Finally, horizontal gray dotted lines show four key temperatures discussed in the text: the equilibrium temperature $T_{\rm eq}$, temperature at the radiative-convective boundary $T_{\rm rcb}$, temperature in the inner radiative region $T_{\rm in}$, and temperature in the outer radiative region $T_{\rm out}$. The thermal profile strongly depends on the relative locations of the $\tau = 1$ surfaces, and therefore on the opacity ratio γ. Values of $\gamma > 1$ produce thermal inversions and high temperatures in the outer atmosphere, while values of $\gamma < 1$ produce cold outer atmospheres, significantly decreasing mass loss rates.

temperature. In the middle, $\gamma \sim 1$ case, $T_{\rm in} \sim T_{\rm out}$, so the optically thin region is nearly isothermal at a temperature slightly lower than the equilibrium temperature. In all cases, the transit radius $R_{\rm trans}$ is positioned close but slightly exterior to the $\tau_{\rm P,\odot} = 1$ surface, reflecting the increased path length of tangent photons compared to radial ones.

5.2.2 Opacities

We use simplified opacities, using physically relevant values based on Freedman et al. (2014). Single-temperature Rosseland mean opacities, $\kappa_{\rm R}$, appropriate for thermal radiation in the optically thick diffusion limit, scale as:

$$\kappa_{\rm R} = 0.1 \left(\frac{\rho}{10^{-3}\,{\rm g\,cm^{-3}}} \right)^{0.6} {\rm cm^2\,g^{-1}}. \tag{5.8}$$

We use a constant value for the Planck single-temperature opacities, $\kappa_{\rm P,therm} = 7.5\,{\rm cm^2\,g^{-1}}$, appropriate for thermal radiation in the optically thin regime. For the two-temperature opacity to incident stellar radiation, $\kappa_\odot$, there is debate in the literature over whether the Rosseland or Planck opacity is more relevant to this problem (Guillot, 2010; Parmentier et al., 2015). Which opacity is more appropriate could have a large impact on our results, since two-temperature Planck means are usually two to four orders of magnitude larger than the corresponding two-temperature Rosseland means (Freedman et al., 2014). We choose to use the Planck opacities, following Guillot (2010). The ratio of opacities of interest here, often termed γ, is then $\kappa_{\rm P,\odot}/\kappa_{\rm P,therm}$.

The opacities are a combination of broadband H absorption and line absorption by molecules in the infrared and alkali metals and oxides in the visible. Therefore, depending on a variety of atmospheric processes, including temperature and density, as well as composition, the value of the ratio could vary significantly from planet to planet. We therefore test a range of values of the opacity to solar radiation $\kappa_{\rm P,\odot}$ ranging from 0.225 to $225\,{\rm cm^2\,g^{-1}}$, corresponding to opacity ratios between 0.03 and 30, which encompass the range of temperature, density, and compositions relevant to sub-Neptunes (Freedman et al., 2014). In this way we remain agnostic to the actual opacity sources that cause the atmospheric effects we study here, and rather seek to quantify the magnitude of differences which are possible.

5.2.3 Atmospheric evolution theory

In this work, we determine the atmospheric escape rate self-consistently from the AIOLOS hydrodynamic code. In the limit of an isothermal radiative region, as assumed in previous work examining core-powered mass loss, the mass loss rate, $\dot{M}_{\rm iso}$, can be solved analytically as a trans-sonic Parker wind (Parker, 1958):

$$\dot{M}_{\rm iso} = 4\pi R_{\rm s}^2 c_{\rm s} \rho_{\rm s} = 4\pi R_{\rm s}^2 c_{\rm s} \rho_{\rm rcb} \exp\left\{\left[2 - \frac{2R_{\rm s}}{R_{\rm rcb}}\right]\right\}. \tag{5.9}$$

In this equation, the isothermal sound speed $c_{\rm s} = (k_{\rm B}T/\mu)^{1/2}$, in which T is the isothermal temperature and $R_{\rm s}$ is the resulting sonic radius:

$$R_{\rm s} = \frac{GM_{\rm p}}{2c_{\rm s}^2}. \tag{5.10}$$

In the second equality of Equation 5.9, this mass loss rate is expressed in terms of the radius, $R_{\rm rcb}$, and density, $\rho_{\rm rcb}$, at the base of the isothermal region, i.e. the radiative-convective boundary, above which the atmosphere is assumed to follow an exponential density profile (e.g. Misener & Schlichting, 2021).

The planet also cools into space at a luminosity L. These rates allow the definition of two timescales that describe the evolution of small planets. One is the mass loss timescale, $t_{\rm loss} = M_{\rm atm}/\dot{M}$. The other is the cooling timescale $t_{\rm cool} = E/L$. When the mass loss timescale is shorter than the cooling timescale, the planet loses mass more quickly than it can cool and contract, leading to rapid atmospheric depletion. Conversely, if the cooling timescale is shorter than the mass loss timescale, the atmosphere will rapidly contract. Contraction brings the atmosphere deeper into the planet's gravitational potential and thus makes it more difficult to unbind, quickly throttling mass loss and leading to the preservation of the remaining atmosphere (Gupta & Schlichting, 2019; Misener & Schlichting, 2021).

5.2.4 AIOLOS general setup

We use AIOLOS, a 1D radiation-hydrodynamics code first presented in Schulik & Booth (2023). AIOLOS is a Riemann solver code capable of simulating multispecies inflows and outflows using a multiband radiative transfer scheme. In this work, in order to test core-powered mass-loss, we consider an atmosphere of pure hydrogen gas with no incident UV flux. We allow the hydrogen to transition between diatomic and monatomic, though we find that in most of our chosen regimes, the hydrogen stays primarily diatomic due to the relatively low temperatures experienced in a bolometrically heated region. In light of this, we initialize the atmosphere as mostly H_2 with one part in 10^8 H, though our simulations are insensitive to the exact starting composition. We tested allowing ionization but found that it was never relevant in the regime we consider here and greatly increased computation time. Ionization will be vital in future extensions of this work to incorporate photo-evaporation.

In all runs, we initialize the grid between an inner bound, which we change in each run as discussed in the next section, and an outer bound, which is fixed at $8 \times 10^{10}\,\mathrm{cm} \approx 125R_\oplus$. This bound is well beyond the sonic radius of the outflow. The grid is spaced at 500 cells per decade in the inner region, $r < 8 \times 10^9\,\mathrm{cm} \approx 12.5R_\oplus$, to resolve the shocks that sometimes develop early in the simulations, and 200 cells per decade in the outer region, where less resolution is required. The inner boundary is fixed at a constant density but allowed to evolve in temperature, while the outer boundary is open. We assume a flux-limited diffusion (FLD) factor $\xi = 2$, following Schulik & Booth (2023).

5.2.5 Run parameters

For each run, we first specify the planet's mass M_p and semi-major axis a. We then specify the inner domain boundary, R_domain. We also specify the internal flux at this inner boundary, which is expressed in the code as an internal temperature T_int such that the planet's luminosity L is given by

$$L = 4\pi R_\mathrm{domain}^2 \sigma T_\mathrm{int}^4 \tag{5.11}$$

. To avoid numerical instabilities, we add this internal flux to AIOLOS by spreading it over the first three cells in the domain.

We assume the host star is Sun-like in mass, radius, and temperature throughout this work, thus fixing the stellar luminosity as that of the Sun, $L_\odot$. This means that increasing the semi-major axis decreases the equilibrium temperature $T_{\rm eq}$ monotonically following Equation 5.6, with $L_* = L_\odot$.

We fix the density at the bottom of the AIOLOS domain to $\rho_{\rm domain} \equiv \rho(R_{\rm domain}) = 10^{-5}\,{\rm g\,cm^{-3}}$. We chose this value to correspond to a typical Rosseland optical depth between 1 and 10 at the bottom of the AIOLOS domain, as depicted on Fig. 5.1. Such a value balances accuracy and computational speed: a denser domain greatly increases computational time. Meanwhile the deep region has low mach numbers and is optically thick, meaning it is well approximated by a diffusive profile. We thus link the bottom of the AIOLOS domain to a model of the deep atmosphere using a semi-analytic diffusive profile, which we detail in Section 5.2.6.

We initialize the simulation as isothermal at the equilibrium temperature with a hydrostatic density profile. In all runs, we allow the code to iterate from its initialization, solving the hydrodynamics and radiation transport, until it reaches a steady state outflow solution. This typically takes on the order of 10^7 to 10^8 s of simulation time for the regime we consider. In order to prevent instabilities, we ramp up the radiation gradually over the first 10^3 s.

5.2.6 Optically thick extrapolation

To go from the bottom of the AIOLOS domain, which we choose to be weakly optically thick, to the deeper, adiabatic interior, we semi-analytically extrapolate following a diffusive temperature gradient. The bottom of the domain has radius $R_{\rm domain}$, density $\rho_{\rm domain} = 10^{-5}\,{\rm g\,cm^{-3}}$, a temperature found by the the simulation, and an internal luminosity that corresponds to a specified internal temperature via Equation 5.11 above.

Beginning from the bottom of the numerical domain, we increase the pressure by a small increment, $\Delta P = P/100$, and increment the temperature and radius according to Equations 5.4 and

5.5 respectively. We recalculate the gradients, and continue this until the Schwarzschild criterion is met, $\partial \ln T / \partial \ln P = 2/7$. At this radius, the radiative-convective boundary, $R_{\rm rcb}$, we switch to an adiabatic gradient, calculated using the methods of Misener & Schlichting (2021). We integrate this adiabatic profile to infer an atmospheric mass $M_{\rm atm}$, often referred to as a fraction of the planet's total mass, $f \equiv M_{\rm atm}/M_{\rm p}$. In this way, we connect an AIOLOS boundary condition to the atmospheric evolution state it represents.

5.2.7 Evolution

To evolve the planets in time, we first run AIOLOS over a series of domain radii $R_{\rm domain}$, spaced 0.1 Earth radii apart, for each γ, $M_{\rm p}$, and $T_{\rm eq}$. Each run produces a particular atmospheric mass and energy, as well as a mass loss rate and luminosity. For sufficiently low luminosities (i.e., low internal temperatures), the temperature gradient at the base of the AIOLOS domain is nearly zero, so the profiles in the AIOLOS domain are independent of the internal temperature. We verified empirically that so long as $\partial \ln T / \partial \ln P < 0.01$ at $R_{\rm domain}$, using a single run for all $T_{\rm int}$ yielded indistinguishable results from using a run with the actual $T_{\rm int}$, and so we employ one AIOLOS run for all possible $T_{\rm int}$ values in the work presented here to save computational time. We check *a posteriori* that the gradient condition is always satisfied.

As discussed in Section 5.1, as planets emerge from the disk they undergo spontaneous mass loss due to the removal of pressure confinement, a process that takes on the order of the typical disk lifetime, $\sim 10^7$ yr. We therefore choose an initial $R_{\rm rcb}$ by first thermally evolving the planets from an arbitrary size without any escape for 10^7 yr. The resultant radius is virtually independent of the starting radius, and produces a planet with a cooling timescale of a few times 10^7 yr. We choose a fiducial initial atmospheric mass, $M_{\rm atm} = 0.025 M_{\rm p}$, to represent a typical sub-Neptune (e.g. Wolfgang & Lopez, 2015), but we vary this mass in Section 5.3.3. Starting from these initial $R_{\rm rcb}$ and $M_{\rm atm}$, we compute the time evolution by finding the corresponding luminosity and AIOLOS mass loss rate. We interpolate over the grid of AIOLOS runs using the SCIPY `CubicSpline` function to find the mass loss rate as a function of arbitrary $R_{\rm domain}$.

We then subtract the mass and energy lost over a short time period $\Delta t = 0.01\,\mathrm{min}\,(t_{\mathrm{cool}}, t_{\mathrm{loss}})$: $M_{\mathrm{atm,new}} = M_{\mathrm{atm}} - \dot{M}\Delta t$ and $E_{\mathrm{new}} = E - L\Delta t$. This evolution scheme is nearly identical to the methods used in Misener & Schlichting (2021), except with $\dot{M}$ taken from AIOLOS instead of an analytic Parker wind model. We then solve for the AIOLOS parameters L and R_{domain} that correspond to the new mass and energy using the SCIPY `fsolve` root finding method.

5.3 Results

In this section, we present the results of using AIOLOS derived outer atmosphere profiles for a range of visible-to-infrared opacity ratios. In Section 5.3.1, we compare instantaneous atmospheric profiles and demonstrate that incorporating more realistic opacities leads to non-isothermal profiles that can have a major effect on the atmospheric escape rate. Then, in Section 5.3.2, we incorporate these profiles into planetary evolution calculations, finding that the fate of planetary atmospheres depends strongly on the visible-to-infrared opacity ratio γ in the upper atmosphere.

5.3.1 Sensitivity of mass loss rates to opacity

In Fig. 5.2, we compare the thermal (top left) and density (bottom left) profiles and mass loss rates (right) as functions of the ratio of the opacity to incident visible and thermal radiation, γ. Each color is a run with a value of this ratio ranging from 0.3 to 30, with γ increasing as the colors get darker. All seven runs have a fixed radiative-convective boundary radius, $R_{\mathrm{rcb}} = 2R_{\mathrm{c}} = 1.91 \times 10^9\,\mathrm{cm}$, a fixed initial atmospheric mass of $0.025M_{\mathrm{c}}$ and a fixed incident flux equivalent to an equilibrium temperature of 1000 K, which is shown by the gray horizontal line. For each γ value, the solid line represents the output of the AIOLOS code, while the dotted line represents the semi-analytic extrapolation into the optically thick region described in Section 5.2.6. The red dashed lines and red diamond represent the hydrostatic profile of an isothermal outer atmosphere with the same radiative-convective boundary radius and atmospheric mass and an constant temperature equal to $T_{\mathrm{in}} = T_{\mathrm{eq}}/2^{1/4}$.

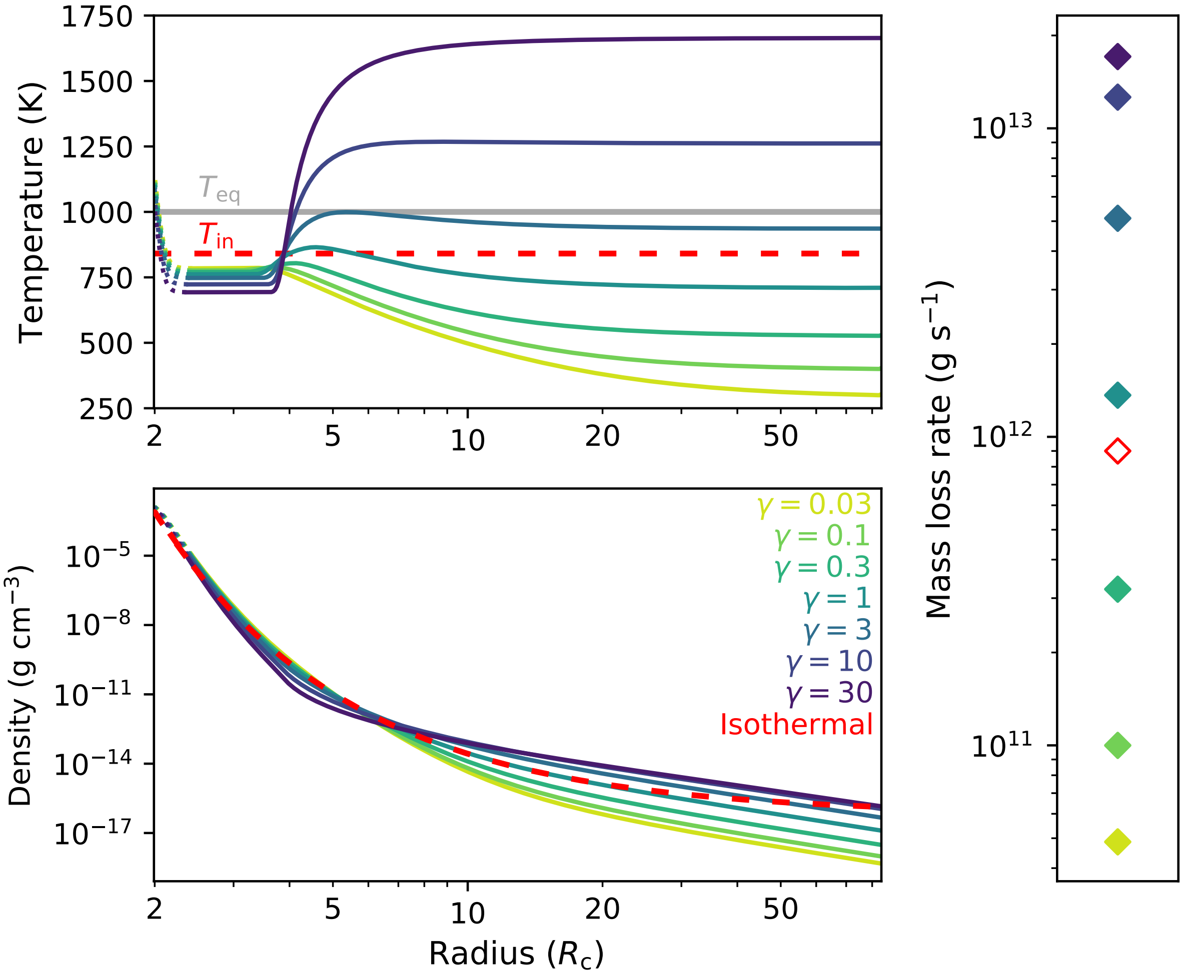

Figure 5.2: Temperature (top) and density (bottom) profiles as functions of radius, in core radii $R_{\rm c}$, and corresponding mass loss rates (right) for seven values of the opacity ratio ranging from 0.03 to 30 (different colors from yellow to purple). All profiles have a fixed radiative-convective boundary location $R_{\rm rcb} = 2R_{\rm c} = 1.91 \times 10^9$ cm, atmospheric mass fraction $f = 0.025$, and incident flux equivalent to an equilibrium temperature $T_{\rm eq} = 1000\,{\rm K}$ (shown by the gray horizontal line on the top panel). Shown in red dashed lines are the equivalent profiles and mass loss rates for an isothermal radiative region at the analytic interior temperature, $T_{\rm in} = T_{\rm eq}/2^{1/4}$. Increasing the opacity ratio leads to different temperature and density profiles and therefore to mass loss rates that vary two orders of magnitude over plausible values. The mass loss rate for the $\gamma = 1$ profile are similar to those for an isothermal outer atmosphere at $T_{\rm in}$.

In general, the numerical thermal profiles reproduce the characteristics described in Section 5.2, thus looking broadly similar to the schematic in Fig. 5.1. As the opacity ratio γ increases, the outer region, optically thin to incident radiation, heats up, with temperatures increasing by a factor of 7 over the studied 1000-fold opacity ratio increase. The outer temperatures range from well below the equilibrium temperature to well above it, and are well-predicted by the $T_{\rm out} = T_{\rm eq}(\gamma/4)^{1/4}$ relation of Schulik & Booth (2023). Meanwhile the inner region, optically thick to outgoing radiation, reaches lower temperatures as γ is increased, decreasing by 100 K over the studied range. In all cases, the inner, optically thick radiative region is a few hundred kelvins cooler than the equilibrium temperature. This temperature is also lower by $\sim 70 - 200$ K than the analytic lower limit of $T_{\rm in}$ discussed in Schulik & Booth (2023). The minimum temperature also increases monotonically with γ, rather than being highest at $\gamma \sim 1$. This may be due to the enhanced cooling as $\kappa_{\rm P,\odot}$ increases, or because the above approximation does not include the effects of beam-spreading, while AIOLOS does.

The increase in the outer temperature with γ leads to an increase in the hydrodynamic mass loss rate, which increases about two orders of magnitude over the ratio range studied. We find that for $\gamma \sim 1$, the profile and resultant mass loss rate are well-approximated by an analytic, hydrostatic outer atmospheric profile at constant temperature $T_{\rm in}$ (in red). Values of $\gamma > 1$ lead to larger mass loss rates than the analytic value, and values of $\gamma < 1$ lead to smaller ones. This is a lower mass loss rate than was typically used in past approximations of core-powered mass loss, in which $T_{\rm eq}$ was used for the isothermal region instead (e.g. Ginzburg et al., 2016; Gupta & Schlichting, 2019; Misener & Schlichting, 2021). This because the low temperatures $\sim T_{\rm in} < T_{\rm eq}$ lead to a rapid dropoff in density that throttles the escape rate. As γ increases, the density in the outer region increases, as expected from the increased temperatures. However, this increase is blunted by the decrease in temperature, and therefore density, in the inner optically thick regions as γ increases, making the high-γ profiles lower in density at intermediate radii ($\sim 3 - 6R_{\rm c}$ here). Therefore, the mass loss rate does not increase very quickly as the outer temperature increases. Additionally, due to the hydrodynamic nature of the outflow, the density drops more quickly in the simulations than in the hydrostatic, analytic approximation, as shown by the red dashed line deviating above the $\gamma = 1$ curve in the bottom panel of Fig. 5.2.

In the top panel of Figure 5.3, we show the mass loss rate as a function of radiative-convective boundary radius for different γ values (in different colors from yellow to purple) taken from our hydrodynamic simulations. The red dashed line represents the mass loss rate given by an isothermal Parker wind at the analytic inner temperature T_{in}. We show the ratio between the simulated mass loss rate and the analytic Parker wind rate in the bottom panel. At small RCB radii, the mass loss rate is a strongly increasing function of γ, as depicted in Fig. 5.2. This is because at low RCB radii, the optically thin region is reached deep below the sonic point. Therefore, much of the atmosphere is nearly isothermal at T_{out}, which depends on γ. For low values of γ, this means the density declines steeply before reaching the sonic radius, which is at cool temperatures and consequently low sound speeds. Conversely, for large values of γ, the density declines slowly and the sound speed at the sonic radius is high, leading to enhanced loss rates.

As the RCB radius increases, the dependence on γ changes. For large RCB radii, the radius of the $\tau_{\text{P}} = 1$ surfaces is sufficiently close to the sonic radius such that much of the radiative upper atmosphere is at T_{in} rather than T_{out}. This change works to make the dependence on γ weaker for large radii planets than for those with small radii: the mass loss rates converge to that given by an isothermal approximation at T_{in} for all values of γ. Additionally, for the lowest γ runs, the mass loss rates increase more quickly with radius than in the analytic approximation. This is because the temperature in the outer regions declines slowly with radius, such that the temperature at the sonic radius can remain higher than T_{out}. This enhances the mass loss rate both by increasing the sound speed and limiting the density drop-off. Meanwhile, in the high γ cases, the interiors are even colder than the low γ cases, leading to rapid density drops compared to the isothermal case as shown in Fig. 5.2. At small RCB radii, the outer high temperature regions allow the densities to ‘recover’ and boost mass loss overall. But for large RCB radii there is not a large enough region of high temperature before the sonic point is reached, leading to mass loss rates increasing more slowly with radius than in the isothermal or low γ cases. In the particular case shown in Figure 5.3,

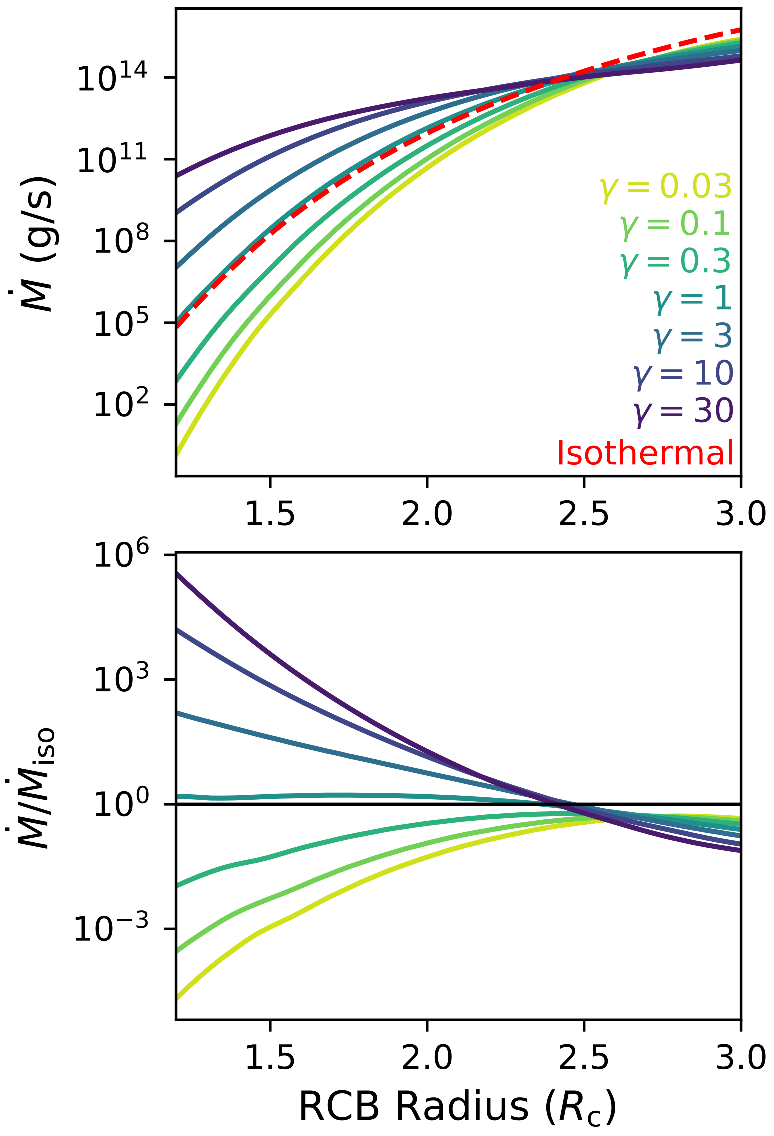

Figure 5.3: Mass loss rate derived from AIOLOS hydrodynamic simulations (top) and ratio of modeled mass loss rates to those found by an analytic isothermal Parker wind at T_{in}(bottom), as functions of radiative-convective boundary radius, R_{rcb}, in units of core radii R_{c}. As in Fig. 5.2, the planets have a fixed atmospheric mass fraction, $f = 0.025$, and incident flux equivalent to an equilibrium temperature $T_{\mathrm{eq}} = 1000\,\mathrm{K}$. Each color from yellow to purple represents a different value of the visible-to-infrared opacity γ ranging from 0.03 to 30, while the red line in the top panel represents the isothermal mass loss rate. Differences between γ values are largest at low RCB radii, while the mass loss rates converge to a value close to the analytic value at high RCB radii.

these effects are strong enough to reverse the dependence of the mass loss rate on γ, such that the lowest values of γ have the highest loss rates, though all are within roughly an order of magnitude of each other and the analytic approximations.

5.3.2 Changes to evolution

The myriad effects of different opacity ratios described in Section 5.3.1 combine to alter the mass and thermal evolution of small planets under core-powered mass loss. In Fig. 5.4, we demonstrate how the evolution in time of a planet and the fate of its atmosphere can depend on the ratio of the opacities in the outer atmosphere. We show the evolution in time of a planet with fixed planet mass $M_\mathrm{p} = 5M_\oplus$, initial RCB radius $R_\mathrm{rcb}(t = 0) = 2.1R_\mathrm{c}$, initial atmospheric mass fraction $f(t = 0) = 0.025$, and equilibrium temperature $T_\mathrm{eq} = 1000$ K, all chosen to represent a typical sub-Neptune emerging from spontaneous mass loss. We vary these parameters and examine the effects in Section 5.3.3. The different colors represent different choices of γ. We also show an evolution track of a planet with the same initial conditions but using an isothermal radiative region at T_in in red. This evolution was conducted using the methods described in Misener & Schlichting (2021), except that the 'energy-limited' mass loss rate is ignored and only the Parker mass loss rate ($\dot{M}_\mathrm{B}$ in that work) is used. Additionally, motivated by the results above, this Parker mass loss rate has been modified to use T_in instead of T_eq. On the top row of Fig. 5.4, as well as Figs. 5.6, 5.7, and 5.8 below, we show the (a) total energy of the atmosphere as a dotted line and thermal energy of the core as a solid line, (b) planet luminosity, and (c) cooling timescale as functions of time. On the middle row, we show the (d) atmospheric mass as a fraction of the initial atmospheric mass, (e) mass loss rate, and (f) mass loss timescale. Finally, on the bottom row we show the (g) radiative-convective boundary radius in units of core radii, (h) transit radius in units of Earth radii, and (i) the ratio of the cooling timescale to the mass loss timescale.

Universal evolutionary outcomes for small planets with H/He envelopes, similar to those studied in detail in previous work such as Misener & Schlichting (2021), emerge in the results presented in Fig. 5.4. When small planets are young and have extended atmospheres, their mass loss timescales

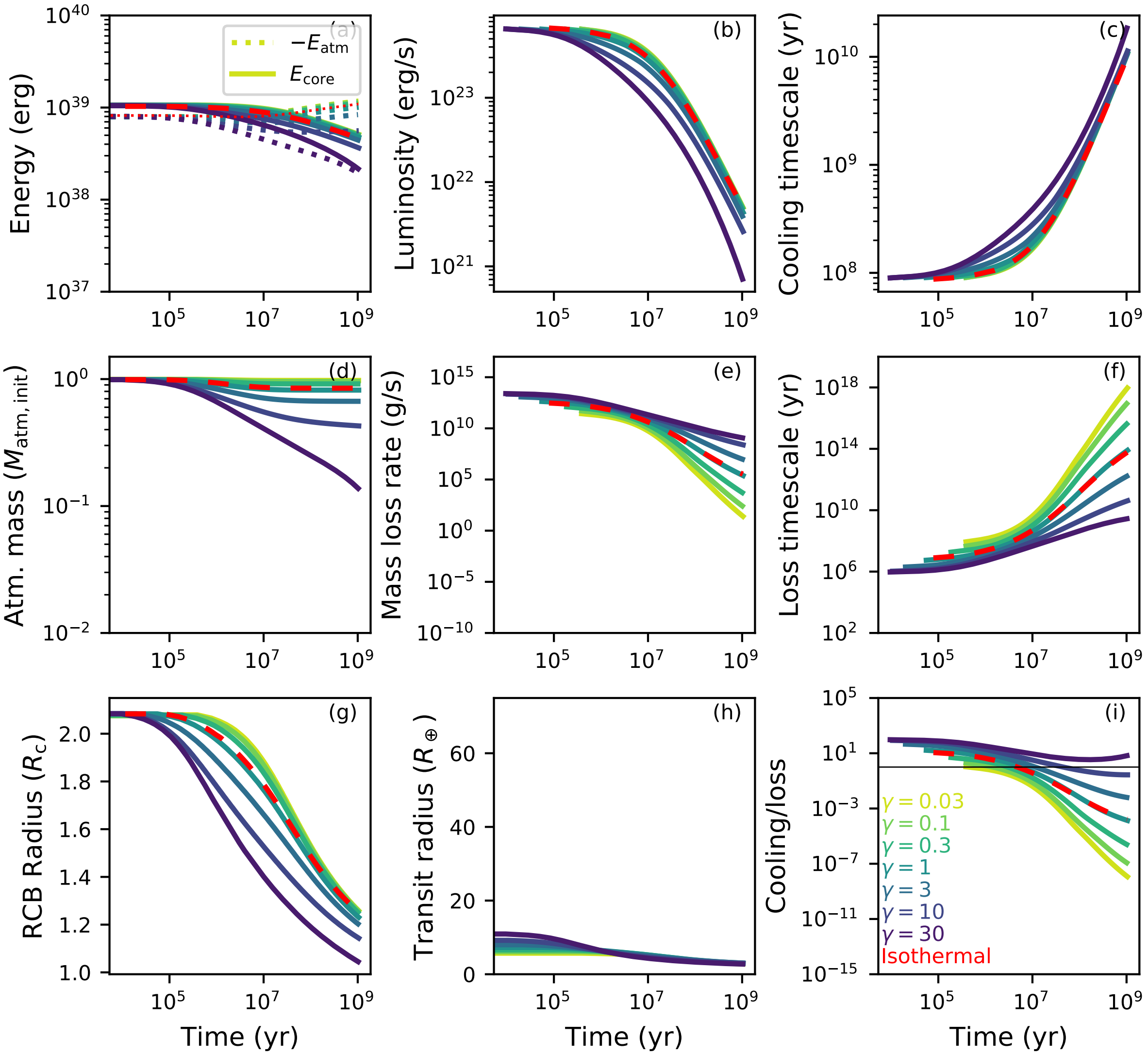

Figure 5.4: Evolution of planets in time using mass loss rates from AIOLOS. In the top row we show the energy, luminosity, and cooling timescale. In the middle row we plot atmospheric mass as a fraction of the planet's total mass, mass loss rate, and mass loss timescale. Finally, displayed on the bottom row are the RCB radius, transit radius, and ratio of the cooling timescale to the mass loss timescale. In all of these simulations, the planet mass $M_{\rm p} = 5M_\oplus$, the initial RCB radius is 2.1 core radii, and the initial atmospheric mass fraction is 0.025 planet masses. Each color represents a different opacity ratio. A fully isothermal evolution, calculated using the methods described in Misener & Schlichting (2021), is shown with the red dashed lines. As the opacity ratio is increased, the planets lose more mass over time. The total mass lost can be either more or less than the isothermal prediction, depending on the value of the opacity ratio, with the $\gamma = 1$ case very similar.

can be short, leading to rapid evolution in mass (panels (c) and (f)). Since the mass loss timescale is initially much shorter than the cooling timescale (panel (i)), these planets can lose significant fractions of their initial atmosphere to hydrodynamic escape (panel (d)). Cooling into space decreases the planet's total available energy (panel (a)), leading to atmospheric contraction (panels (g) and (h)). Significant escape is halted when the cooling timescale becomes shorter than the mass loss timescale (panel (i)). After this time, the planets cool and contract, making the atmospheric energy more negative (panel (a)) and rapidly decreasing the mass loss rate (panel (e)).

Despite the qualitative similarities, Fig. 5.4 shows that different choices of opacities in the outer envelope can significantly alter the long-term evolution predicted by core-powered mass-loss. We find that as γ increases, a planet loses more atmosphere over its lifetime (panel (d)). As shown in Section 5.3.1, this is due to the change in the temperature profile in the outer atmosphere, which changes the mass loss rate predicted for a given radius. Overall, different choices of upper atmospheric opacity can vary the final atmospheric mass by a factor of 10 or more. In addition, the apparent radius of these planets in transit also widely differs based on γ: the high γ cases appear much larger in transit early in their evolution due to their large values of $\kappa_{\mathrm{P},\odot}$ (panel (h)).

Additional perspective on these evolutionary differences can be gained from plotting the ratio between the mass loss rate found here and those predicted from the simulation that uses the analytic, isothermal mass loss rate as a function of time, which we show in Figure 5.5. Again, each color represents a different value of γ. Initially, the high γ cases have moderately higher mass loss rates, but all the rates are fairly close to the isothermal value. However, these slightly higher mass loss rates allow the high γ models to contract more quickly (Fig. 5.4, panel (g)). While their mass loss rate declines with time due to this contraction (see Fig. 5.4, panel (e)), the mass loss rate relative to the isothermal approximation increases. This is because as the planets contract, mass loss becomes relatively more efficient for the high γ cases and much less efficient for low γ cases, as is depicted in Fig. 5.3. This allows the $\gamma > 1$ runs to sustain mass loss rates above those of the isothermal simulation on billion year timescales, while the lower γ runs essentially stop losing mass entirely, with the difference increasing with time. This result indicates that differences in γ could control

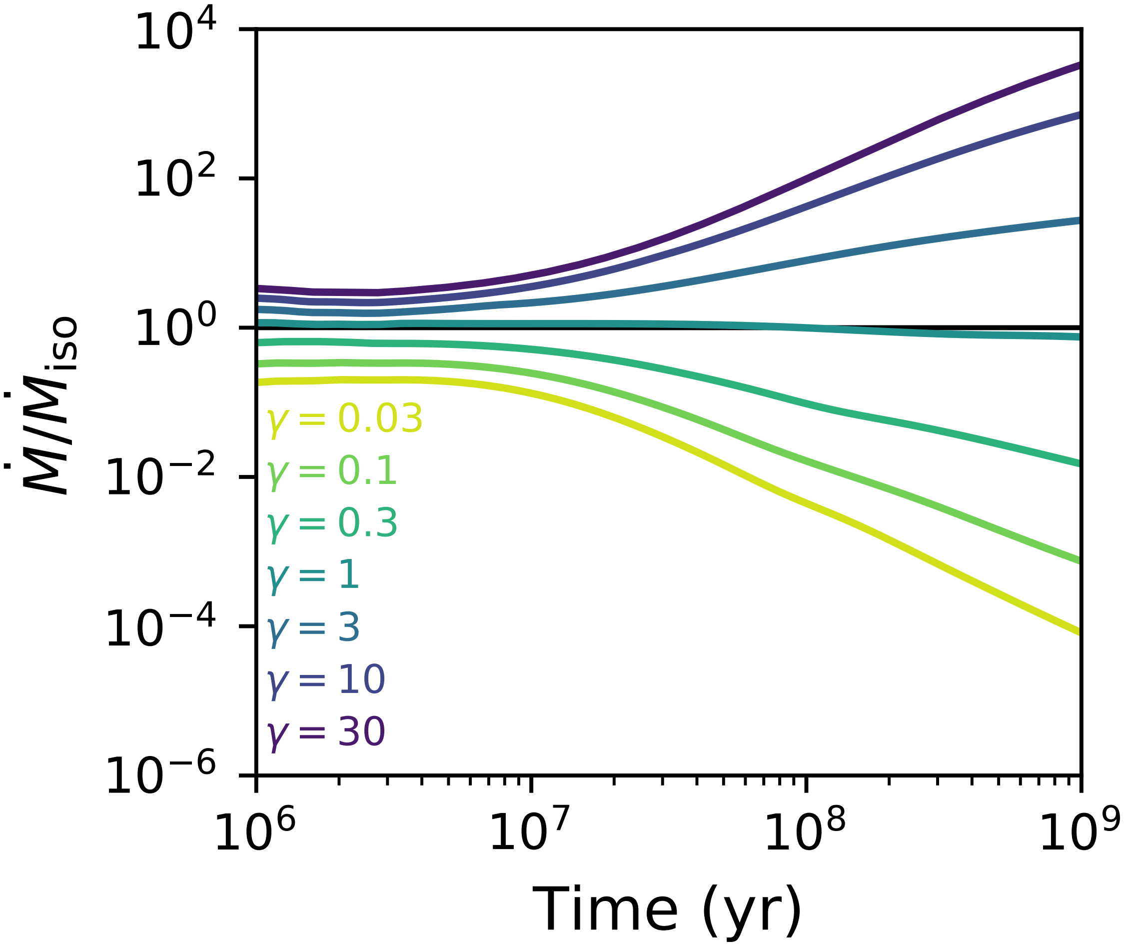

Figure 5.5: The ratio of the mass loss rates found using a hydrodynamic model to those predicted analytically as functions of time since the beginning of the evolution. The evolution tracks are the same as those shown in Fig. 5.4. Each color represents a different value of γ. Initially, the simulated mass loss rates are very similar to those predicted analytically. Faster mass loss allows faster contraction for the higher γ cases. While this lowers the mass loss rate, it brings the planet to radii for which the high temperatures of the outer radiative region greatly enhance loss (see Fig. 5.3). Therefore, as the planets contract, mass loss becomes more efficient for the high γ cases relative to the isothermal case, leading to them sustaining higher mass loss rates over the course of the simulation. Conversely, the lower γ cases become much less efficient at losing mass.

whether or not atmospheric escape from a small planet is detectable via transit spectroscopy (see Section 5.4.2 for further discussion).

5.3.3 Variation with planet mass, equilibrium temperature, and initial atmospheric mass

The effects of changing the opacity ratio vary depending on the planet mass, equilibrium temperature, and atmospheric mass. In Fig. 5.6, we show the variation in atmospheric evolution for different planet masses. All the models have the same equilibrium temperature, $T_{\rm eq} = 1000$ K and initial atmospheric mass fraction $f = 0.025$, with the initial radii chosen as described in Section 5.2. The purple lines represent 3 $M_\oplus$, the blue lines represent 5 $M_\oplus$, and the green lines represent 10 $M_\oplus$. For each mass, the lighter colored line represents an evolution using a low opacity ratio, $\gamma = 0.03$, while the darker colored line represents an evolution using a high opacity ratio, $\gamma = 30$. The panel meanings remain the same as in Fig. 5.4. For reference, the 5 $M_\oplus$ planet tracks shown are the same as the $\gamma = 0.03$ and $\gamma = 30$ cases of Fig. 5.4, and these will also be shown in Figs. 5.7 and 5.8 below.

As expected, the least massive planet loses the most mass (panel (d)). In fact, the high γ, 3 $M_\oplus$ planet (dark purple) clearly undergoes rapid core-powered mass loss, in which contraction is slowed (panel (g)) by the heat released by the core, leading to a sharp increase in the luminosity and decrease in the cooling timescale with time (panels (b) and (c)), essentially becoming completely stripped. This is a marked difference from the low γ $3M_\oplus$ run, which loses only about 80% of its initial atmospheric mass before cooling sufficiently (panel (d)). In this case, the choice of upper atmosphere thermal profile is the difference between a planet retaining a 0.5% weight percent, $\sim 10^4$ bar hydrogen-dominated envelope after core-powered mass loss and none at all. The 10 $M_\oplus$ planet loses essentially no mass at all irrespective of the choice of γ, as it begins its evolution with its cooling timescale close to or shorter than its mass loss timescale (panel (i)).

In Fig. 5.7, we show the variation in atmospheric evolution for planets with equilibrium temperatures of 500, 750, 1000 and 1250 K. All four models have the same planet mass, $5M_\oplus$, initial

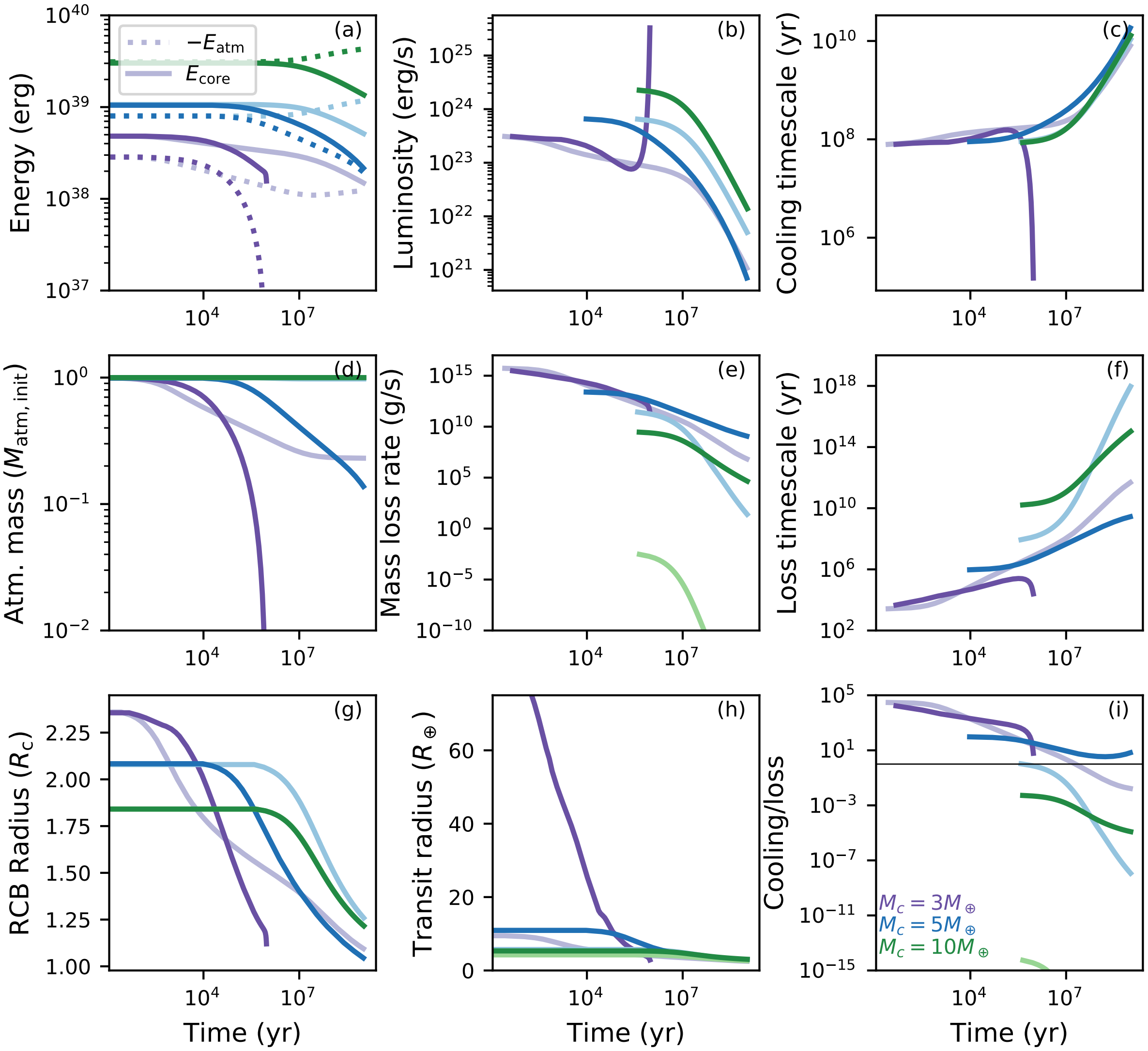

Figure 5.6: Evolution of planets of different masses in time using mass loss rates from AIOLOS hydrodynamics simulations. The panels are defined as they were in Fig. 5.4. Purple curves represent $3M_\oplus$, blue curves represent $5M_\oplus$, and green curves represent $10M_\oplus$. The lighter shade for each color represents a low opacity ratio, $\gamma = 0.03$, and the darker shade represents a high opacity ratio, $\gamma = 30$, depicting the range of outcomes possible under different upper atmosphere opacities.

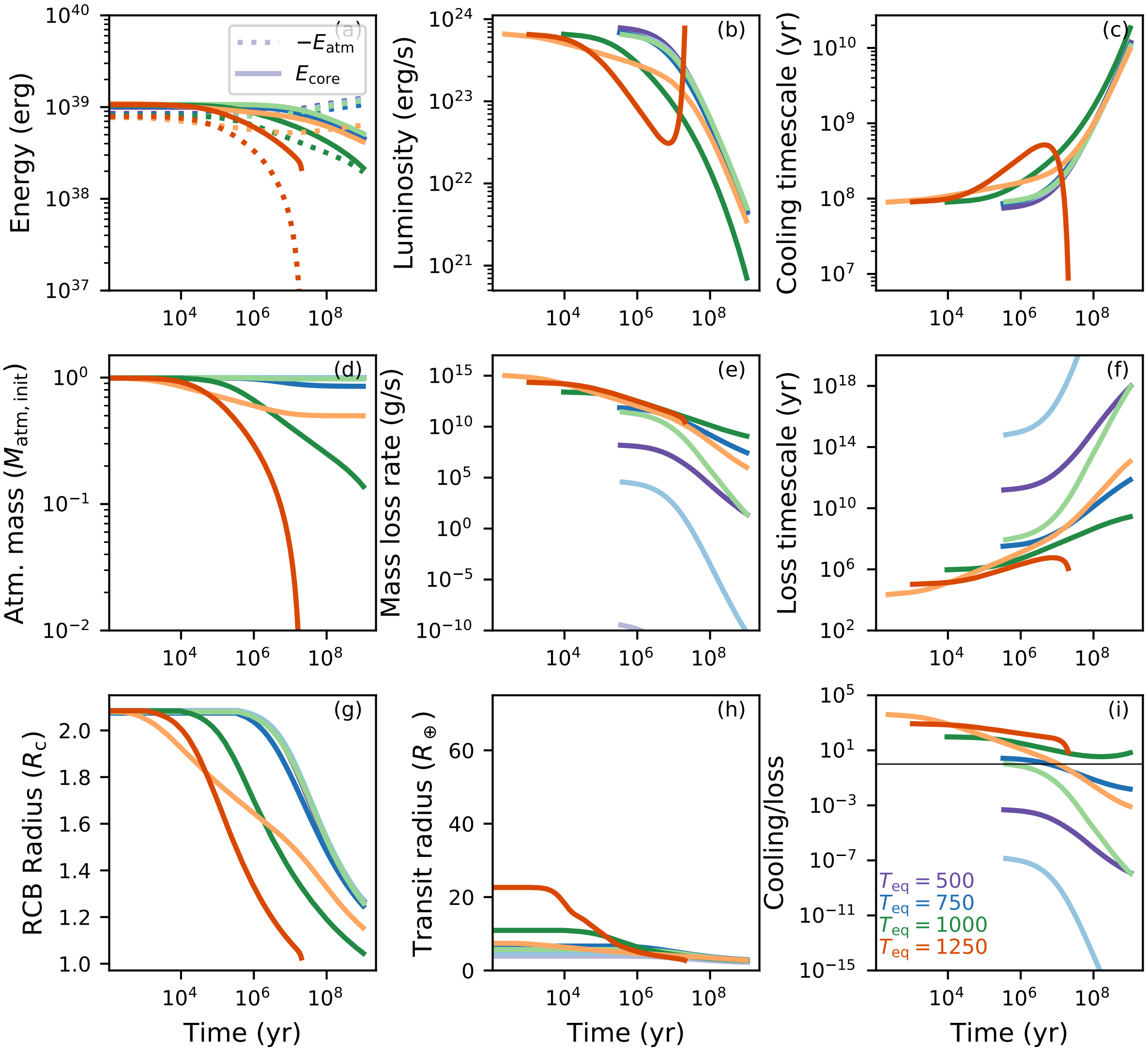

Figure 5.7: Evolution of planets of different equilibrium temperatures in time using mass loss rates from AIOLOS hydrodynamics simulations. The panels are defined as they were in Fig. 5.4. Purple curves represent $T_{\rm eq}$ = 500 K, blue curves represent $T_{\rm eq}$ = 750 K, green curves represent $T_{\rm eq}$ = 1000 K, and orange curves represent $T_{\rm eq}$ = 1250 K. The lighter shade for each color represents a low opacity ratio, γ = 0.03, and the darker shade represents a high opacity ratio, γ = 30, depicting the range of outcomes possible under different upper atmosphere opacities.

atmospheric mass fraction $f = 0.025$, and initial RCB radius $R_{\rm rcb} = 3R_{\rm c}$. As expected, the hotter planets lose more mass, while the coolest planet loses essentially none, similar to the large core mass planet above. For the coolest $T_{\rm eq} = 500$ K planet, essentially no mass is lost no matter the value of γ. The differences are more notable for the three hotter cases. As with the $3M_\oplus$ case, the choice of γ determines whether 50% of the initial envelope or essentially none of it remains for the hottest, $T_{\rm eq} = 1250$ K case.

In Fig. 5.8, we show the variation in atmospheric evolution for planets with initial atmospheric mass fractions of 1, 2.5, 5 and 10 per cent. All four models have the same planet mass, $5M_\oplus$ and equilibrium temperature $T_{\rm eq} = 1000$ K, with the initial RCB radius again chosen as described in Section 5.2. The more massive atmospheres begin larger and thus begin losing mass more quickly. All four planets lose at least twice as much mass over gigayear timescales in the $\gamma = 30$ cases as in the $\gamma = 0.03$ cases.

5.4 Discussion

5.4.1 Implications for planet demographics

Using an isothermal approximation for the outer atmosphere, core-powered mass loss has been shown to be consistent with the observed radius valley (Gupta & Schlichting, 2019). In this work, we have demonstrated that changing the value of γ in the outer atmosphere can change whether an atmosphere is retained or lost under the influence of core-powered mass loss. Due to these large variations in atmospheric escape different γ values impart, it may be possible to constrain the γ distribution consistent with observed demographics. However, such an inference would be highly degenerate with other unknown population-level characteristics, such as the core mass distribution. It is also plausible that γ varies highly from planet to planet due to the diversity of compositions possible for sub-Neptune atmospheres.

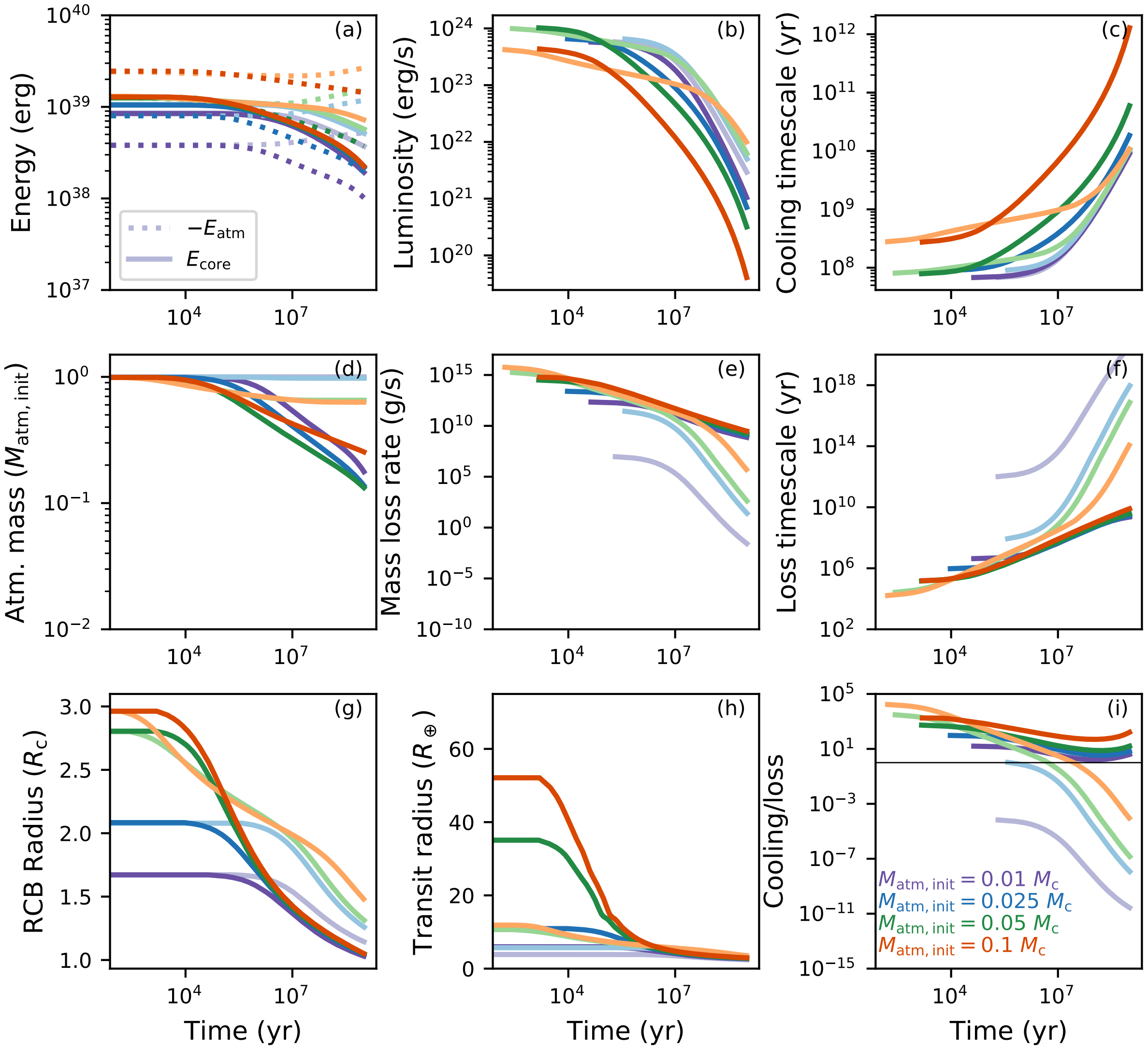

Figure 5.8: Evolution of planets of different initial atmospheric masses in time using mass loss rates from AIOLOS hydrodynamics simulations. The panels are defined as they were in Fig. 5.4. Purple curves represent $f = 0.01$, blue curves represent $f = 0.025$, green curves represent $f = 0.05$, and orange curves represent $f = 0.10$. The lighter shade for each color represents a low opacity ratio, $\gamma = 0.03$, and the darker shade represents a high opacity ratio, $\gamma = 30$, depicting the range of outcomes possible under different upper atmosphere opacities.

5.4.2 Comparison to direct observations

Observations of escaping atmospheres probe their mass loss rates. If these planets are undergoing bolometrically-driven escape, these measurements will constrain the temperature of the upper atmosphere, and therefore the atmospheric opacity ratio. Escape detections have been made using hydrogen Ly α 121 nm in the UV (e.g. Kulow et al., 2014; Ehrenreich et al., 2015) and He 1083 nm in the NIR (e.g. Mansfield et al., 2018) lines (see Dos Santos (2023) for a recent review). The mass loss rate is difficult to constrain precisely from these measurements, due to degeneracies between escape velocity and ionization by the stellar wind (Owen et al., 2023). But using existing models, these measurements have been fit by mass loss rate estimates for sub-Neptunes as low as 10^9 g s^{-1} (Ehrenreich et al., 2015; Mansfield et al., 2018). This measured rate is within the range of escape rates we predict on billion year timescales for some planet-γ combinations, indicating that directly testing upper atmospheric structure with escape observations is within reach of existing telescopic capabilities. However, such predictions will benefit from a fuller understanding of the transition between core-powered and photo-evaporative loss (see Section 5.4.4 below).

Spectroscopic observations, such as with the *James Webb Space Telescope*, can probe the milli- to microbar temperature structure of small exoplanets. With sufficient precision, these can put direct constraints on the possible γ values for those planets. In particular, inversions characteristic of high γ values lead to infrared molecular features in emission rather than absorption.

5.4.3 Opacity variations in space and time

In this work, we have assumed Planck opacities are constant as functions of planet radius and throughout a planet's evolution. However, these opacities depend on the composition of the atmosphere, which may vary significantly with both radius and time. From observations, sub-Neptunes appear to have a diversity of atmospheric compositions, with estimates varying from relatively low metallicities corresponding to solar composition or even more metal-poor (e.g. Barat et al., 2023) to nearly even mixtures by mass of H/He and heavier species (e.g. Benneke et al., 2024).

Theoretically, the chemical composition, and thus the opacity, of the upper atmosphere depends on a host of factors. Depending on the temperature profile, different gas species could be stable at chemical equilibrium, leading to variations in opacity and the opacity ratio with temperature (Freedman et al., 2014). Vertical mixing could then make the composition of the upper atmosphere more uniform, causing apparent disequilibrium chemistry (Fortney et al., 2020), but vigor of such vertical mixing in sub-Neptune atmospheres, often parameterized as the diffusion parameter K_{zz}, is highly uncertain. Recent work has also shown the importance of chemical reactions with the interior for sub-Neptune atmospheric composition, since in these planets, the bulk of the mass remains in the interior (Schlichting & Young, 2022). Considering these reactions leads to the potential for unexpected atmospheric constituents, such as silane (Misener et al., 2023), underscoring the inherent uncertainties in the opacity ratios typical of sub-Neptune upper atmospheres. The dependence of such reactions on the hydrogen content of the planet (Schlichting & Young, 2022; Rogers et al., 2024b) also highlights the potential for an evolution in atmospheric composition as hydrogen-rich material is removed via escape. This work establishes that such complexities may impact not just the interpretations of spectroscopic data from sub-Neptunes, but the evolution of the entire small planet population.

5.4.4 Inclusion of photo-evaporation

In this work, we do not include XUV radiation from the host star, and we therefore do not capture the effects of photo-evaporation. Photo-evaporation has long been thought to play an important role in the evolution of super-Earths and sub-Neptunes, leading to the prediction of the radius valley before its discovery (Owen & Wu, 2013). In all likelihood, core-powered mass loss and photo-evaporation both play a role in the evolution of small planets. The outflow may transition from being bolometrically-driven to XUV-driven as the planet contracts and loses mass, with the core's internal heat and the interior profile set by the absorption of bolometric radiation enhancing the atmospheric escape predicted from an XUV-driven outflow (Owen & Schlichting, 2024). However, the specifics of such a transition or mass loss enhancement have not been tested using hydrodynamic simulations. The AIOLOS code is capable of modelling XUV-driven outflows that reproduce previous results (Schulik & Booth, 2023). Future work will include XUV absorption in evolution models similar to those presented here to gain a more complete picture of the atmospheric evolution of small planets.

5.5 Conclusions

In this work, we model core-powered mass loss using a self-consistent radiative hydrodynamic code for the first time. We find that different opacity assumptions, specifically varying γ, the ratio between the opacity to incident stellar and the opacity to outgoing thermal radiation, changes the thermal and density profile in the upper atmosphere. Since the mass loss rate is sensitive to the temperature and density at the sonic radius, these changes in density structure affect the mass loss rate. We find that over a range of physically plausible values of γ, core-powered mass loss rates can vary by orders of magnitude. For a $5M_\oplus$ planet at $T_{\rm eq} = 1000$ K and an RCB radius $\sim 1.2R_{\rm c}$, the mass loss rate can vary a factor of 10^{10} over a factor of 1000 change in γ. The differences between γ values decrease for more inflated planet radii, converging to an analytic value given by approximating the wind as an isothermal Parker-type outflow at temperature $T = T_{\rm in} = T_{\rm eq}/2^{1/4}$. We incorporate these mass loss rates into a mass and thermal evolution model and show that varying γ leads to variations in the evolution and expected final state of the atmosphere. Depending on the planet's parameters, including planet mass, atmospheric mass, and equilibrium temperature, the choice of γ can make the difference between whether a planet retains a significant hydrogen atmosphere after core-powered mass loss. More massive atmospheres are favored for lower γ values due to the lower temperatures in the upper atmosphere.

These results are relevant for predicting mass loss rates for known exoplanets. For $\gamma = 1$, an isothermal outflow is a good approximation of our hydrodynamic results, but at a temperature slightly lower than the equilibrium temperature. But if γ is known by other methods, such as retrievals of the temperature profile or an inferred composition, then the mass loss rate could be substantially different than the isothermal approximation. These considerations are most important for planets which have already contracted, allowing more of the outer radiative region at $T \sim T_{\rm out}$ to enter the sub-sonic region. For inflated planets, the isothermal formula well-approximates our hydrodynamic results.

Inverting this problem, these results indicate an avenue to directly constrain the opacity ratio γ via detections of atmospheric escape. Knowledge of the relative opacities in the upper atmosphere could then allow for inferences the composition of the upper atmosphere. Moreover, by modeling core-powered mass loss in a hydrodynamic radiative-transfer code, this work paves the way for the self-consistent combination of core-powered and photo-evaporative escape.

Acknowledgements

In this work we use the NUMPY (Harris et al., 2020), MATPLOTLIB (Hunter, 2007), and SCIPY (Virtanen et al., 2020) packages.

CHAPTER 6

Summary

Planetary science has been revolutionized by the discovery of thousands of exoplanets. These discoveries have shown us that many planets formed and evolved in pathways distinct from the Solar System planets. In particular, the insight that super-Earths and sub-Neptunes, planets between about 1 and 4 Earth radii which receive more flux from their host stars than Mercury, are abundant and may all accrete substantial primordial hydrogen envelopes has prompted extensive theoretical work. My dissertation has advanced our knowledge of these planets by demonstrating that the link between these planets' interiors and atmospheres is fundamental to understanding sub-Neptunes as physical systems. I have shown that these planets' basic structure, evolution in time, and the current state and composition of their atmosphere all hinge on the nature of atmosphere-interior interactions. I summarize the main results below:

- **To cool is to keep: Residual H/He atmospheres of super-Earths and sub-Neptunes**
  In Chapter 2, published as Misener & Schlichting (2021), I show that core-powered mass loss does not result in completely stripped primordial H-rich atmospheres for some super-Earths. Core-powered mass loss occurs because the silicate core has a sufficiently large heat capacity to dominate the energy budget of the planet, resupplying energy into the atmosphere as it cools into space. This fundamental physics requires the system's mass loss timescale to be shorter than its cooling timescale to sustain atmospheric stripping. But as planets lose significant atmospheric mass, they cool more quickly into space. This cooling can in some cases outpace mass loss as core-powered mass loss proceeds, allowing atmospheric contraction and preserving whatever atmosphere remains. I use analytic arguments and planet mass

and thermal evolution models to demonstrate that the preserved atmospheric mass is a strong function of the planet's mass and equilibrium temperature. My finding that some super-Earths may retain reducing hydrogen atmospheres after undergoing hydrodynamic atmospheric escape has important implications for understanding what appears to be a common rocky planet formation pathways. It predicts strongly reducing atmospheres to play a long-term role in these planets' chemical evolution. The existence of primordial atmospheres also implies that some super-Earths may be amenable to characterization by transmission spectroscopy, which would be much more difficult if their atmospheres were dominated by heavier species. Strong XUV flux from the star may imperil the gigayear-timescale preservation of the thinner atmospheres predicted.

- **The importance of silicate vapor in determining the structure, radii, and envelope mass fractions of sub-Neptunes**
  In Chapter 3, published as Misener & Schlichting (2022), I show that the link between sub-Neptune atmospheres and interiors goes beyond their thermal coupling. At chemical equilibrium at the conditions expected at the base of sub-Neptune atmospheres, silicate vapor is abundant in the gas phase. Its gas phase abundance then declines with altitude as temperatures decrease. The condensation of silicate vapor induces a steep molecular weight gradient in the atmosphere. Such a gradient stabilizes an atmosphere against convection, due to the weight of deeper parcels overcoming their thermal buoyancy. Therefore, silicate vapor leads to deep non-convective regions within sub-Neptunes that change the structure of the atmosphere. I demonstrated using atmospheric structure models that non-convective regions decrease the radius of a planet compared to the typically used, fully convective models. Therefore, inferences of atmospheric mass from observed exoplanets using these fully convective models tend to under-estimate the hydrogen mass fraction of known sub-Neptunes. I implemented these new structure models into a thermal evolution model to demonstrate that the deviations from a fully convective model are largest for younger planets, but persist on gigayear timescales for some sub-Neptunes.

- **Atmospheres as windows into sub-Neptune interiors: coupled chemistry and structure of hydrogen-silane-water envelopes**

  In Chapter 4, published as Misener et al. (2023), I show that silicate vapor present at the base of sub-Neptune atmospheres reacts strongly with the background hydrogen gas. This reaction produces significant quantities of endogenic water in these planets, as well as reduced silicon species, such as silane, SiH_4. It also changes the chemical balance of the deep atmosphere, drawing more silicates out of the interior. I couple chemical equilibrium models with atmospheric structure models to show that these compositional details alter the entire atmospheric profile. My findings provide a new observable signature of atmosphere-interior interactions and demonstrate that consideration of this coupling leads to dramatic new insights about planetary composition and evolution.

- **Gone with the non-isothermal wind: hydrodynamic modeling of core-powered mass loss with non-grey opacities**

  In Chapter 5, currently in preparation for submission, I show that mass evolution core-powered mass loss is sensitive to the thermal structure of the upper radiative region of the atmosphere. In previous work, this region had been modeled analytically as isothermal at the equilibrium temperature. Using AIOLOS, a hydrodynamic radiative transfer code, I demonstrate that for plausible non-gray opacities, in which the opacity to incident stellar radiation is not equal to the opacity to outgoing thermal radiation, the mass loss rate can be strongly affected. If the opacity to visible, stellar radiation is larger than the opacity to infrared, thermal radiation, a thermal inversion occurs, heating the outer atmosphere and increasing the mass loss rate. Conversely, if the opacity to stellar radiation is less than the opacity to thermal radiation, then the outer atmosphere is cold, decreasing the mass loss rate. I show that the differences between opacity assumptions are largest for small planet radii, while large planets are well-approximated by an isothermal wind at a temperature slightly below the equilibrium temperature. I then couple these mass loss rates to thermal evolution to demonstrate that lower stellar-to-thermal opacity ratios lead to more hydrogen retention.

> These differences in mass loss rate could put constraints on the thermal structure of planets with observed mass loss, and they set the stage for combined hydrodynamic modeling of core-powered and photo-evaporative mass loss.

My dissertation work has trail-blazed many exciting paths forward in the field of exoplanetary science, especially in probing the interactions implied by the inferred compositions of planets. One potential avenue enabled by my thesis work is coupling more complex mantle chemical models which include the full expected composition with atmospheric structure models. Including additional mantle species will determine how variations in interior composition manifest in atmospheric composition, mapping the way to probing bulk elemental abundances with atmospheric spectroscopy. Another near-term potential route is the full combination of core-powered and photo-evaporative mass loss into one self-consistent hydrodynamic model, which will allow predictions of how planets evolve in mass and ultimately to distinguish how these processes determine the observed demographics. Finally, my work has paved the way toward fully understanding the end state of super-Earth atmospheres which have been subject to strong coupling between their natal hydrogen atmospheres and rocky interiors. This knowledge is fundamental to understanding the current state and potential for life of the most common class of terrestrial planets known to date. These directions will be enhanced by the ongoing discoveries of the *James Webb Space Telescope*, the enhanced demographics enabled by the ongoing *TESS* (Kunimoto et al., 2022) and future *Plato* (Matuszewski et al., 2023) and *Roman* spacecraft (Wilson et al., 2023), advances in ground-based spectroscopy and radial velocity measurements enabled by Extremely Large Telescopes (Gandhi et al., 2020), and the atmospheric census enabled by the *Ariel* mission (Edwards & Tinetti, 2022). Most fundamentally, the passion, insight, and innovation of planetary and exoplanetary scientists will continue to produce incredible advances in humanity's comprehension of the beauty of the universe around us.

Bibliography

Agol, E., & Fabrycky, D. C. 2018, in Handbook of Exoplanets, ed. H. J. Deeg & J. A. Belmonte, 7

Alderson, L., Wakeford, H. R., Alam, M. K., et al. 2023, Nature, 614, 664

Bailey, E., & Stevenson, D. J. 2021, PSJ, 2, 64

Barat, S., Désert, J.-M., Vazan, A., et al. 2023, arXiv e-prints, arXiv:2312.16924

Batalha, N. E., Wolfgang, A., Teske, J., et al. 2023, AJ, 165, 14

Bauschlicher, Charles W., J., Jacobson, N. S., & Fegley, Bruce, J. 2023, Journal of Physical Chemistry A, 127, 8892

Bean, J. L., Raymond, S. N., & Owen, J. E. 2021, Journal of Geophysical Research (Planets), 126, e06639

Benneke, B., & Seager, S. 2012, ApJ, 753, 100

Benneke, B., Knutson, H. A., Lothringer, J., et al. 2019a, Nature Astronomy, 3, 813

Benneke, B., Wong, I., Piaulet, C., et al. 2019b, ApJ, 887, L14

Benneke, B., Roy, P.-A., Coulombe, L.-P., et al. 2024, arXiv e-prints, arXiv:2403.03325

Berger, T. A., Huber, D., Gaidos, E., van Saders, J. L., & Weiss, L. M. 2020, AJ, 160, 108

Bézard, B., Charnay, B., & Blain, D. 2022, Nature Astronomy, 6, 537

Biersteker, J. B., & Schlichting, H. E. 2019, MNRAS, 485, 4454

—. 2021, MNRAS, 501, 587

Birch, F. 1964, J. Geophys. Res., 69, 4377

Bitsch, B., Raymond, S. N., & Izidoro, A. 2019, A&A, 624, A109

Blunt, S., Carvalho, A., David, T. J., et al. 2023, AJ, 166, 62

Brande, J., Crossfield, I. J. M., Kreidberg, L., et al. 2024, ApJ, 961, L23

Brouwers, M. G., & Ormel, C. W. 2020, A&A, 634, A15

Burn, R., Mordasini, C., Mishra, L., et al. 2024, Nature Astronomy, arXiv:2401.04380 [astro-ph.EP]

Burningham, B., Faherty, J. K., Gonzales, E. C., et al. 2021, MNRAS, 506, 1944

Burrows, A., Hubeny, I., Budaj, J., Knutson, H. A., & Charbonneau, D. 2007, ApJ, 668, L171

Burrows, A., & Sharp, C. M. 1999, ApJ, 512, 843

Chachan, Y., & Stevenson, D. J. 2018, ApJ, 854, 21

Charnoz, S., Falco, A., Tremblin, P., et al. 2023, A&A, 674, A224

Chase, Jr., M. 1998, Journal of Physical and Chemical Reference Data, Monograph 9, 1

Christiansen, J. L., Zink, J. K., Hardegree-Ullman, K. K., et al. 2023, AJ, 166, 248

Cloutier, R., & Menou, K. 2020, AJ, 159, 211

Cumming, A., Helled, R., & Venturini, J. 2018, MNRAS, 477, 4817

Dai, F., Masuda, K., Winn, J. N., & Zeng, L. 2019, ApJ, 883, 79

Dauphas, N., & Pourmand, A. 2011, Nature, 473, 489

David, T. J., Contardo, G., Sandoval, A., et al. 2021, AJ, 161, 265

Donahue, T. M., Hoffman, J. H., Hodges, R. R., & Watson, A. J. 1982, Science, 216, 630

Dorn, C., & Lichtenberg, T. 2021, ApJ, 922, L4

Dorn, C., Venturini, J., Khan, A., et al. 2017, A&A, 597, A37

Dos Santos, L. A. 2023, IAU Symposium, 370, 56

Doyle, A. E., Young, E. D., Klein, B., Zuckerman, B., & Schlichting, H. E. 2019, Science, 366, 356

Edwards, B., Mugnai, L., Tinetti, G., Pascale, E., & Sarkar, S. 2019, AJ, 157, 242

Edwards, B., & Tinetti, G. 2022, AJ, 164, 15

Ehrenreich, D., Bourrier, V., Wheatley, P. J., et al. 2015, Nature, 522, 459

Emsenhuber, A., Mordasini, C., Burn, R., et al. 2021, A&A, 656, A70

Erkaev, N. V., Kulikov, Y. N., Lammer, H., et al. 2007, A&A, 472, 329

van Eylen, V., Agentoft, C., Lundkvist, M. S., et al. 2018, MNRAS, 479, 4786

Fabrycky, D. C., Lissauer, J. J., Ragozzine, D., et al. 2014, ApJ, 790, 146

Falco, A., Tremblin, P., Charnoz, S., Ridgway, R. J., & Lagage, P.-O. 2024, A&A, 683, A194

Fegley, B., & Cameron, A. G. W. 1987, Earth and Planetary Science Letters, 82, 207

Fegley, Jr., B., & Lodders, K. 1994, Icarus, 110, 117

Fegley, Jr., B., & Schaefer, L. 2012, arXiv e-prints, arXiv:1210.0270

Fegley, Bruce, J., Jacobson, N. S., Williams, K. B., et al. 2016, ApJ, 824, 103

Fortney, J. J., Lodders, K., Marley, M. S., & Freedman, R. S. 2008, ApJ, 678, 1419

Fortney, J. J., Mordasini, C., Nettelmann, N., et al. 2013, ApJ, 775, 80

Fortney, J. J., Visscher, C., Marley, M. S., et al. 2020, AJ, 160, 288

Freedman, R. S., Lustig-Yaeger, J., Fortney, J. J., et al. 2014, ApJS, 214, 25

Freedman, R. S., Marley, M. S., & Lodders, K. 2008, ApJS, 174, 504

French, M., Becker, A., Lorenzen, W., et al. 2012, ApJS, 202, 5

Fressin, F., Torres, G., Charbonneau, D., et al. 2013, ApJ, 766, 81

Fulton, B. J., & Petigura, E. A. 2018, AJ, 156, 264

Fulton, B. J., Petigura, E. A., Howard, A. W., et al. 2017, AJ, 154, 109

Gaillard, F., & Scaillet, B. 2014, Earth and Planetary Science Letters, 403, 307

Gandhi, S., Brogi, M., & Webb, R. K. 2020, MNRAS, 498, 194

Gao, P., & Powell, D. 2021, ApJ, 918, L7

Gibson, S. R., Howard, A. W., Rider, K., et al. 2020, in Society of Photo-Optical Instrumentation Engineers (SPIE) Conference Series, Vol. 11447, Society of Photo-Optical Instrumentation Engineers (SPIE) Conference Series, 1144742

Ginzburg, S., Schlichting, H. E., & Sari, R. 2016, ApJ, 825, 29

—. 2018, MNRAS, 476, 759

Graham, R. J., Lichtenberg, T., Boukrouche, R., & Pierrehumbert, R. T. 2021, PSJ, 2, 207

Greene, T. P., Line, M. R., Montero, C., et al. 2016, ApJ, 817, 17

Guillot, T. 1995, Science, 269, 1697

—. 2010, A&A, 520, A27

Gupta, A., & Schlichting, H. E. 2019, MNRAS, 487, 24

—. 2020, MNRAS, 493, 792

—. 2021, MNRAS, 504, 4634

Hansen, B. M. S., & Murray, N. 2012, ApJ, 751, 158

Hardegree-Ullman, K. K., Zink, J. K., Christiansen, J. L., et al. 2020, ApJS, 247, 28

Harris, C. R., Jarrod Millman, K., van der Walt, S. J., et al. 2020, Nature, 505, 357

Hayashi, C. 1981, Progress of Theoretical Physics Supplement, 70, 35

Helled, R., & Fortney, J. J. 2020, Philosophical Transactions of the Royal Society of London Series A, 378, 20190474

Hirschmann, M. M., Withers, A. C., Ardia, P., & Foley, N. T. 2012, Earth and Planetary Science Letters, 345, 38

Huang, C., Rice, D. R., & Steffen, J. H. 2022, MNRAS, 513, 5256

Hubeny, I., Burrows, A., & Sudarsky, D. 2003, ApJ, 594, 1011

Hunten, D. M., Pepin, R. O., & Walker, J. C. G. 1987, Icarus, 69, 532

Hunter, J. D. 2007, Computing in Science and Engineering, 9, 90

Ikoma, M., & Hori, Y. 2012, ApJ, 753, 66

Inamdar, N. K., & Schlichting, H. E. 2015, MNRAS, 448, 1751

Innes, H., Tsai, S.-M., & Pierrehumbert, R. T. 2023, ApJ, 953, 168

Ito, Y., Ikoma, M., Kawahara, H., et al. 2015, ApJ, 801, 144

Izidoro, A., Ogihara, M., Raymond, S. N., et al. 2017, MNRAS, 470, 1750

Izidoro, A., Schlichting, H. E., Isella, A., et al. 2022, ApJ, 939, L19

Jackson, A. P., Davis, T. A., & Wheatley, P. J. 2012, MNRAS, 422, 2024

JWST Transiting Exoplanet Community Early Release Science Team, Ahrer, E.-M., Alderson, L., et al. 2023, Nature, 614, 649

Karato, S.-i., Karki, B., & Park, J. 2020, Progress in Earth and Planetary Science, 7, 76

Kasting, J. F. 1993, Science, 259, 920

Kempton, E. M. R., Bean, J. L., Louie, D. R., et al. 2018, PASP, 130, 114401

Kempton, E. M. R., Zhang, M., Bean, J. L., et al. 2023, Nature, 620, 67

Kim, T., Wei, X., Chariton, S., et al. 2023, Proceedings of the National Academy of Science, 120, e2309786120

Kite, E. S., Fegley, Jr., B., Schaefer, L., & Ford, E. B. 2019, ApJ, 887, L33

Kite, E. S., Fegley, Bruce, J., Schaefer, L., & Ford, E. B. 2020, ApJ, 891, 111

Koepferl, C. M., Ercolano, B., Dale, J., et al. 2013, MNRAS, 428, 3327

de Koker, N., & Stixrude, L. 2009, Geophysical Journal International, 178, 162

Kreidberg, L., Bean, J. L., Désert, J.-M., et al. 2014, Nature, 505, 69

Krenn, A. F., Fossati, L., Kubyshkina, D., & Lammer, H. 2021, A&A, 650, A94

Kubyshkina, D., Fossati, L., Erkaev, N. V., et al. 2018, ApJ, 866, L18

Kulow, J. R., France, K., Linsky, J., & Loyd, R. O. P. 2014, ApJ, 786, 132

Kunimoto, M., Winn, J., Ricker, G. R., & Vanderspek, R. K. 2022, AJ, 163, 290

Leconte, J., Selsis, F., Hersant, F., & Guillot, T. 2017, A&A, 598, A98

Leconte, J., Spiga, A., Clément, N., et al. 2024, arXiv e-prints, arXiv:2401.06608

Ledoux, P. 1947, ApJ, 105, 305

Lee, E. J., & Chiang, E. 2015, ApJ, 811, 41

Lee, E. J., Chiang, E., & Ormel, C. W. 2014, ApJ, 797, 95

Libby-Roberts, J., Mahadevan, S., Masuda, K., et al. 2024, in American Astronomical Society Meeting Abstracts, Vol. 56, American Astronomical Society Meeting Abstracts, 444.04

Lichtenberg, T. 2021, ApJ, 914, L4

Lichtenberg, T., Bower, D. J., Hammond, M., et al. 2021, Journal of Geophysical Research (Planets), 126, e06711

Lodders, K. 2021, Space Sci. Rev., 217, 44

Lopez, E. D., & Fortney, J. J. 2013, ApJ, 776, 2

—. 2014, ApJ, 792, 1

Lopez, E. D., Fortney, J. J., & Miller, N. 2012, ApJ, 761, 59

Loyd, R. O. P., Shkolnik, E. L., Schneider, A. C., et al. 2020, ApJ, 890, 23

Luque, R., & Pallé, E. 2022, Science, 377, 1211

Madhusudhan, N., Nixon, M. C., Welbanks, L., Piette, A. A. A., & Booth, R. A. 2020, ApJ, 891, L7

Madhusudhan, N., Sarkar, S., Constantinou, S., et al. 2023, ApJ, 956, L13

Malsky, I., Rogers, L., Kempton, E. M. R., & Marounina, N. 2023, Nature Astronomy, 7, 57

Mamajek, E. E. 2009, in American Institute of Physics Conference Series, Vol. 1158, Exoplanets and Disks: Their Formation and Diversity, ed. T. Usuda, M. Tamura, & M. Ishii, 3

Mankovich, C. R., & Fuller, J. 2021, Nature Astronomy, 5, 1103

Mansfield, M., Bean, J. L., Oklopčić, A., et al. 2018, ApJ, 868, L34

Markham, S., Guillot, T., & Stevenson, D. 2022, A&A, 665, A12

Markham, S., & Stevenson, D. 2021, PSJ, 2, 146

Marois, C., Zuckerman, B., Konopacky, Q. M., Macintosh, B., & Barman, T. 2010, Nature, 468, 1080

Matuszewski, F., Nettelmann, N., Cabrera, J., Börner, A., & Rauer, H. 2023, A&A, 677, A133

Mayor, M., & Queloz, D. 1995, Nature, 378, 355

Mazeh, T., Holczer, T., & Faigler, S. 2016, A&A, 589, A75

McDonald, G. D., Kreidberg, L., & Lopez, E. 2019, ApJ, 876, 22

McWilliams, R. S., Dalton, D. A., Mahmood, M. F., & Goncharov, A. F. 2016, Phys. Rev. Lett., 116, 255501

Misener, W., Krijt, S., & Ciesla, F. J. 2019, ApJ, 885, 118

Misener, W., & Schlichting, H. E. 2021, MNRAS, 503, 5658

—. 2022, MNRAS, 514, 6025

Misener, W., Schlichting, H. E., & Young, E. D. 2023, MNRAS, 524, 981

Moran, S. E., Stevenson, K. B., Sing, D. K., et al. 2023, ApJ, 948, L11

Moses, J. I., Line, M. R., Visscher, C., et al. 2013, ApJ, 777, 34

Mousis, O., Deleuil, M., Aguichine, A., et al. 2020, ApJ, 896, L22

Movshovitz, N., & Fortney, J. J. 2022, PSJ, 3, 88

Müller, A., Keppler, M., Henning, T., et al. 2018, A&A, 617, L2

Murray-Clay, R. A., Chiang, E. I., & Murray, N. 2009, ApJ, 693, 23

National Academies of Sciences, E., & Medicine. 2021, Pathways to Discovery in Astronomy and Astrophysics for the 2020s

Nixon, M. C., & Madhusudhan, N. 2021, MNRAS, 505, 3414

Olson, P. L., & Sharp, Z. D. 2019, Physics of the Earth and Planetary Interiors, 294, 106294

Ormel, C. W., Vazan, A., & Brouwers, M. G. 2021, A&A, 647, A175

Otsuka, K., & Karato, S.-I. 2011, Physics of the Earth and Planetary Interiors, 189, 27

Owen, J. E., & Jackson, A. P. 2012, MNRAS, 425, 2931

Owen, J. E., & Mohanty, S. 2016, MNRAS, 459, 4088

Owen, J. E., & Schlichting, H. E. 2024, MNRAS, 528, 1615

Owen, J. E., & Wu, Y. 2013, ApJ, 775, 105

—. 2016, ApJ, 817, 107

—. 2017, ApJ, 847, 29

Owen, J. E., Murray-Clay, R. A., Schreyer, E., et al. 2023, MNRAS, 518, 4357

Owens, A., Yachmenev, A., Thiel, W., Tennyson, J., & Yurchenko, S. N. 2017, MNRAS, 471, 5025

Parker, E. N. 1958, ApJ, 128, 664

Parmentier, V., & Guillot, T. 2014, A&A, 562, A133

Parmentier, V., Guillot, T., Fortney, J. J., & Marley, M. S. 2015, A&A, 574, A35

Pearl, J. C., & Conrath, B. J. 1991, J. Geophys. Res., 96, 18921

Pearl, J. C., Conrath, B. J., Hanel, R. A., Pirraglia, J. A., & Coustenis, A. 1990, Icarus, 84, 12

Pepe, F., Cristiani, S., Rebolo, R., et al. 2021, A&A, 645, A96

Petersburg, R. R., Ong, J. M. J., Zhao, L. L., et al. 2020, AJ, 159, 187

Petigura, E. A., Howard, A. W., & Marcy, G. W. 2013, Proceedings of the National Academy of Science, 110, 19273

Petigura, E. A., Rogers, J. G., Isaacson, H., et al. 2022, AJ, 163, 179

Pierrehumbert, R. T. 2023, ApJ, 944, 20

Piette, A. A. A., Gao, P., Brugman, K., et al. 2023, ApJ, 954, 29

Piso, A.-M. A., & Youdin, A. N. 2014, ApJ, 786, 21

Pollack, J. B., Hubickyj, O., Bodenheimer, P., et al. 1996, Icarus, 124, 62

Poppenhaeger, K., Ketzer, L., & Mallonn, M. 2021, MNRAS, 500, 4560

Rafikov, R. R. 2006, ApJ, 648, 666

Rogers, J. G., Gupta, A., Owen, J. E., & Schlichting, H. E. 2021, MNRAS, 508, 5886

Rogers, J. G., & Owen, J. E. 2021, MNRAS, 503, 1526

Rogers, J. G., Owen, J. E., & Schlichting, H. E. 2024a, MNRAS, 529, 2716

Rogers, J. G., Schlichting, H. E., & Owen, J. E. 2023, ApJ, 947, L19

Rogers, J. G., Schlichting, H. E., & Young, E. D. 2024b, arXiv e-prints, arXiv:2402.14072

Rogers, L. A., & Seager, S. 2010, ApJ, 712, 974

Rustamkulov, Z., Sing, D. K., Mukherjee, S., et al. 2023, Nature, 614, 659

Salz, M., Czesla, S., Schneider, P. C., & Schmitt, J. H. M. M. 2016, A&A, 586, A75

Schaefer, L., & Fegley, B. 2004, Icarus, 169, 216

Schlichting, H. E. 2014, ApJ, 795, L15

—. 2018, in Handbook of Exoplanets, ed. H. J. Deeg & J. A. Belmonte (Springer), 141

Schlichting, H. E., & Young, E. D. 2022, PSJ, 3, 127

Schulik, M., & Booth, R. A. 2023, MNRAS, 523, 286

Scipioni, R., Stixrude, L., & Desjarlais, M. P. 2017, Proceedings of the National Academy of Science, 114, 9009

Seager, S., Bains, W., & Hu, R. 2013, ApJ, 777, 95

Seager, S., Huang, J., Petkowski, J. J., & Pajusalu, M. 2020, Nature Astronomy, 4, 802

Seager, S., Kuchner, M., Hier-Majumder, C. A., & Militzer, B. 2007, ApJ, 669, 1279

Seifahrt, A., Bean, J. L., Kasper, D., et al. 2022, in Society of Photo-Optical Instrumentation Engineers (SPIE) Conference Series, Vol. 12184, Ground-based and Airborne Instrumentation for Astronomy IX, ed. C. J. Evans, J. J. Bryant, & K. Motohara, 121841G

Shinozaki, A., Hirai, H., Ohfuji, H., et al. 2013, American Mineralogist, 98, 1604

Shinozaki, A., Kagi, H., Hirai, H., et al. 2016, Physics and Chemistry of Minerals, 43, 277

Shinozaki, A., Kagi, H., Noguchi, N., et al. 2014, American Mineralogist, 99, 1265

Soubiran, F., Militzer, B., Driver, K. P., & Zhang, S. 2017, Physics of Plasmas, 24, 041401

Steffen, J. H., Fabrycky, D. C., Agol, E., et al. 2013, MNRAS, 428, 1077

Steinmeyer, M.-L., & Johansen, A. 2024, A&A, 683, A217

Stevenson, D. J., Spohn, T., & Schubert, G. 1983, Icarus, 54, 466

Stixrude, L., Baroni, S., & Grasselli, F. 2021, PSJ, 2, 222

Tamblyn, I., & Bonev, S. A. 2010, Phys. Rev. Lett., 104, 065702

Tanaka, H., Takeuchi, T., & Ward, W. R. 2002, ApJ, 565, 1257

Tennyson, J., Yurchenko, S. N., Al-Refaie, A. F., et al. 2016, Journal of Molecular Spectroscopy, 327, 73

Thiemens, M. M., Sprung, P., Fonseca, R. O. C., Leitzke, F. P., & Münker, C. 2019, Nature Geoscience, 12, 696

Thompson, S. J., Queloz, D., Baraffe, I., et al. 2016, in Society of Photo-Optical Instrumentation Engineers (SPIE) Conference Series, Vol. 9908, Ground-based and Airborne Instrumentation for Astronomy VI, ed. C. J. Evans, L. Simard, & H. Takami, 99086F

Trierweiler, I. L., Doyle, A. E., & Young, E. D. 2023, PSJ, 4, 136

Tu, L., Johnstone, C. P., Güdel, M., & Lammer, H. 2015, A&A, 577, L3

Unterborn, C. T., Desch, S. J., Hinkel, N. R., & Lorenzo, A. 2018, Nature Astronomy, 2, 297

Valencia, D., O'Connell, R. J., & Sasselov, D. 2006, Icarus, 181, 545

Vazan, A., & Helled, R. 2020, A&A, 633, A50

Vazan, A., Helled, R., & Guillot, T. 2018, A&A, 610, L14

Vazan, A., & Ormel, C. W. 2023, A&A, 676, L8

Vazan, A., Sari, R., & Kessel, R. 2022, ApJ, 926, 150

Venturini, J., Guilera, O. M., Haldemann, J., Ronco, M. P., & Mordasini, C. 2020, A&A, 643, L1

Virtanen, P., Gommers, R., Oliphant, T. E., et al. 2020, Nature Methods, 17, 261

Visscher, C., & Fegley, Jr., B. 2013, ApJ, 767, L12

Visscher, C., Lodders, K., & Fegley, Jr., B. 2010a, ApJ, 716, 1060

Visscher, C., Moses, J. I., & Saslow, S. A. 2010b, Icarus, 209, 602

Wahl, S. M., Hubbard, W. B., Militzer, B., et al. 2017, Geophys. Res. Lett., 44, 4649

Watson, A. J., Donahue, T. M., & Walker, J. C. G. 1981, Icarus, 48, 150

Weidenschilling, S. J. 1977, MNRAS, 180, 57

Weiss, L. M., & Marcy, G. W. 2014, ApJ, 783, L6

Wiechert, U., Halliday, A. N., Lee, D. C., et al. 2001, Science, 294, 345

Wilson, H. F., & Militzer, B. 2010, Phys. Rev. Lett., 104, 121101

Wilson, R. F., Barclay, T., Powell, B. P., et al. 2023, ApJS, 269, 5

Wogan, N. F., Catling, D. C., Zahnle, K. J., & Lupu, R. 2023, PSJ, 4, 169

Wolfgang, A., & Lopez, E. 2015, ApJ, 806, 183

Wordsworth, R. D., Schaefer, L. K., & Fischer, R. A. 2018, AJ, 155, 195

Wunderlich, F., Scheucher, M., Grenfell, J. L., et al. 2021, A&A, 647, A48

Xiao, B., & Stixrude, L. 2018, Proceedings of the National Academy of Science, 115, 5371

Yang, C.-C., Johansen, A., & Carrera, D. 2017, A&A, 606, A80

Young, E. D., Shahar, A., & Schlichting, H. E. 2023, Nature, 616, 306

Zahnle, K. J., & Kasting, J. F. 1986, Icarus, 68, 462

Zeng, L., Jacobsen, S. B., Sasselov, D. D., et al. 2019, Proceedings of the National Academy of Science, 116, 9723

Zilinskas, M., Miguel, Y., van Buchem, C. P. A., & Snellen, I. A. G. 2023, A&A, 671, A138